Sulphide Re-Os Characterisation and Nitrogen Aggregation State of the Ellendale diamonds, Kimberley Province, Australia

Karen Vena Smit

Submitted in fulfilment of the
requirements of the degree of
MASTER OF SCIENCE

December 2008

Department of Geological Sciences

The University of Cape Town

Trust in the Lord with all your heart
and lean not on your own understanding
but in all your ways acknowledge Him
and He will direct your paths

Abstract

A suite of sulphide-bearing diamonds recovered from the Ellendale 4 and 9 pipes in the Ellendale diamond province of lamproite intrusions in north-western Australia have been investigated for their nitrogen aggregation state and the Re-Os isotope geochemistry of the sulphide inclusions.

The Ellendale lamproites, dated at ca. 20 Ma (Allsopp *et al.*, 1985) intrude the King Leopold Mobile Belt just south of the Kimberley craton and are thus an atypical, off-craton diamondiferous locality. The diamonds contain roughly equal proportions of peridotitic and eclogitic inclusions (Hall & Smith, 1984; Griffin *et al.*, 1988; Jaques *et al.*, 1989).

The diamonds in this study range in size from 0.26 to 0.92 carats and are dominated, with the exception of one octahedron, by highly resorbed tetrahexahedroida. The diamonds are mainly yellow, with variable degrees of colour intensity including twelve colourless specimens. Cathodoluminescence images of the diamond plates were taken in order to reveal internal growth zonation. The diamonds exhibit an octahedral growth habit, consistent with growth under conditions of lower carbon supersaturation (Sunagawa, 1984a,b) though some diamonds show complex growth zones indicating several micro growth centres.

The diamonds in this study are dominated by Type IaAB diamonds that have a high average nitrogen content ($\sim$ 600 ppm) and high levels of nitrogen aggregation (71% of analyses have $>$ 50% IaB). Time-averaged mantle temperatures (1114 - 1229 °C) for a mantle residence time of 1500 Ma were calculated after Taylor *et al.* (1990). The high aggregation state of the diamonds, as well as the mantle storage temperatures, are consistent with diamonds from mobile belt settings, for example, Argyle (Halls Creek mobile belt), Venetia (Kaapvaal-Zimbabwe craton) and George Creek (Colorado-Wyoming kimberlite province).

Twelve sulphide inclusions were recovered from ten diamonds. The majority of the sulphides are very small (1 - 2 μg) and are dominated by high Ni (peridotitic / P-type) pentlandite-rich compositions, although four low Ni (eclogitic / E-type) inclusions, with pyrrhotite-rich and chalcopyrite-rich compositions, were analysed.

A regression plotted through the six peridotitic sulphide inclusions that showed the best colinearity, gives an age of 1432 $\pm$ 130 Ma with a low initial $^{187}Os/^{188}Os$ ratio of 0.1039 $\pm$ 0.0037. Although the age regression has a large uncertainty due to limited spread in $^{187}Re/^{188}Os$, as

well as the Re blank correction applied to such tiny samples, the upper and lower limits on the age still indicate peridotitic diamond formation below the King Leopold Mobile Belt during the Proterozoic. The Ellendale peridotitic diamonds are of similar age to eclogitic diamonds from Argyle, which were dated at 1580 ± 60 Ma using the Sm-Nd isotope system on their silicate inclusions (Richardson, 1986).

The initial $^{187}Os/^{188}Os$ ratio is low for the convecting mantle at ~ 1.43 Ga, with γ_{Os} = -32.25. The upper and lower limits on the initial ratio (0.1039 ± 0.0037) give Re depletion ages (T_{RD}) of 2.96 and 3.93 Ga, respectively, indicating that a deep sub-continental lithospheric mantle (SCLM) has been preserved since at least the Mesoproterozoic and during any subsequent continent-margin accretion around the Kimberley Craton. This is in agreement with seismic studies which indicate that the high velocity zone representing dense cold lithosphere (underlying the Kimberley craton to depths of ~ 225 - 250 km) extends much further south than is suggested by the surface cratonic edge (van der Hilst *et al.*, 1998; Kennett, 2003; Fishwick *et al.*, 2005).

This study indicates that the extent of Archaean SCLM cannot be determined based on the outcrop of Archaean crustal rocks alone, as younger crustal rocks may be transported over older Archaean lithosphere, without the destruction of the local SCLM. It appears that due to the presence of a deep SCLM, the formation processes for diamonds emplaced into these mobile belt settings are similar to those operating beneath Archaean cratons. However, higher ambient mantle residence temperatures are indicated for these diamonds compared to on - craton diamond localities.

Declaration

I hereby declare that the work presented in this thesis is my own,
except where otherwise stated in the text

Signed by candidate

Karen Smit

Acknowledgements

Kimberley Diamond Corporation and Gem Diamonds generously donated samples for the study.

My supervisors, without whom this thesis would not have been possible:
John Gurney, Steve Richardson, Anton le Roex, Steve Shirey and Craig Smith.

Miranda Waldon of the Electron Microscope Unit at the University of Cape Town, assisted in obtaining backscatter images of the diamonds.

Eva Stredder assisted with Fourier Transform Infrared (FTIR) analyses and data processing.

Russel Hemley, Joseph Lai and Chih-Shiue Yan provided access to laser cutting and polishing facilities at the Geophysical Laboratory (GL).

Mary Horan and Tim Mock are thanked for support provided in the clean laboratories and mass spectroscopy laboratories at the Department of Terrestrial Magnetism (DTM).

Tim Rose and Eloise Gaillou provided access to cathodoluminescence (CL) and FTIR facilities at the Smithsonian's Department of Mineral Sciences.

The project was partially supported by the National Research Foundation (NRF), South Africa.

Johann Diener is thanked for help with Latex and trying to solve the p116 mystery.

Thank you to everyone at DTM / GL and in DC who made my stay so memorable.

Contents

List of Figures

List of Tables

Chapter 1

INTRODUCTION

The predominant primary source for diamonds is the mantle, with diamonds transported to the surface of the Earth in highly explosive kimberlitic or lamproitic magmas. Diamond grade in kimberlite/lamproite is typically very low (less than 1.2 ppm; Gurney *et al.*, 2005) and is a consequence of the random sampling of the lithospheric mantle by the host magma as it makes its way to the surface. Sm-Nd and Rb-Sr isotope analysis of garnet inclusions in diamonds from Kimberley and Finsch (Kaapvaal craton) yielded $\sim$ 3.3 -3.2 Ga model ages (Richardson *et al.*, 1984). This study, along with Kramers (1979), indicated that diamonds are xenocrysts in their host magmas.

The association between diamondiferous kimberlites and old cratons was first recognised by Clifford (1966) and later also by Gurney & Switzer (1973), Boyd & Gurney (1986) and Janse (1994). Cratons have been tectonically inactive for billions of years (Sykes, 1978) and are characterised by deep keels of thick, less dense sub-continental lithosphere (e.g. Jordan, 1975, 1978, 1988; Boyd, 1973; Boyd *et al.*, 1985; Finnerty & Boyd, 1987; Walker *et al.*, 1989) that are chemically isolated from the convecting mantle.

Cratons have the lowest heat flow of any region on Earth with a typical conductive geotherm, assuming that the lithosphere has no internal heat production, of 40 mW/m^2 (Pollack & Chapman, 1977; Nyblade & Pollack, 1993). One definition of the base of the lithosphere is defined where the conductive geotherm intersects the adiabatic geotherm of the convecting mantle (Rudnick *et al.*, 1998; Rudnick & Nyblade, 1999). From geotherms calculated from mantle xenoliths and the cratonic conductive geotherm, Rudnick & Nyblade (1999) suggest that globally the continental lithosphere typically extends to depths of $\sim$ 200 - 250 km.

Diamonds reside in the SCLM at depths of at least $\sim$ 150 - 180 km corresponding to the

intersection of the cratonic geothermal gradient with the diamond stability field at temperatures exceeding ~ 950 to 1000 °C (e.g. Richardson *et al.*, 1984; Boyd *et al.*, 1985; Boyd & Gurney, 1986; Haggerty, 1986). Diamond host rocks in the mantle can be determined from the composition of mineral inclusions in diamonds, as well as the presence of diamond in mantle xenoliths. Two main parageneses, peridotitic and eclogitic, are recognised. Typical inclusion mineralogy that distinguishes eclogitic diamonds are pyrope - almandine garnet; omphacitic clinopyroxene; kyanite; rutile; corundum and coesite. Inclusions characteristic of peridotitic diamonds are Cr - pyrope; enstatite; Mg-rich olivine; chromite and diopside (e.g. Meyer & Boyd, 1972; Gurney & Switzer, 1973; Harris & Gurney, 1979).

Diamond inclusions are isolated from the mantle, and are thus protected from metasomatic events as well as the rapid diffusion of elements that occur at high temperatures in the mantle. These inclusions are essentially closed systems, unless linked to the surface of a diamond through cracks, and can provide information on lithosphere conditions at the time of diamond crystallisation (e.g Richardson, 1990).

Diamond - dating studies have helped constrain whether diamond formation in the sub-continental lithospheric mantle (SCLM) is continuous or episodic, with a number of studies contributing to the current understanding that diamonds form during discrete events in the SCLM. The oldest Archaean diamonds are generally of harzburgitic paragenesis and related to continental mantle keel stabilisation, with the formation of lherzolitic and eclogitic parageneses believed to be related to tectonothermal modification of the SCLM during the Proterozoic (Shirey *et al.*, 2002; Richardson *et al.*, 2004).

To date, there is no direct method to date diamonds and the only reliable method to obtain age information from diamonds is through radiogenic isotope analysis of silicate and sulphide mineral inclusions encapsulated in the diamond. Mineral inclusions may be protogenetic (grown before the diamond), epigenetic (grown after the host diamond) or syngenetic (grown at the same time as the diamond). Dating of syngenetic mineral inclusions provides formation ages of the host diamond.

Harris (1968) and Harris & Gurney (1979) provide criteria with which to distinguish between syngenetic and epigenetic inclusions. Syngenetic mineral inclusions exhibit cubo-octahedral morphologies imposed by the host diamond, as opposed to morphologies that would normally develop - e.g. monoclinic pyrrhotite and tetragonal chalcopyrite.

The main radiogenic isotopic systems that have been applied to dating mineral inclusions are Sm - Nd in garnet and clinopyroxene, Ar - Ar in clinopyroxene and Re - Os in sulphide.

As Nd is not abundant enough in single garnet inclusions for ^{147}Sm - ^{144}Nd isotope analysis, inclusions are composited into harzburgitic, lherzolitic and eclogitic parageneses based on Cr_2O_3 and CaO content and colour. Even though isochrons are produced from diamonds that may not be in equilibrium, the obtained isochron age is still geologically significant. As the range in $^{147}Sm/^{144}Nd$ is much greater for eclogitic inclusions compared to peridotitic inclusions, more precise ages can be obtained can be obtained for the former.

^{40}Ar - ^{39}Ar dating can only be applied to clinopyroxene, due to its relatively high K content. However, this method has limited applicability: radiogenic Ar is trapped at the inclusion-diamond interface, due to negligible diffusion rates in diamond, which is then released during cleaving and extraction of the inclusion. Therefore only Ar produced since eruption of diamonds is measured and ^{40}Ar - ^{39}Ar ages should be regarded as eruption ages rather than diamond genesis ages. Philips *et al.* (2004) provides a description of the applicability of this method to inclusions in diamonds. Re - Os was first applied to peridotitic and eclogitic sulphide inclusions from Koffiefontein (Kaapvaal craton) by Pearson *et al.* (1998). Since then, it has become the preferred method, as analyses can be performed on single sulphide inclusions. More detail on this method is described in Chapter 3 and Chapter 6.

In addition to radiometric techniques, the time and temperature dependence of nitrogen aggregation in diamond can provide semi - quantitative constraints on both mantle storage temperatures (if residence time is known) and mantle residence time (if the mantle storage temperatures are known) (Taylor *et al.*, 1990). Nitrogen geothermometry has shown that mantle storage temperatures of cratonic diamonds are very similar, with a compilation of worldwide data by Stachel & Harris (2008) showing that the mean storage temperature (for a 3 Ga residence time) for eclogitic diamonds is 1141 ± 48 °C , with 1146 ± 50 °C for peridotitic diamonds, essentially equivalent. Nitrogen aggregation has limited applicability as a geochronometer, as the thermal history of diamonds is difficult to constrain accurately.

The SCLM beneath the King Leopold

Typical diamond localities, as shown by Clifford (1966), are kimberlites/lamproites that intrude cratonic areas that are underlain by a highly depleted Archaean mantle lithosphere, that is partially within the diamond stability field. Ellendale is one of the only two producing diamond mines in Australia, which are both located in Proterozoic mobile belts adjacent to the Kimberley craton and are thus atypical diamond localities. The Ellendale lamproites (West Kimberley Province) intrude into the King Leopold Mobile Belt to the south of the Kimberley craton,

and the Argyle lamproite pipes (East Kimberley Province) are found in the Halls Creek Mobile Belt to the south-east of the Kimberley craton. As there are no exposed Archaean rocks in the Kimberley area, this is seemingly in violation of Clifford (1966).

However, through host-lamproite and mantle xenolith studies as well as seismic tomography, the presence of ancient lithospheric mantle beneath both the Kimberley craton and the adjacent Halls Creek and King Leopold Mobile Belts has been confirmed. The seismic tomographic model (van der Hilst *et al.*, 1998; Kennett, 2003; Fishwick *et al.*, 2005) confirms that the Kimberley craton is underlain by a high velocity zone representing dense cold lithosphere to depths of at least 150 - 200 km. Xenolith studies by Jaques *et al.* (1986, 1989, 1990); Lucas *et al.* (1989); Ramsay *et al.* (1994); Smith *et al.* (1994); Griffin & Ryan (1995); Graham *et al.* (1999); Wyatt *et al.* (1999); Downes *et al.* (2007); Luguet *et al.* (2008) have indicated the presence of Archaean lithospheric mantle below the Kimberley craton and the adjacent mobile belts. This implies preservation of the local SCLM during and after Proterozoic amalgamation of the Halls Creek and King Leopold Mobile Belts. The SCLM is largely lherzolitic in composition, with rare harzburgite (Hall & Smith, 1984; Jaques *et al.*, 1989; Lucas *et al.*, 1989). In addition, using xenoliths from the Ellendale 4 and 9 olivine lamproites, Griffin & Ryan (1995) have determined a typical cratonic palaeogeotherm of 40 mW/m^2 for the West Kimberley province.

Ellendale Diamonds

The formation processes of the Ellendale diamonds are still poorly defined. Studies on the $\delta^{15}N$ and $\delta^{13}C$ of Ellendale diamonds (van Heerden *et al.*, 1995) as well as inclusion studies by Hall & Smith (1984); Griffin *et al.* (1988); Jaques *et al.* (1989) have shown that Ellendale has both lherzolitic and eclogitic diamond populations, in roughly equal proportions. Nitrogen aggregation and geothermometry studies by (Taylor *et al.*, 1990) have shown that Ellendale and Argyle diamonds have distinct origins in both time and space, and suggest that the Ellendale diamond population is younger than Argyle. Taylor *et al.* (1990) suggest that diamonds in the West Kimberley province were stored in a stable Archaean SCLM. However, in the East Kimberley province, the SCLM has been underplated with eclogite, with the Halls Creek Mobile Belt representing the suture zone between the Kimberley craton and the rest of the North Australian craton (see Chapter 2).

A focus of this research project is to date the sulphide-bearing Ellendale diamonds and compare the age of diamond growth episode/s with the geological processes in the region, such as stabilisation of the Kimberley craton as well as later continent-margin accretion along the

King Leopold Mobile Belt. A more complete understanding of these processes is important for understanding diamond formation in mobile belt settings as well as for diamond exploration programmes, which currently mainly target cratonic environments.

This suite of Ellendale diamonds were dated through characterisation of their sulphide inclusions, using the Re-Os isotope system. Diamond plates were analysed with Fourier Transform Infrared Spectroscopy (FTIR) to determine nitrogen content and aggregation state as well as mantle storage temperatures for the diamonds. Results of the study are compared to published work on the Argyle diamond deposit in order to constrain whether the timing of the diamond-forming event/s below the Kimberley craton are related. In addition, the mantle storage conditions, as defined by FTIR analyses, are compared to published work on other mobile belt diamond localities such as Venetia (Limpopo Mobile Belt) and George Creek (Colorado-Wyoming Kimberlite Province).

Chapter 2

REGIONAL GEOLOGY

The suite of diamonds forming the core of this project was recovered from the Ellendale lamproite pipes in north-western Australia. The Ellendale lamproites are an atypical craton-margin locality as they intrude the King Leopold Mobile Belt just south of the Kimberley craton.

2.1 Australian Cratons

There are three main Precambrian units in Australia, namely the West, North and South Australian cratons, all of which evolved separately and became coherent entities by $\sim$ 1.86 - 1.83 Ga (Myers *et al.*, 1996; Tyler & Page, 1996) (Figure 2.1). The West Australian craton was established by collision of the Pilbara and Yilgarn cratons along the Capricorn Orogen which peaked at 1.84 - 1.79 Ga although deformation lasted until $\sim$ 1700 Ma (Myers, 1990; Myers *et al.*, 1996; Tyler *et al.*, 1999).

The South Australian craton is an amalgamation of proto-Gawler and Curnamona cratons, joined by the Kimban Orogen (Myers *et al.*, 1996) and was part of an earlier larger continent, the Mawson continent, which included East Antarctica (Daly *et al.*, 1998). However, a Palaeoproterozoic reconstruction of the South Australian craton by Giles *et al.* (2004) implies that there was no distinction between the North and South Australian cratons before 1.5 Ga. In this reconstruction, the South Australian craton is rotated 52 °counterclockwise with the 1.8 to 1.6 Ga orogenic belts of the Gawler craton aligned with those preserved in the Arunta Inlier and the 1.6 to 1.5 Ga orogenic belts of the Curnamona Province aligned with those in the Mount Isa Block. After 1.5 Ga the South Australian craton must have separated from the North Australian craton. In support of this are the $\sim$ 1.5 to 1.3 Ga sedimentary basins in Eastern

Australia that may be due to extension during this time, for example, the Roper Superbasin and South Nicholson Basin (Plumb *et al.*, 1990) and the Cariewerloo Basin (Daly *et al.*, 1998).

The North Australian craton includes the Kimberley, Pine Creek, Arnhem, Lucas and Altjwarra cratons with suture zones between these fragments marked by the King Leopold, Halls Creek, Tennant Creek and proto-Isan orogenies (Plumb *et al.*, 1981; Myers *et al.*, 1996). The North Australian craton was joined to the northeastern margin of the West Australian craton by $\sim$ 1.3 Ga (Myers *et al.*, 1996, and references therein). However, palaeomagnetic results from Li (2000) suggest the possibility that the two cratons had joined together much earlier, at $\sim$ 1.7 Ga. These combined cratons collided with the South Australian craton along the Albany-Fraser and Musgrave Orogenies as part of the assembly of the Rodinia supercontinent at $\sim$ 1.33 to 1.10 Ga (Myers, 1993; Myers *et al.*, 1996; Giles *et al.*, 2004). After assembly, the combined cratons show intracratonic deformation associated with the breakup of Rodinia (Myers *et al.*, 1996).

2.2 The Kimberley Craton

The Kimberley Basin lies within the boundary of the larger North Australian craton (Plumb, 1979) and is bounded to the east and south by the intracratonic and King Leopold Mobile Belts, respectively (Figure 2.2). The Kimberley Basin has a platform cover of $\pm$ 1.9 - 1.65 Ga sandstone-dominated sediments and volcanics (Gellatly, 1971; Thom, 1975; Atkinson *et al.*, 1984). This cover remains largely undeformed, except in areas in close proximity to the adjacent mobile belts (e.g. Gellatly, 1971). There are no exposed Archaean rocks in the Kimberley region (Gellatly, 1971; Wellman, 1978), though there is evidence which indicates the presence of subcontinental lithospheric mantle beneath both the Kimberley block and the adjacent Halls Creek and King Leopold Mobile Belts.

The seismic tomographic model (van der Hilst *et al.*, 1998; Kennett, 2003; Fishwick *et al.*, 2005) confirms that the Kimberley craton is underlain by a high seismic velocity zone, which represents cold lithospheric mantle, to depths of at least 150 - 200 km (Figure 2.3). This zone extends much further than is suggested by the surface cratonic edge, and includes the Halls Creek and King Leopold Mobile Belts. Preservation of the lithospheric mantle keel indicates that these mobile belts are shallow crustal features transported over older lithosphere.

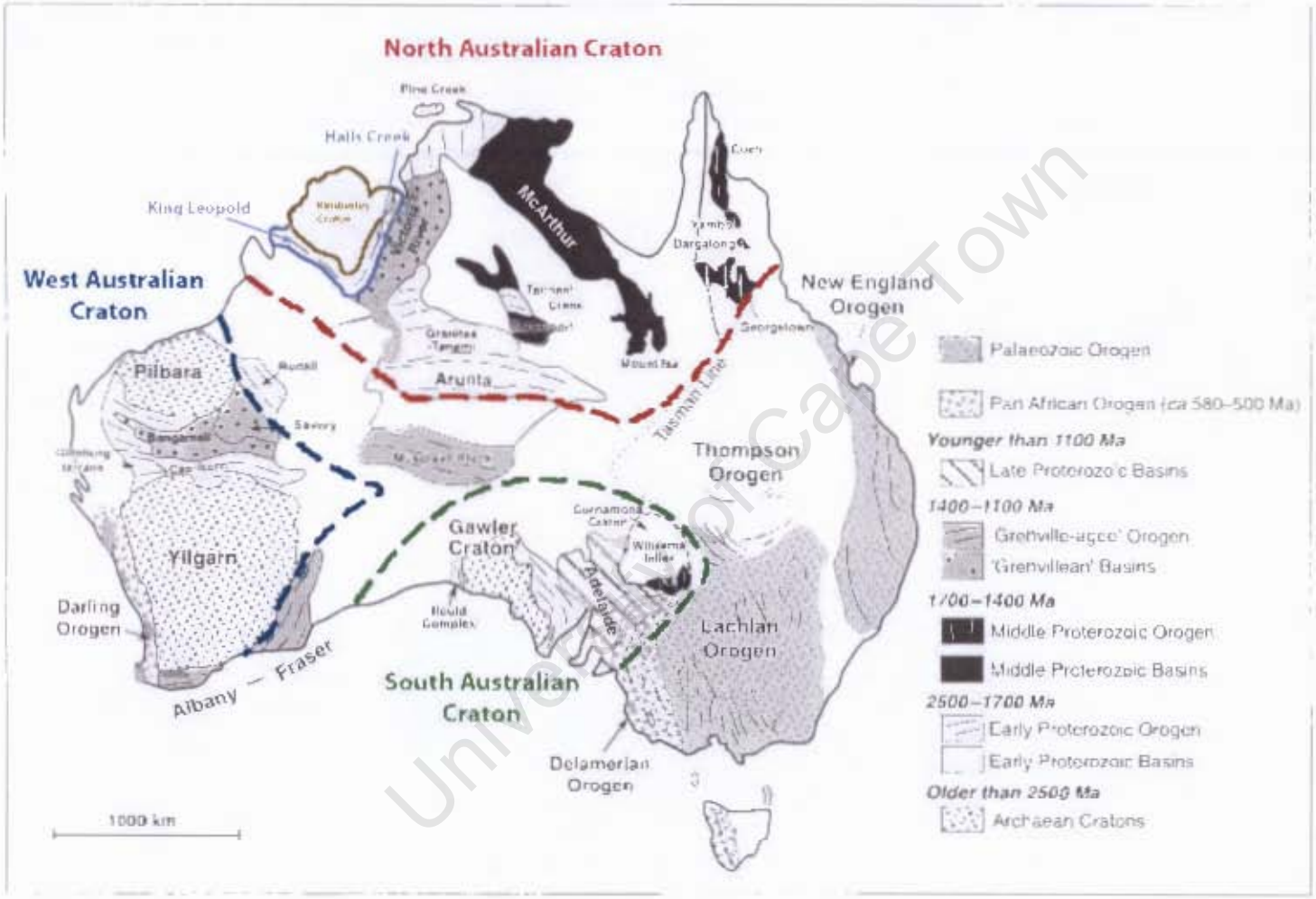

Figure 2.1: Geological terranes of Australia (Betts *et al.*, 2002, after Myers *et al.* (1996) and Foster & Gray (2000)).

Griffin & Ryan (1995) have determined a typical cratonic palaeogeotherm (Boyd, 1973; Pollack & Chapman, 1977) of 40 mW/m^2 beneath the West Kimberley province (see below) from garnets in the Ellendale 4 and 9 olivine lamproites. In addition, cool geotherms of 40 - 44 mW/m^2 (Jaques *et al.*, 1990) have been established for the East Kimberley province (see below) and $\sim$ 40 mW/m^2 for the north Kimberley (Griffin & Ryan, 1995; Wyatt *et al.*, 1999). A considerably higher palaeogeotherm of $\sim$ 48 mW/m^2 was determined for the mantle beneath the Skerring kimberlite in North Kimberley by Taylor *et al.* (2000).

Xenolith studies by (Jaques *et al.*, 1989, 1990; Lucas *et al.*, 1989; Ramsay *et al.*, 1994; Smith *et al.*, 1994; Griffin & Ryan, 1995; Wyatt *et al.*, 1999; Downes *et al.*, 2007) have shown that the lithospheric mantle beneath the Kimberley craton is largely lherzolitic in composition (with rare harzburgite). Two lherzolite xenoliths from Argyle, one hypabyssal lamproite sample from Argyle and one chromite from the Seppelt kimberlite in the North Kimberley Province yield a Re-Os isochron age of 3.4 $\pm$ 1.3 Ga (Graham *et al.*, 1999). This age is imprecise due to limited spread in Re/Os and may be an overestimate as the lherzolitic xenoliths show evidence of metasomatic alteration. However, Luguet *et al.* (2008) also reports Archaean Re depletion ages for peridotite xenoliths from Argyle, indicating that the lithospheric mantle beneath the Kimberley craton and adjacent Halls Creek Mobile Belt was indeed stabilised in the Archaean.

In addition, Nd isotope data indicate that the Argyle lherzolite xenoliths and the Argyle lamproite magma, with unradiogenic initial ε_{Nd} = - 3.2 and -5 to -6, respectively, was extracted from an old source which had subsequently been reworked or enriched in light rare earth elements (LREE) (Graham *et al.*, 1999). This is supported by a low initial Nd isotopic composition (ε_{Nd} = - 3) for eclogitic silicate inclusions from Argyle (Richardson, 1986). Also, Hf model ages of zircons from xenoliths from the Aries Kimberlite intruded into the Kimberley craton, indicate that Hf is inherited from an older Archaean protolith, at least 2.7 Ga old (Downes *et al.*, 2007).

A convergent margin along the southeast boundary for much of the Proterozoic before $\sim$ 1.9 Ga (Tyler *et al.*, 1999; Griffin *et al.*, 2000), as well as zircon ages which range from 2.5 to 1.91 Ga (Tyler *et al.*, 1999), indicate that the early Proterozoic was a time of continual crustal formation and reworking. A post-collisional environment has been proposed for the 1.86 - 1.85 Ga felsic magmatism of the Paperbark suite that dominates the Hooper and Lamboo Complexes (Figure 2.2). These granites were sourced from magmatic arcs and continental fragments underlying the Speewah and Kimberley Basins (Sheppard *et al.*, 1997) and were emplaced following northwesterly terrane accretion to the Kimberley craton (Griffin *et al.*, 2000). Other late Archaean to early Proterozoic orogenic belts in Australia include the Gascoyne Complex (Nutman

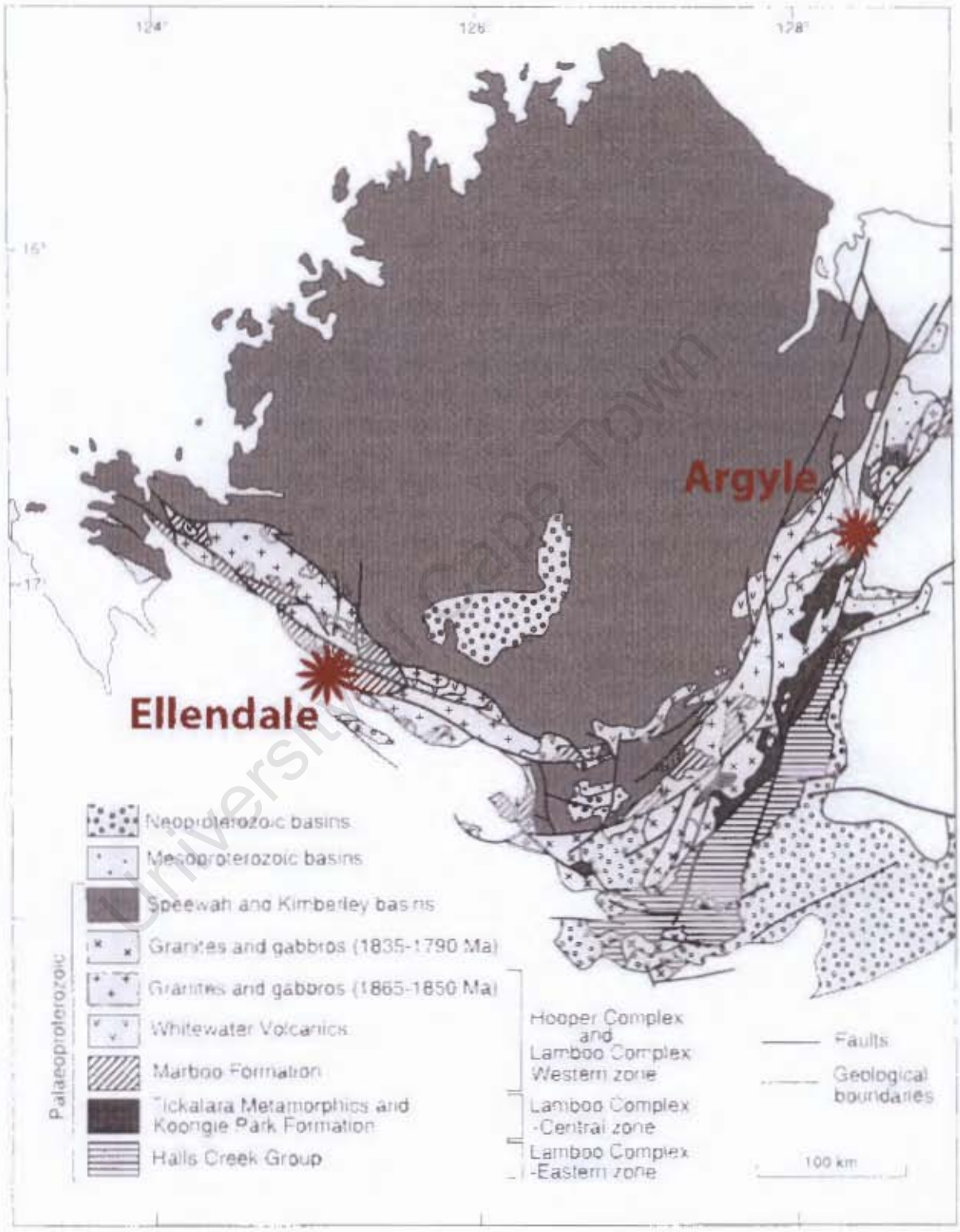

Figure 2.2: Geology of the Kimberley region (from (Tyler *et al.*, 1999)). Location of the Ellendale and Argyle diamond localities in the King Leopold and Halls Creek Mobile Belts, respectively.

& Kinny, 1994; Nelson, 1998), the Rudall Complex (Nelson, 1995) and the Mount Isa Block (McDonald *et al.*, 1997).

The Paperbark suite of felsic rocks predate the collision and suturing of the Kimberley craton with the Lucas craton as part of the greater North Australian craton, marked by the Halls Creek orogeny at 1.83 - 1.8 Ga and 1.83 - 1.79 Ga Sally Downs granitic intrusions into the Lamboo Complex (Myers *et al.*, 1996; Tyler & Page, 1996; Griffin *et al.*, 2000; Page *et al.*, 2001).

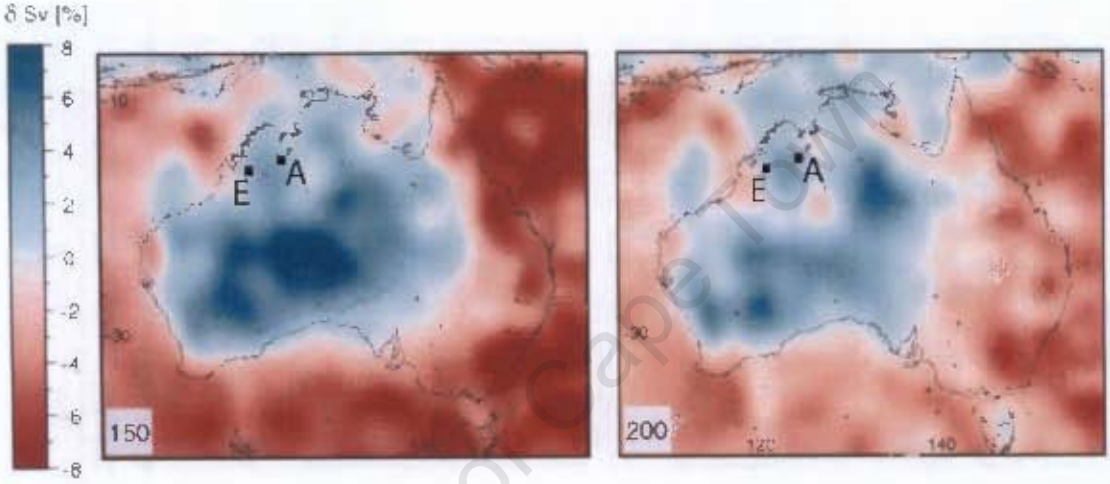

Figure 2.3: Seismic s-wave tomographic image of Australia at 150 km and 200 km depths (Fishwick *et al.*, 2005). The location of Ellendale (E) and Argyle (A) diamond localities is indicated.

2.3 King Leopold Mobile Belt

The King Leopold Mobile Belt consists of two tectonic units namely the Hooper Terrane, a crystalline complex of Early Proterozoic (1.88 - 1.84 Ga) plutonic, volcanic and sedimentary rocks; and the folded rocks of the Kimberley Basin Succession (1.84 - 1.76 Ga). The Mobile Belt has been affected by the various deformational events, which are described below.

The earliest deformation event (1.88 Ga) is recognised by small-scale layer-parallel structures in the metasedimentary rocks of the Hooper Terrane (Tyler & Griffin, 1990). No large-scale fold structures are seen. The deformation is consistent with listric faulting and shearing at high structural levels and may have developed in an extensional environment where turbidite sequences were deposited.

The second deformation event (D2), as recognised by Tyler & Griffin (1990), took place after the intrusion of the 1.86 - 1.85 Ga granites, porphyries and felsic volcanic rocks (Griffin *et al.*,

2000, and references therein) but predates the 1.83 - 1.79 Ga granitic intrusions. The intrusion of these granites was strongly controlled by shear zones developed during D2 deformation (Tyler & Griffin. 1990). The deformation produced upright open to tight folds with NW-trending axial surfaces that typically plunge moderately to steeply NW or SE (Tyler & Griffin, 1990). Intrusion of the 1.83 - 1.79 Ga granites effectively signalled cratonisation and the incorporation of the Hooper Terrane as part of the Kimberley craton (Tyler & Griffin, 1990).

The Hart Dolerite intruded at 1.76 Ga and is one of the most extensive dolerite bodies in the world (Griffin & Grey, 1990). Sun *et al.* (1986) suggests that the dolerite was derived either from enriched mantle or from interaction of depleted mantle with Archaean crust and/or lithosphere.

The deformation that produced the Yampi Fold Belt is divided into two phases, the first of which produced large-scale near isoclinal folds. The second phase produced large-scale N-facing folds. Both phases produced folds with axial surfaces that dip SSW. Strain during deformation was partitioned into pre-existing shear zones and the rocks in areas between these were largely undeformed (Tyler & Griffin, 1990). The development of the Yampi Fold Belt occurred after the intrusion of the Hart Dolerite and before the deposition of the 670 Ma Mount House glacigene sequence (Tyler & Griffin, 1990). Bodorkos & Reddy (2004) give a possible $\sim$ 900 Ma $^{40}Ar/^{39}Ar$ age for the Yampi orogen. It represents intracratonic compression that could be related to a collision towards the SW of the King Leopold Orogen (Tyler & Griffin, 1990) and is associated with the assembly of Early Proterozoic cratons as part of the Rodinian Supercontinent (Myers *et al.*, 1996; Li *et al.*, 2008).

The development of the Precipice Fold Belt post-dated the 670 Ma glacigene sequence and involved large-scale folding and SW-directed thrusting of the Kimberley Basin over the Hooper Terrane (Griffin & Myers, 1988; Griffin, 1989; White & Muir, 1989; Tyler & Griffin, 1990). Folds and thrusts trend WNW with axial surfaces that dip to the NNE.

Break-up of Rodinina in the late Proterozoic resulted in intracratonic deformation along previous lines of weakness with reactivation of older sutures between the North, South and West Australian cratons (Myers *et al.*, 1996). This may be related to plate movements beyond the present boundaries of Australia. In this context, deformation in the King Leopold orogeny (560 - 530 Ma) is related to NE-SW thrusting in an overall compressive regime (Myers *et al.*, 1996).

2.4 Kimberley Diamond Provinces

The leucite lamproites of the West Kimberley were first recognised in the early 1900's. However, the first detailed study on these rocks was by Rex Prider for his PhD thesis at Cambridge University in the late 1930's. This work was published as Wade & Prider (1940). Diamonds were discovered in the Kimberley region as part of an extensive exploration programme launched in Western Australia by the Ashton Joint Venture in 1972. The known shield areas, namely the Kimberley, Yilgarn and Pilbara cratons, were prime targets for exploration after Clifford (1966). Exploration was extended into the Halls Creek and King Leopold Mobile Belts surrounding the Kimberley craton, due to the suggestion by Wade & Prider (1940) and Prider (1960) that the leucite lamproites in the Fitzroy Trough could be genetically related to kimberlite. Exploration methods are summarised in Atkinson *et al.* (1984).

The Kimberley diamond province comprises three main areas, namely the North Kimberley Province, the East Kimberley Province and the West Kimberley Province. The North Kimberley Province is located on the northern parts of the Kimberley craton. Five kimberlites are known which are virtually barren of diamond, associated with some uneconomic diamondiferous alluvials (Atkinson *et al.*, 1984; Sobolev *et al.*, 1989). The East Kimberley Province contains two diamond source rock types. Kimberlites occur on the eastern margin of the Kimberley craton, whereas the Argyle AK1 lamproite pipe, as well as the related Bow and Lissadell Road dykes are in the Halls Creek Mobile Belt adjacent to the craton (Atkinson *et al.*, 1984). The Argyle lamproite has been dated at 1129 $\pm$ 9 Ma through Rb-Sr dating by Skinner *et al.* (1985).

The distribution of the lamproite and kimberlite intrusions in the Kimberley province show structural control due to major deep-seated fracture zones associated with the early Proterozoic mobile belts and Phanerozoic rifting and continental break-up (Atkinson *et al.*, 1984). The intrusions of the East Kimberley province are aligned N-NE, parallel to the major fault structures in the area (Atkinson *et al.*, 1984).

The Kimberley lamproite pipes show several distinctive differences from the mode of kimberlite emplacement described by Hawthorne (1975). Lamproite pipes have a champagne-glass shape, with short, narrow feeder pipes or diatremes and broad shallow craters (Atkinson *et al.*, 1984; Smith & Lorenz, 1989), compared to the typical carrot-shaped diatremes of kimberlite. Lamproites are typically very explosive, with late stage lava flows. As a result, crater tuffs are commonly overlapped or intruded by plugs of the magmatic lamproite or late-stage sills. This is not a common association for kimberlitic diatremes, as outlined in the Hawthorne model where the magmatic kimberlite is found only in dykes, sills and the deeper levels of the pipe (Atkinson

et al., 1984; Jaques *et al.*, 1984). The diamond content of the magmatic phase of the lamproite is normally very low, with average diamond grades much lower than kimberlites. They typically contain small diamonds that are usually severely etched and pitted. The tuffs from the initial explosive phase can however have much higher diamond grades than most kimberlites, e.g. The Argyle lamproitic tuffs have a grade of 500 carats/100 tons compared to 20 - 80 carats/100 tons for most kimberlites (Mitchell & Bergman, 1991).

2.5 West Kimberley Diamond Province

The West Kimberley Diamond Province is a suite of more than one hundred lamproitic intrusives that occur at the northeastern margin of the Canning Basin and the southern margin of the King Leopold Mobile Belt (Mitchell & Bergman, 1991). The main fields that comprise the West Kimberley Diamond Province are, from north to south, the Ellendale, Calwynyardah and Noonkabah lamproite fields (Mitchell & Bergman, 1991; White *et al.*, 1995). These lamproite fields are emplaced in the hanging wall of the Oscar Shear system, which forms the contact between the King Leopold Mobile Belt and the Lennard Shelf (White *et al.*, 1995). The Oscar Shear system is a reactivated part of the King Leopold Mobile Belt and has been traced into the upper mantle by deep seismics (Drummond *et al.*, 1989).

The distribution of lamproites in the West Kimberley Province has been strongly controlled by the W-NW trending structures of the King Leopold Mobile Belt (Atkinson *et al.*, 1984). The strong structural control of kimberlitic and lamproitic intrusions, with their distribution localised by deep mantle structures, have been established by various authors including Crocket & Mason (1968), Black *et al.* (1985) and White *et al.* (1995).

About 45 % of the West Kimberley lamproites are diamondiferous (Hughes & Smith, 1990) and the Ellendale field, closest to Kimberley craton has the highest diamond grade (White *et al.*, 1995). K-Ar and Rb-Sr dating by Wellman (1973), Jaques *et al.* (1984) and Pidgeon *et al.* (1989) established the Miocene age (24 - 19 Ma) of these intrusions. A summary of the age results for the West Kimberley lamproites is given in Allsopp *et al.* (1985).

The lamproites in the West Kimberley Province are bimodal and show geochemical variation from olivine-rich to leucite lamproites (Jaques *et al.*, 1984, 1989; Stachel *et al.*, 1991), with magma rising as lava lakes in the olivine lamproites and as lava domes in the more viscous leucite lamproites (Stachel *et al.*, 1991). These two lamproite groups show distinctly different major and trace element and isotopic characteristics, with the initial Sr ratios of the olivine lamproites

less radiogenic than the leucite lamproites (McCulloch *et al.*, 1983; Jaques *et al.*, 1984). Chesler (2008) proposes that the observed geochemical variation is due to varying degrees of crustal assimilation during lamproite emplacement.

The West Kimberley lamproites have Ti-rich phlogopite, diopside and richterite compositions, with enrichment in incompatible elements (F, Ba, Rb, Sr, Pb, Th, U, Ti, Zr, Nb and LREE) (Jaques *et al.*, 1984). The lamproites also have high $^{87}Sr/^{86}Sr$ (0.711 to 0.720) and unradiogenic ε_{Nd} (-7 to -15) (McCulloch *et al.*, 1983; Jaques *et al.*, 1984). These compositions are consistent with derivation from an ancient enriched mantle source.

2.6 Ellendale Lamproite Field

There are forty-eight volcanic bodies in the Ellendale field, the majority of which are volcanic crater deposits, although small sills do occur (Hughes & Smith, 1990). At Ellendale, only the leucite lamproites show an extensive development of sills, and they appear to predate the central plug and form a large portion of the diatreme. Forty-three of the forty-five crater lamproite pipes at Ellendale are aligned in an elongate belt along the Oscar Fault (Smith & Lorenz, 1989) (Figure 2.4).

Smith & Lorenz (1989) outline evidence for the interaction of the Ellendale lamproitic magma with groundwater as it ascended. This caused phreatomagmatic eruptions resulting in the formation of maars and diatremes. Subsequent erosion has removed the maar tephra rings and tephra sheets, exposing the underlying volcanic pipes. A review of the phreatomagmatic model is given by Lorenz (2003). Stachel *et al.* (1991) details the geology, petrography, mineral chemistry and geochemistry of these pipes.

The two largest olivine lamproites in the Ellendale field are Ellendale 4 and Ellendale 9, while Mt North and 81 Mile Vent are the larger leucite lamproites (Stachel *et al.*, 1991) (Figure 2.4). The olivine lamproites carry more diamonds (71 % are diamond-bearing) whereas the leucite lamproites are generally lower grade (only 36 % are diamond-bearing) (Jaques *et al.*, 1984; Hughes & Smith, 1990). The Ellendale lamproite pipes have a much lower diamond grade (<1 carat per tonne) than Argyle (5 - 6 carats per tonne) (Gurney *et al.*, 2005). The Ellendale 4 (14 carats / 100 metric tons) and Ellendale 9 (5 carats / 100 metric tons) have the highest diamond grades in the West Kimberley Field (Taylor *et al.*, 1990).

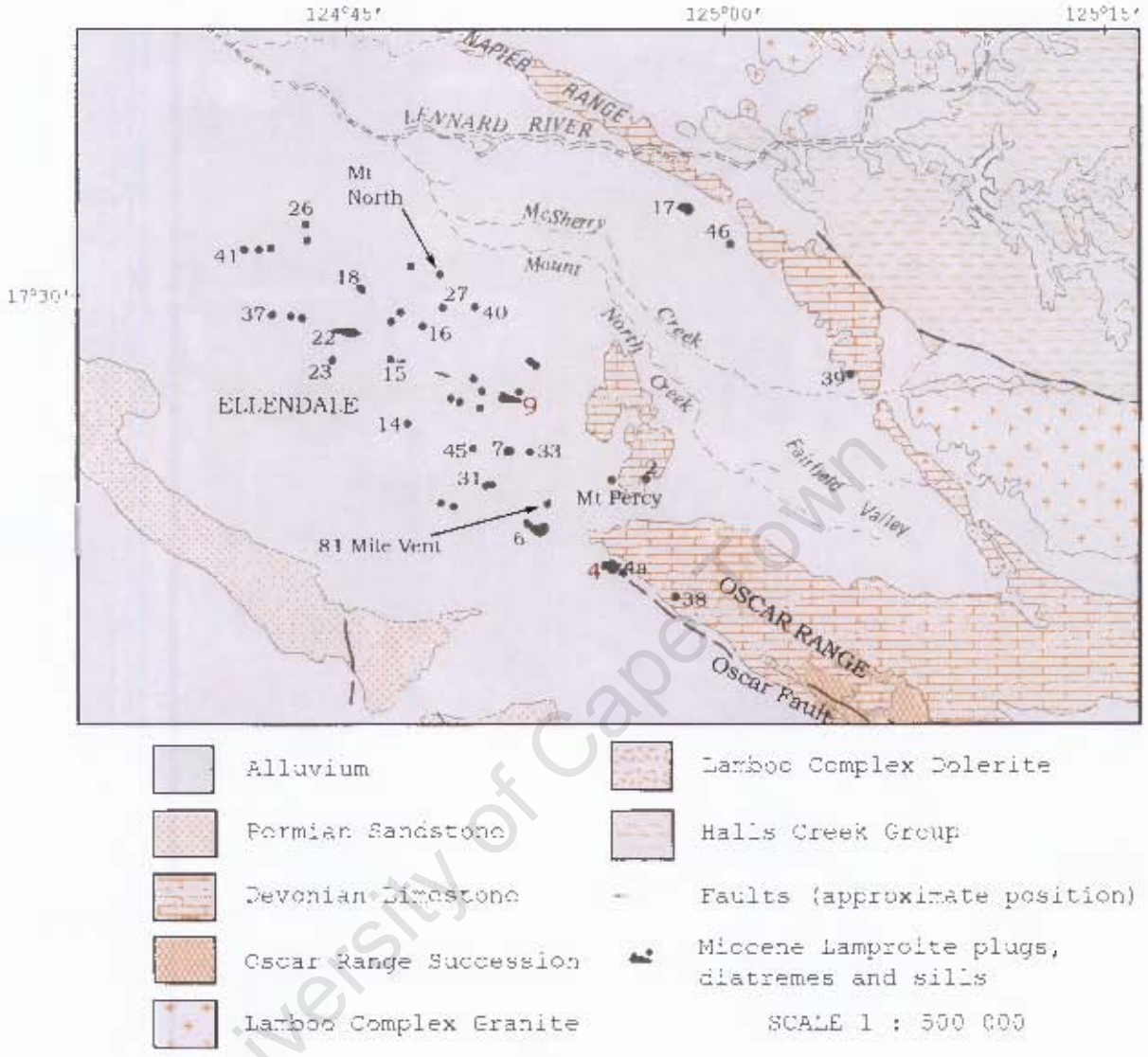

Figure 2.4: The Ellendale lamproite intrusions, adapted from the map "Lamproite Intrusions of the West Kimberley Area, W.A." (Jaques *et al.*, 1986). The positions of the Ellendale 4 and 9 pipes are indicated in red.

2.6.1 Classification and petrogenesis of lamproites

Lamproites are typically more silica-rich than kimberlites. They are rich in K_20 compared to other mafic magmas, resulting in high levels of incompatible elements. The salient features of lamproite geochemistry are summarised in Table 2.1. Minerals present as primary constituents in lamproite are olivine, clinopyroxene (typically diopside), phlogopite (typically titaniferous), leucite, amphibole (typically potassic richterite), orthopyroxene, sanidine and glass (formed due to rapid cooling) (Wade & Prider, 1940; Jaques *et al.*, 1984). Rare accessory minerals such as wadeite ($K_2ZrSi_3O_9$), priderite [$(K,Ba(Ti,Fe)_8O_{16}$], perovskite [$(Ca,Na,Fe^{2-},Ce,Sr)(Ti,Nb)O_3$]

and apatite [$Ca_5(PO_4)_3(OH,F,Cl)$] may be present due to extreme enrichment of incompatible elements or country rock assimilation. Nepheline, ilmenite and spinel may also be present.

Table 2.1: Average lamproitic geochemical compositions

Silica content	43 - 55 wt % SiO_2
Ultrapotassic	4 - 12 wt % K_2O; $K_2O/Na_2O > 5$
Peralkaline	$Al < Na + K$
Enriched in REE and incompatible elements	Rb, Sr, Ba, Zr, Ni, Cr, Co, Sc

Many cratonic regions have limited or no lamproitic suites. It is probable that the source characteristics and tectonic environment required for ultrapotassic lamproite magma generation is less common than that of kimberlite. Lamproite source regions are typically enriched in Rb and LREE with higher Rb/Sr and lower Sm/Nd ratios than bulk earth (Mitchell, 2006) and are mainly sourced from the non-convecting lithospheric mantle. Lamproites have a low CO_2 content < 1 %, compared to $\pm$ 8 % CO_2 in kimberlite. According to Foley (1989) the major difference between kimberlites and lamproites are the different fluid compositions. Although both lamproites and kimberlites have deep-seated mantle source regions, kimberlites are produced in a more oxidised mantle, while lamproites are formed in more reducing conditions with CH_4 present as the dominant carbon species. Lamproites are however enriched in F and H_2O. The isotope and volatlile content of lamproite, as well as experimental studies by Eggler (1978), Eggler & Wendlandt (1979) and Wyllie (1979), suggest that these rocks formed by the partial melting of metasomatised phlogopite-bearing harzburgite in conditions that are F-rich, and CO_2-poor (Jaques *et al.*, 1984; Foley, 1989, 1991, 1992; Mitchell, 1995).

Chapter 3

ANALYTICAL TECHNIQUES

3.1 Diamond Descriptions

Diamonds were examined and photographed under an optical microscope as well as imaged using a SEI detector on the LEO S440 Scanning Electron Microscope (SEM) in the Electron Microscope Unit at the University of Cape Town. Backscatter imaging allowed for the observation of features on the surface of the diamonds and was done in order to document any interesting features on the diamonds before plates were cut.

3.2 Diamond plate cutting and Cathodoluminescence (CL) imaging

Diamond plates of between 1.2 - 2.7 mm thickness were cut using the automated Bettonville laser cutter in facilities at the Geophysical Laboratory (GL) of the Carnegie Institution of Washington. Diamond plates were polished using a polishing wheel with embedded diamond chips, also at GL. Polished diamond plates were ultrasonically cleaned in ethanol and water. CL images that reveal internal growth zoning of the diamonds were obtained on the JEOL JX-8100 electron microprobe at the University of Cape Town. Colour CL images were obtained using the luminoscope at the Smithsonian Institution's Department of Mineral Sciences in Washington, DC. Diamond plates were kept at vacuum better than 100 milliTorr with beam voltage and current at 15 kV and 0.5 mA, respectively. The ideal orientation for a diamond plate to be cut is parallel to the {110} crystal plane (i.e. parallel to the c-axis). If a diamond plate is cut parallel to the {111} octahedral planes then no growth zones will be seen. In the case of

tetrahexahedroida, it is extremely difficult to judge the position of the c axis. As the diamonds were quite large, a few images (normally four) of the different portions of the diamond were taken. These were mosaicked using DoubleTake image software. Occasionally the contrast of the different sections of the diamond varied, resulting in uneven mosaicking of images.

3.3 FTIR Analysis

Prior to FTIR analysis, the diamond plates were ultrasonically cleaned in 10 % decon solution, followed by ethanol and water. Diamond plates were mounted along the side of a glass slide with double-sided tape.

Spectra for samples EL01 to EL50 were measured at the Department of Geological Sciences, University of Cape Town with a Nicolet Magna-IR 560 spectrometer attached to a KBr beam splitter and a MCT/A detector that was cooled with liquid nitrogen. The sample chamber was purged with dry nitrogen gas to prevent CO_2 build-up in the space around the sample.

Spectra for samples EL51 to EL69 were measured on a Bio-Rad Excalibur FTS 3000 spectrometer at the Department of Mineral Sciences of the Smithsonian Institution in Washington, DC. The spectrometer is attached to a KBr beam splitter and a MCT detector that was cooled with liquid nitrogen. Dry air was purged over the sample to ensure a non-condensing environment.

All spectra were recorded over the mid infrared range (4000 - 650 cm^{-1}), with resolution set at 8 cm^{-1} and an aperture of 100 μm. Background spectra were recorded with every analysis and subtracted from the diamond spectra to correct for non-sample contributions. Bruker OPUS/3D software was used for baseline correction of the spectra. Spectral decomposition to quantify nitrogen content and aggregation state, was done on a spreadsheet provided by David Fisher of the DTC Research Centre in Maidenhead, UK. Nitrogen concentration in the different sites is calculated from the absorption coefficient at the respective peak absorption wavelength:

$[N_A]$ = 16.5 X μA (1282 cm^{-1}) (Boyd *et al.*, 1994)

$[N_B]$ = 79.4 X μB (1282 cm^{-1}) (Boyd *et al.*, 1995)

3.4 Re-Os Isotope Analysis

Sulphide inclusions were analysed using facilities at the Department of Terrestrial Magnetism (DTM) and the Geophysical Laboratory (GL) of the Carnegie Institution of Washington. Dia-

mond plates were broken in a tungsten-carbide-lined steel cracker to release the sulphide inclusions. Sulphide inclusions were then mounted on conductive carbon tape for identification on a scanning electron microscope (SEM) using both backscatter and secondary electron imaging, as well as energy-dispersive X-ray fluorescence spectrometry (EDS) for major element analyses. Operating voltage and current for the SEM were 15 kV and 1 nA, respectively. Data reduction followed the ZAF procedure, with the following standards: Pyrite for Fe and S, Chalcopyrite for Cu, and synthetic Ni sulphide for Ni.

Re and Os isotopes were analysed by negative thermal ionisation mass spectrometry (N-TIMS) on a modified 15 inch radius mass spectrometer at DTM, which was designed for and dedicated to Re - Os isotope analysis. After sulphide inclusion characterisation and cleaning, a mixed ^{185}Re - ^{190}Os spike solution was added and Re and Os analysed using microchemistry and mass spectrometry techniques following Shirey & Walker (1995), Pearson *et al.* (1998), Carlson *et al.* (1999), Shirey *et al.* (2000) and Richardson *et al.* (2001). These are described below:

3.4.1 Sample Preparation

Prior to use, virgin Teflon vials were boiled in Aqua Regia for 2 hours, HNO_3 for 1 hour and MQ H_2O for 1 hour. Glass vials were boiled in Aqua Regia for 2 hours and MQ H_2O for 1 hour.

Once sulphides had been liberated from the carbon tape, they were transferred to a glass vial containing acetone to be ultrasonically cleaned. Sulphides were weighed on a Mettler UMT2 microbalance and transferred to a Teflon cap. During this process Teflon beakers and caps were wrapped in aluminium foil in order to minimise static charging, which may cause sulphides to pop out of the cap.

Spike solutions were weighed out into separate Teflon caps and dried down in a laminar flow hood for $\pm$ 1/2 hour. Re-Os spikes of different concentration were used, depending on the sulphide paragenesis. Peridotitic sulphides have higher Os concentrations and were spiked with a solution that has higher Re and Os concentrations, while eclogitic sulphides were spiked with a dilute Re-Os solution.

Very dilute Re-Os spike (DTM spike 06-4-53):

$[^{190}Os] = 1.237 \times 10^{-13}$ mol/g

$[^{185}Re] = 8.0456 \times 10^{-13}$ mol/g

Concentrated Re-Os spike (DTM spike 99-4-50):

$[^{190}Os] = 9.239 \times 10^{-12}$ mol/g

$[^{185}Re] = 2.367 \times 10^{-12}$ mol/g

After the spike solution had dried down, 10 μL 12N H_2SO_4 was added to the spike cap and the spike solution transferred onto the sulphide in the other Teflon cap.

3.4.2 Os distillation

10 μL HBr was added to the tip of a conical beaker and 10 μL Cr_2O_3 to the sulphide and spike solution on the cap. The upside-down capped beaker was placed on a hot plate for 90 minutes at 75 °C to distill the Os into the HBr drop. Cr_2O_3 is a strong oxidising agent and is added to bring Os to its highest oxidation state. OsO_4 is highly volatile at low temperatures and it is reduced by the HBr drop to $OsBr_6^{2-}$. At temperatures above 80 °C , some of the Cr solution may also be transferred to the HBr drop, which will interfere with reduction of Os.

Once distillation was complete, the Os fraction was dried down under the heat lamps until ± 1 μL was left. Once dried, it is ready to be loaded onto a filament for mass spectrometry. The distillation residue was capped until it was ready for column chemistry.

3.4.3 Re Anion Exchange Column Chemistry

The residue was transferred into a conical beaker via pipette, with 0.5 ml of 1M HCl. 10 μL 30 % H_2O_2 was added to the beaker in order to reduce Cr^{6+} to Cr^{3+}. The solution was set aside until the reduction reaction was complete, i.e. the solution had turned blue and there were no more bubbles.

Columns set aside for Re-Os sulphide inclusion work were rinsed with 3 aliquots of MQ H_2O. BioRad AG1 X8 Resin was loaded into columns and the columns cleaned by passing through 4 aliquots of 6M HCl, followed by 0.5 ml MQ H_2O and 1 aliquot 8M HNO_3.

Once the columns were equilibrated with 2 X 0.5 ml of 1M HCL, the sample was loaded dropwise onto the resin. After the sample was loaded, the beaker was rinsed three times with MQ H_2O and fluxed with 4M HNO_3 in the oven until it is to be used for Re collection.

The Fe-Cu-Ni cut was collected in 2 X 0.5 ml 1M HCl. The Pb cut was collected in a further

4 X 0.5 ml 1M HCl. Columns were washed with 0.5 ml 0.8M HNO_3 and finally Re was collected in 2 X 1.0 ml 4M HNO_3. The Re cut was dried down in Aqua Regia in the laminar flow hood to get rid of any organics from the resin.

3.4.4 Mass Spectrometry

Re and Os were both loaded onto Pt wire filaments (opposed to Re filaments used for other isotope analyses). Re was picked up from the conical beaker in HNO_3. If the Os cuts had dried all the way down, they can be loaded in 0.5M HBr. The Re and Os salts were dried onto the filaments.

When the Os salt was dried, current was passed through the filament, under vacuum, in order to metalise the Os, i.e. the Os forms an alloy with the filament. Os is extremely volatile, so the metallisation process helps control ionisation in the mass spectrometer. EL51 did not yield any reliable data, as the Os did not metalise well due to the current that kept fluctuating in the filament position, possibly due to a poor electrical contact.

$Ba(NO_3)_2$ was added onto both the Re and Os filaments. Ba is an electron donor and aids ionisation, so that Re and Os are ionised as ReO_4^- and OsO_3^-, respectively.

Filaments were turned up slowly and data only collected once a stable beam had been obtained. O_2 was leaked into the source during Os runs in order to improve the ionisation efficiency.

Mass spectrometer fractionation was corrected by normalising $^{192}Os/^{188}Os$ to 3.082614 (Creaser *et al.*, 1991). Since Re and Os are run as negative oxides, data needs to be corrected for interferences from three O isotopes, with $^{17}O/^{16}O = 0.00037$ and $^{18}O/^{16}O = 0.002047$ (Nier, 1950).

Analyses were corrected for minimum procedural blanks of 3 fg Os and 120 fg Re. $^{187}Os/^{188}Os$ 2σ errors were calculated based on in-run precision and 50 % uncertainty in the total Os content of the blank. $^{187}Re/^{188}Os$ 2σ errors were calculated based on in-run precision.

Chapter 4

PHYSICAL CHARACTERISTICS AND INTERNAL MORPHOLOGY

4.1 Introduction and sample selection

The samples in this study comprise a suite of sixty-nine diamonds recovered from the Ellendale 4 and 9 pipes in the Ellendale province of lamproite intrusions in north-western Australia. Studies by Hall & Smith (1984), as well as Jaques *et al.* (1989), have shown the diamond population at the Ellendale 4 and 9 pipes to be dominated by highly resorbed chemically polished tetrahexahedroidal forms, many of which are yellow. Octahedra are very rare, however, a 9.92 carat yellow octahedral diamond was recovered in the alluvial deposits at Ellendale in 2005. Many diamonds from Ellendale have high value due to their intense yellow colour, and are classified as fancies, although colourless diamonds are also common.

The Ellendale run-of-mine diamonds also have a sub-population of octahedral stones in a size range of up to ± 0.3 carats. These stones were found to have inclusions of the peridotitic paragenesis and are described by Jaques et al. (1991). Their unresorbed nature is explained by Jaques *et al.* (1991) to be a result either of late stage diamond formation or through shielding of the diamonds in peridotite xenoliths. The latter is most likely, having also been observed to occur elsewhere, as described in Robinson (1979) and Gurney (1989).

The diamonds for this study were selected due to the presence of rosette fracture systems, characteristic of sulphide inclusions. Twelve diamonds are from the Ellendale 4 (E4) pipe (EL51 to EL62), with six diamonds from the Ellendale 9 (E9) pipe (EL64 to EL69). The majority of the diamonds (EL01 to EL50) are of unspecified E4 and E9 origin. The diamonds were

examined under an optical microscope and their morphology, colour, form and surface features described. The physical characteristics of the suite of Ellendale diamonds studied are summarised in Table 4.1. It was not one of the aims of this study to explain the observed properties, but they were recorded as an aid to the interpretation of other observations such as FTIR analyses, CL imaging and sulphide inclusion Re-Os geochemical data.

Thirty-five diamond plates were investigated for their internal morphology by cathodoluminescence imaging. Descriptions of the growth layering for each diamond, with relation to the FTIR traverses, are given in Appendix 2. CL images of the front and back of all the plates are presented in Appendix 3. A brief description capturing salient growth features identified in the CL images is given below.

4.2 Colour and Size

Impurities in the diamond structure may cause absorption in the visible spectrum and account for their colour (Robinson, 1979, and references therein). The most common colours in diamond are colourless, yellow and brown (Harris *et al.*, 1975). Colourless diamonds typically have minor impurities and are more pure. Diamonds with no detectable nitrogen in the lattice are classified as Type IIa, but are extremely rare (see Chapter 5). The presence of nitrogen atoms causes absorption in the blue region of the visible spectrum, resulting in a yellow colour (Bruton, 1978; King *et al.*, 2005). Brown, and sometimes pink and red diamonds are associated with plastic deformation of diamond at great depths (more detail in Section 4.4.1) (Robinson, 1979, and references therein). Slip lines develop in the diamond due to plastic deformation, along which graphite or amorphous carbon crystallise, giving rise to the brown colour (Urusovskaya & Orlov, 1964; Robinson, 1979). There are however, diamonds that show lamination lines without the development of a brown colour. The diamonds in this Ellendale suite range in size from 0.26 to 0.92 carats and are mainly yellow, with variable degrees of colour intensity. There are thirteen colourless diamonds in the suite, namely, EL10, EL18, EL35, EL36, EL50, EL54, EL55, EL58, EL59, EL65, EL67 and EL68.

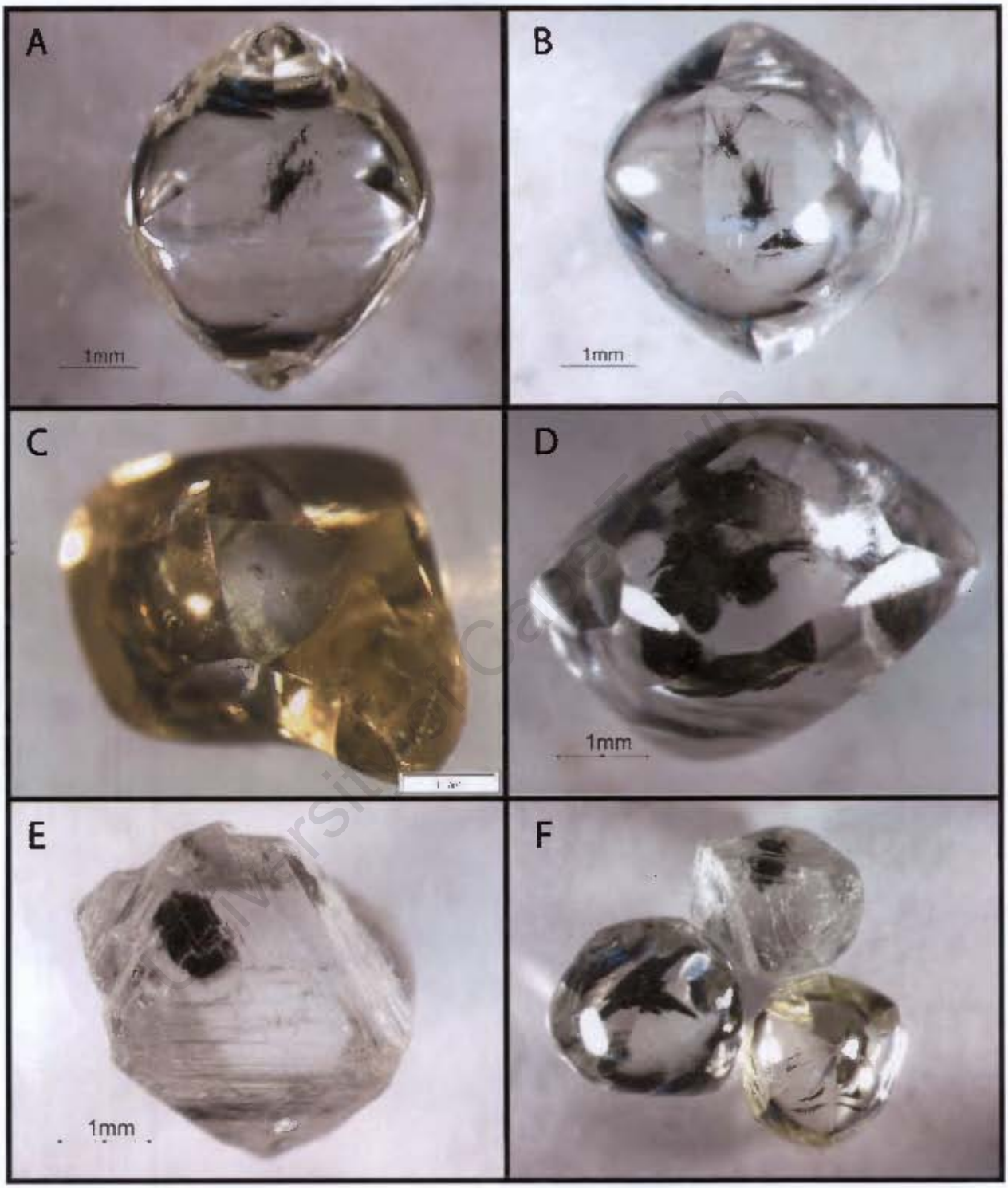

Figure 4.1: External morphology of the Ellendale diamonds in this study. A (EL02) and B (EL28): Tetrahexahedroida (THH) showing even resorption. C (EL32) and D (EL66): THH with uneven resorption resulting in irregular (C) or elongated (D) forms. E: EL59, the only octahedron in the suite. F: Two THH diamonds alongside the octahedron EL59.

4.3 Morphology

4.3.1 Tetrahexahedroida

Diamonds can grow in both octahedral and cubic habit, though octahedra are the most common form (Robinson, 1979). Diamond growth can take place on the {001}, {011} and {111} crystal planes, with regular growth along the {111} index planes resulting in an octahedron with eight planar surfaces equidistant from the origin. (Sunagawa, 1984a,b) has shown that this growth occurs under conditions of low carbon supersaturation in a diamond-forming fluid. Growth along the {001} index planes results in a cubic form (Wilks & Wilks, 1991). Cubes typically display rough faces and fibrous growth and form under conditions of higher carbon supersaturation (Kamiya & Lang, 1964; Moore & Lang, 1972; Sunagawa, 1984a,b).

Tetrahexahedroida are a secondary form that typically result from the resorption of primary forms (Moore & Lang, 1972) due to oxidising agents. It has been suggested that most diamond resorption occurs during and after incorporation of diamonds into the kimberlite (or lamproite, in the case of Ellendale) magma (Robinson *et al.*, 1989). Robinson (1979) has shown that a 45 % loss of mass is needed to convert a regular octahedron to a tetrahexahedroid. Tetrahexahedroida (THH) are commonly rounded with twelve curved crystal faces (Robinson, 1979). These curved surfaces sometimes lead people to refer to them as rounded dodecahedra, however THH are different from regular dodecahedra in that they never have flat {011} faces (Wilks & Wilks, 1991). Diamonds that have smooth, rounded tetrahexahedroidal surfaces dominate the suite of diamonds in this study. Some diamonds are equidimensional, resulting from even resorption on all sides (Figure 4.1 A and B), whereas some diamonds have irregular forms, due to uneven resorption (Figure 4.1 C and D). EL59 is the only octahedron in the suite (Figure 4.1 E and F). In several cases, remnant octahedral layering is still visible on the apices of the diamond (Figure 4.2 A, C, E).

Resorbed surfaces are typically characterised by fine to ultrafine hillock patterns. The elongation of the hillocks is parallel to the growth of octahedral layers, which indicate that the hillocks reflect the resistance of individual layers to resorption (Robinson, 1979). The tetrahexahedroida in this suite, however, lack any abundant hillock patterns and have been subjected to chemical polishing, which renders smooth, shiny faces. Hillock resorption patterns have been partially retained in a few samples, resulting in a cloudy surface texture.

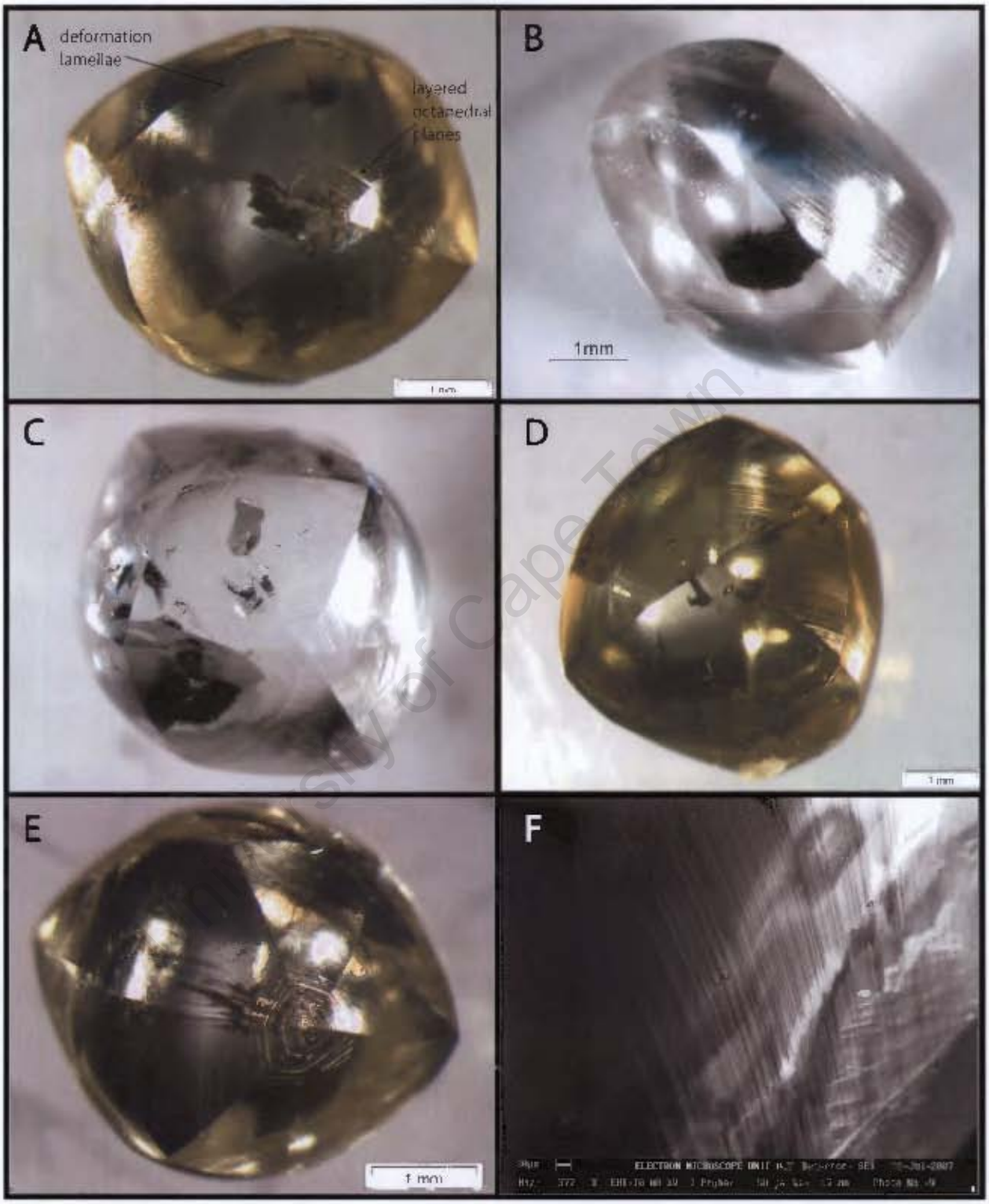

Figure 4.2: Layered octahedral planes still visible on the surface after resorption and deformation lamellae. A: EL15. B: EL35 has deformation lamellae without the development of a pervasive yellow/brown colour. C: EL51 with octahedral layering visible on the apices. D: EL47 shows deformation lamellae associated with a brown diamond colour. E: Octahedral layering visible on the apex of EL28. F: Secondary electron image of deformation lamellae visible on the surface of a diamond.

4.3.2 Twins

Twin crystals are produced when a change in the crystallographic orientation of the growth planes occur along a twin plane (Wilks & Wilks, 1991). The most common twin form is a contact twin or macle, which has a triangular shape and is a flattened pair of octahedra with the twin plane parallel to the larger pair of {111} crystal faces (Harris *et al.*, 1975; Wilks & Wilks, 1991) (Figure 4.3 A). The twin plane is identified by a herringbone pattern on the side of the diamond, centred on the twinplane. Often inclusions in the diamond will be found along the twin plane, and possibly play a role in promoting the twin crystal growth. In this suite of Ellendale diamonds, the twin planes are only partially visible due to extensive resorption. Figure 4.3 B shows a macle, with its twin plane identified on the one edge on the basis of its herringbone pattern. Several macles were identified in this suite, namely EL03, EL08, EL16, EL20, EL50, EL56, EL60, EL61 and EL69.

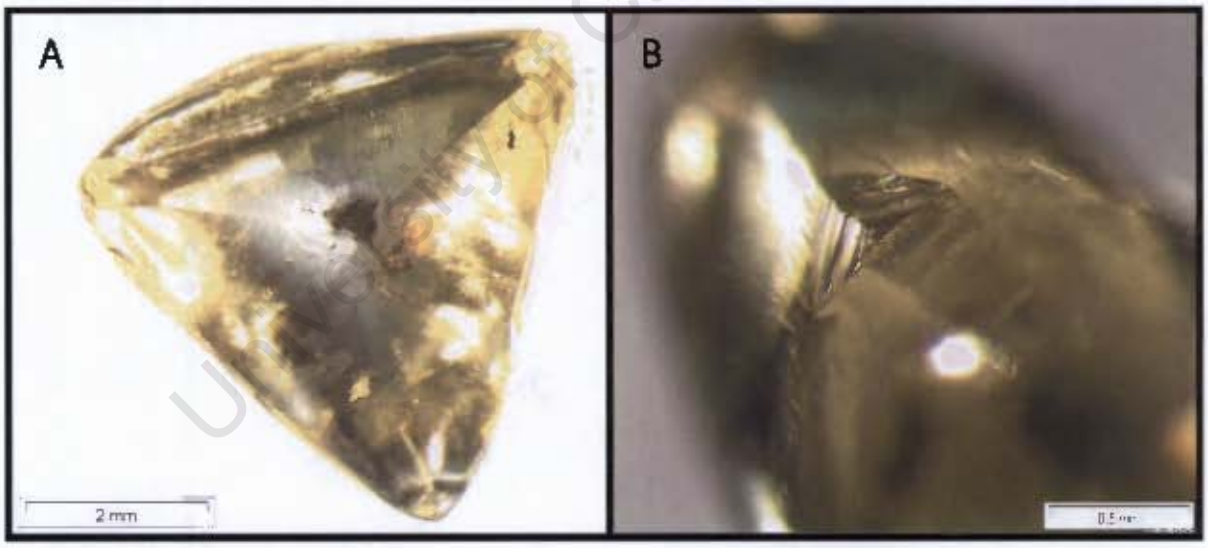

Figure 4.3: A: EL03 is a macle with a typical flattened triangular shape. B: The twin plane on EL03 is only partially visible due to resorption.

4.4 Surface Features

All the diamonds in the suite are highly resorbed tetrahexahedroida that have been smoothed by extensive resorption and chemical polish in the host lamproite. Chemical polish is caused by reaction with dry CO_2 gas, at temperatures above 950 °C (Phaal, 1965) and sees the destruction

of many surface features as it post-dates both resorption and the processes that form etch pits (Robinson, 1979). The development of the main surface features observed in this suite is described below.

4.4.1 Deformation

Lamination lines on the surface of a resorbed diamond are generally accepted to be the result of plastic deformation of diamond (e.g. Harris, 1992), which occurs at temperatures greater than 1000 °C at 30 kbar and requires grain-boundary contact (de Vries, 1975). Lamination lines occur as sets of fine lines parallel to the {111} octahedral faces and are typically only visible due to the effects of crystal resorption (Robinson, 1979). Colour may be an additional indicator of deformation, with the brown colouration resulting from carbon recrystallising as graphite along these deformation planes (Orlov, 1973). However, there are diamonds that show the development of deformation lamellae without a pervasive brown colour. On the basis of lamination lines, deformation was recognised in sixteen of the Ellendale diamonds. EL47 exhibits both deformation lamellae as well as a deep yellow/brown colour (Figure 4.2 B). The deep colour could also be due to deformation of an already yellow diamond. However, EL35, a colourless diamond also has extensive deformation lamellae (Figure 4.2 E).

4.4.2 Etch Features

Triangular pits (or trigons) are the result of dissolution (Robinson, 1979; Sunagawa, 1984a,b) and not due to growth failure as suggested by Tolansky (1965) and others. Negatively-orientated etch pits are typically formed at high temperatures in excess of 950 °C with steam and wet CO_2 gas (Robinson, 1979). These pits are the opposite orientation to the octahedral face. Positively-orientated etch pits are normally formed due to O_2 gas and pressurised steam at lower temperatures between 450 and 1000 °C (Robinson, 1979). These pits are the same orientation as the octahedral face. Both positive and negatively orientated trigons may be either pyramidal or flat-bottomed. According to Robinson (1979), trigons are flat-bottomed when they stop developing on surfaces that are resistant to etching.

Resorption channels, or ruts can also be caused by etchants such as steam or gas and develop along zones of weakness in the diamond (Robinson, 1979). While the tetrahexahedroidal diamonds in this suite are predominantly smooth and polished, some diamonds show the development of both trigonal and cubic etch pits. These are mainly localised in ruts or resorption channels on the diamonds (Figure 4.4 A to E). These ruts are zones of weakness or cracks that

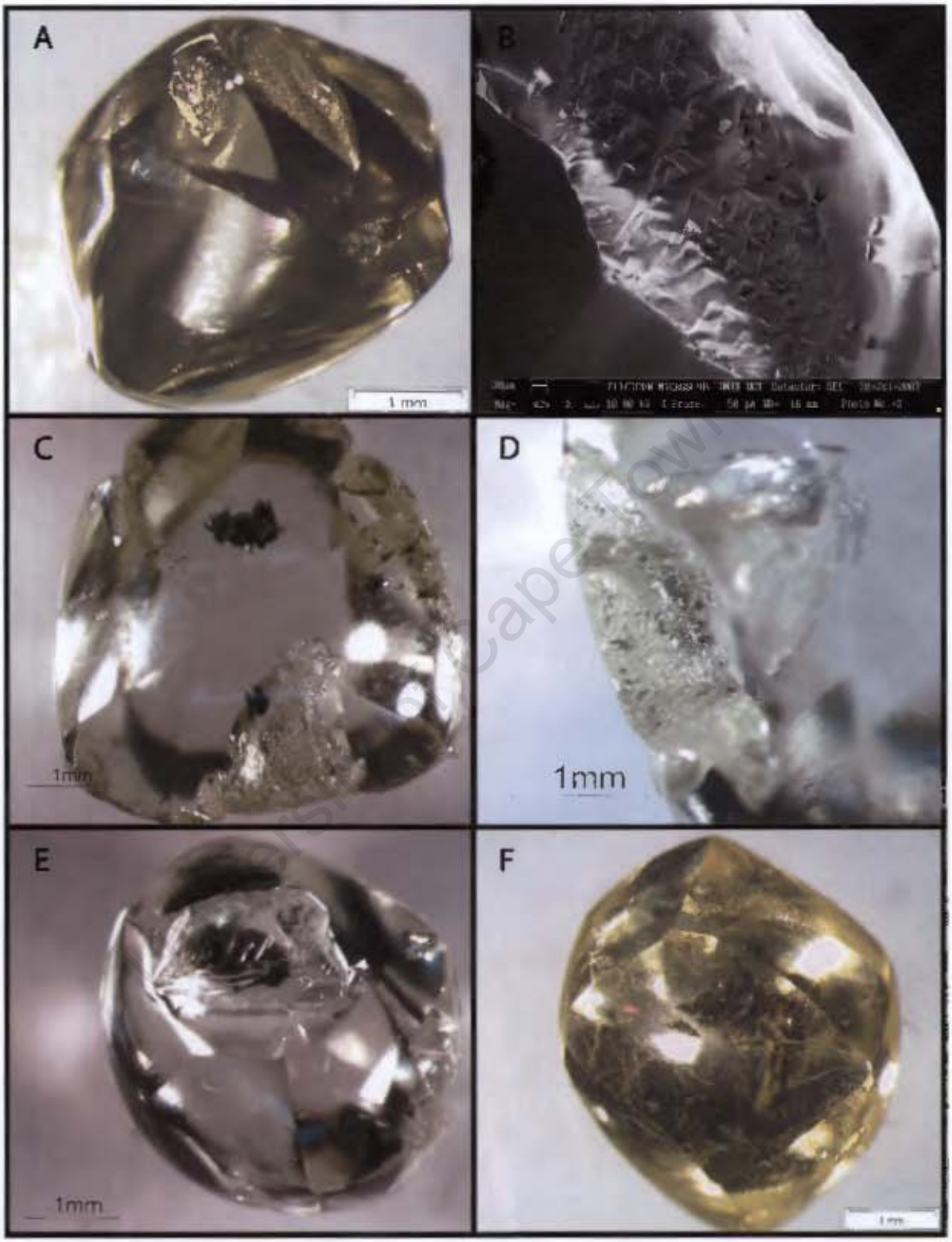

Figure 4.4: Etch features on the Ellendale diamonds are typically confined to ruts and channels on the surface. A: Two etch ruts on EL43. B: SEM image of the etch pits in the rut on EL43. C and D: Etch ruts on EL69. E. Etch features in what is most likely an inclusion cavity on the surface on EL53. F: Scratch-like marks on the surface of EL49.

are widened by resorption or etching (Orlov, 1977; Robinson, 1979). Mineral inclusions may be released during resorption resulting in isolated cavities, which generally exhibit trigonal etch pits. An example is seen in EL53 (Figure 4.4 E). Cavities do not always show the external form of an inclusion, since when inclusions are liberated, they may also remove a portion of the diamond, with the cavity reflecting the cleavage of the diamond (Robinson, 1979).

4.4.3 Scratch Marks

Scratch-like marks are present on EL44 and EL49 (Figure 4.4 F) and are more severe than most marine diamonds show. The exact nature of their origin is not understood, however they must have occurred after both the resorption and chemical polish events and could represent mechanical or frictional damage. One possibility is that these features show plant or mining damage, however other diamonds in the suite do not exhibit this.

4.5 Internal Morphology

4.5.1 Background

Studies by Seal (1963, 1965) and Harrison & Tolansky (1964) were the first to reveal the internal structures of diamonds through etching in potassium nitrate. The etch medium is affected by impurities and imperfections in the diamond, so the etch pattern reveals the different internal growth layers. Other techniques, such as X-ray topography (Hanley *et al.*, 1977; Lang, 1963, 1964, 1965, 1974, 1979), ultra-violet transmission topography and birefringence topography (Takagi & Lang, 1964) were later applied. The most common technique used today to study the internal zonation in diamonds is cathodoluminescence topography, with one of the earliest studies by Moore & Lang (1975). The origin of cathodoluminescence in diamonds is complex, the details of which are reviewed in Davies (1979) and Walker (1979). In short, electrons are excited from valence bands under electron-beam bombardment and when they relax back to their ground state, they emit light of a characteristic wavelength (Davies, 1979).

The most common internal structure in diamond is layered growth bands or zones parallel to the {111} crystallographic direction or parallel to the outline of octahedral crystals. Cathodoluminescence has the ability to recognise distinctions between different growth layers that have differences in defect (nitrogen) concentration. Growth layers may be octahedral parallel to the {111} crystallographic direction, or cubic - parallel to the {001} direction (Moore & Lang, 1972; Seal, 1963; Robinson, 1979). Some diamonds show both octahedral and cubic layering in different

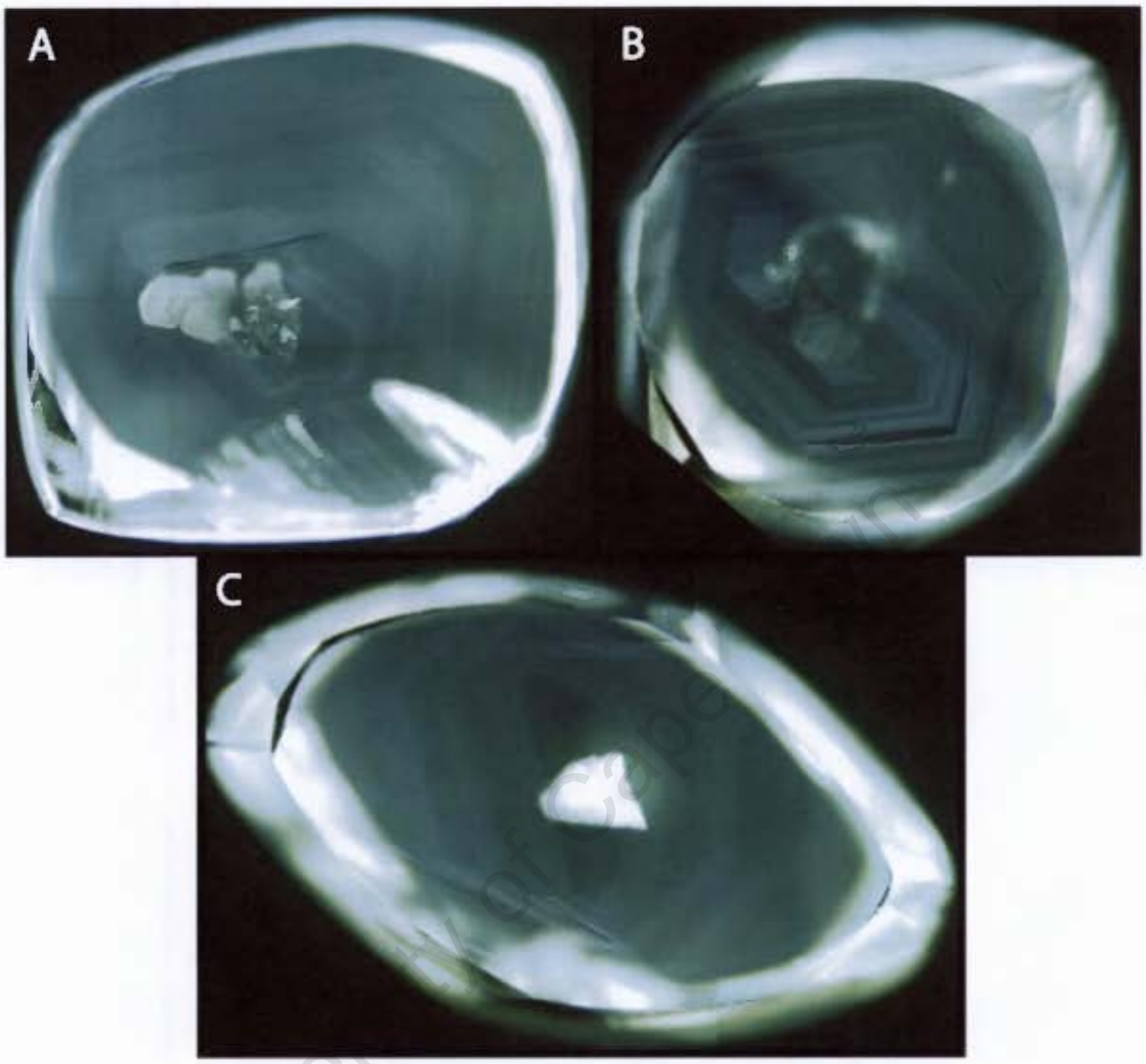

Figure 4.5: Diamonds showing regular octahedral zonation. A: EL01. B: EL12. C: EL52.

growth zones (Suzuki & Lang, 1976a,b), whereas some diamonds show mixed cubo-octahedral growth in their cores due to fluctuating growth rates, characterised by a centre-cross.

Diamonds typically show complex growth histories due to various factors including: episodic growth which may or may not be separated by periods of resorption, fluctuating growth rates, fluctuation in volatile species (H, H_2O, CO_2 or N) in the diamond-forming fluid, morphology changes, changes in nucleation rates and/or incorporation of fluid or mineral inclusions (Seal & Wasmund, 1969; Robinson, 1979). By viewing the growth zones and internal structures of diamonds, one is able to gain a better understanding of the growth history of diamond. Different growth layers often differ in impurity or defect content with highly luminescent zones indicating higher nitrogen content and non-luminescent zones reflecting lower nitrogen content.

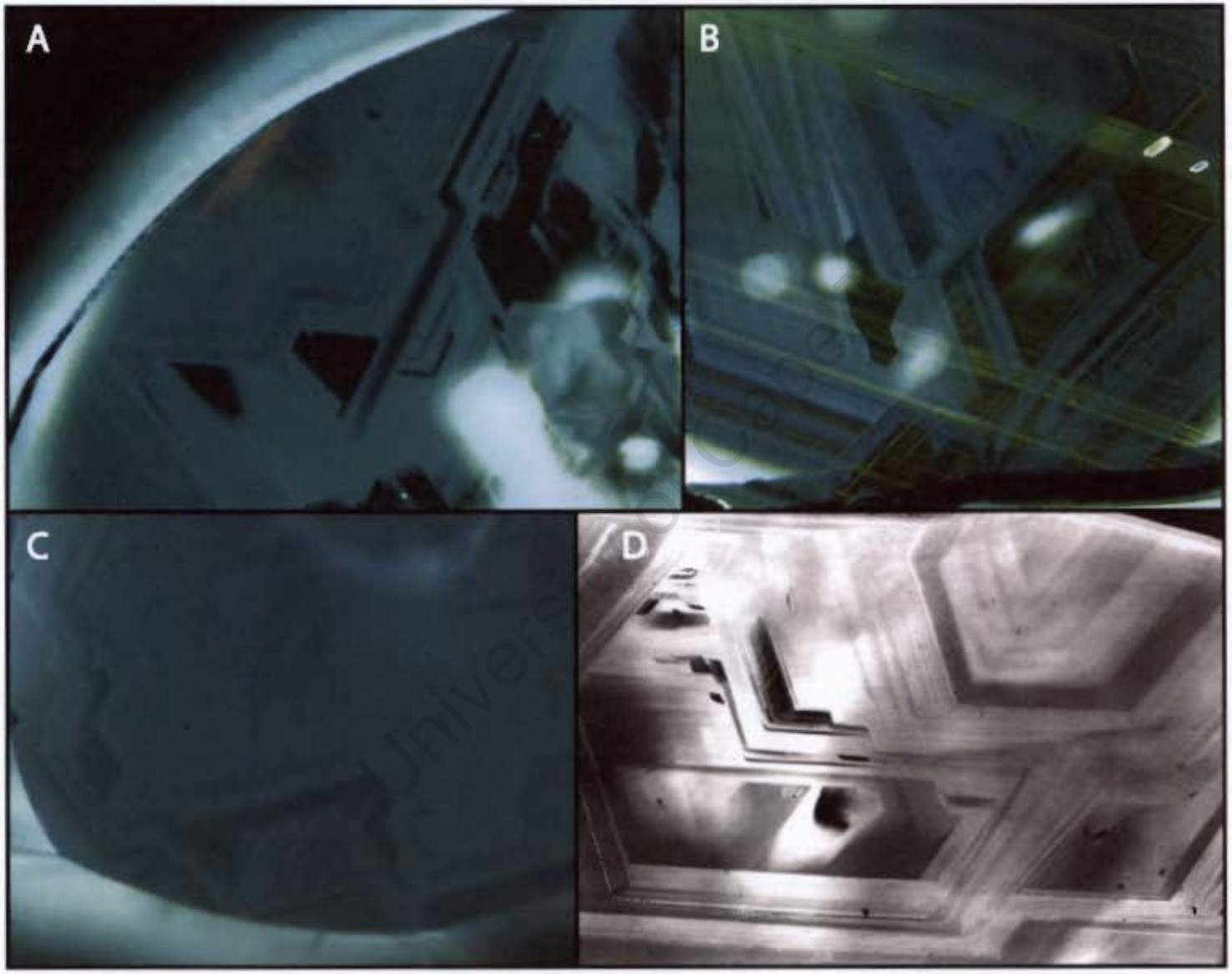

Figure 4.6: Diamonds showing several growth centres. A: EL26. B: EL35. C: EL57. D: EL31.

4.5.2 Growth Habit

The Ellendale diamonds all show predominantly octahedral growth habit, with truncation of the octahedral growth layers at their edges, confirming their origin by resorption. Diamonds that exhibit more or less regular octahedral zonation from core to rim are EL01, EL12 and EL52 (Figure 4.5). However, EL12 has cross-cutting octahedral layers of slightly higher luminescence towards the bottom of the plate, indicating a period of resorption (Figure 4.5 C).

A few diamonds show several micro growth centres within an overall octahedral growth habit. This is illustrated in Figure 4.6. The different centres typically do not all have similar luminescence, indicating that they probably did not form at the same time, but rather represent multiple growth events that eventually coalesced to a single crystal.

4.5.3 Multi-stage Growth/Resorption

Several diamonds show cross-cut octahedral layers, often of different luminescence, which indicate different episodes of diamond growth interrupted by a period of resorption. The most dramatic examples are EL32, EL36, EL55 and EL67 where the diamonds have cores of highly luminescent diamond with uneven or curved edges typical of resorption (Figure 4.7 A to D). In all these diamonds, resorption is followed by growth with much lower luminescence, indicating fluctuation of the N content in the diamond-forming fluid.

4.5.4 Twins

Due to the highly resorbed nature of the Ellendale diamonds, twin planes were only partially preserved. In some cases a herringbone pattern was not observed at all and the diamond could only be identified as a twin from the internal morphology. CL images for selected twins from the suite are shown in Figure 4.8. EL61 shows etch pits all along the twin plane through the diamond (Figure 4.8 E).

4.5.5 Deformation

Deformation lines, which are visible as green-yellow lines on the CL images were observed in three diamond plates, namely EL35, EL36 and EL65 (Figure 4.9).

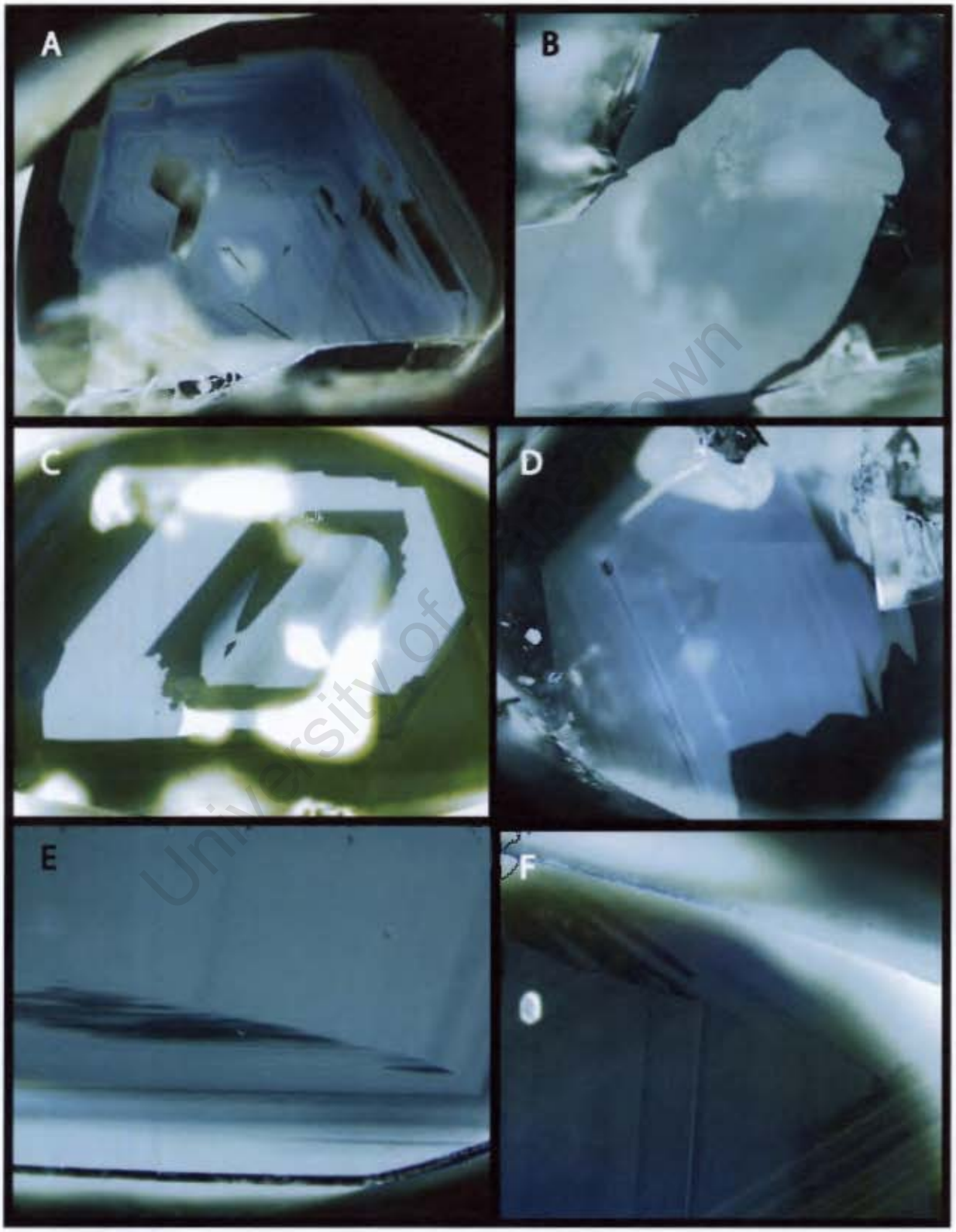

Figure 4.7: Diamonds showing evidence of resorption interrupting growth events. A: EL32. B: EL67. C: EL36. D: EL55. E: EL50. F: EL35.

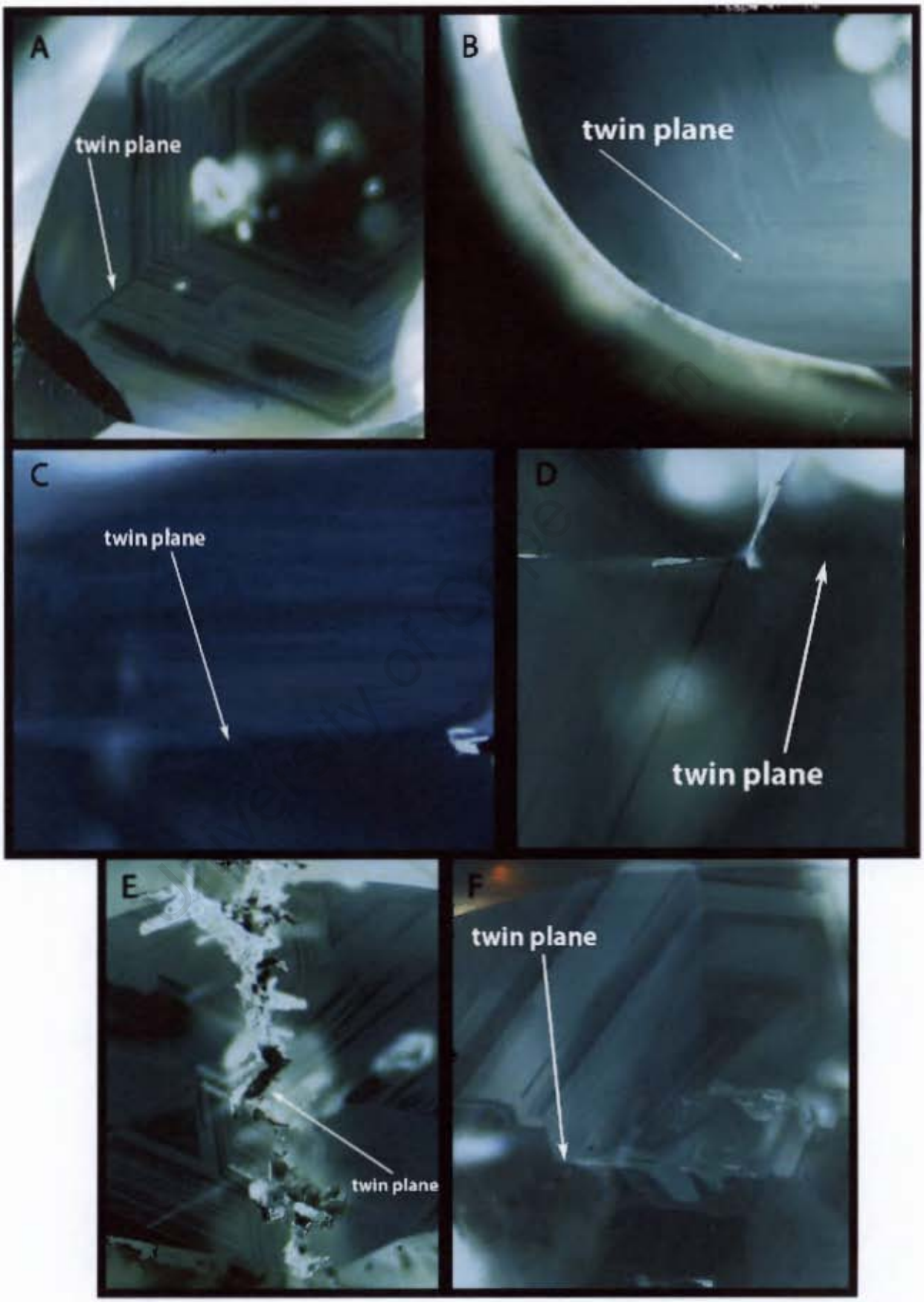

Figure 4.8: Twinned diamond crystals, with the twin planes indicated on each image. A: EL16. B: EL20. C: EL69. D: EL50. E: EL61. F: EL60.

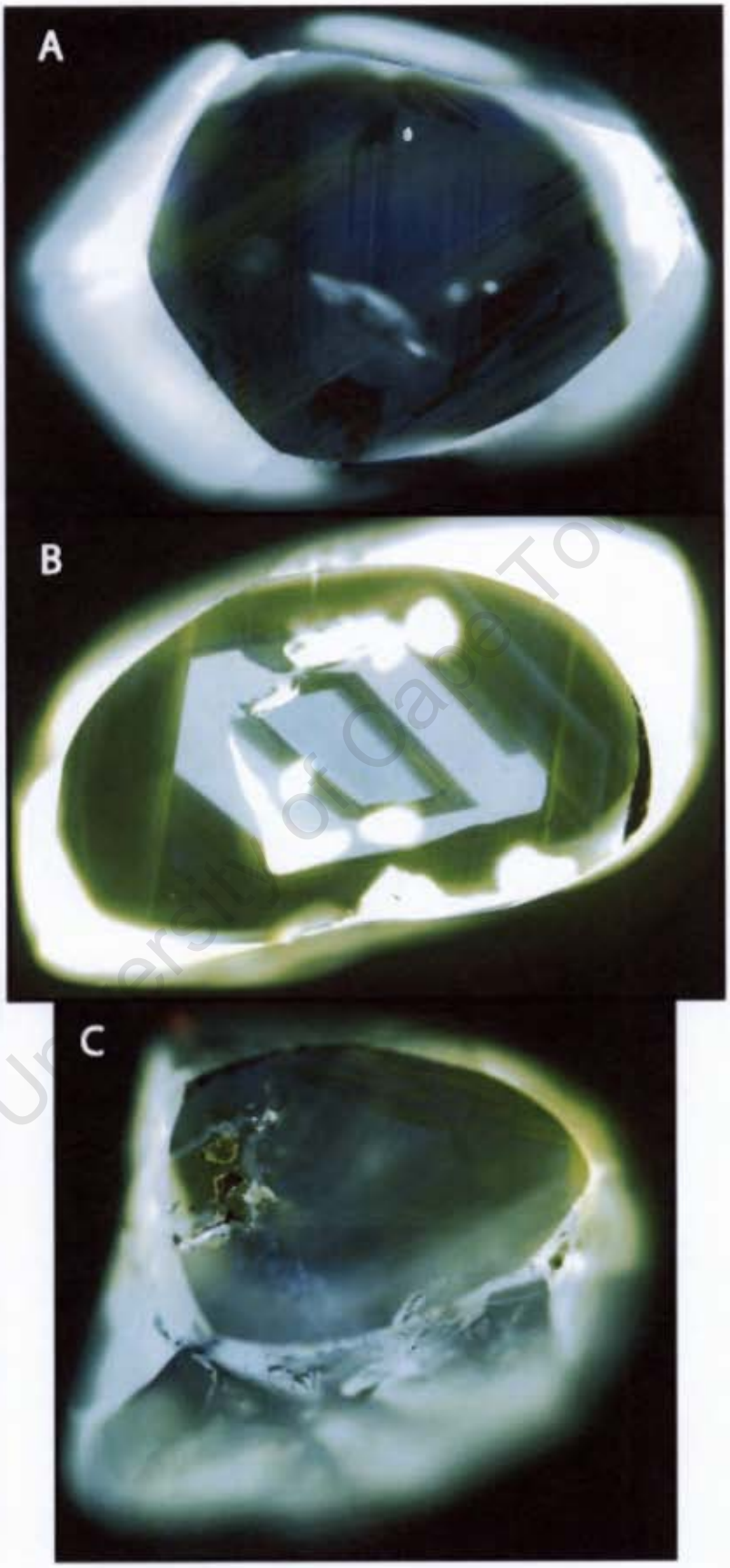

Figure 4.9: Three diamond plates showed yellow-green CL lines indicative of deformation lamellae. A: EL35. B: EL36. C: EL65.

4.5.6 Miscellaneous

EL33 and EL52 have cores with oscillatory zonation. This could be consistent with cuboid diamond growth in the core or else due to the presence of an inclusion/s or intermittent periods of resorption (Figure 4.10 and Figure 4.5 B). A set of hairline fractures is visible in EL23, along which several growth zones are offset (Figure 4.11 A and B), indicative of brittle deformation, as reported by Chinn (1995) for George Creek diamonds, Colorado , USA.

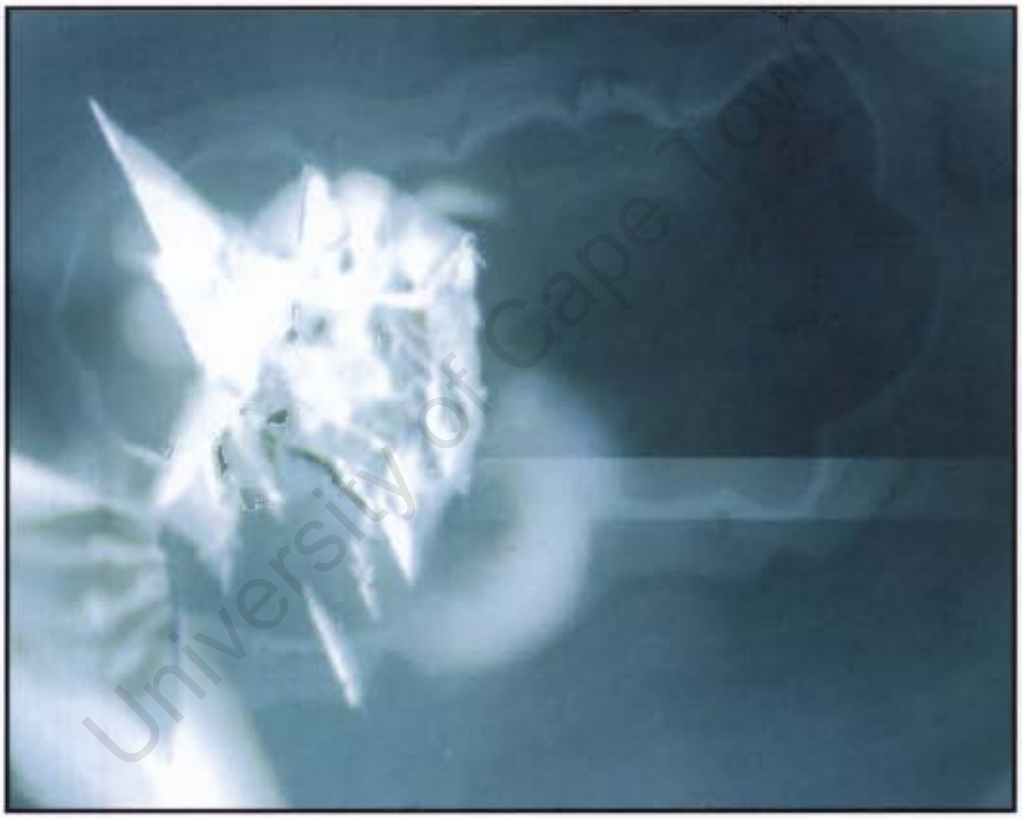

Figure 4.10: EL33 has a core with oscillatory zoning.

4.6 Summary

The internal zonation of the Ellendale diamonds reveals that the diamonds grew in several episodes accompanied by fluctuating volatile content of the diamond-forming fluid/s. Multiple growth and resorption events are identified in the suite, which could indicate that some diamond resorption must have occurred during storage in the mantle, consistent with their long mantle residence time (1400 Ma - see Re-Os chapter). The overall octahedral habit of the diamonds

indicates growth under conditions of lower carbon supersaturation (Sunagawa, 1984a,b).

All the diamonds show resorption on all the faces, with no xenolith shielding effects, which indicates they were liberated from their host rock at an early stage during transport to the surface, for attack by the lamproitic fluids. The diamonds generally have a smooth surface lustre, due to an extensive late stage chemical polish, though there are several diamonds which show the development of etch pits.

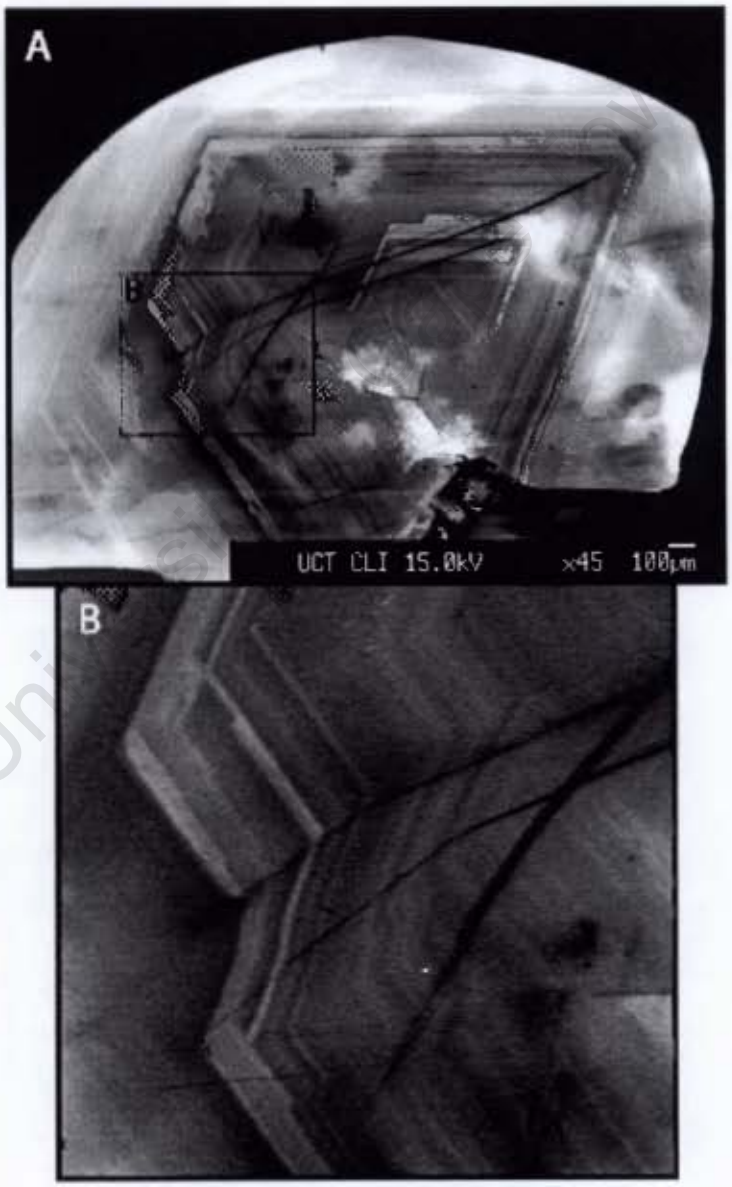

Figure 4.11: Some of the growth layers in EL23 are offset due to the presence of fractures, indicative of brittle deformation.

Table 4.1: Physical Characteristics of the Ellendale diamonds.

Sample Number	Weight (mg)	Weight (ct)	Plate thickness	Morphology	Form	Colour	Colour Intensity	Twin	Hillock Resorption Patterns	Etch Features	Octahedral layering	Deformation lamellae	Other
EL01	96.06	0.48	1.15 mm	THH	A	Y	1				X		
EL02	110.19	0.55		THH	A	Y	2				X		
EL03	97.58	0.49		THH	macle	Y	1	X		X	X		
EL04	86.05	0.43		THH	A	Y	1		X	X	X		
EL05	113.45	0.57	1.58mm	THH	A	Y	2				X		
EL06	123.81	0.62		THH	B	Y	1				X		
EL07	120.47	0.60		THH	A	Y	2			X	X	X	
EL08	53.02	0.27		THH	macle	Y	1	X		X	X	X	
EL09	56.35	0.28		PHM		Y	1			X	X	X	broken crystal
EL10	62.26	0.31	1.77mm	THH	A	W	0		X	X	X	X	grew in rock or uneven surface
EL11	130.38	0.65		THH	A	Y	1				X		
EL12	60.84	0.30	1.67mm	THH	C	Y	2				X		
EL13	66.56	0.33		THH	A	Y	2			X	X	X	grew in rock or uneven surface
EL14	101.21	0.51		THH	elongate	Y	1		X	X	X	X	
EL15	97.51	0.49		THH	A	Y	2		X	X	X	X	
EL16	57.65	0.29	1.57mm	THH	macle	Y	1	X		X	X		
EL17	80.69	0.40		THH	A	Y	1				X		
EL18	84.37	0.42		THH	A	W	0				X		
EL19	96.45	0.48		THH	A	Y	1				X		
EL20	127.25	0.64	1.76mm	THH	macle	Y	1	X			X		
EL21	116.30	0.58		THH	A	Y	1			X	X		
EL22	118.70	0.59		THH	A	Y	2				X		
EL23	97.36	0.49	1.65mm	THH	A	Y	1		X		X		
EL24	87.72	0.44	1.60mm	THH	elongate	Y	1				X		

Sample Number	Weight (mg)	Weight (ct)	Plate thickness	Morphology	Form	Colour	Colour Intensity	Twin	Hillock Resorption Patterns	Etch Features	Octahedral layering	Deformation lamellae	Other
EL25	75.14	0.38	1.30mm	THH	C	Y	1			X			
EL26	114.97	0.57	1.50mm	THH	distorted	Y	1				X		
EL27	123.93	0.62		THH		Y	1			X		X	uneven resorption
EL28	102.29	0.51		THH	A	Y	1				X		
EL29	108.33	0.54		THH	both flat and elongated	Y	2			X			
EL30	106.81	0.53		THH	A	Y	2						
EL31	115.60	0.58	1.83mm	THH	C	Y	1				X		
EL32	96.80	0.48	1.65mm	THH	A	Y	1		X	X			
EL33	86.58	0.43	1.68mm	THH	A	Y	1		X	X	X		
EL34	72.06	0.36	2.08mm	THH	C	Y	2		X	X	X	X	
EL35	104.51	0.52	2.16mm	THH	elongate	W	0				X	X	
EL36	92.63	0.46	1.88mm	THH	C	W	0		X	X	X	X	
EL37	79.18	0.40		THH	C	Y	2			X	X		
EL38	114.00	0.57	2.39mm	THH	A	Y	1						
EL39	111.94	0.56		THH	A	Y	1				X		
EL40	121.97	0.61		THH	A	Y	1			X	X		
EL41	106.07	0.53		THH	A	Y	1				X	X	
EL42	78.21	0.39		THH	A	Y	2			X	X	X	two white diamond portions - aggregate or is yellow colour a late skin?
EL43	101.78	0.51	2.16mm	THH	B	Y	1		X	X	X		
EL44	87.87	0.44		THH	A	Y	2			X	X		scrach-like marks on surface

Sample Number	Weight (mg)	Weight (ct)	Plate thickness	Morphology	Form	Colour	Colour Intensity	Twin	Hillock Resorption Patterns	Etch Features	Octahedral layering	Deformation lamellae	Other
EL45	79.01	0.40		THH	A	Y	2				X		
EL46	104.76	0.52		THH	A	Y	2				X		
EL47	123.30	0.62		THH	B	Y	2			X	X	X	
EL48	87.48	0.44		THH	A	Y	2				X		
EL49	78.53	0.39		THH	A	Y	2				X		scratch-like marks on surface
EL50	126.68	0.63	1.99mm	THH	macle	W	0	X	X		X		
EL51	110.80	0.55	2.01mm	THH	A	Y	1		X		X		
EL52	96.60	0.48	1.80mm	THH	A	Y	2				X		
EL53	102.70	0.51	2.19mm	THH	A	Y	1			X			
EL54	115.50	0.58	2.70mm	THH	A	W	O				X	X	
EL55	93.60	0.47	2.29mm	THH	C	W	O		X		X		
EL56	95.90	0.48	2.48mm	THH	twin	Y	1	X			X		
EL57	117.10	0.59	1.99mm	THH	B	Y	1				X		
EL58	93.90	0.47		THH	C	W	O				X		
EL59	69.80	0.35	1.21mm	OCTA	A	W	O				X		
EL60	111.00	0.56	2.97mm	THH	twin	Y	1	X		X	X		
EL61	112.60	0.56	2.35mm	THH	twin	Y	1	X		X	X		
EL62	71.10	0.36	1.90mm	THH	C	Y	1				X		
EL63	57.60	0.29		THH	macle	Y	1	X	X	X			
EL64	76.70	0.38	2.44mm	THH	A	Y	2						
EL65	94.70	0.47	1.83mm	THH	B	W	O			X	X	X	
EL66	103.60	0.52	2.52mm	THH		Y	1				X		uneven resorption
EL67	118.50	0.59	2.74mm	THH	C	W	O		X	X			
EL68	142.30	0.71		THH	C	W	O		X	X	X		
EL69	184.50	0.92	2.03mm	THH	twin	Y	2	X		X			

Chapter 5

NITROGEN CONTENT AND NITROGEN AGGREGATION CHARACTERISTICS

5.1 Introduction

Nitrogen is the main substitutional trace element in diamond and may be present as both single and aggregate forms. Nitrogen can be measured using Fourier Transform Infrared absorption Spectroscopy (FTIR) and the concentrations of the various forms, including total nitrogen can be calculated from the intensities and absorption coefficients. The main significance of nitrogen is the temperature-time dependence of the A to B conversion that allows calculation of time-averaged mantle storage temperatures or alternatively, mantle storage time (e.g. Evans & Qi, 1982; Taylor *et al.*, 1990).

5.2 Infra-red classification of diamonds

All diamonds show absorption due to two and three phonon transitions in the mid infrared range from 4500 to 650 cm^{-1} (e.g. Sutherland *et al.*, 1954; Lax & Burstein, 1955) and have been grouped into two groups based on their nitrogen content (Robertson *et al.*, 1934). Type I diamonds contain nitrogen in various forms and Type II diamonds contain no detectable nitrogen ($<$ 20 ppm). The majority of diamonds are Type I, with Type II diamonds accounting for less than 5 % of natural diamonds. Both these groups can be further subdivided according to their infrared (IR) absorption features, which are described below and summarised in Figure 5.1. Characteristic FTIR spectra for diamonds containing nitrogen, in its various forms, and other

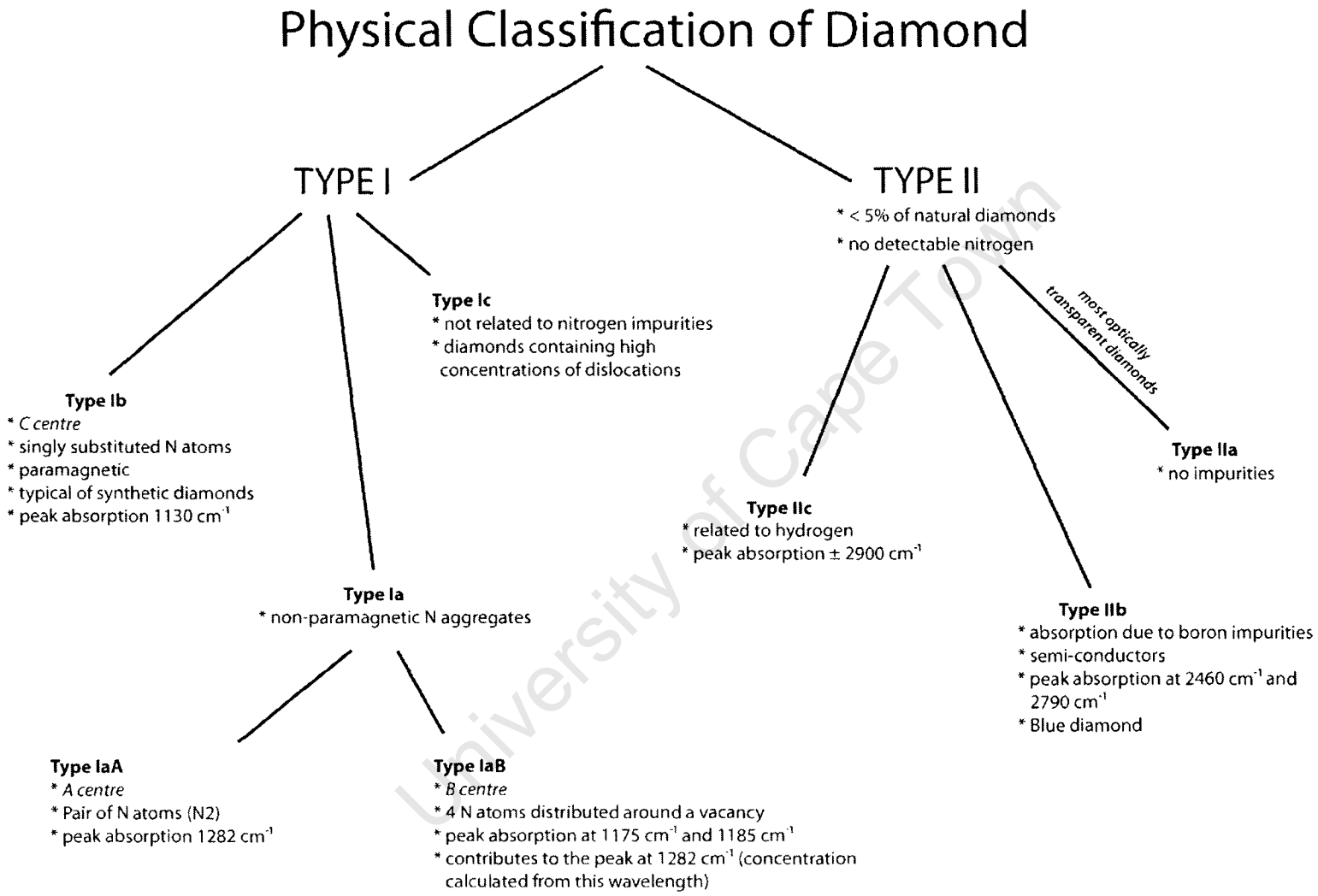

Figure 5.1: Physical Classification of Diamond using infra-red absoprtion and nitrogen impurities, compiled from Robertson *et al.* (1934), Sobolev *et al.* (1968), Davies (1981), Loubser & van Wyk (1981), Collins & Woods (1982), Woods & Collins (1983), Bursill & Glaisher (1985) and Wilks & Wilks (1991).

impurities are given in Figure 5.2 and Figure 5.3.

5.2.1 C Centre (Single Nitrogen Centre)

This is a paramagnetic centre, with a single N atom replacing a C atom in the diamond lattice. The paramagnetism is due to an extra electron on the N atom (Wilks & Wilks, 1991, and references therein). Peak absorption occurs at 1130 cm^{-1}, though a subsidiary peak also occurs at 1344 cm^{-1} (Collins & Woods, 1982).

5.2.2 A Centres

Interpretation of ultraviolet absorption spectra after uniaxial stresses were applied in different directions, allowed Davies (1976) to conclude that the A centre is due to a pair of N atoms, as first suggested by Sobolev *et al.* (1968). The position of maximum IR absorption due the A centre is 1282 cm^{-1}.

5.2.3 B Centres

The B Centre consists of four adjacent N atoms surrounding a vacancy (Loubser & van Wyk, 1981; Bursill & Glaisher, 1985). Peak absorption occurs at 1175 cm^{-1} (Davies, 1981), though Wilks & Wilks (1991) give a slightly higher value at 1185 cm^{-1}. The B centre also contributes to absorption at 1282 cm^{-1}.

5.2.4 Hydrogen Peak

The infrared spectrum of diamond containing hydrogen shows two peaks at 3107 cm^{-1} and 1405 cm^{-1} (Chrenko *et al.*, 1967; Davies *et al.*, 1984). Woods & Collins (1983) give a complete discussion of the origin of these peaks. They suggest that vibrations of the sp^2 bonds in the C = CH_2 group, situated at inclusion - matrix interfaces, cause the observed hydrogen peaks.

5.2.5 Platelet Peak

Absorption at 1359 -1378 cm^{-1} is due to the development of platelets (Sobolev *et al.*, 1968) on the {100} crystal planes. Platelets are planar features and can range in size from 8 nm to a few μm (Evans & Qi, 1982). Platelets do not occur in Type Ib diamonds (Phaal & Zuidema, 1966; Sobolev *et al.*, 1968) and Humble (1982, and references therein), mention that there is a

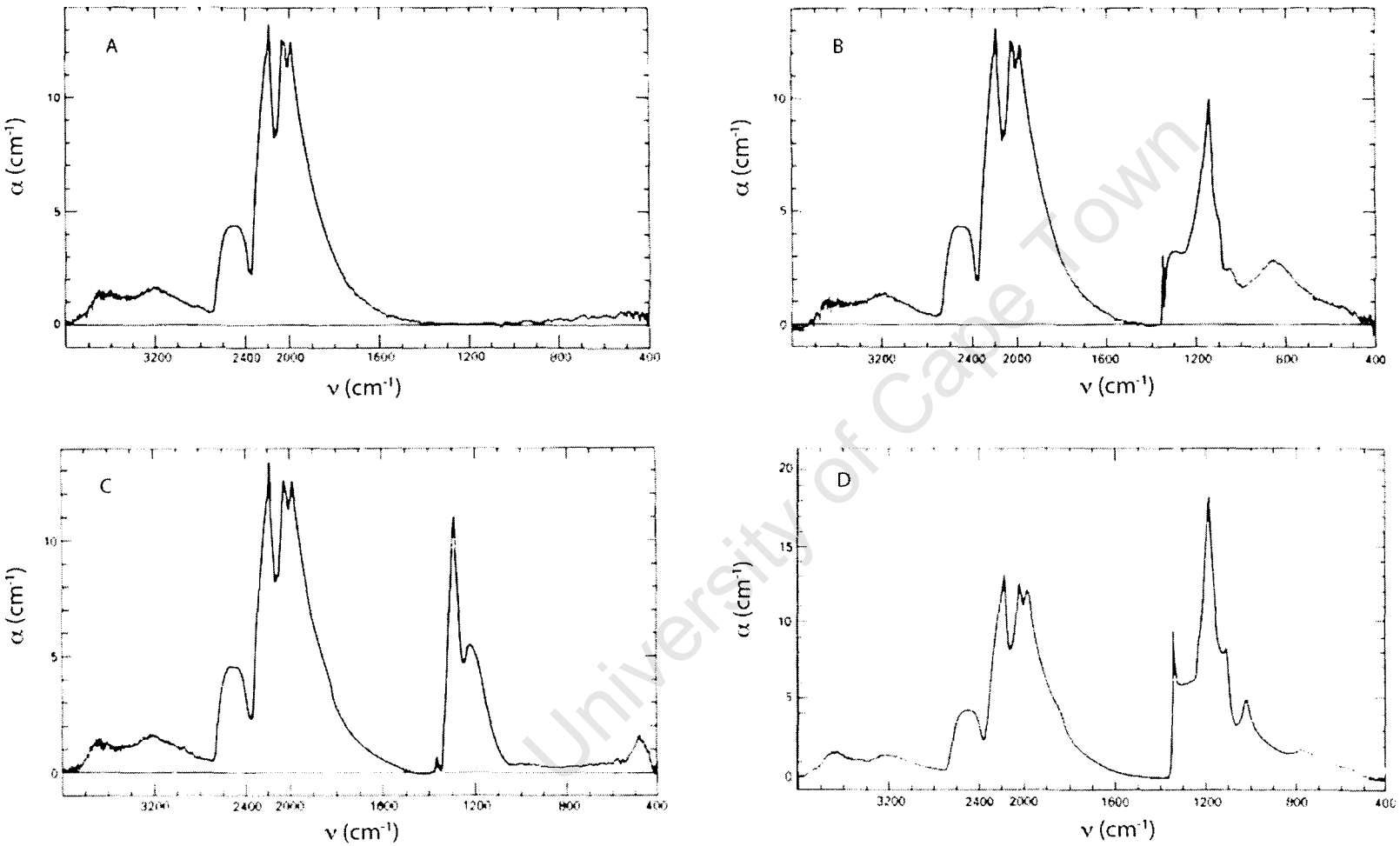

Figure 5.2: Characteristic FTIR spectra of diamonds (Wilks & Wilks, 1991) A. Diamond with no impurities (Type IIa). B. Type Ib spectrum due to the presence of single unaggregated nitrogen centres. C. Type IaA spectrum due to the presence of nitrogen pairs (A centres). D. Type IaB spectrum due to the presence of B centres - four adjacent nitrogen atoms surrounding a vacancy.

correlation between the presence of platelets and the aggregation of nitrogen. Various authors (Lang, 1964, 1974; Bursill & Glaisher, 1985; Barry *et al.*, 1985) considered nitrogen to be a major constituent of platelets though Humble (1982) and Woods (1986) suggested that platelets form due to the aggregation of interstitial carbon atoms. According to Woods (1986), platelets are carbon atoms that are removed/expelled from the lattice when B nitrogen aggregates form. Therefore, high nitrogen contents would promote nitrogen aggregation and rapid nucleation of small sized platelets. Larger platelets would grow where there is lower nitrogen content and lower nitrogen aggregation and nucleation rates. Platelet composition was confirmed through electron energy-loss spectroscopy (Bruley, 1992; Fallon *et al.*, 1995). Diamonds were termed regular by Woods (1986) if they show a linear relationship between platelet intensity and %N as IaB. Diamonds that do not show this correlation are termed irregular and have undergone platelet degradation to form dislocation loops and voidites in the {001} planes. Voidites are octahedral nitrogen defects in the diamond lattice (e.g. Kiflawi & Bruley, 2000) Platelet degradation is the final step in the nitrogen aggregation sequence and typically occurs at high temperatures (Evans *et al.*, 1995; Kiflawi & Bruley, 2000).

5.3 Nitrogen Aggregation

In young and synthetic diamonds, nitrogen starts out as single nitrogen atoms. With increased mantle residence time, singly substituted N atoms aggregate to form pairs of N atoms and eventually form three atom N defect centres plus a vacancy (e.g. Evans & Harris, 1989; Taylor *et al.*, 1990; Mendelssohn & Milledge, 1995a,b). However, singly substituted nitrogen is extremely rare in natural diamonds, with less than 1 % of natural diamonds containing single N (Mohammed *et al.*, 1982). Also, Boyd *et al.* (1987) found that young diamonds that have crystallised from kimberlitic magmas contain mainly nitrogen pairs. Kesson & Ringwood (1989) suggest that under mantle oxygen fugacity conditions it is more reasonable that nitrogen starts out as nitrogen pairs.

Nitrogen aggregation is sensitive to temperature, time and total N content (Allen & Evans, 1981; Evans & Harris, 1989). The conversion rate from single N (Type Ib) to N pairs (A centres - Type IaA) has been determined by (Taylor *et al.*, 1996). The rate is strongly controlled by the activation energy, with $E_A = 6.0 \pm 0.2$ eV for cubic growth zones and $E_A = 4.4 \pm 0.3$ eV for octahedral growth zones. These values indicate that aggregation occurs at a faster rate on octahedral growth zones.

The conversion from N pairs (A centres - Type IaA) to N aggregates (B aggregates - Type

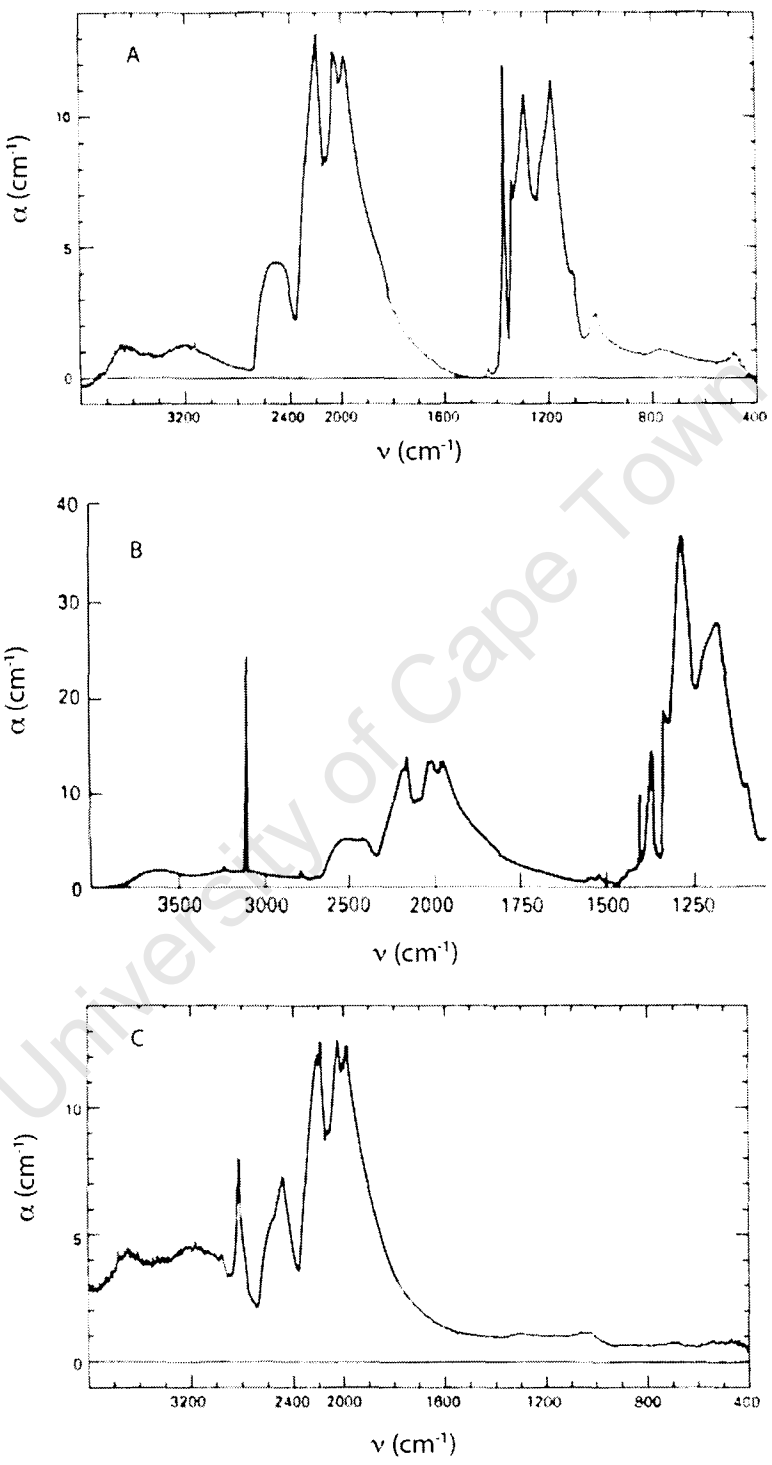

Figure 5.3: Characteristic FTIR spectra of diamonds (Wilks & Wilks, 1991). A. Type IaAB spectrum, with a strong platelet peak at 1359 - 1378 cm^{-1}. B. Type IaAB spectrum with peaks at 3107 and 1405 cm^{-1} due to the presence of hydrogen. C. Type IIb spectrum, with absorption due to boron.

IaB) is much slower. Evans & Qi (1982) and Evans & Harris (1989) were some of the early studies to model the A to B conversion kinetically in an attempt to quantify the relationships between temperature, time and N content. The conversion is assumed to follow second order kinetics (Evans & Harris, 1989) with the rate-determining step involving the combination of two A centres. The success of the kinetic models has depended on the accurate determination of the activation energy. Evans & Harris (1989) determined an activation energy of 6.88 eV, while Kesson & Ringwood (1989) suggested a lower value of 6.5 eV. Ea = 7.03 eV, the value determined by Taylor *et al.* (1990) is the most widely accepted value.

The nitrogen aggregation state is mainly sensitive to temperature (Navon, 1999) so that if diamonds have a mantle residence time greater than 200 Ma, the nitrogen aggregation state can be used as a thermometer. Diamonds with highly aggregated nitrogen states are more likely to have resided in warmer lithospheric conditions whereas those with low aggregation states, likely resided in a cooler lithosphere. This thermometer gives an average temperature experienced by the diamond during its mantle residence. The nitrogen aggregation rate in diamond may be increased by the presence of defects in the diamond (Evans, 1992) and as there are many variables in the temperature calculation, the calculated temperature may only be semi-quantitative.

If the nitrogen aggregation state is known from FTIR analyses, time-averaged mantle temperatures can be calculated using the formula below (Evans & Qi, 1982):

$$T_{NA}(^{\circ}C) = \frac{E_a}{R} \times \left\{ \ln \frac{\frac{N_{TOT}}{N_A} - 1}{t_{MR} \times N_{TOT} \times A} \right\}^{-1} - 273.15 \qquad (5.1)$$

With:

E_A (activation energy) = 7.03 eV = 678 289.55 J mol^{-1} (Taylor *et al.*, 1990)

R (gas constant) = 8.31451 J K^{-1} mol^{-1}

A (Arrhenius constant) = 2.94181 x 105 s^{-1} ppm^{-1}

t_{MR} (mantle residence time in seconds) with 1 Ma = 3.1536 x 10^{13} s

N_{tot} = total nitrogen content (ppm)

N_A = total nitrogen in A centres (ppm)

In principle, if the mantle storage temperatures can be calculated accurately through an-

other means, the formula can be re-arranged to yield mantle residence times. It is important to remember that these are average temperatures and therefore may not necessarily correlate with temperatures calculated from silicate inclusions, as ambient mantle temperatures may fluctuate over a billion year timescale.

5.4 FTIR Results

FTIR analyses were done in traverses across the diamond plates to show across-plate variations of nitrogen content, nitrogen aggregation, platelet peak strength and hydrogen peak strength, with growth layering. Complete FTIR data is presented in Appendix 1. In some cases the values are plotted on a log scale so that all the parameters can be plotted on one diagram. The approximate positions of the FTIR analyses are indicated on the CL images, as the FTIR stage does not have sensitive position control. Analyses don't always correspond with individual growth layers, as the resolution of the analysis is often much larger than fine-scale layering. In addition, growth layers are commonly inclined to the surface of the diamond (Mendelssohn & Milledge, 1995b) and if the contact between different growth layers isn't perpendicular to the surface, the FTIR analysis will measure a gradual zonation. This is particularly likely in diamond plates where the CL images of the front and back of the plate don't correlate exactly. Analyses therefore often represent averages through multiple growth layers, each of which may have distinctly different nitrogen contents and/or nitrogen aggregation. FTIR traverses and growth zoning for each diamond are described and presented in Appendix 2.

5.4.1 Nitrogen Content

Nitrogen content in the suite of diamonds varies, on average, between 100 and 1000 ppm, with one diamond (EL25) having significantly higher nitrogen at 1400 ppm. Average nitrogen content in the suite is 638 ppm. There are three diamonds that have significantly lower nitrogen contents than the rest of the suite, namely EL10 (154 ppm), EL35 (94 ppm) and EL65 (125 ppm). These diamonds have less saturated yellow colours or are colourless. The diamonds with the highest average nitrogen contents (> 1000 ppm) are EL12 (1046 ppm), EL25 (1399 ppm) and EL34 (1019 ppm) all of which have high intensity yellow colours. No distinction between the nitrogen content of the eclogitic and peridotitic diamonds is seen. Nitrogen content is not a useful indicator of parageneses, as both parageneses show a large range in nitrogen content, as also shown by Taylor *et al.* (1990).

Table 5.1: FTIR analyses and mantle storage temperatures, calculated for a 1400 Ma mantle residence time. Temperatures are averaged for each diamond.

Sample	IaA (ppm)	IaB (ppm)	N total (ppm)	%N as IaB	Temp (°C)
EL01	324	370	693	53	1150
EL05	238	716	954	75	1166
EL10	106	49	154	29	1162
EL12	388	659	1046	63	1150
EL16	99	122	221	35	1171
EL20	522	397	920	43	1133
EL23	487	396	883	44	1135
EL24	684	249	933	27	1115
EL25	812	586	1399	42	1122
EL26	321	308	628	48	1148
EL31	433	455	888	49	1142
EL32	334	474	808	58	1152
EL33	377	497	874	57	1148
EL34	227	793	1019	78	1168
EL35	41	54	94	55	1204
EL36	25	197	222	66	1223
EL38	298	334	632	52	1151
EL43	336	498	834	60	1152
EL50	270	244	513	46	1151
EL51	153	444	597	74	1177
EL52	115	549	664	83	1188
EL53	131	451	582	78	1183
EL54	138	129	267	49	1171
EL55	144	322	465	69	1177
EL56	82	464	546	85	1197
EL57	168	368	535	69	1173
EL59	274	394	667	55	1155
EL60	92	370	463	80	1193
EL61	119	334	454	73	1184
EL62	219	522	741	71	1167
EL64	47	495	542	91	1215
EL65	68	58	125	46	1187
EL66	141	312	453	69	1178
EL67	43	419	462	91	1216
EL69	89	449	538	83	1195

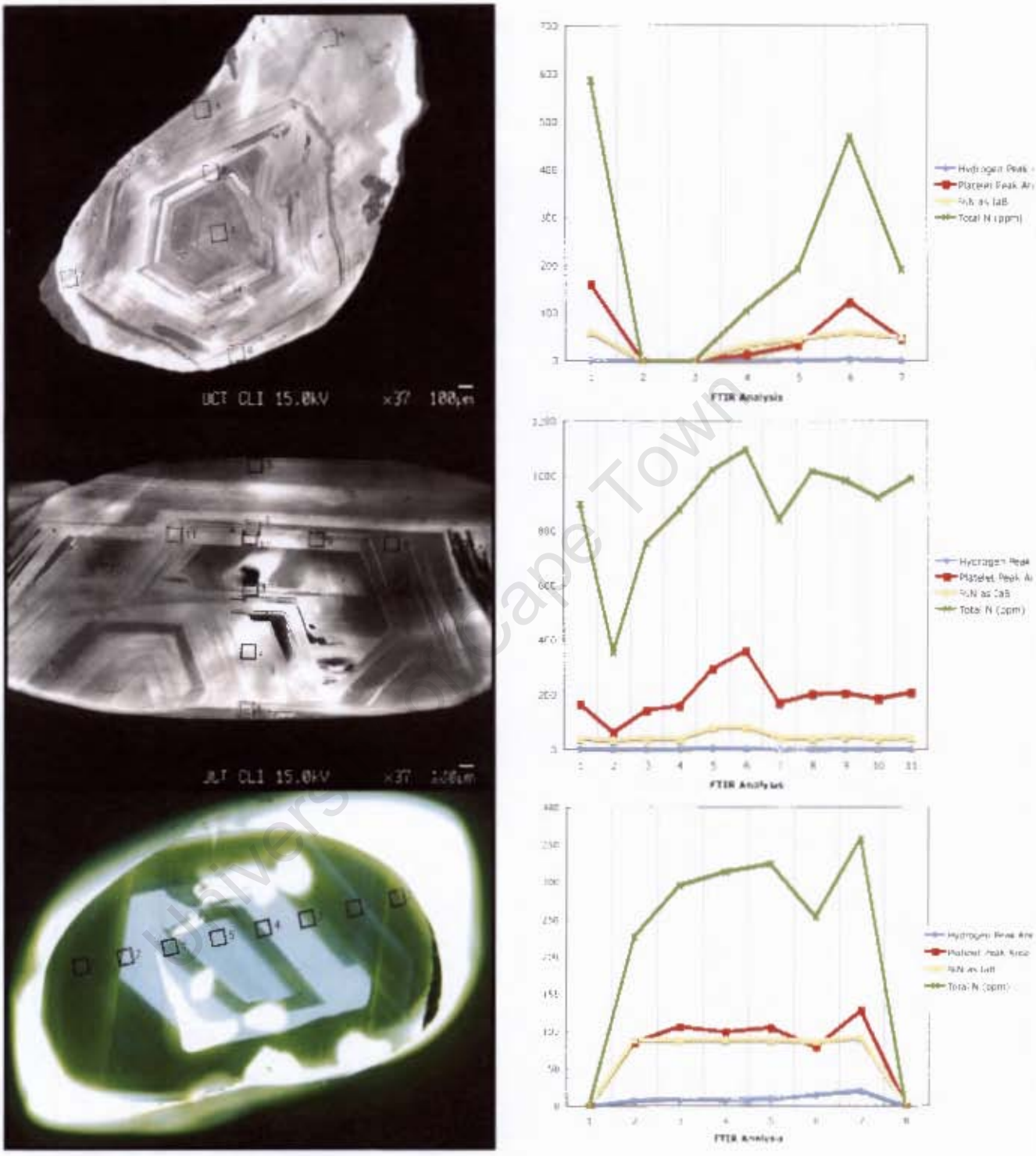

Figure 5.4: CL images and FTIR traverses for diamonds with a strong variation in N content. TOP: EL16. MIDDLE: EL32. BOTTOM: EL36.

Analyses of the plates show that nitrogen content can vary dramatically in one diamond. Different growth layers are typically characterised by different nitrogen content, which reflect fluctuating conditions of growth. EL16 shows the most dramatic variation of nitrogen content with

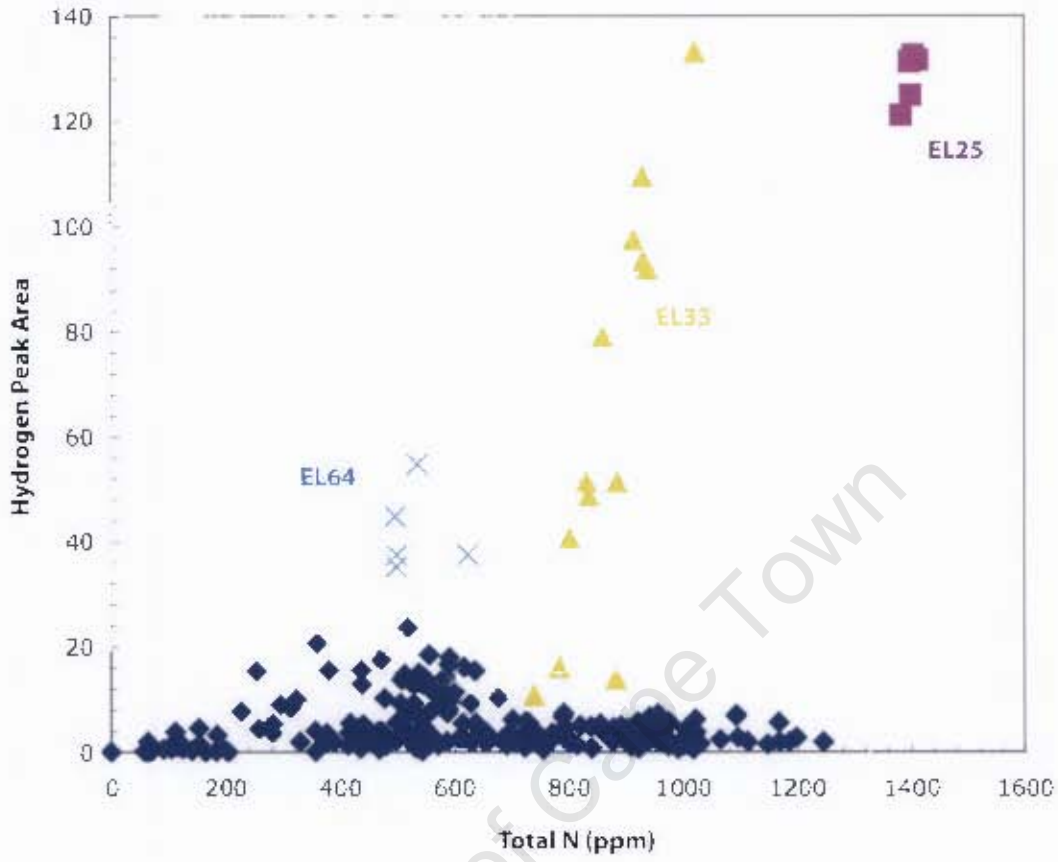

Figure 5.5: Diamonds with high hydrogen peak areas are typically rich in nitrogen. The three diamonds in this suite with the highest hydrogen contents are EL25, EL33 and EL64.

Type II growth layers fluctuating with layers that are relatively rich in nitrogen (590 ppm). EL36 shows strong contrast between layers of no nitrogen content with layers of high nitrogen content on the CL image. Two analyses show Type II compositions along the rim, with the inner layer analyses probably representing averages through multiple growth layers, with nitrogen content varying between 220 and 360 ppm. Other diamonds that show large variation in nitrogen content are EL32 (530 - 1170 ppm) and EL31, which shows multi-centred growth with variation in nitrogen content between 360 and 1100 ppm. The traverse diagrams for EL16, EL32 and EL36 are shown in Figure 5.4.

5.4.2 Hydrogen Peak Area vs Nitrogen Content

Blinova *et al.* (1988) suggest that diamonds with high hydrogen contents are rich in nitrogen. This is demonstrated in Figure 5.5, with the three diamonds in the suite that show the highest hydrogen content, all showing increasingly higher nitrogen contents. The reverse is not true however, and diamonds that are nitrogen-rich don't necessarily have high hydrogen contents.

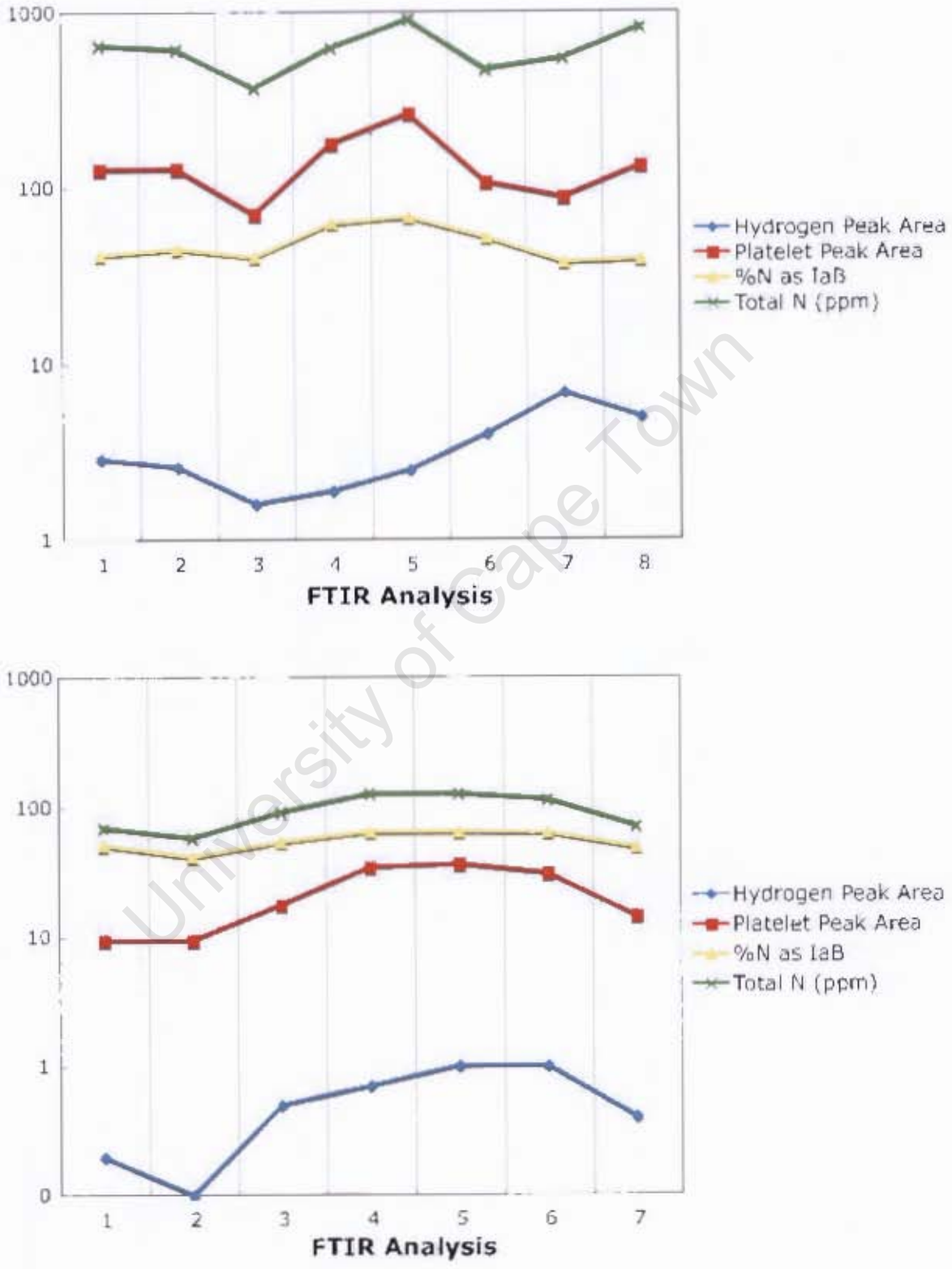

Figure 5.6: TOP: The majority of diamonds in the suite show no correlation between H peak area and N content (e.g. EL26). BOTTOM: Only 11 diamonds (e.g. EL35) show a positive correlation between H peak area and N content.

Although hydrogen-rich diamonds show some elevated nitrogen contents, there is no obvious relationship between hydrogen and nitrogen in the whole suite. Twenty diamond plates (EL05, EL20, EL23, EL26, EL32, EL38, EL50, EL51, EL52, EL53, EL55, EL56, EL57, EL59, EL60, EL61, EL62, EL64, EL65, EL67) show no linear correlation between hydrogen and nitrogen content, whereas only 11 diamond plates (EL01, EL10, EL12, EL31, EL33, EL34, EL35, EL36, EL43, EL54) show increase in hydrogen peak strength with increased nitrogen contents between growth zones. The traverse diagrams for EL26, which shows no correlation and EL35, which shows a positive correlation between H peak area and N content are shown in Figure 5.6.

5.4.3 Platelet Size vs Nitrogen Content

Diamond zones with low nitrogen content have inhibited platelet nucleation and slow growth of platelets to large sizes (Woods, 1986). Similarly, high nitrogen content will promote rapid nucleation of platelets, all of small size. Platelet size can be related to platelet peak position, with lower peak positions ($\sim$ 1359 cm^{-1}) corresponding to relatively large platelets and higher peak positions ($\sim$ 1373 cm^{-1}) corresponding to smaller platelets (e.g. Hanley *et al.*, 1977; Mendelssohn & Milledge, 1995a). These relationships are illustrated in Figure 5.7 where the position of the platelet peak is positively correlated with the diamond nitrogen content. Low wavenumber peak positions ($<$ 1362 cm^{-1}) are only seen in diamonds with less than 500 ppm total nitrogen.

5.4.4 Platelet Peak Strength vs %B aggregation

A plot of percentage B aggregation against the platelet peak strength illustrates that many of the samples in this study show a positive linear relationship between platelet peak strength and %B aggregation, with a broad increase in platelet peak strength with increasing B aggregation. Diamonds defining this trend are termed regular by Woods (1986). If samples plot below this trend, they are termed irregular and suggest platelet degradation, which is typically related to mantle heating or deformation events (Woods, 1986; Evans *et al.*, 1995). Ellendale diamonds do not show pervasive platelet degradation and only a few samples plot just below this trend which may be suggestive of low levels of platelet degradation (Figure 5.8). Only three of the 'irregular' samples show evidence for plastic deformation namely EL35, EL36 and EL65. Other samples which show an irregular correlation between platelet peak strength and %B aggregation are EL25, EL33, EL51, EL53, EL55, EL56, EL57, EL60, EL62 and partially, EL64. All the analyses from EL64 plot on the regular trend, apart from one analysis that shows an anomalously low platelet peak area.

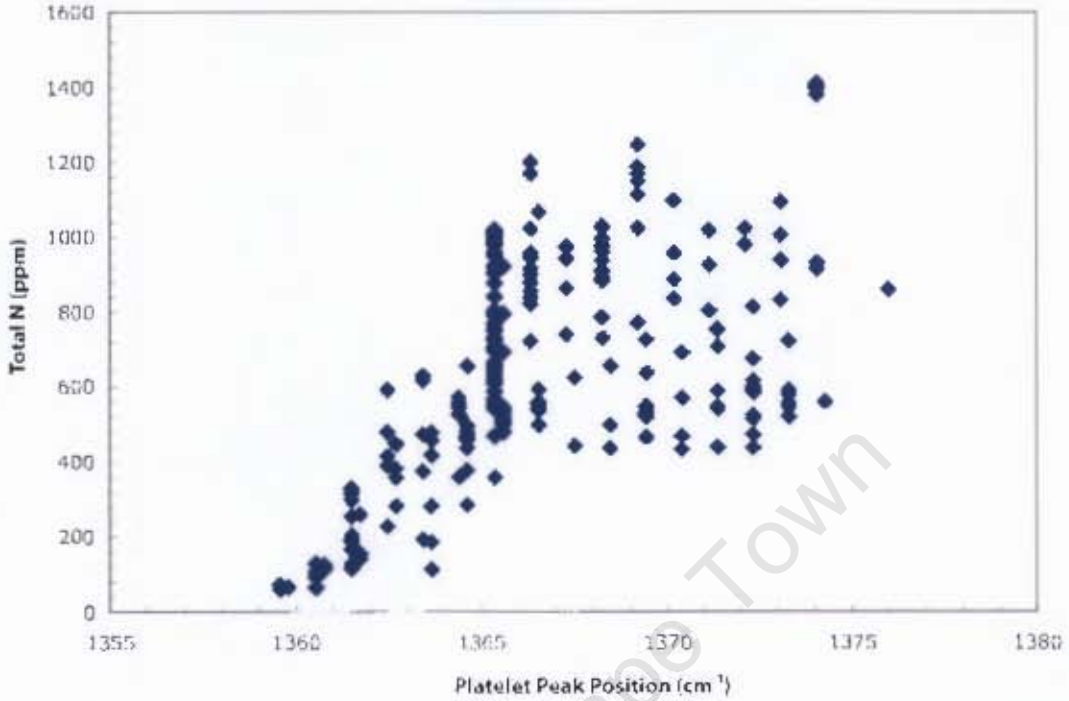

Figure 5.7: The position of the platelet peaks plotted as a function of the total nitrogen content.

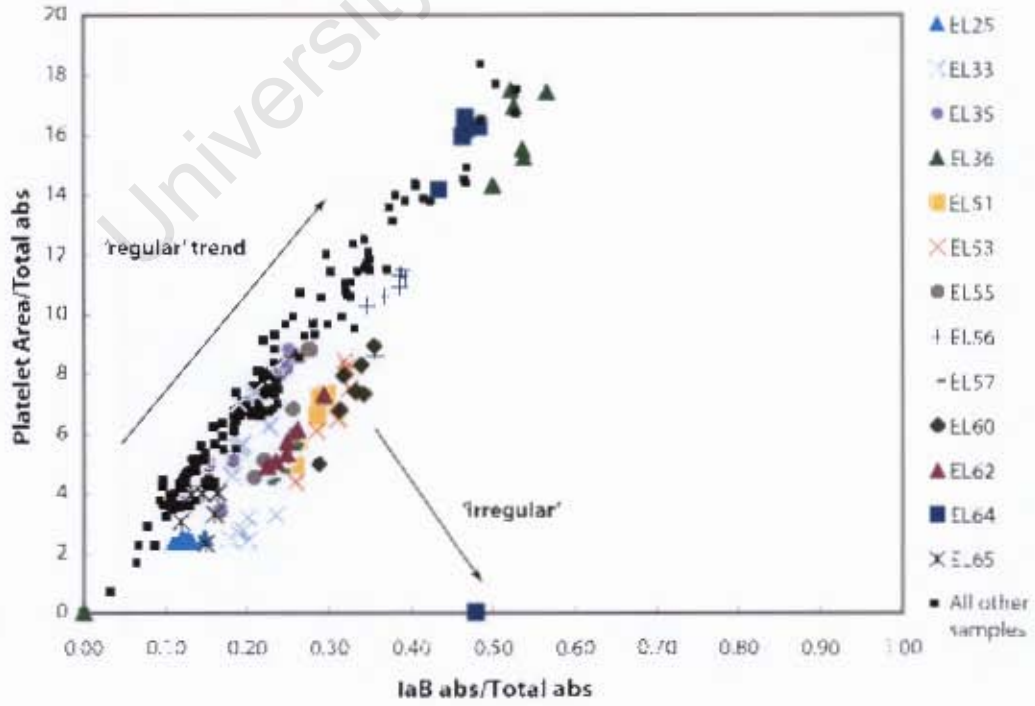

Figure 5.8: Platelet peak area vs B aggregation. Ellendale diamonds do not show pervasive platelet degradation as would be defined by the 'irregular' trend.

5.4.5 Nitrogen Aggregation and Temperature Calculations

The diamonds in this study are dominated by nitrogen-rich Type IaAB diamonds and are characterised by high levels of B aggregation, with an average %N as IaB around 62 %. Some diamonds show up to 93 % B aggregation (Figure 5.9). Nitrogen aggregation state is a function of temperature, nitrogen concentration and mantle residence time. For example, EL35 has very low nitrogen content (< 130 ppm) with B aggregation between 40 and 64 %. For the 1400 Ma residence time of the diamonds (see below), high storage temperatures are needed to attain this level of aggregation, given the low N content of the diamond. Conversely, EL24 has very high nitrogen content (~ 900 ppm) and due its low aggregation state (~ 26 %), was stored at much lower ambient mantle temperatures.

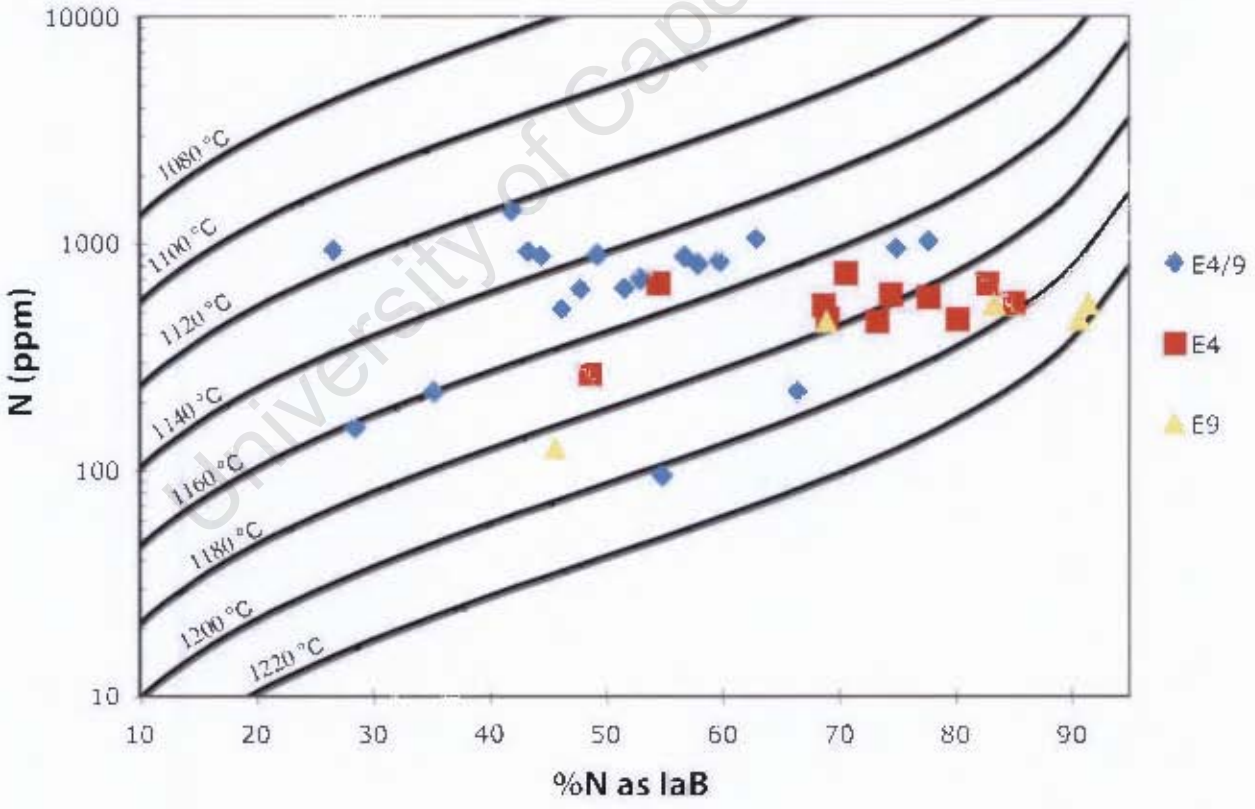

Figure 5.9: Nitrogen content and aggregation state of all the Ellendale diamonds in this suite. Data points are averages for each diamond (Table 5.1). E4/9 represents a mixed population from E4 and E9 lamproite pipes. Isotherms are calculated for a 1400 Ma mantle residence time.

Nitrogen aggregation state (%N as IaB) is plotted as a function of the logarithm of the nitrogen content (Figure 5.9) with isotherms representing aggregation state resulting from storage at a particular temperature for a given mantle residence time. Time-integrated isotherms were constructed for mantle residence times of 1400 Ma, with peridotitic diamond crystallisation at $\sim$ 1432 Ma (see Chapter 6) and lamproite emplacement at $\sim$ 20 Ma. From these diagrams, the diamonds show a temperature range from 1114 to 1229 °C , with an average of 1167 °C . No distinct differences could be seen between diamonds from the different lamproite pipes, although it does seem that diamonds sampled by E9 resided at slightly higher temperatures in the mantle ($\sim$ 20 °C), than those sampled by E4 (Table 5.2 and Figure 5.9). Individual diamond plates that define nitrogen aggregation trends sub-parallel to the isotherms typically indicate single-stage growth. Some plates however exhibit much wider scatter which indicates multi-stage diamond growth, with different growth layers displaying vastly different nitrogen contents, aggregation state and cathodoluminescence properties (Figures 5.10 and 5.11). The overall range in mantle storage temperatures calculated for the suite of diamonds could be explained in terms of diamond storage and lamproite sampling at different depths in the mantle.

Table 5.2: Temperatures calculated for the Ellendale diamonds in this study, based on a mantle residence time of 1400 Ma.

Sample	Pipe	Average Temp (°C)	Range in Temp (°C)
EL01 to EL50	E4/9	1154	1114 - 1229
EL51 to EL62	E4	1178	1150 - 1202
EL64 to EL69	E9	1201	1174 - 1223
All samples		1167	1114 - 1229

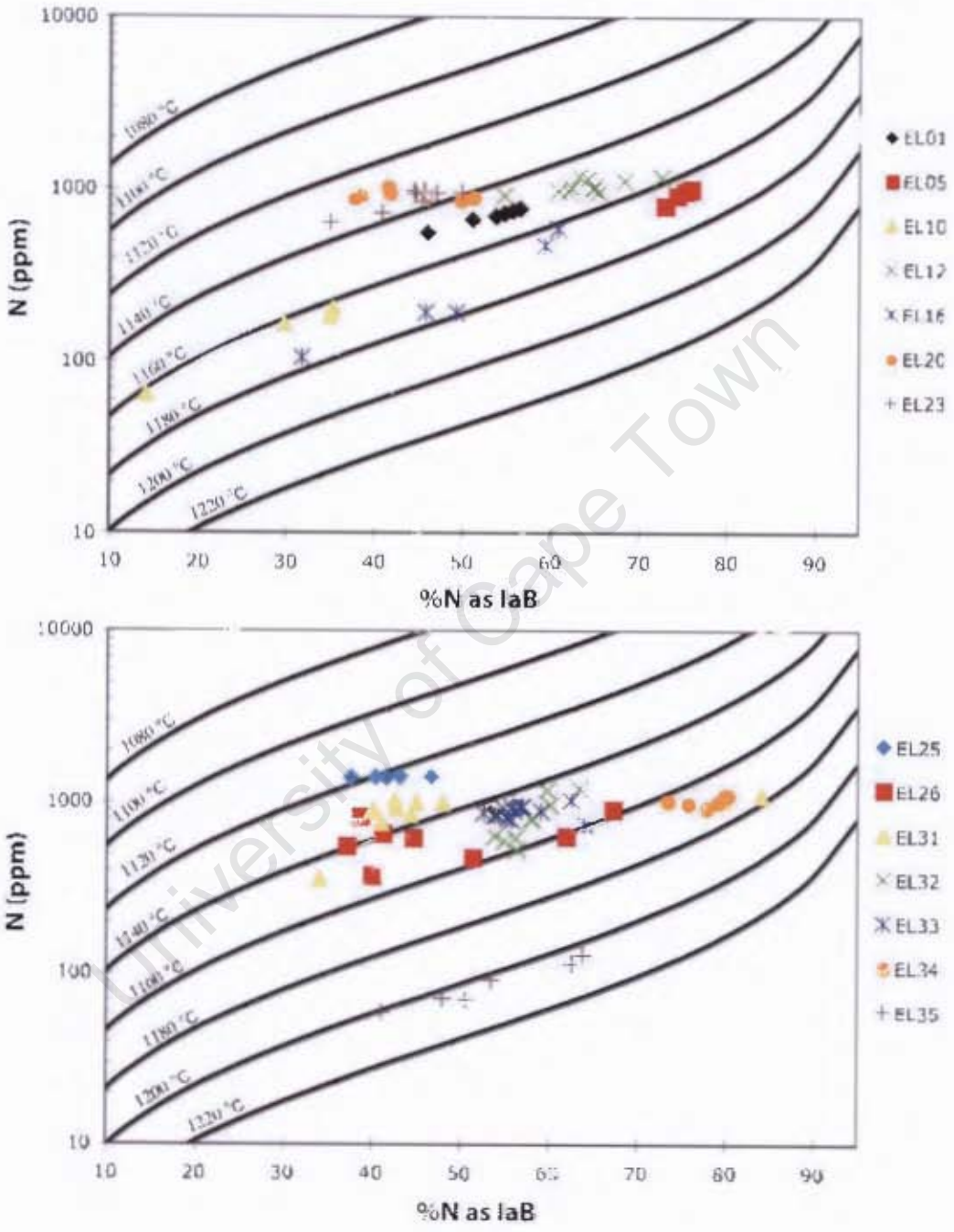

Figure 5.10: Nitrogen content and aggregation state for individual analyses on each diamond, with isotherms calculated for a 1400 Ma mantle residence time. Several diamonds exhibit horizontal trends that crosscut isotherms. This is indicative of spectral overlap, with analyses representing an average though multiple growth layers with differing nitrogen aggregation characteristics.

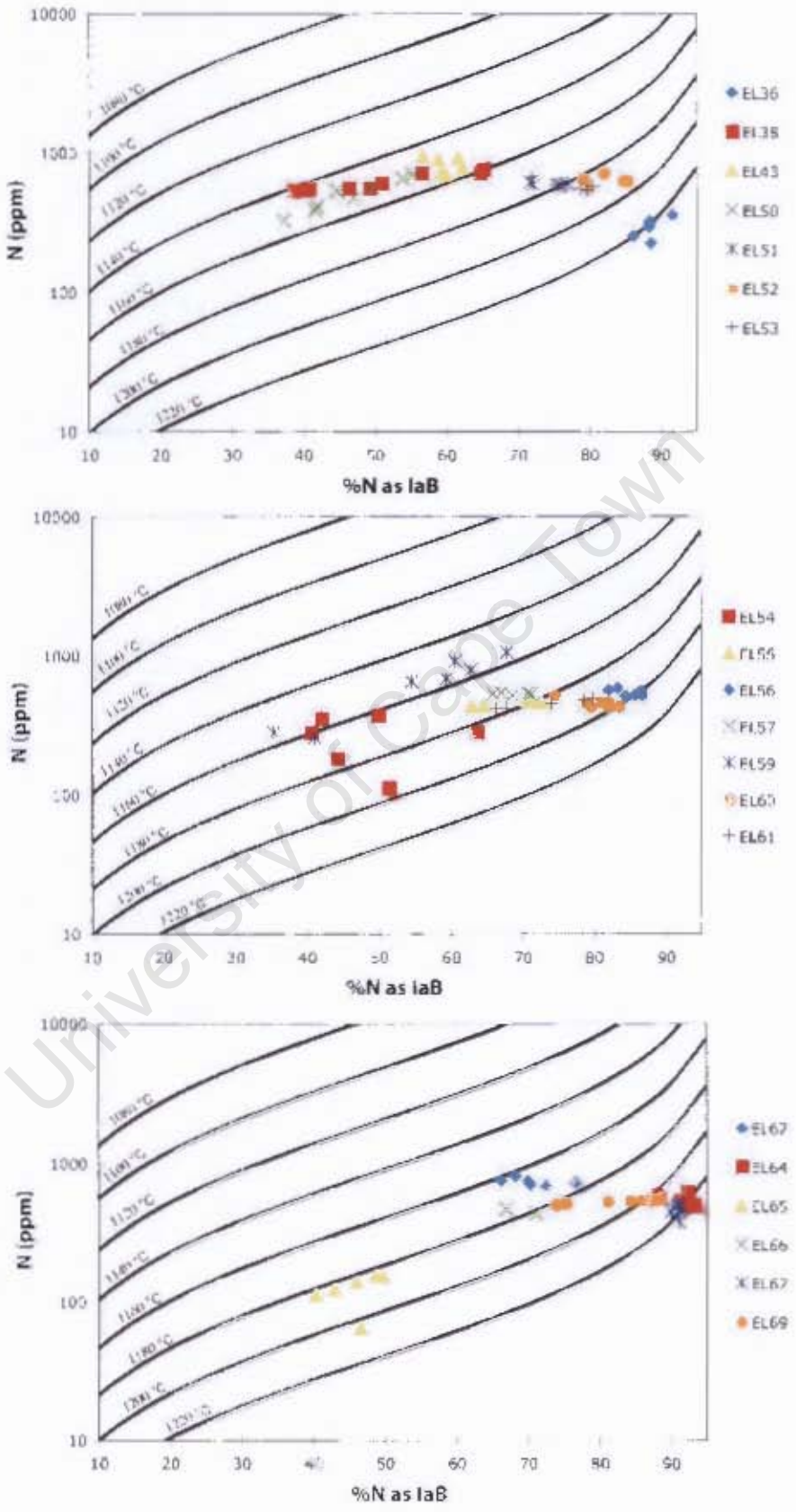

Figure 5.11: Nitrogen contour and aggregation state for individual analyses on each diamond. Isotherms for 1400 Ma residence time. Several diamonds exhibit horizontal trends that crosscut isotherms. This is indicative of spectral overlap, with analyses representing an average though multiple growth layers with differing nitrogen aggregation characteristics.

Comparison of eclogitic and peridotitic diamonds

Eclogitic and peridotitic paragenesis was classified on the basis of sulphide inclusion chemistry (see Chapter 6). There are no age data for the eclogitic diamond population at Ellendale and temperatures for these diamonds were calculated assuming the same mantle residence time (1400 Ma) as the peridotitic diamonds. No distinction between the temperatures of the eclogitic and peridotitic diamonds could be distinguished (Figure 5.12). The temperature equations are more sensitive to temperature than to time, given that the diamonds are older than 200 Ma (Navon, 1999). Thus, no significant error would be introduced into the temperature calculations if a different residence time is used. The Ellendale eclogitic diamonds were plotted on isotherms for

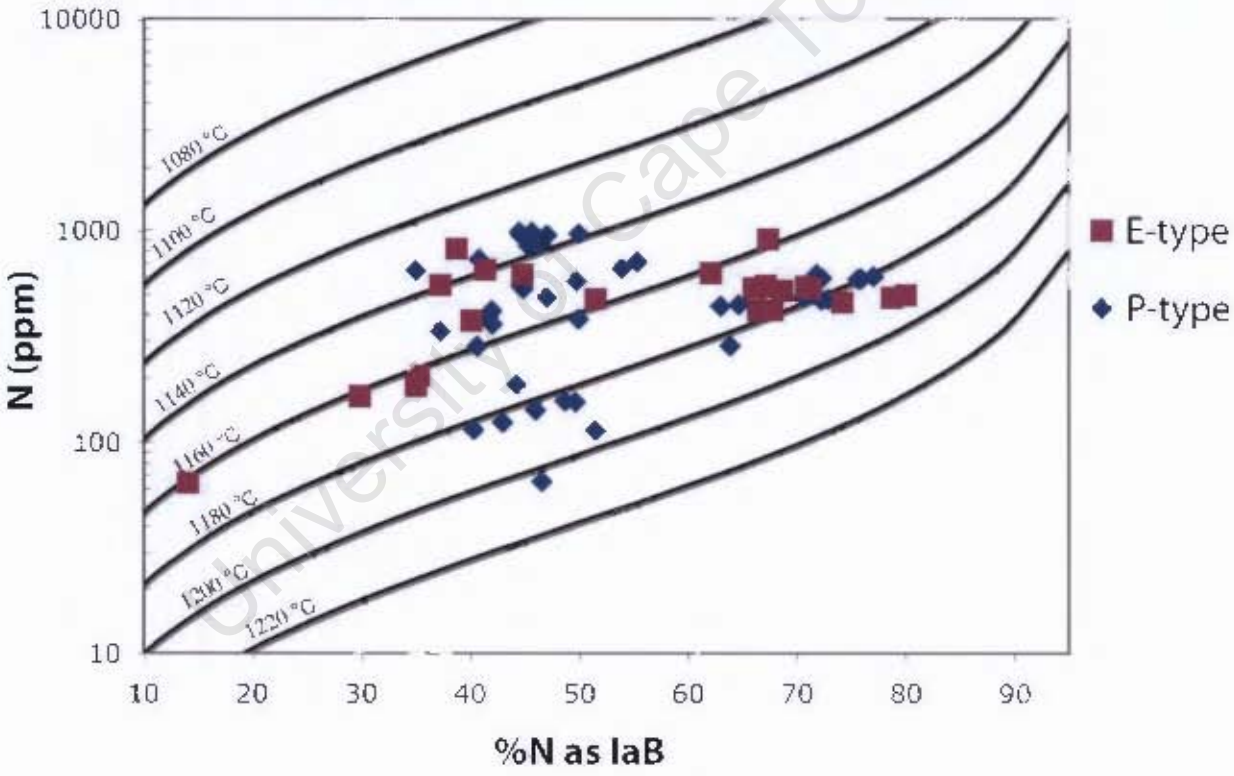

Figure 5.12: Nitrogen content and aggregation state for the eclogitic and peridotitic diamonds, classified on the basis of their sulphide inclusion chemistry. Isotherms for 1400 Ma residence time.

both 1400 Ma and 400 Ma residence times (Figures 5.13 and 5.14). Temperatures calculated for a significantly shorter mantle residence time of 400 Ma are only 30 °C higher than for 1400 Ma, which is still in range of the temperatures calculated for the peridotitic diamonds. There is thus no distinguishable difference between the temperature regimes of the two parageneses. Average temperatures calculated for the Ellendale eclogitic diamonds are shown in Table 6.1.

Although different mantle residence times were inserted into the equations, the temperatures are still within range of the Ellendale peridotitic temperatures (1129 - 1203 °C , with an average of 1158 °C), for which a mantle residence time is known. This does not correspond to the observation that peridotitic diamonds evolve at lower temperatures than eclogitic diamonds (Gurney, 1989). However, a compilation of worldwide data by Stachel & Harris (2008) suggest that formation and mantle storage of both peridotitic and eclogitic diamonds occur at similar temperatures.

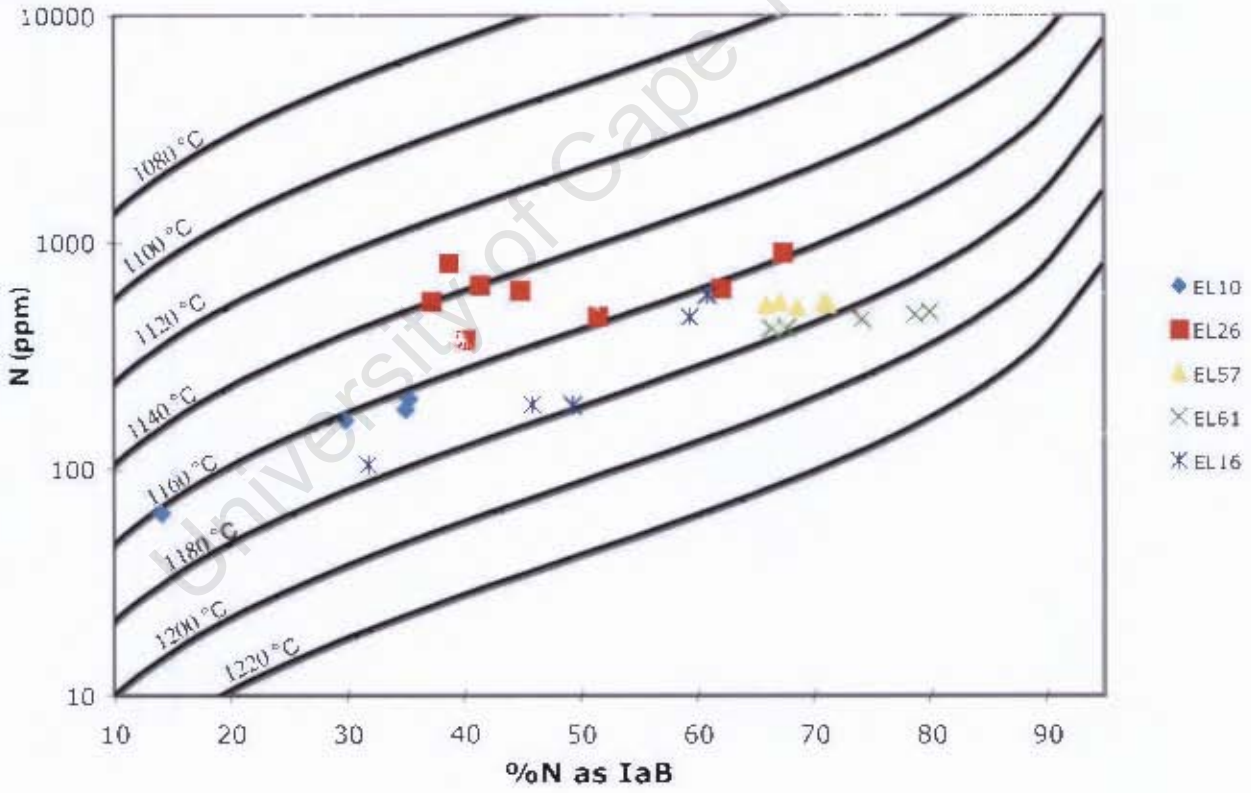

Figure 5.13: Temperatures calculated for eclogitic diamonds, with isotherms calculated for a 1400 Ma mantle residence time.

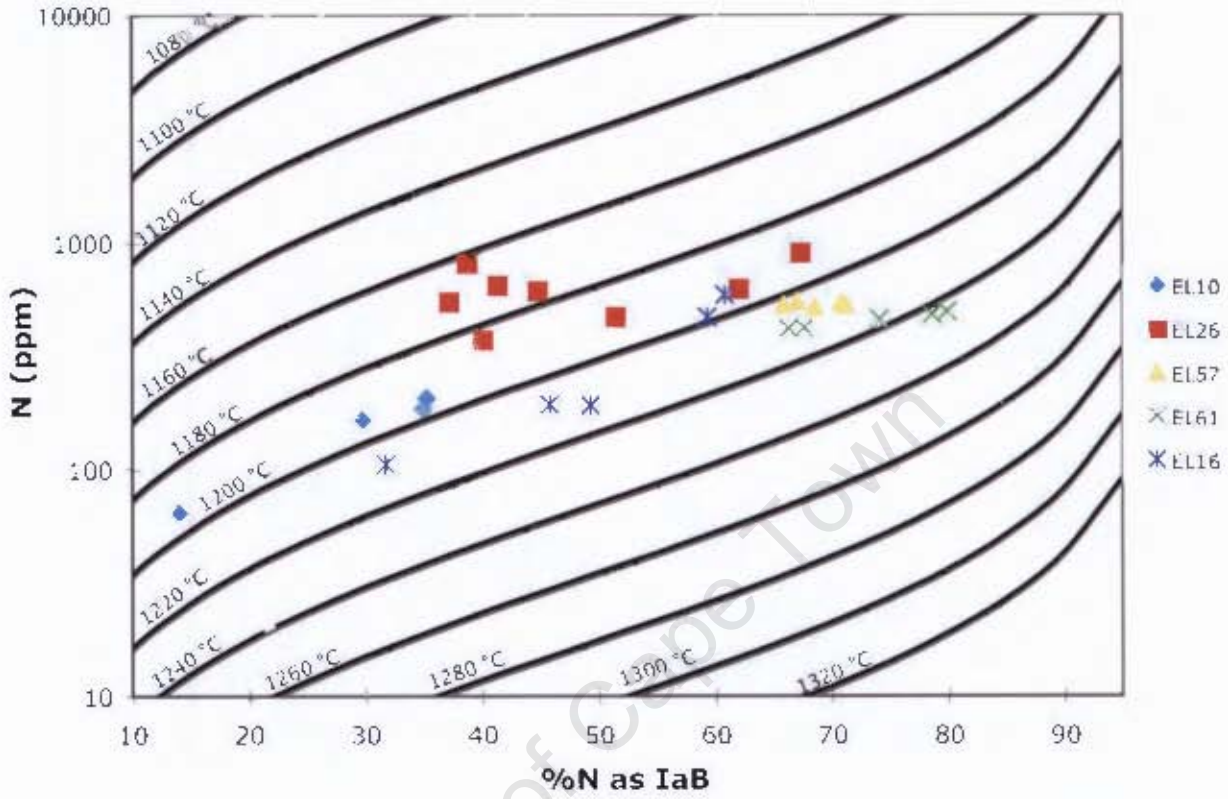

Figure 5.14: Temperatures calculated for eclogitic diamonds, with isotherms calculated for a 400 Ma mantle residence time.

Table 5.3: Average temperatures calculated for the Ellendale eclogitic population, using different mantle residence times.

Residence Time (Ma)	Average Temp(°C)	Range in Temp(°C)
400	1198	1162 - 1223
800	1180	1144 - 1205
1200	1170	1134 - 1194
1400	1165	1131 - 1190
1600	1162	1128 - 1186
2000	1157	1122 - 1180

Comparison to other Ellendale data

Calculated mantle residence temperatures from this study correspond well to equilibration temperatures for mineral pairs from Ellendale (Jaques *et al.*, 1989, and references therein). Eclogitic inclusions were found to have T_{av} = 1250 °C , with lower temperatures for the peridotitic inclusions (T_{av} = 1155 °C).

Nitrogen data from van Heerden *et al.* (1995) were plotted on the isotherm diagram alongside data from this study (Figure 5.15). On average, much lower temperatures were deduced from the van Heerden *et al.* (1995) data, though there is some overlap. The difference in temperature could be real, in which case it could be explained in terms of samples that are not representative of the entire population of diamonds at Ellendale. van Heerden *et al.* (1995) estimated nitrogen aggregation state from reference FTIR spectra, using the method of Davies (1981). This method has uncertainties of up to 40 % on the aggregation state and $\sim$ 5 % on the nitrogen content. Thus, the temperatures calculated from the van Heerden *et al.* (1995) data may have significant uncertainties.

The suite of Ellendale diamonds studied by Taylor *et al.* (1990) is dominated by nitrogen-rich Type Ia diamonds, which apart from one peridotitic diamond from E9, show limited IaB aggregation of nitrogen. The study was based on a very limited dataset with two peridotitic diamonds from E9 yielding temperatures from 1146 to 1241 °C and three eclogitic diamonds from E4 yielding temperatures between 1059 to 1075 °C . Taylor *et al.* (1990) followed the assumption that the Ellendale diamonds are Proterozoic in age and that they formed at the same time as the eclogitic diamond population at Argyle (Richardson, 1986) and thus temperatures were calculated based on a 1600 Ma residence time. While the temperatures for the diamonds from E9 are within range of the diamonds in this study, the temperatures calculated by (Taylor *et al.*, 1990) for E4 are very low. The latter temperatures correspond to those at the graphite-diamond transition, assuming a conductive geotherm of 40 - 44 mW/m^2, typical of cratonic areas, and were interpreted to indicate that 1600 Ma is probably a maximum age for the Ellendale diamonds. If the E4 temperatures had to be recalculated for residence times of 1400 Ma, as in this study, temperatures will only be $\sim$ 10 °C higher.

The diamonds in the limited dataset of Taylor *et al.* (1990) show very low aggregation states, which are not comparable to the diamonds in this study. However, it is mentioned by Taylor *et al.* (1990) that the dominant crystal form and colour for smaller size ranges are colourless or pale brown octahedra, whereas the larger sized diamonds (as in this study) are typically yellow, resorbed tetrahexahedroida of gem quality.

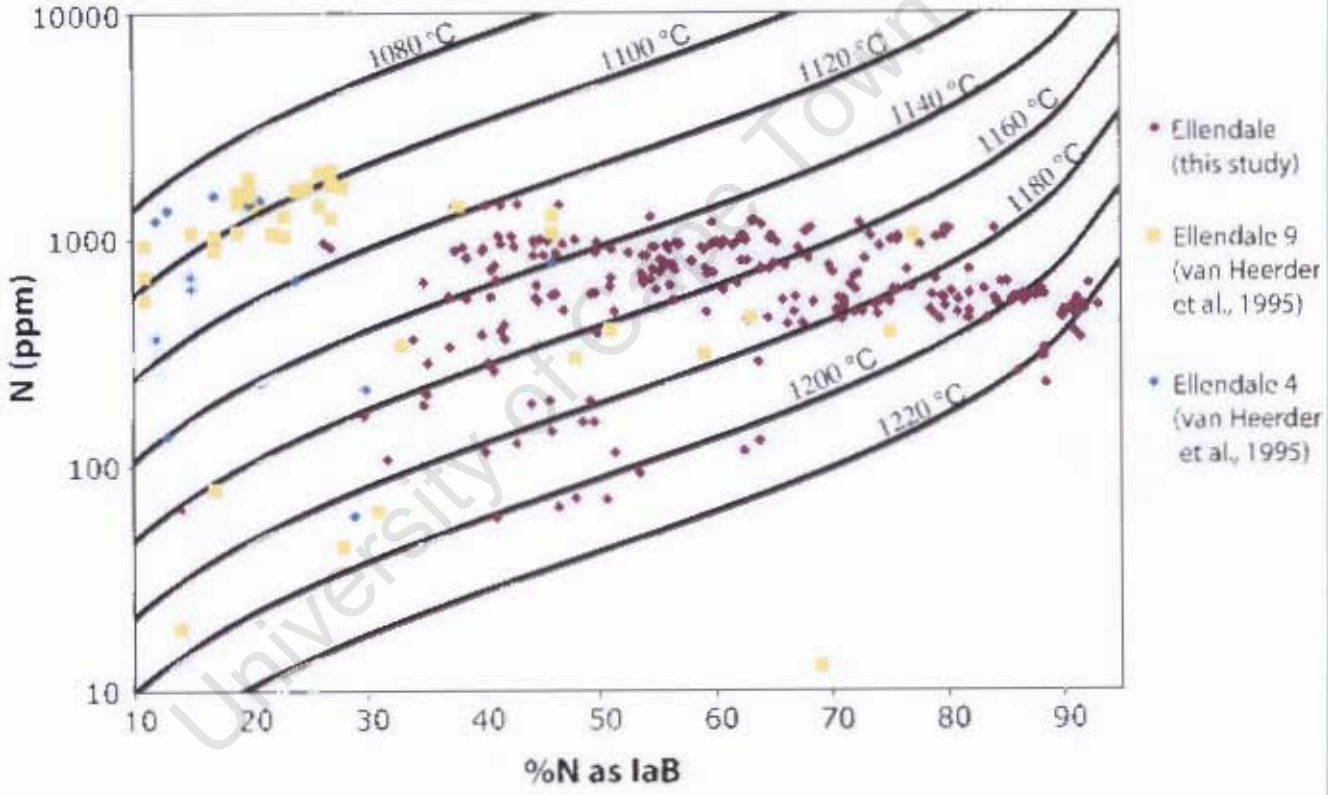

Figure 5.15: Data from this study compared to data from van Heerden *et al.* (1995).

Chapter 6

RE - OS ISOTOPE CHARACTERISATION OF THE SULPHIDE INCLUSIONS

6.1 Background Principles

Re has two isotopes: ^{185}Re (37.40 at%) and ^{187}Re (62.60 at%), with an atomic weight of 186.207 (Gramlich *et al.*, 1973). Os has seven isotopes: ^{184}Os (0.0177 at%), ^{186}Os (1.593 at%), ^{187}Os (1.513 at%), ^{188}Os (13.29 at%), ^{189}Os (16.22 at%), ^{190}Os (26.38 at%) and ^{192}Os (40.98 at%). Atomic weight is given as 190.2 but varies in nature as ^{186}Os and ^{187}Os are both products of radioactive decay. ^{187}Re decays to ^{187}Os by β^- emission. The decay constant of 1.666 X 10^{-11} year^{-1} (with a 1 % uncertainty) was determined by Smoliar *et al.* (1996) from Re-Os isochrons of iron meteorites, for which accurate ages had been established by Lugmair & Galer (1992).

Isotope ratios are reported normalised to ^{188}Os. Early studies reported isotope ratios normalised to ^{186}Os as the ^{187}Os/^{186}Os of chondrites and the average upper mantle are close to 1. Due to the low abundance of ^{186}Os, ^{187}Os/^{188}Os is more accurately measured in the mass spectrometer and ^{187}Os/^{186}Os was calculated based on a constant ^{186}Os/^{188}Os ratio. However, the abundance of ^{186}Os varies due to alpha decay of ^{190}Pt (Walker *et al.*, 1997), so this was not particularly accurate. Normalisation to ^{188}Os is now common practice.

6.2 Re-Os Systematics

Re and Os both show strong siderophile (Allègre & Luck, 1980) and chalcophile (Foster *et al.*, 1996) behaviour and as such sulphide is a primary host of these elements in the mantle. Dur-

ing mantle melting, Os behaves as a compatible element whereas Re behaves as a moderately incompatible element and is partitioned into the melt (Mitchell & Keays, 1981; Morgan *et al.*, 1981). Crustal materials therefore have higher Re concentrations and with time develop radiogenic $^{187}Os/^{188}Os$ isotopic ratios. The strong fractionation of these elements between mantle and crustal systems means that the Re - Os system is useful for dating melt depletion events and residual peridotite formation as opposed to Rb - Sr, Sm - Nd and U - Th - Pb isotope systems, where both parent and daughter isotopes are highly incompatible lithophile elements.

6.2.1 Mantle peridotites

Mantle peridotites rarely show isochronous relationships, even among whole rocks or sulphides that have a similar age and mantle history, as they may be affected by Re or Os mobility that resets the Re - Os isotope ratios subsequent to melt extraction. This may be due to, amongst others, late stage metasomatic addition of Re from kimberlites or carbonatites (Walker *et al.*, 1989; Carlson *et al.*, 1999; Chesley *et al.*, 1999) and Re loss as a result of sulphide breakdown (Handler *et al.*, 1997).

For example, Re content in subducted basalts from the Zermatt-Saas ophiolite is very low, and is seen as evidence for Re loss into the overlying mantle wedge during subduction (Dale *et al.*, 2007). This is further supported by suprachondritic $^{187}Os/^{188}Os$ in some arc peridotites, along with variable Re enrichment (Brandon *et al.*, 1999). Harzburgite xenoliths and harzburgite sulphide inclusions in Panda diamonds, from the Slave craton, also showed suprachondritic $^{187}Os/^{188}Os$, which implies a subduction wedge origin for these diamonds, with Re addition from the subducting plate (Westerlund *et al.*, 2006). Remixing of oceanic crust back into the upper mantle, with up to 60% Re removed from the subducting plate (Becker, 2000; Dale *et al.*, 2007) may be responsible for a uniform less depleted $^{187}Os/^{188}Os$ composition for the upper mantle (Meisel *et al.*, 2001).

Peridotite xenoliths from Kimberley on the Kaapvaal craton have an average Re - Os model age of 2.88 $\pm$ 0.11 Ga (Carlson *et al.*, 1999), corresponding to the time of the end of subduction and amalgamation of western and eastern Kaapvaal. This could be taken as evidence that subduction-related metasomatism may modify the composition of the lithospheric mantle or it could represent the time of its original depletion. The low closure temperature of Os exchange in pyrrhotite (400 °C Brenan *et al.*, 2000) implies Os diffusion may occur for sulphides that are not encapsulated in diamond. This could explain, in part, scatter observed in Re - Os isochrons for mantle sulphides and mafic intrusions (Brenan *et al.*, 2000). As Re is moderately incompatible,

it can be relatively mobile during mantle metasomatism and melting events, which could lead to variable Re addition in peridotites, with the result that these rocks may rarely plot on an isochron (e.g. Gao *et al.*, 2002).

6.2.2 Sulphide Inclusions in Diamonds

In contrast to sulphides in mantle xenoliths, sulphide inclusions in diamonds are isolated and protected from metasomatic events and Re mobilisation that can affect sulphides in peridotites (e.g. Pearson *et al.*, 1998) and as such may represent primary compositions of mantle sulphides.

Re-Os dating can be applied to single inclusions in diamonds, obtaining model ages, with isochrons obtained from multiple inclusions in a single diamond. The system therefore has a great advantage over other isotopic systems - the application of the Rb - Sr and Sm - Nd isotopic systems to garnet and clinopyroxene inclusions require composites in order to produce isochrons, due to the low concentrations of Sm, Nd, Rb and Sr in these minerals (e.g. Shirey *et al.*, 2004).

The syngenetic nature of inclusions, and thus the validity of diamond ages, have been questioned by Navon (1999) and Spetsius *et al.* (2002). Archaean Re-Os model ages were found for sulphides included in much younger zircon megacrysts, with U - Pb ages equivalent to kimberlite emplacement (Spetsius *et al.*, 2002). These authors suggest that the same could be true for diamonds, where older sulphides formed in mantle rocks may be encapsulated in diamond, with the model/isochron age indicating peridotite formation in the mantle rather than diamond formation. However, as pointed out by Richardson *et al.* (2004) and Westerlund *et al.* (2006) consistent isochron relationships are improbable in mineral grains that are stored separately in the mantle before encapsulation in diamonds.

Although sulphide is one of the most common inclusion phases in diamond, advances in the Re-Os analytical method have only recently enabled the full exploitation of this technique. Re and Os are present at femtogram to picogram levels in sulphide inclusions and high sensitivity techniques are needed for accurate analyses. Os has a high ionisation potential which prevents the formation of positive ions at temperatures attainable in conventional thermal ionisation mass spectrometry. However, a solid osmium sample can yield negative ions (Völkening *et al.*, 1991) and be analysed using negative thermal ionisation mass spectrometry (N - TIMS) with precision better than $\pm$ 0.1 % (2σ) (Creaser *et al.*, 1991). This improved significantly on previous mass spectrometry techniques, such as secondary ionisation mass spectrometry (SIMS), resonance ionisation mass spectrometry (RIMS) and inductively coupled plasma mass spectrometry (ICP - MS), which could only achieve 2σ precision of around 1 - 2 %. Micro-chemistry techniques

for Re and Os separation from sulphide inclusions in diamonds were refined by Pearson *et al.* (1998) from techniques described by Roy-Barman & Allègre (1994) and Birck *et al.* (1997). This technique allows for the analysis of individual inclusions with as little as 1 pg of Os and precludes the need for compositing inclusions that may or may not be related, as with the application of the Sm - Nd and Rb - Sr isotope systems to silicate mineral inclusions. The analytical techniques used in this study are fully described in Chapter 3.

6.3 Sulphide Characteristics

Sulphide inclusion minerals including pyrrhotite (monoclinic), chalcopyrite (tetragonal) and pentlandite (isometric) do not display morphologies characteristic of their crystal systems, but typically exhibit cubo-octahedral morphologies as imposed by the diamond and, as such, are assumed to be syngenetic. Harris (1968) and Harris & Gurney (1979) provide criteria with which to recognise syngenetic and epigenetic inclusions. Sulphides are typically surrounded by rosette fractures that develop due to differential decompression between the diamond and the sulphide during eruption of the kimberlite/lamproite - i.e. the inclusion expands at a greater rate than the diamond with decrease in pressure (Henriques, 1965; Harris *et al.*, 1970). Due to the lower pressure in these fractures graphitisation occurs, which along with complex intergrowths of Fe-Cu-Ni-rich sulphides, result in the dark colour (Harris, 1968; Bobrievich *et al.*, 1959; Harris *et al.*, 1975).

During diamond formation, sulphides are incorporated as Fe-Ni-Cu monosulphide solution (mss), in the temperature range 900 to 1200 °C (Bulanova *et al.*, 1996). Exsolution of sulphide phases from the mss occurs during cooling, with crystallisation along the rosette fractures. The first phases to exsolve from the mss are chalcopyrite at 930 °C followed by pentlandite at 600 °C . Once these phases have exsolved, pyrrhotite remains as residual phase. The phase relationships in the Cu-Fe-Ni-S system are detailed in Craig & Kullerud (1969).

Sulphide paragenesis can be characterised by the Ni content, as well as Os concentrations (Deines & Harris, 1995; Pearson *et al.*, 1998). Eclogitic sulphide inclusions are typically lower in Ni and Os due to the compatible nature of these elements during mantle melting, whereas peridotitic sulphide inclusions have higher Ni content and Os concentrations. From sulphide inclusions in Siberian diamonds, Yefimova *et al.* (1983) distinguished eclogitic sulphides with <8 wt % Ni from peridotitic sulphides with >8 wt % Ni. The subdivision has been refined by studies of sulphides from other localities with Shirey *et al.* (2003) suggesting a Ni content <9

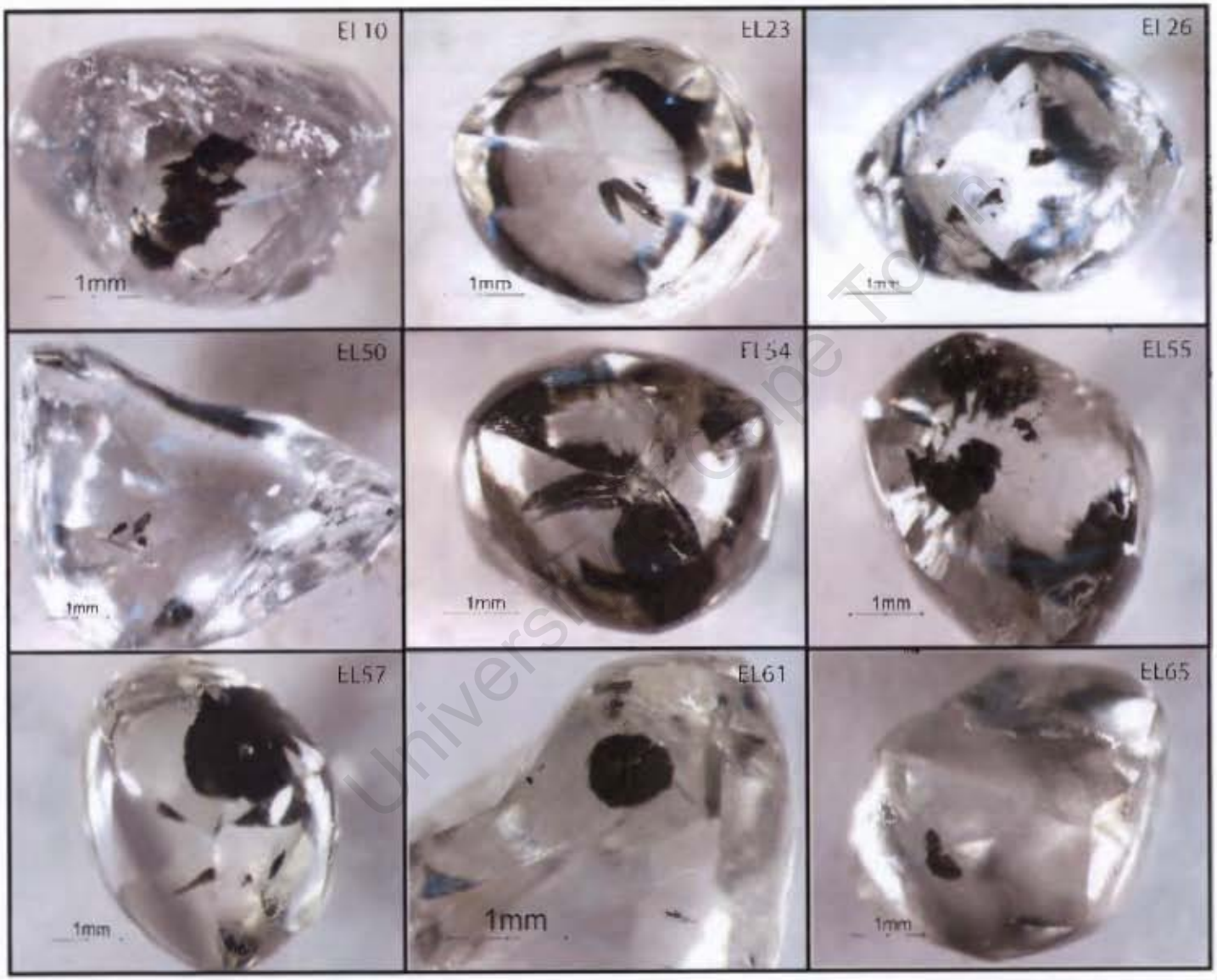

Figure 6.1: Diamonds with sulphides extracted for Re - Os isotope analyses. The sulphides are all surrounded by characteristic fractures, which may be simple disc-shaped fractures or more complex rosette fractures. Apart from EL54, the diamonds have no obvious cracks to the surface, which may have resulted in sulphide inclusion alteration.

wt % for eclogitic sulphides and >16 wt % for peridotitic sulphides. Based on this, pentlandite-rich inclusions are considered peridotitic, whereas chalcopyrite- and pyrrhotite-rich inclusions are considered eclogitic. The review by Stachel & Harris (2008) has a discussion on the discrimination of sulphide paragenesis according to their Ni contents.

Table 6.1: Sulphide colour and composition

Sulphide	Colour	Formula
Pyrrhotite	Bronze yellow	$(Fe_{1-x}S)$
Chalcopyrite	Brass yellow tarnished iridescent	$CuFeS_2$
Pentlandite	Pinkish brown	$(FeNi)_9S_8$

6.3.1 Ellendale Sulphides

Twelve sulphide inclusions were extracted from ten diamonds, which were all assumed to be syngenetic due to their cubo-octahedral morphologies. The fractures associated with the sulphides, were either simple disc-shaped fractures (EL23, EL55, EL61, EL65) or more complex rosette fractures (see Figure 6.1). The integrity of each sulphide inclusion was checked before breakout for Re-Os analysis with the majority of diamond showing no cracks linking them to the surface of the diamond that could alter the sulphide.

Apart from EL51 and EL54, the diamonds had no cracks that linked the sulphides or their rosette fractures to the surface. Although limited oxide alteration does occur on the surface of suphide EL54_3, it does not appear to have disturbed the Re-Os isotope characteristics, as the sulphide still maintains an isochronous relationship with the other peridotitic sulphides in the suite. EL51 shows substantial surface oxide alteration, however, this sample did not yield any reliable analytical data and is not included on the isochron. EL55 did not appear to have any cracks to the surface of the host diamond, although sulphide EL55_2 did show some oxide alteration on its surface. Inclusions in diamonds EL10 and EL57 are both very near the surface, but there are no visible cracks. Figure 6.1 shows the diamonds for which sulphide inclusions were extracted for Re - Os isotope analyses.

Once the inclusions were extracted from the diamond, they were mounted on carbon con-

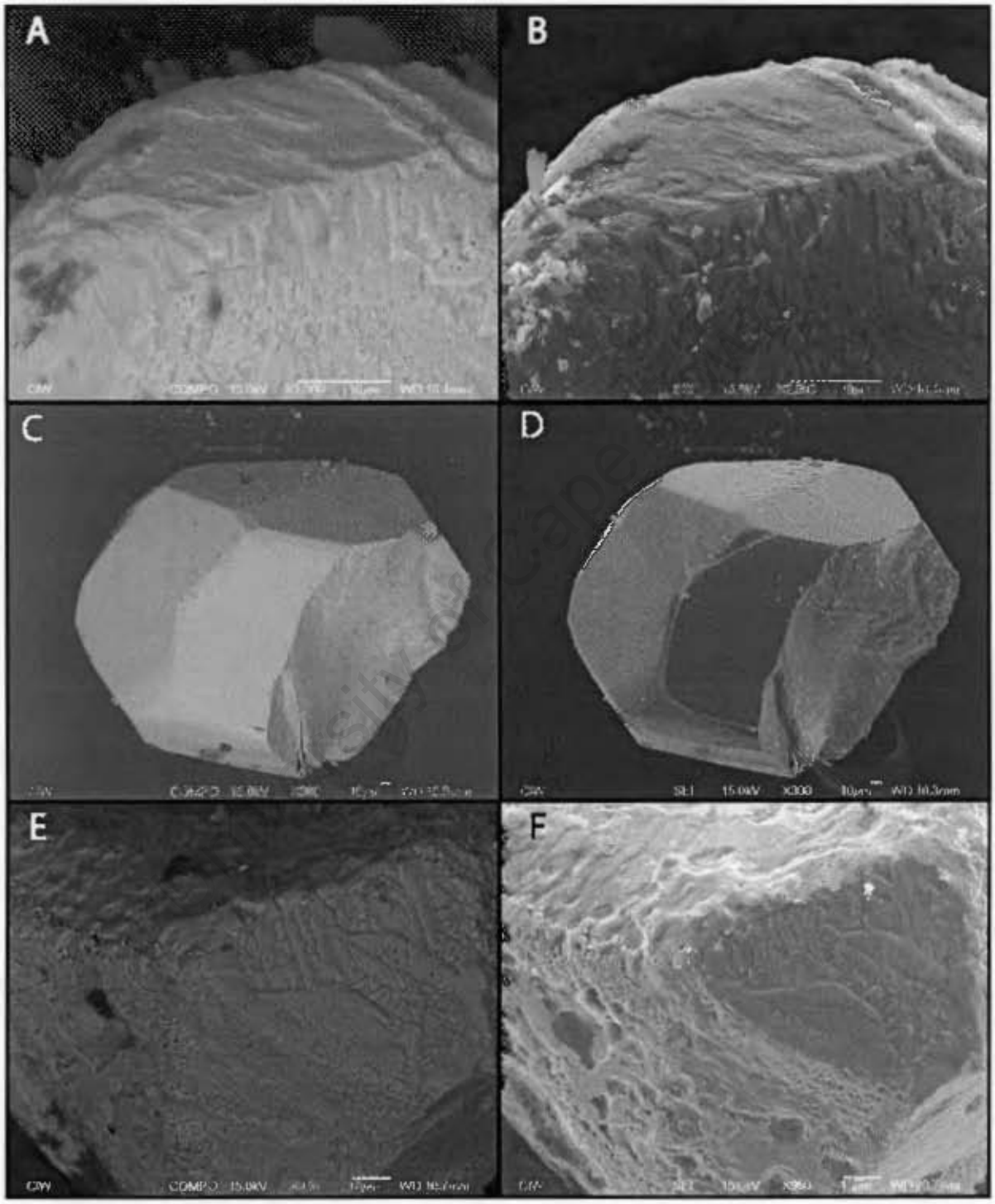

Figure 6.2: Backscatter and secondary electron images of selected sulphide inclusions. A and B: EL26. C and D: EL10. E and F: EL57.

ductive tape and analysed by energy dispersive spectroscopy (EDS) on the scanning electron microscope (SEM) in order to positively identify sulphides and obtain major element compositions. This enabled petrogenetic classification of sulphides as either eclogitic or peridotitic based on the Ni content. Ni content also provides a rough indication of Os content in the sulphides (e.g. Pearson *et al.*, 1998), important for estimates of the amount of spike solution required during Re - Os isotope analysis. Backscatttered and secondary electron images of selected sulphides are shown in Figure 6.2 and Figure 6.3.

The suite of Ellendale sulphide inclusions are pyrrhotite-pentlandite-chalcopyrite assemblages, and were divided into peridotitic and eclogitic sulphides, based on their Ni content. Their major element compositions are described below and reported in Table 6.2. There are four eclogitic sulphides: three pyrrhotite-rich (EL10, EL26, EL61) inclusions and one chalcopyrite-rich (EL57) inclusion. These all have extremely low Ni content, typically less than 5 %, apart from EL61 that has up to 13 % Ni. EL10 contains the largest sulphide in the suite (33 μg). There are eight peridotitic sulphides in the inclusion suite, (EL23, EL50, EL51, EL54_1, EL54_3, EL55_1, EL55_2 and EL65) that weigh between 1 and 2 μg. EL65, however, weighs less than 1 μg, which could not be quantified on the balance. The peridotitic inclusions were classified on the basis of their high Ni content and are all characterised by pentlandite-rich compositions with $\sim$ 20 - 30 % Ni.

Table 6.2: Semi-quantitative major element analyses of the sulphide inclusions.

Sample	Ni (wt%)	Fe (wt%)	Cu (wt%)	S (wt%)
EL10	0-1	57-59	-	37-42
EL26	0-2	54-55	3-4	40-41
EL57	0-4	37-40	23	31-40
EL61	0-13	46-54	-	39-45
EL23	19-22	40	-	37-40
EL50	14-25	37-41	12	36-40
EL51	7-20	-	-	32-38
EL54_1	10-26	33-40	10-13	37-40
EL54_3	16-32	26-43	0-4	24-40
EL55_1	15-18	41-43	8	32-43
EL55_2	17-21	33-43	-	30-41
EL65	20-34	31-36	13-14	33-40

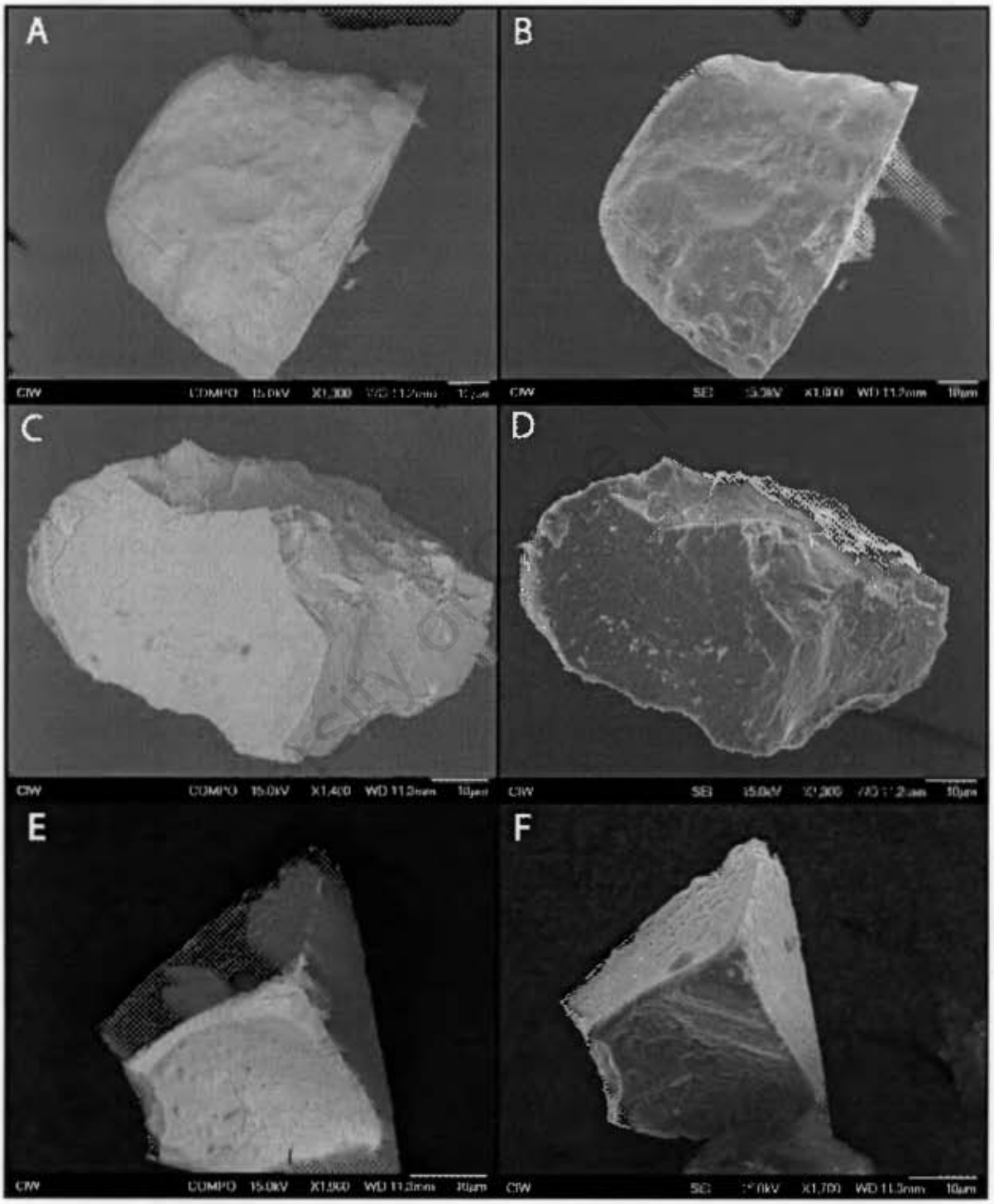

Figure 6.3: Backscatter and secondary electron images of selected sulphide inclusions. A and B: EL55_2. C and D: EL61. E and F: EL65.

Table 6.3: Sulphide paragenesis, classified by Ni content, with Re-Os concentrations and isotopic compositions.

Sample	Sulphide Wt (μg)	Composition	Ni (wt%)	Paragenesis	Re (ppb)	Os (ppb)	$^{187}Re/^{188}Os$	$\pm$	$^{187}Os/^{188}Os$	$\pm$	T_{MA} (Ma)	$\pm$
EL10	33	pyrrhotite	0-1	Eclogitic	9	4	164	9	4.71	0.07	1658	47
EL26	2	pyrrhotite	0-2	Eclogitic	493	6	587	74	4.35	0.34	430	32
EL57	6	chalcopyrite	0-4	Eclogitic	764	262	18.4	0.9	2.506	0.019	7457	178
EL61	1	pyrrhotite	0-13	Eclogitic	255	12	168	28	2.51	0.11	847	73
EL23	1	pentlandite	19-22	Peridotitic	73	89	4.12	0.52	0.208	0.0062	1264	100
EL50	2	pentlandite	14-25	Peridotitic	981	1274	3.755	0.113	0.195	0.002	1171	27
EL51	1	pentlandite	7-20	Peridotitic	2411	-	-		-			
EL54_1	1	pentlandite	10-26	Peridotitic	1076	9967	0.52	0.0016	0.1186	0.0005	-8281	218
EL54_3	2	pentlandite	16-32	Peridotitic	3780	17626	1.033	0.031	0.126	0.0004	-362	22
EL55_1	1	pentlandite	15-18	Peridotitic	723	11460	0.303	0.009	0.1109	0.001	7973	324
EL55_2	2	pentlandite	17-21	Peridotitic	513	1279	1.94	0.066	0.127	0.007	-104	140
EL65	< 1	pentlandite	20-34	Peridotitic	> 664	$> 12\ 369$	0.2603	0.0078	0.112	0.006	5773	946

6.4 Re and Os concentrations of the Sulphide Inclusions

The sulphides have a wide range in Re and Os concentrations that are consistent with their paragenesis, as classified by Ni content (see Table 6.3). The eclogitic sulphides show Re > Os, whereas the peridotitic sulphides have Os > Re. The eclogitic sulphides have Os concentrations that range from 4 to 12 ppb, with the chalcopyrite-rich inclusion (EL57), having a significantly higher Os (262 ppb) than the three pyrrhotite-rich inclusions. The Os concentrations of the peridotitic sulphides range from 1274 to 17 626 ppb, with one pentlandite-rich inclusion (EL23) that has much lower Os concentration (89 ppb). This same sulphide also has much lower Re concentration (73 ppb) than the other peridotitic sulphide inclusions (513 - 3780 ppb). Re concentrations for the eclogitic sulphides range from 255 to 764 ppb, with the pyrrhotite-rich inclusion from EL10 having significantly lower Re concentration (9 ppb). This same inclusion also has the lowest Os concentration in the suite (4 ppb). EL54_3, a peridotitic sulphide, has the highest Re and Os concentrations in the entire suite (3800 and 17 626 ppb, respectively). Though EL55_1 and EL55_2 are two inclusions from the same diamond, they show distinctly different Os content - EL55_1 has 11 460 ppb, an order of magnitude higher than EL55_2 with 1279 ppb. This is not reflected in the Re concentration, which is fairly similar in both inclusions.

The Re and Os concentrations of the sulphide inclusions as well as sulphides from other diamond localities and peridotitic and eclogitic mantle xenoliths are plotted in Figure 6.4. Re/Os ratios from sulphide inclusions show a clear correlation with ratios from mantle xenoliths, which, as pointed out by (Pearson *et al.*, 1998), point to a strong petrogenetic similarity. It also indicates that the bulk of the Re and Os in mantle xenoliths is hosted by/partitioned into sulphide phases similar to those included in diamonds (Pearson *et al.*, 1998; Pearson & Shirey, 1999). The diagonal lines on the figure represent constant Re/Os values.

The eclogitic sulphides show similar Re/Os ratios to eclogite xenoliths from Udachnaya (Pearson *et al.*, 1995a,b) and eclogitic sulphide inclusions from Koffiefontein (Pearson *et al.*, 1998). The range in Os concentrations for the Ellendale peridotitic inclusions (1274 to 17 626 ppb) is much lower than peridotitic sulphides from studies in the literature. Data from peridotitic sulphides have been dominated by the harzburgitic paragenesis, with sulphides from Panda and Lac de Gras on the Slave craton yielding Os concentrations of 351 ppm and 18.5 ppm, respectively (Westerlund *et al.*, 2006; Aulbach *et al.*, 2008). The more limited dataset of lherzolitic sulphides, yield much lower Os concentrations corresponding to the range observed for the peridotitic sulphide inclusions at Ellendale. For example, three sulphide inclusions in

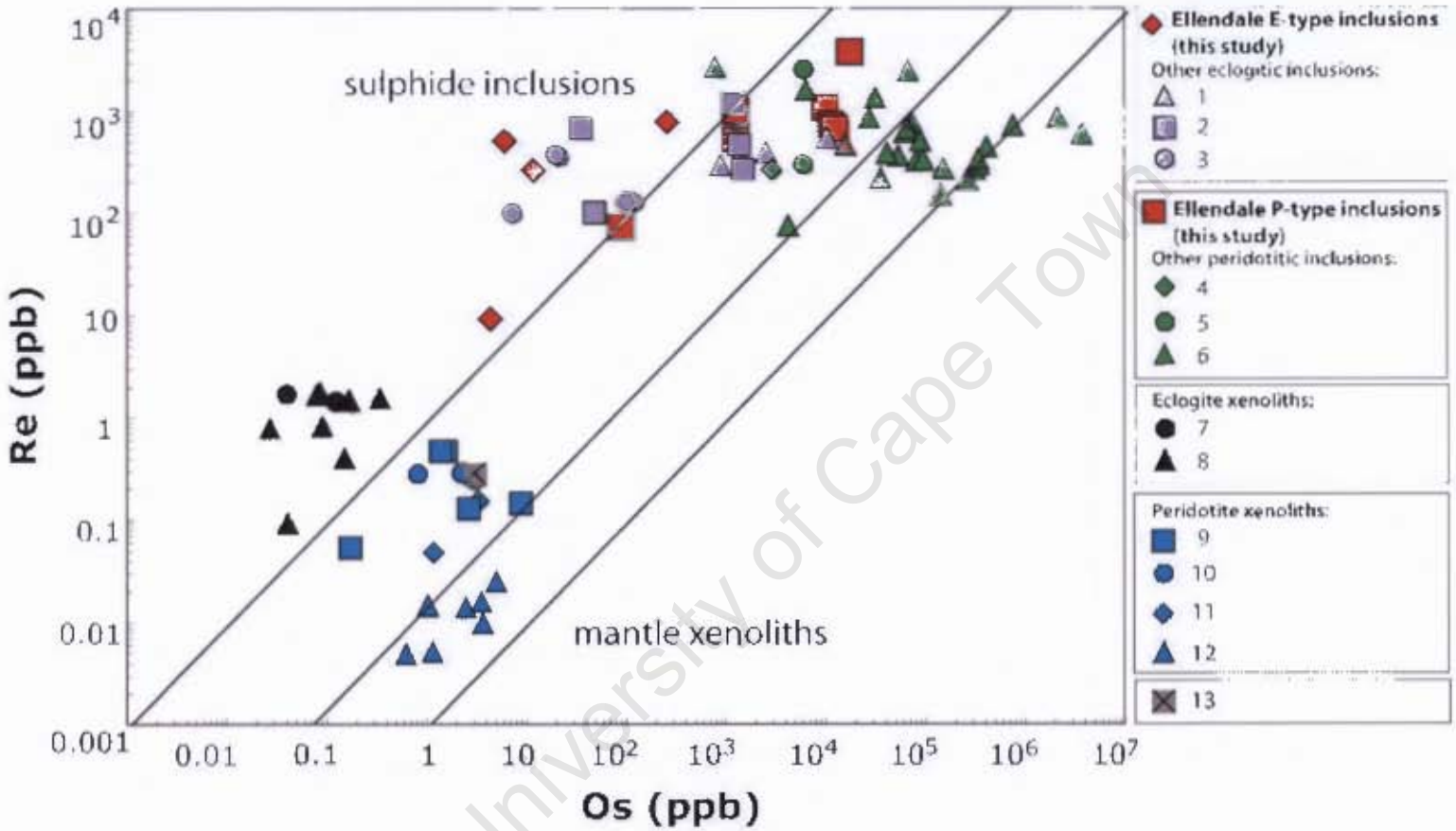

Figure 6.4: Re and Os concentrations of the Ellendale sulphide inclusions, compared to published sulphide inclusion data, as well as data from eclogite and peridotite mantle xenoliths. Diagonal lines give constant Re/Os. Literature data: 1 Premier eclogitic inclusions (Richardson & Shirey, 2008); 2 Venetia eclogitic inclusions (Richardson & Shirey, 2008); 3 Koffiefontein eclogitic inclusions (Pearson *et al.*, 1998); 4 Venetia peridotitic inclusions (Richardson & Shirey, 2008); 5 Koffiefontein peridotitic inclusions (Pearson *et al.*, 1998); 6- Panda peridotitic inclusions (Westerlund *et al.*, 2006); 7 Udachnaya eclogite xenoliths (Pearson *et al.*, 1995a); 8 - Udachnaya eclogite xenoliths (Pearson *et al.*, 1995b); 9 Udachnaya peridotite xenoliths (Pearson *et al.*, 1995b); 10 Udachnaya lherzolite xenoliths (Pearson *et al.*, 1995a); 11 Argyle lherzolite xenoliths (Graham *et al.*, 1999); 12 Panda harzburgite xenoliths (Westerlund *et al.*, 2006). 13 Primitive upper mantle composition (Meisel *et al.*, 1996).

a single Udachnayan diamond have Os concentrations from ~ 2000 to 6600 ppb Os (Pearson *et al.*, 1999), similar to the Os concentration of two sulphide inclusions from a Koffiefontein diamond (5000 to 6000 ppb) (Pearson *et al.*, 1998). From Figure 6.4 it can also be seen that the Re/Os ratios for the Ellendale sulphides are similar to lherzolitic xenoliths from Udachnaya (Pearson *et al.*, 1995a,b) and Argyle (Graham *et al.*, 1999).

6.5 Re-Os Isotope Characterisation

The $^{187}Re/^{188}Os$ and $^{187}Os/^{188}Os$ ratios for the Ellendale sulphide inclusions and calculated model ages are given in Table 6.3. A model age (T_{MA}) gives the time of extraction from the convecting upper mantle and is calculated using the formula (Shirey & Walker, 1998):

$$T_{MA} = \frac{1}{\lambda} \times \ln\left\{ \frac{\left(\frac{^{187}Os}{^{188}Os}(pm) - \frac{^{187}Os}{^{188}Os}(samp)\right)}{\left(\frac{^{187}Re}{^{188}Os}(pm) - \frac{^{187}Re}{^{188}Os}(samp)\right)} + 1 \right\} \tag{6.1}$$

with primitive upper mantle compositions from Meisel *et al.* (2001):

$$\frac{^{187}Re}{^{188}Os}_{(pm)} = 0.43464$$

$$\frac{^{187}Os}{^{188}Os}_{(pm)} = 0.1296$$

and the decay constant from (Smoliar *et al.*, 1996):

$$\lambda = 1.666 \text{ x } 10^{-11} \text{ year}^{-1}$$

Errors on the model ages were calculated based on equations given by Sambridge & Lambert (1997) and include errors on mass spectrometry and blank correction. Errors do not take into account error on the decay constant or the primitive upper mantle composition.

$$\sigma^2 = {g_1}^2{\sigma_1}^2 + {g_2}^2{\sigma_2}^2 \tag{6.2}$$

where:

$$g_1 = \frac{1}{\eta_1 + \eta_2 - \eta_3 - \eta_4} \tag{6.3}$$

$$g_2 = \frac{(\eta_3 - \eta_1)}{(\eta_2 - \eta_4)(\eta_1 + \eta_2 - \eta_3 - \eta_4)} \tag{6.4}$$

and:

$\eta_1 = \frac{^{187}\mathrm{Os}}{^{188}\mathrm{Os}(sample)}$; $\eta_2 = \frac{^{187}\mathrm{Re}}{^{188}\mathrm{Os}(sample)}$; $\eta_3 = \frac{^{187}\mathrm{Os}}{^{188}\mathrm{Os}(mantle)}$; $\eta_4 = \frac{^{187}\mathrm{Re}}{^{188}\mathrm{Os}(mantle)}$

σ_1 = error associated with η_1

σ_2 = error associated with η_2

6.5.1 Eclogitic Sulphides

The four eclogitic inclusions all have radiogenic $^{187}Os/^{188}Os$ ratios, which range from 2.5 to 4.7. The sulphides show no correlation in their Re - Os isotope data and as they do not have an isochronous relationship, a regression could not be calculated (Figure 6.5). Similarly, no correlation between the model ages for the eclogitic sulphides could be found. Model ages for the two sulphides, EL10 and EL61, yield Proterozoic ages of 1658 Ma and 847 Ma, respectively. The chalcopyrite inclusion from EL57 gives a model age older than the age of the Earth, while EL26 gives a model age of 430 Ma. The model ages are plotted on an Os isotope evolution diagram (Figure 6.6). While the Re - Os isotope data may indicate more than one eclogitic diamond-forming event, more analyses on eclogitic sulphides from Ellendale are needed before any meaningful interpretations can be made.

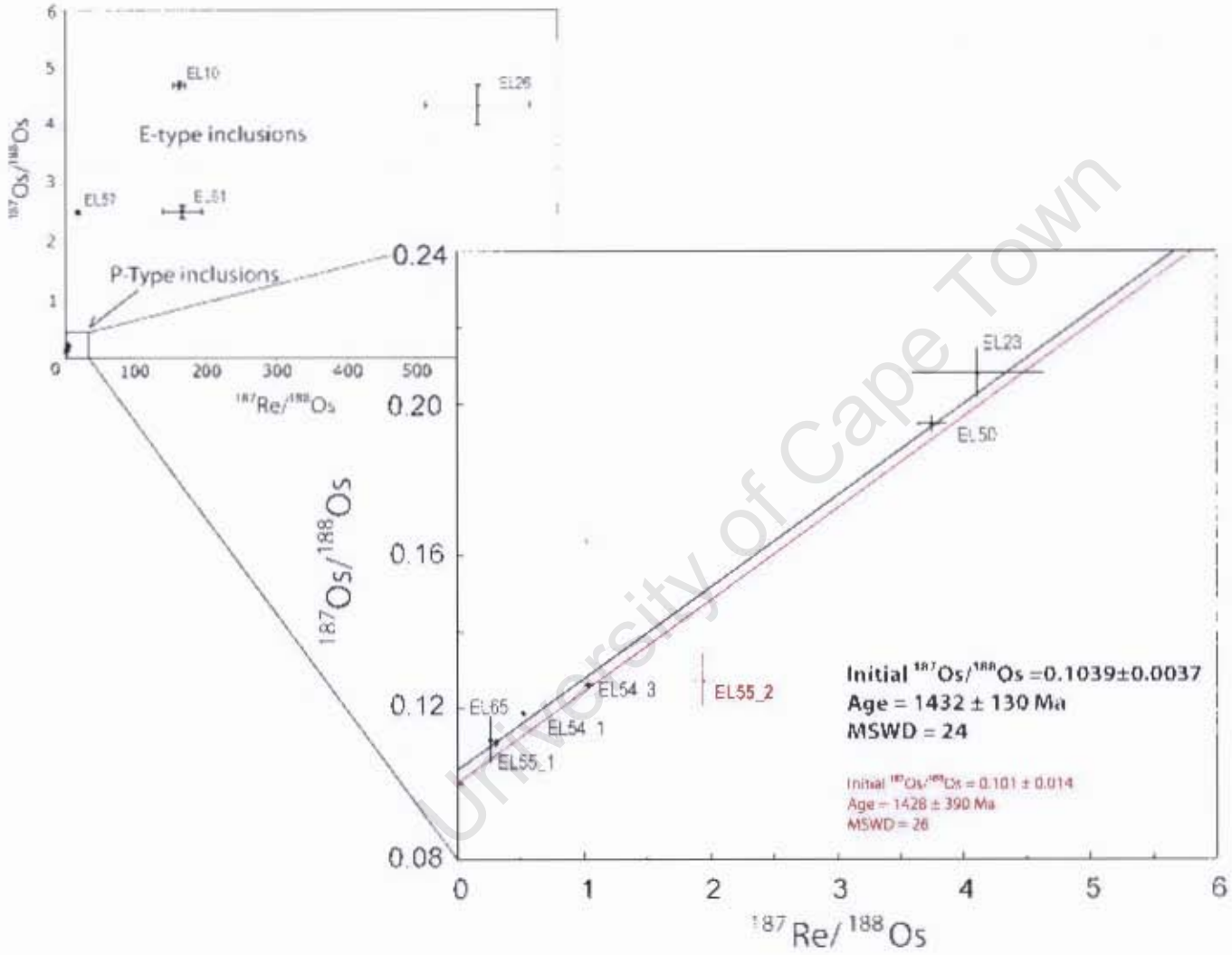

Figure 6.5: Re - Os isotopic compositions plotted on an isochron diagram. Regression 1 excludes EL55 2 and is shown in black. Regression 2 is shown in red and includes sample EL55.2. See text for details. Error bars show 2σ errors.

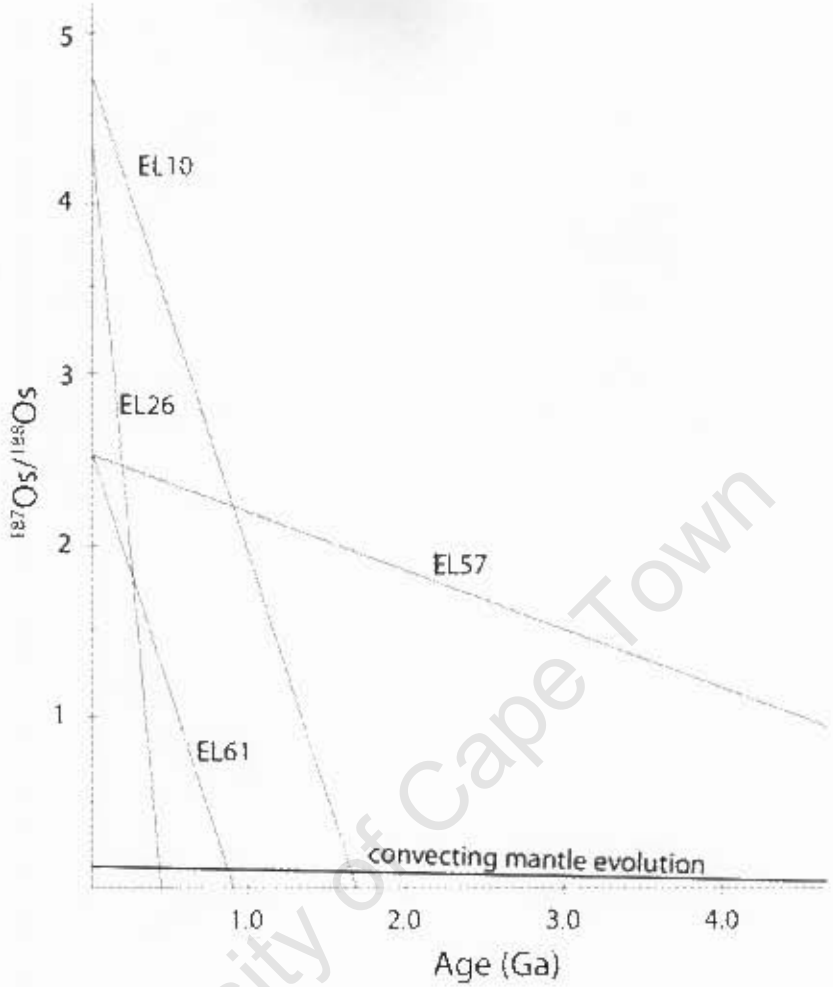

Figure 6.6: Osmium isotope evolution diagram for the eclogitic sulphide inclusions. The calculated model ages show no correlation.

6.5.2 Peridotitic Sulphides

The seven peridotitic inclusions have unradiogenic $^{187}Os/^{188}Os$ ratios, with a much narrower range in $^{187}Os/^{188}Os$ from 0.1109 - 0.208, compared to the eclogitic sulphides which show a wider range in $^{187}Os/^{188}Os$. The Re - Os isotopic compositions of the peridotitic sulphides show a linear correlation, which allows for regression analyses (Figure 6.5). All data regressions and mean squared weighted deviates (MSWD) were calculated using the Isoplot program (Ludwig, 1991). MSWD is calculated from the square of the residuals and the degrees of freedom in the regression (number of data points).

A regression through the peridotitic sulphides yields an age of 1428 ± 390 Ma, with an initial $^{187}Os/^{188}Os$ ratio of 0.101 ± 0.014. However, sulphide EL55_2 plots below the other sulphide inclusions. If it is excluded and a regression is calculated only through the six sulphides that

show the best linearity - EL23, EL50, EL54_1, EL54_3, EL55_1 and EL65, an age of 1432 ± 130 Ma is calculated. This does not change the age of the diamonds significantly as there is only a 4 Ma year difference, however, the uncertainty on the age is reduced. Although both regressions indicate a Proterozoic age, the regression excluding sulphide EL55_2 is preferred as the sulphides show a more coherent isochronous relationship and a more precise initial $^{187}Os/^{188}Os$ ratio of 0.1039 ± 0.0037.

Re is preferentially partitioned into chalcopyrite-rich sulphide phases during exsolution, and as chalcopyrite is concentrated on exterior surfaces of the sulphide grain, total inclusion recovery is required in order to minimise scatter in Re/Os (Richardson *et al.*, 2001). Sulphide EL55_2 fractured into at least 4 different pieces during extraction from the diamond and thus, incomplete inclusion recovery could account for the observed variation in Re/Os ratio. From EDS analyses, sulphide EL55_2 has no Cu content, which could suggest that the chalcopyrite may have been lost if there was incomplete recovery of the sulphide. In addition, EDS analyses of the sulphide EL55_2, indicate some oxide alteration on the surface of the sulphide, which may also explain the scatter in its Re-Os isotopes from the other peridotitic sulphides.

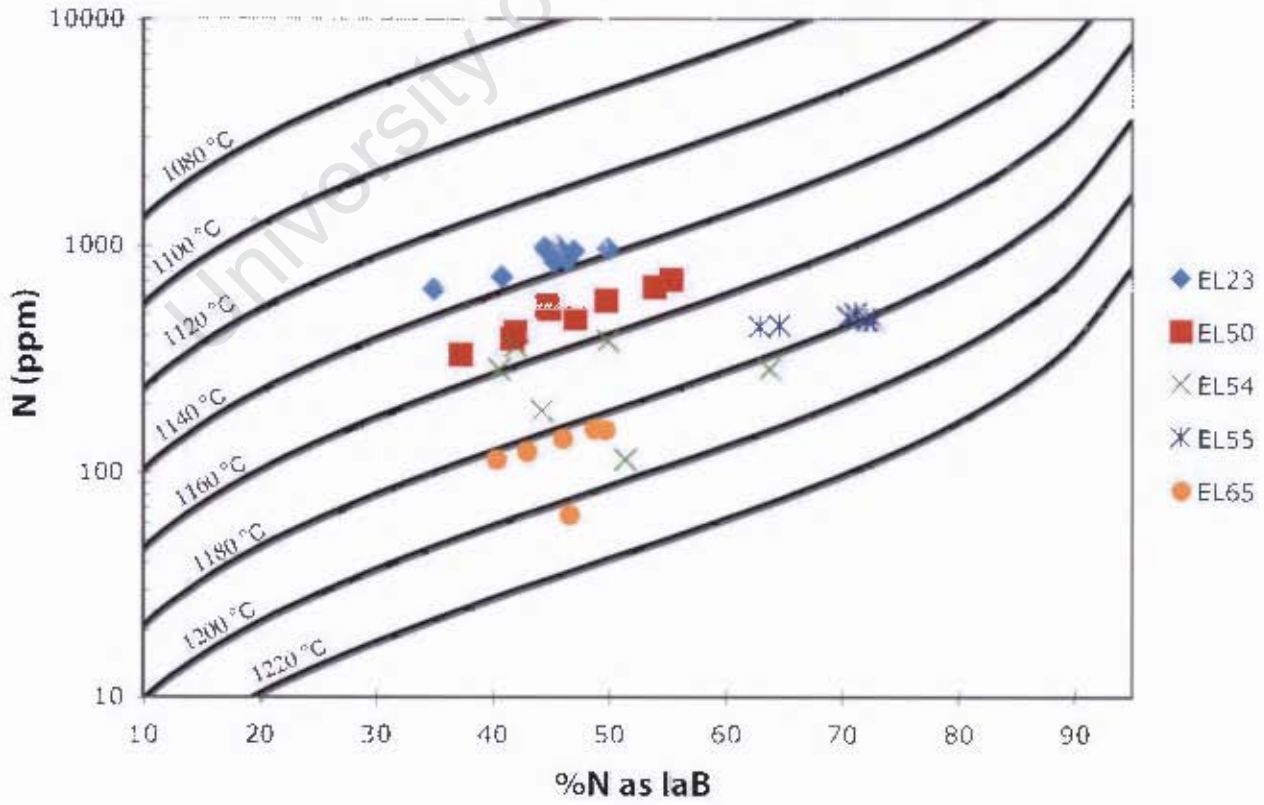

Figure 6.7: The nitrogen aggregation characteristics for the host diamonds of the peridotitic sulphides plotted on the isochron.

The MSWD of the isochron regression is high (MSWD = 24), with scatter greater than experimental error, which may result from limited spread in $^{187}Re/^{188}Os$, as well as Re blank corrections to such small samples, all with low Re concentrations.

Plotting inclusions on an isochron has the important assumption that all samples were derived from the same source that had equilibrated before incorporation by the diamond host. This assumption may not always hold true, as some evidence for this is seen by differences in nitrogen aggregation state and calculated temperatures between diamonds. The nitrogen aggregation characteristics for the diamonds from which sulphides were extracted are plotted in Figure 6.7. These peridotitic diamonds show a range in mantle storage temperatures from 1135 °C to 1187 °C (see Table 5.1 in Chapter 5), which could be taken to indicate that the diamonds experienced different temperature-time histories, however the 50 °C range is within the accuracy of conventional geothermobarometry and may not be geologically significant. These diamonds also have a similar range in nitrogen aggregation, between 34 % IaB to 55 % IaB, apart from EL55, which has higher nitrogen aggregation, between 62 and 71 %.

The isochronous relationship between the sulphide inclusions in the Ellendale diamonds does not seem to be affected by the range in mantle storage temperatures for the diamonds. This could indicate that the diamonds were stored at different depths in the mantle and that the same metasomatic diamond-forming fluids infiltrated the entire mantle depth range indicated by the mantle storage temperatures.

The initial Os isotopic ratio calculated from the regression (0.1039 ± 0.0037) is significantly lower than the convecting mantle at the indicated time of diamond formation, with γ_{Os} = -32.25. γ_{Os} is the percentage difference between the Os isotopic composition and the average mantle Os isotopic composition at an indicated time (e.g. Shirey & Walker, 1998).

γ_{Os} can be calculated according to the following formula (Shirey & Walker, 1998):

$$\gamma_{\mathrm{Os}} = \left[\frac{\left(\frac{^{187}\mathrm{Os}}{^{188}\mathrm{Os}\,(\mathrm{samp})(1.43)} \right)}{\left(\frac{^{187}\mathrm{Os}}{^{188}\mathrm{Os}\,(\mathrm{pm})(1.43)} \right)} - 1 \right] \times 100 \tag{6.5}$$

With :

$$\frac{^{187}\mathrm{Os}}{^{188}\mathrm{Os}_{(\mathrm{pm})(1.43)}} = \frac{^{187}\mathrm{Os}}{^{188}\mathrm{Os}_{(\mathrm{i})}} + \frac{^{187}\mathrm{Re}}{^{188}\mathrm{Os}_{(\mathrm{pm})}} (e^{\lambda(4.588\times10^{9})} - e^{\lambda(1.43\times10^{9})}) \tag{6.6}$$

$$= 0.152236$$

and primitive upper mantle compositions from Meisel *et al.* (2001):

$$\frac{^{187}\mathrm{Re}}{^{188}\mathrm{Os}\,(pm)} = 0.43464$$

$$\frac{^{187}\mathrm{Os}}{^{188}\mathrm{Os}\,(pm)} = 0.1296$$

and the decay constant from (Smoliar *et al.*, 1996):

$$\lambda = 1.666 \text{ x } 10^{-11} \text{ year}^{-1}$$

As expected from the unradiogenic γ_{Os} (-32.25), the model ages calculated for the peridotitic sulphides show wide variation, with three sulphides (EL54_1, EL54_3 and EL55_2) giving negative (future) model ages and two sulphides yielding ages older than the age of the Earth (EL55_1 and EL65) (Table 6.3). An Os isotope evolution diagram, with the calculated model ages for the sulphide inclusions, is seen in Figure 6.8. The samples, excluding EL55_2, show a convergence close to the initial ratio calculated from the regression ($^{187}\mathrm{Os}/^{188}\mathrm{Os} = 0.1039$ at $\sim$ 1.43 Ga), consistent with their isochronous relationship. The initial ratio from the regression which includes sample EL55_2 ($^{187}\mathrm{Os}/^{188}\mathrm{Os} = 0.101$) is substantially lowered due to scatter on sample EL55_2 and would plot outside the area where the other samples converge.

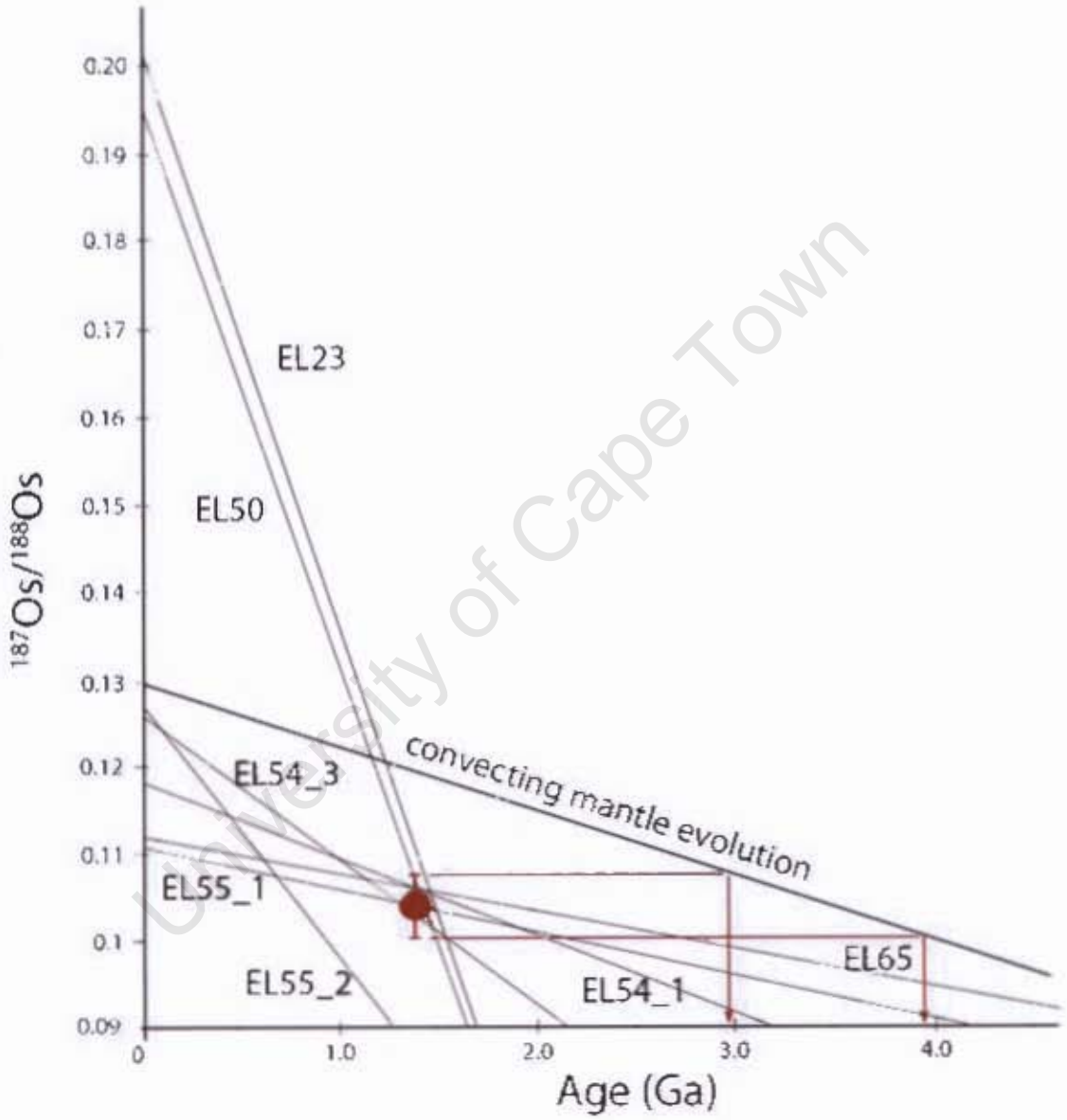

Figure 6.8: Osmium isotope evolution diagram for peridotitic sulphide inclusions. The initial ratio calculated from the isochron regression (0.1039 ± 0.0037) is plotted in red with its upper and lower limits and their respective T_{RD} of 2.96 and 3.93 Ga.

The upper and lower limits on the initial ratio (0.1039 ± 0.0037) give Re depletion ages (T_{RD}) of 2.96 and 3.93 Ga, respectively. This is the minimum age for melt depletion in the mantle. As peridotites may experience variable degrees of melt depletion, T_{RD} is calculated by assuming all Re was removed from the samples during melt extraction. On the Os isotope evolution diagram, these are illustrated as the red horizontal lines, representing the minimum age that allowed for the development of the measured $^{187}Os/^{188}Os$ ratio. T_{RD} is quantified according to the following formula (Walker *et al.*, 1989):

$$T_{RD} = \frac{1}{\lambda} \times \ln\left\{ \frac{\left(\frac{^{187}Os}{^{188}Os}(pm) - \frac{^{187}Os}{^{188}Os}(samp)\right)}{\left(\frac{^{187}Re}{^{188}Os}(pm)\right)} + 1 \right\} \tag{6.7}$$

with primitive upper mantle compositions from Meisel *et al.* (2001):

$$\frac{^{187}Re}{^{188}Os}_{(pm)} = 0.43464$$

$$\frac{^{187}Os}{^{188}Os}_{(pm)} = 0.1296$$

and the decay constant from (Smoliar *et al.*, 1996):

$$\lambda = 1.666 \text{ x } 10^{-11} \text{ year}^{-1}$$

6.6 Summary of Results

This suite of Ellendale diamonds has both lherzolitic and eclogitic diamond populations, as also shown by previous studies on silicate diamond inclusions (Hall & Smith, 1984; Griffin *et al.*, 1988; Jaques *et al.*, 1989). Inclusions of peridotitic nature included olivine, enstatite, Cr-diopside, and calcic Cr-pyrope, whereas those of eclogitic origin are orange garnet, omphacite, coesite and rutile (Griffin *et al.*, 1988; Jaques *et al.*, 1989). Also, stable carbon isotope characteristics of the Ellendale diamonds indicated both lherzolitic and eclogitic populations (van Heerden *et al.*, 1995).

6.6.1 Eclogitic

The eclogitic sulphides show low-Ni pyrrhotite-rich compositions with elevated Re/Os ratios typical for eclogitic sulphides. The sulphides have radiogenic $^{187}Os/^{188}Os$ ratios indicative of long-term elevated Re/Os ratios compared to the convecting mantle. This is consistent with ancient fractionation of the two elements by melt extraction, which due to their difference in compatibility, result in higher Re concentrations in the melt and lead to radiogenic Os isotopic compositions in basaltic crust over time. This crustal signature is preserved during subduction into the mantle and subsequent accretion of the crustal component to the sub-continental lithospheric mantle keel. As the eclogitic sulphides show no linear correlation, an age regression could not be calculated.

6.6.2 Peridotitic

Re/Os ratios point to a lherzolitic paragenesis for the peridotitic inclusions, with similar Re/Os values to both lherzolitic sulphide inclusions and xenoliths from other localities. Depleted harzburgitic compositions in the SCLM are due to continual melt depletion events whereas lherzolitic compositions in the SCLM are attained through melt refertilisation events, with basaltic melt introduction resulting in less depleted compositions (Shirey *et al.*, 2002, 2004; Richardson *et al.*, 2004).

Six of the seven peridotitic sulphides show an isochronous relationship and a regression was calculated which yielded an age of 1432 ± 130 Ma. Although the age regression has uncertainties due to limited spread in $^{187}Re/^{188}Os$ as well as Re blank correction to such tiny samples, the upper and lower limits on the age still indicate peridotitic diamond formation below the King Leopold Mobile Belt during the Proterozoic. The $^{187}Os/^{188}Os$ initial ratio is low for the

convecting mantle at $\sim$ 1.43 Ga, with γ_{Os} = -32.25. From the Os isotope evolution diagram, a two-stage development for the Os isotopic compositions is suggested, with the sulphide Os residing in a precursor with unradiogenic Os isotope ratios. The low initial ratio (0.1039) is supported by low initial Nd isotopic compositions (ε_{Nd} = -3 at 1580 Ma) of silicate inclusions from Argyle (Richardson, 1986). Also, Sm-Nd isotopic data from an Argyle lherzolite xenolith give ε_{Nd} = -3.2 (Graham *et al.*, 1999). The most likely mechanism to produce these compositions is ancient Re removal by melt extraction, with long-term isolation from the convecting mantle in the sub-continental lithospheric mantle (SCLM). The upper limit on the initial ratio has a Re depletion age of 2.96 Ga, indicating the presence of SCLM below the Kimberley craton since at least the Meso-archaean.

In conclusion, the age regression calculated for the peridotitic sulphide population, found as inclusions in diamonds at Ellendale indicates a diamond-forming event in the Mesoproterozoic. The unradiogenic initial $^{187}Os/^{188}Os$ ratio points to a precursor that resided in the sub-continental lithospheric mantle beneath the King Leopold Mobile Belt. This precursor must have been isolated since at least the Archaean. The lherzolitic diamond-forming event is much younger and unrelated to the craton keel stabilisation in the Archaean.

Chapter 7

DISCUSSION AND CONCLUSIONS

7.1 Diamond - forming events in the SCLM

Richardson *et al.* (1993) have shown that there are age differences between diamonds of different parageneses: harzburgitic diamonds typically yield Archaean ages, with eclogitic and lherzolitic diamonds giving younger Proterozoic ages. Multiple generations of diamonds formed in the lithospheric mantle below the Kaapvaal - Zimbabwe craton have been shown to reflect the history of creation, assembly and modification of the craton (Shirey *et al.*, 2002). This can also be extended to other cratons. Harzburgitic diamonds are related to early cratonic keel formation and subsequent metasomatism (Richardson *et al.*, 2004, and references therein). These cratonic nuclei are inferred to form by subduction with partial melting occurring at shallow depths in the mantle wedge accompanied by fluid infiltration from the subducting plate, which accounts for incompatible element enrichment in mantle xenoliths and silicate diamond inclusions (Carlson *et al.*, 2005, and references therein). These metasomatic fluids are typically high in CO_2, LREE, K, Rb, Sr and H_2O (Gurney *et al.*, 2005). (Westerlund *et al.*, 2006) showed that Panda harzburgitic diamond formation ($\sim$ 3.52 Ga) on the Slave craton was coeval with lithosphere formation at 3.5 - 3.3 Ga (Aulbach *et al.*, 2004). The sulphide inclusions in the diamonds attained their radiogenic $^{187}Os/^{188}Os$ signature from fluids with a radiogenic Os signature, introduced from the subducting plate, with isotopically distinct sulphides in different growth zones.

Eclogitic diamonds reflect craton stabilisation through late Archaean to Proterozoic accretionary events along the margins of cratonic nuclei with underplating of oceanic crust onto the SCLM (reviews by Gurney *et al.*, 2005; Stachel & Harris, 2008). For example, $\sim$ 2.9 Ga eclogitic diamonds at Jwaneng and Kimberley are related to amalgamation of the western and eastern

Kaapvaal cratons along the Colesberg lineament at 2.92 Ga (Richardson *et al.*, 1993, 2001, 2004; Carlson *et al.*, 1999; Schmitz, 2002; Schmitz *et al.*, 2004). Also, 2.2 - 1.8 Ga eclogitic diamonds at Lac de Gras on the Slave craton may be related to Proterozoic collisional events (Aulbach *et al.*, 2008). Lherzolitic diamonds have been related not to craton keel development and stabilisation but to subsequent metasomatic alteration and modification of the SCLM during the Proterozoic (Richardson *et al.*, 1993; Shirey *et al.*, 2002, 2004; Richardson *et al.*, 2004), with reworking of the lithosphere by addition of basaltic components (e.g. Ca, LREE), resulting in less depleted SCLM compositions (Richardson et al., 2004). The Venetia ($\sim$ 2.0 Ga) (Richardson *et al.*, 2008) and Premier lherzolitic diamonds (1.93 $\pm$ 0.04 Ga) (Richardson *et al.*, 1993) post-date the magmatism of the Bushveld Igneous Complex at $\sim$ 2.05 Ga, which indicates that magmatism did not destroy the SCLM below the Kaapvaal, but resulted in its modification to less depleted compositions. In addition, Viljoen *et al.* (2004) have shown that a fertile lherzolite xenolith from Premier, resulted from metasomatic overprinting of an older harzburgite. The 2.01 $\pm$ 0.06 Ga lherzolitic diamonds from Udachnaya on the Siberian craton have been related to localised reworking events, with the introduction of basaltic melts or fluids into older lithospheric mantle (Richardson & Harris, 1997). The Archaean age for the SCLM is indicated by Sm - Nd model ages for the garnet inclusions in diamond and by Re - Os model ages of mantle xenoliths (Pearson *et al.*, 1995a; Richardson & Harris, 1997).

7.2 Major findings from this study

This suite of Ellendale diamonds has both eclogitic and peridotitic sulphide inclusions, indicated by their Ni content, with eclogitic sulphides containing less than 8 wt % Ni and the peridotitic sulphides containing much higher Ni ($\sim$ 15 - 35 wt %). The eclogitic sulphides have high Re/Os ratios (between 2 and 80), similar to eclogitic sulphides in both inclusions in diamonds and mantle xenoliths (Figure 6.4; Pearson *et al.*, 1998; Richardson & Shirey, 2008). Re/Os ratios for peridotitic sulphide inclusions from Ellendale are much lower, from 0.01 to 1, and are equivalent to Re/Os ratios from both lherzolite xenoliths and lherzolite diamond inclusions from other diamond localities (Figure 6.4; Pearson *et al.*, 1995a,b; Graham *et al.*, 1999). This indicates a lherzolitic paragenesis for these diamonds and is consistent with studies that have shown Ellendale diamonds to have both lherzolitic and eclogitic silicate inclusions. For example, silicate inclusions from the Ellendale diamonds analysed by Lucas *et al.* (1989) and Jaques *et al.* (1991) yielded relatively low Mg/(Mg+Fe) olivine, Cr - diopside, as well as lherzolitic G9 pyrope. In addition, δ^{13}C for Ellendale diamonds indicate both lherzolitic and eclogitic parageneses, with

the lherzolitic diamonds at Ellendale (van Heerden *et al.*, 1995), showing a wider range in $\delta^{13}C$ than harzburgitic diamonds from diamond localities on the Kaapvaal craton (van Heerden & Gurney, 1995). Ellendale lacks an extensive harzburgitic suite of diamonds, as would be indicated by a lack of clinopyroxene in the inclusion assemblage and subcalcic Cr pyropes (G10 compositions).

The eclogitic sulphide inclusions show no correlation in their Re - Os isotopic data and an age regression could not be calculated. The Re - Os isotopic compositions of the lherzolitic sulphides demonstrate more linearity than the eclogitic sulphides and regression analysis indicates a Proterozoic age of 1432 $\pm$ 130 Ma, with an unradiogenic initial Os isotopic composition (0.1039 $\pm$ 0.0037). This indicates that the lherzolitic diamond-forming event is much younger and unrelated to the craton keel stabilisation in the Archaean.

Whereas depleted harzburgitic compositions in the SCLM are due to continual melt depletion events, lherzolitic compositions in the SCLM may be due to refertilisation of peridotite by subduction fluids or to localised metasomatic alteration events in the mantle, both of which would see the introduction of basaltic melts, resulting in less depleted peridotitic compositions (Shirey *et al.*, 2002, 2004; Richardson *et al.*, 2004). However, at Ellendale, subduction processes are ruled out, since the sulphide inclusions in the diamonds would attain a radiogenic $^{187}Os/^{188}Os$ signature from fluids with a radiogenic Os signature introduced from the subducting plate, as has been shown for the Panda diamonds on the Slave craton (Westerlund *et al.*, 2006).

The Ellendale diamonds have a high N content, as suggested by their pervasive yellow colour and confirmed by FTIR analyses of the diamond plates (see Chapter 5). High average N content for this suite of Ellendale diamonds ($\sim$ 600 ppm) could be due to either higher N content in the diamond-forming fluids or higher N incorporation due to the faster crystal growth. Different growth zones with distinctly different N contents seemingly indicate multiple fluids with varying N content.

Ellendale diamonds were stored at time averaged temperatures around 1167 °C (Table 5.1), only slightly higher than the average for cratonic areas ($\sim$ 1150 °C ; see review by Stachel & Harris, 2008). Similar mantle storage temperatures are indicated for both the eclogitic and peridotitic diamond populations at Ellendale, consistent with diamond formation subsequent to cratonisation in the Kimberley area at $\sim$ 1.8 Ga (Thom, 1975; Tyler & Griffin, 1990) so that the different chemical environments (peridotitic and eclogitic) would have equivalent diamond equilibration and storage temperatures.

The Ellendale diamonds do not show pervasive evidence for widespread deformation or ex-

tensive platelet degradation as indicated for the Argyle diamonds (Harris & Collins, 1985; Taylor *et al.*, 1990; Viljoen, 2002). Diamonds with high N contents, such as the Ellendale diamonds, are more resistant to plastic deformation, with experiments by (Wild *et al.*, 1967) indicating that Type II diamonds can be deformed at much lower critical stresses than Type I diamonds. This may explain why the pink/brown diamonds at Argyle, with lower N contents, show much more evidence of deformation. Platelets are sensitive to tectonothermal events in the lithosphere and destruction of platelets may be indicative of large-scale heating events in the mantle. The lack of extensive platelet degradation at Ellendale suggests that the diamonds had a relatively undisturbed 1.4 Ga mantle storage history and experienced lower temperatures than the Argyle diamonds (Viljoen, 2002). This could indicate that the Yampi and King Leopold orogenies which post-date lherzolitic diamond formation at $\sim$ 900 Ma (Bodorkos & Reddy, 2004) and 560 - 530 Ma (Myers *et al.*, 1996) resulted only in crustal deformation, with the underlying SCLM remaining largely unaffected.

7.3 Age of the SCLM beneath the King Leopold Mobile Belt

The presence of deep sub-continental lithospheric mantle below the King Leopold Mobile Belt (and the Kimberley craton) has been indicated by seismic tomography (van der Hilst *et al.*, 1998; Kennett, 2003; Fishwick *et al.*, 2005) and cratonic conductive geotherms for the West Kimberley Province (Griffin & Ryan, 1995). The Archaean age of this SCLM is indicated by the unradiogenic initial $^{187}Os/^{188}Os$ ratio (0.1039 $\pm$ 0.0037, with γ_{Os} = -32.25) for the lherzolitic sulphide inclusions in diamonds at Ellendale. This implies long-term isolation of the sulphide precursor from the convecting mantle, since at least the Mesoarchaean, with the Re depletion ages (T_{RD}) for the upper limit of the initial ratio calculated at 2.96 Ga. Archaean SCLM also extends to beneath the Halls Creek Mobile Belt, to the south-east of the Kimberley craton, with mantle xenoliths yielding Palaeoproterozoic to Neoarchaean T_{RD} ages of 2.2 - 2.9 Ga (Luguet *et al.*, 2006, 2008) and an imprecise Re - Os isochron age of 3.4 Ga (Graham *et al.*, 1999).

The age of the mantle below the Kimberley craton is significantly older than the oldest exposed crust in the area - the sandstone-dominated platform cover of the Kimberley is dated at 1.9 to 1.65 Ga (Gellatly, 1971; Thom, 1975). The oldest crust in the Halls Creek Mobile Belt is $\sim$ 1.92 Ga, with the $\sim$ 1.88 to 1.88 Ga Hooper Terrane forming the oldest rocks in the King Leopold Mobile Belt. Therefore, despite early Proterozoic convergent margins and new crustal formation (Tyler *et al.*, 1999; Griffin *et al.*, 2000), the underlying continental mantle was preserved. This indicates that crust and mantle in the Kimberley region were decoupled (Luguet

et al., 2008) with preservation of the lithosphere during accretion and amalgamation of the Halls Creek and King Leopold Mobile Belts. This is in contrast to the Siberian craton which shows synchronous stabilisation of the crust and SCLM due to a correspondence of Archaean Re - Os and Sm - Nd model ages (Pearson *et al.*, 1995a) for the SCLM with the oldest crustal ages from the Anabar and Aldan Shields on the Siberian craton (Turchenko, 1993; Nutman *et al.*, 1992).

7.4 Composition of the SCLM below the King Leopold Mobile Belt and its diamonds

The lherzolitic composition for the Ellendale sulphide inclusions is consistent with studies by McCulloch *et al.* (1983) and Jaques *et al.* (1984) that have indicated lherzolitic composition for the West Kimberley lamproitic source, as indicated by Ti - rich phlogopite, diopside and richterite compositions, as well as LREE - and LILE - enriched trace element compositions. These compositions, along with high $^{87}Sr/^{86}Sr$ (0.711 - 0.720) and unradiogenic Nd isotopic ratios (ε_{Nd} = -7 to -15) (McCulloch *et al.*, 1983; Jaques *et al.*, 1984), indicate derivation of the lamproites from a peridotitic source that had experienced long term enrichment by metasomatism, with addition of incompatible element-enriched fluid phases to depleted mantle. The lherzolitic composition of the SCLM is extended below the rest of the Kimberley craton and the Halls Creek Mobile Belt, with the lherzolitic xenoliths from Argyle and the Argyle lamproites also indicating derivation from an old source that had seen subsequent enrichment in LREE (Graham *et al.*, 1999).

Although lherzolitic Cr - pyrope is the most common garnet composition in the SCLM below the Kimberley craton, minor subcalcic Cr - pyrope (G10) has been recovered from both kimberlites on the Kimberley craton and lamproites in the adjacent mobile belts (Lucas *et al.*, 1989), which suggests that the SCLM may also be partly harzburgitic in composition. Single harzburgitic pyrope inclusions were found at Argyle (CaO 5 wt%, Cr_2O_3 14.64 wt%; Jaques *et al.*, 1989) and Ellendale (CaO 2.76 wt%, Cr_2O_3 6.84 wt%; Hall & Smith, 1984), however, an extensive harzburgitic diamond population has not been described at either locality. This could imply that only few harzburgitic diamonds were formed during early cratonic keel formation, or that harzburgitic diamonds were destroyed by subsequent melt metasomatic events in the mantle.

The lherzolitic diamond-forming event at 1.43 ± 0.13 Ga cannot be directly correlated with any metasomatic events in the region, which may have modified the composition of the SCLM by adding a basaltic component. However, Graham *et al.* (1999) indicate that there is evidence for

Proterozoic metasomatic event/s below the Kimberley craton, with the Os isotopic composition of the Argyle lherzolites and lamproite influenced by a $\sim$ 1500 Ma enriched - mantle component (represented by a picroilmenite megacryst from the Maude Creek kimberlite on the eastern Kimberley craton, with initial γ_{Os} = + 27). The correspondence of diamond formation ages of the lherzolitic diamonds at Ellendale and the eclogitic diamonds at Argyle (1.58 $\pm$ 0.06 Ga; Richardson, 1986), occurring to the south and south-east of the Kimberley craton, respectively, suggest that the Proterozoic metasomatic event/s could have been craton-wide.

It may be interesting to note that palaeomagnetic data from the McArthur Basin on the North Australian Craton indicate a change in trajectory of Australia at $\sim$ 1.5 Ga (Idnurm *et al.*, 1995; Idnurm, 2000; Betts *et al.*, 2007). While this is not necessarily a correlation with the lherzolitic diamond-forming event, this rotation may be due to changes in tectonic regime, which could result in remobilisation of fluids and refertilisation of the SCLM.

Eclogitic diamonds make up nearly half of the diamond population at Ellendale (Jaques *et al.*, 1989). The eclogitic sulphides at Elllendale show no linear correlation/s of their Re - Os isotopic compositions and therefore an age regression could not be calculated. It is therefore not known whether there were one or multiple eclogitic diamond-forming events, and whether they could be related to peridotitic diamond formation at Ellendale in the Proterozoic or the tectonic events that affected the King Leopold Mobile Belt during this time. e.g. deformation in the Hooper Terrane at $\sim$ 1.88 Ga and its subsequent incorporation into the Kimberley craton, ending at $\sim$ 1.79 Ga (Tyler & Griffin, 1990); or the Yampi and King Leopold orogenics at $\sim$ 0.9 Ga and 0.56 - 0.53 Ga, respectively (Myers *et al.*, 1996; Bodorkos & Reddy, 2004) (see Chapter 2).

7.5 Diamonds from mobile belt settings

Clifford's Rule requires that in order for kimberlites and lamproites to be diamond-bearing they need to intrude into Archaean cratons that are associated with the presence of deep SCLM, which is partially in the diamond stability field (Clifford, 1966). Cratons have low conductive geotherms, corresponding to surface heat flow of 40 mW/m^2 (Pollack & Chapman, 1977), which brings the graphite-diamond transition to much shallower depths than areas with higher geothermal gradient. The Ellendale diamonds are emplaced into a mobile belt, however, the presence of Archaean SCLM below the King Leopold Mobile Belt indicates that Clifford's Rule may still be valid. It is also seemingly valid for other diamond localities in mobile belt settings:

- Argyle is located in the Halls Creek Mobile Belt on the eastern margin of the Kimberley craton, for which the presence of a deep SCLM has been inferred from Re - Os studies on mantle xenoliths (Graham *et al.*, 1999; Luguet *et al.*, 2008) and seismic tomography (van der Hilst *et al.*, 1998; Kennett, 2003; Fishwick *et al.*, 2005).

- Venetia, River Ranch and other diamond localities intruded the Limpopo Mobile Belt, (Kaapvaal - Zimbabwe craton), however, the the presence of a deep SCLM beneath the Limpopo Mobile Belt has been inferred from seismic tomography (James *et al.*, 2001) and the depleted dunite-harzburgite assemblage of peridotite xenoliths (Smith *et al.*, 2008).

- The Prairie Creek lamproite province in Arkansas is located in a Proterozoic (> 1.5 Ga) terrane, much further south than the North American craton. This seems anomalous, however, the Ouachita Mountains (into which the lamproites intrude) may represent a boundary between continental and oceanic crust, with the mountain range thrust onto and over the North American craton (Lillie, 1985; Mickus & Keller, 1992).

- The kimberlites of the Colorado - Wyoming Kimberlite Province (including Sloan and George Creek) are intruded into Proterozoic rocks of the Colorado Front Ranges (Karlstrom & Houston, 1984), much further south than the suture marking the accretion of the continent - island arc with the Archaean rocks of the Wyoming craton (Eggler *et al.*, 1988; Otter, 1990; McCallum, 1991).

These localities indicate that the extent of Archaean SCLM cannot be determined based on the outcrop of Archaean crustal rocks alone, as younger crustal rocks may be thrust over older Archaean lithosphere, without the destruction of the local SCLM. It appears that due to the presence of a deep SCLM, the formation processes for diamonds emplaced into these mobile belt settings are similar to those operating beneath Archaean cratons. However, higher ambient mantle residence temperatures are indicated for these diamonds compared to on - craton diamond localities. The nitrogen aggregation characteristics and mantle storage temperatures for Ellendale and other craton - margin diamond localities are given in Table 7.1.

The higher nitrogen aggregation state of mobile belt diamonds may be a consequence of high mantle storage temperatures, indicative of higher ambient mantle temperatures towards the craton margin, as opposed to those of diamonds stored in the interior of the craton. The characteristics of the Ellendale and Venetia diamonds are similar, with regard to dominance of regular diamonds with little or no platelet degradation. In addition, these diamonds show little evidence of deformation, consistent with diamond formation during more passive mantle refertilisation (Ellendale - this study; Venetia - Viljoen, 2002).

Table 7.1: Nitrogen aggregation and mantle storage temperatures for diamonds from mobile belt settings

	Ellendale (this study)	Venetia (Viljoen, 2002)	George Creek (Chinn, 1995)	Argyle (Viljoen, 2002)
% IaB	71 % of analyses have > 50 % IaB	52 % of diamonds have > 50 % IaB	Average 85 % IaB	66 % of diamonds have > 80 % IaB
Mantle Storage Temperatures (°C)	1114 - 1229	999 - 1262	1151 - 1279	1085 - 1366
Average Temp (°C)	1167	1163	1223	1243
Residence Time	1.4 Ga	assumed 3 Ga	assumed 1.25 Ga	0.4 Ga

Temperatures calculated for Venetia may be higher, if calculated for a 1.5 Ga residence time, based on more recent Sm-Nd and Re-Os dating of Venetia diamonds (Richardson *et al.*, 2006, 2008).

In contrast, the diamonds from George Creek and Argyle are highly deformed and show a high percentage of irregular diamonds with high degrees of platelet degradation Also, at both these localities, the diamonds have anomalously high nitrogen aggregation (George Creek - Chinn, 1995; Argyle - Taylor et al., 1990; Viljoen, 2002). At Argyle, this is consistent with tectonic processes at the craton margin and underthrusting of the SCLM by eclogitic material during the Halls Creek orogeny, which marks the suture between the Kimberley craton and the Lucas craton as part of the greater North Australian craton (Myers *et al.*, 1996; Tyler & Page, 1996; Griffin *et al.*, 2000; Page *et al.*, 2001).

Bibliography

Allègre, C. J. & Luck, J.-M., 1980. Osmium isotopes as petrogenetic and geological tracers. *Earth and Planetary Science Letters*, **48**, 148–154.

Allen, B. P. & Evans, T., 1981. Aggregation of nitrogen in diamond, including platelet formation. *Proceedings of the Royal Society of London*, **A 375**, 93–104.

Allsopp, H. L., Bristow, J. W., Skinner, E. M. W., Scott-Smith, B. H. & Danchin, R. V., 1985. Rb-Sr Geochronology of some Miocene West Australian Lamproites. *Transactions of the Geological Society of South Africa*, **88**, 341–345.

Atkinson, W. J., Hughes, F. E. & Smith, C. B., 1984. A Review of the Kimberlitic Rocks of Western Australia. In: *Kimberlites I: Kimberlites and Related Rocks. Proceedings of the 3rd International Kimberlite Conference*, (ed. Kornprobst, J.), Elsevier Science Publishers, Amsterdam.

Aulbach, S., Griffin, W. L., Pearson, N. J., O'Reilly, S. Y., Kivi, K. & Doyle, B. J., 2004. Mantle formation and evolution, Slave craton: Constraints from HSE abundances and Re-Os isotope systematics of sulfide inclusions in mantle xenocrysts. *Chemical Geology*, **208**, 61–88.

Aulbach, S., Stachel, T., Creaser, R. A., Heaman, L. M., Shirey, S. B., Muehlenbachs, K., Eichenberg, D. & Harris, J. W., 2008. Sulfide survival and diamond genesis during formation and evolution of Archaean subcontinental lithosphere: Kaapvaal vs Slave. *9th International Kimberlite Conference Extended Abstracts*, **9IKC-A-00293**.

Barry, J. C., Bursill, L. A. & Hutchinson, J. L., 1985. On the structure of {100} platelet defects in Type Ia diamond. *Philosophical Magazine A*, **48**, 109–121.

Becker, H., 2000. Re-Os fractionation in eclogites and blueschists and the implications for recycling of oceanic crust into the mantle. *Earth and Planetary Science Letters*, **177**, 287–300.

Betts, P. G., Giles, D., Lister, G. S. & Frick, L. R., 2002. Evolution of the Australian lithosphere. *Australian Journal of Earth Sciences*, **49**, 661–695.

Betts, P. G., Giles, D., Schaefer, B. F. & Mark, G., 2007. 1600-1500 Ma hotspot track in eastern Australia: implications for Mesoproterozoic continental reconstructions. *Terra Nova*, **19**(6), 496–501.

Birck, J. L., Barman, M. R. & Capmas, F., 1997. Re-Os Isotopic Measurements at the Femtomole Level in Natural Samples. *Geostandards Newsletter*, **20**(1), 19–27.

Black, R., Lameyre, J. & Bonin, R., 1985. The structural setting of Alkaline complexes. *Journal of African Earth Sciences*, **3**, 5–14.

Blinova, G. K., Gurkina, G. A. & Sinakov, S. K., 1988. Some chemical properties of the medium from which natural diamonds crystallise. *Doklady Akademii Nauk SSSR*, **301**, 207–209.

Bobrievich, A. P., Bondarenko, M. N., Gnevushev, M. A., Krasov, A. M., Smirnov, G. I. & Yurkevich, R. K., 1959. *The diamond deposits of Yakutia*, Moscow: State Scientific and Technical Publishing House.

Bodorkos, S. & Reddy, S. M., 2004. Proterozoic cooling and exhumation of the northern central Halls Creek Orogen, Western Australia: constraints from a reconnaissance $^{40}Ar/^{39}Ar$ study. *Australian Journal of Earth Sciences*, **51**, 591–609.

Boyd, F. R., 1973. A pyroxene geotherm. *Geochimica et Cosmochimica Acta*, **37**, 2533–2546.

Boyd, F. R. & Gurney, J. J., 1986. Diamonds and the African lithosphere. *Science*, **232**, 472–477.

Boyd, F. R., Gurney, J. J. & Richardson, S. H., 1985. Evidence for a 150-200 km thick Archaean lithosphere from diamond inclusion thermobarometry. *Nature*, **315**, 387 – 389.

Boyd, S. R., Kiflawi, I. & Woods, G. S., 1994. The relationship between infrared absorption and the A defect concentration in diamond. *Philosophical Magazine B*, **69**(6), 1149–1153.

Boyd, S. R., Kiflawi, I. & Woods, G. S., 1995. Infrared absorption by the B nitrogen aggregate in diamond. *Philosophical Magazine B*, **72**(3), 351–361.

Boyd, S. R., Mattey, D. P., Pillinger, C. I., Milledge, H. J., Mendelssohn, M. & Seal, M., 1987. Multiple growth events during diamond genesis: an integrated study of carbon and nitrogen isotopes and nitrogen aggregation state in coated stones. *Earth and Planetary Science Letters*, **86**, 341–353.

Brandon, A. D., Becker, H., Carlson, R. W. & Shirey, S. B., 1999. Isotopic constraints on time scales and mechanisms of slab material transport in the mantle wedge, evidence from the Simcoe mantle xenoliths, Washington, USA. *Chemical Geology*, **160**, 387–407.

Brenan, J. M., Cherniak, D. J. & Rose, L. A., 2000. Diffusion of osmium in pyrrhotite and pyrite: Implications for closure of the Re-Os isotopic system. *Earth and Planetary Science Letters*, **180**, 399–413.

Bruley, J., 1992. Detection of nitrogen at {100} platelets in a Type IaA/B diamond. *Philosophical Magazine*, **66**, 47–56.

Bruton, E., 1978. *Diamonds*, N.A.G. Press, London.

Bulanova, G. P., Griffin, W. L., Ryan, C. G., Shestakova, O. Y. & Barnes, S.-J., 1996. Trace elements in sulphide inlcusions from Yakutian diamonds. *Contributions to Mineralogy and Petrology*, **124**, 111–125.

Bursill, L. A. & Glaisher, R. W., 1985. Aggregation and dissolution of small and extended defect structures in Type Ia diamond. *American Mineralogist*, **70**(5-6), 608–618.

Carlson, R. W., Pearson, D. G. & James, D. E., 2005. Physical, Chemical, and Chronological Characteristics of Continental Mantle. *Reviews of Geophysics*, **43**, RG1001.

Carlson, R. W., Pearson, D. G., Boyd, F. R., Shirey, S. B., Irvine, G., Menzies, A. H. & Gurney, J. J., 1999. Re-Os systematics of lithosphere peridotites: Implications for lithosphere formation and preservation. In: *Volume 1: Implications for lithosphere formation and preservation. Proceedings of the 7th International Kimberlite Conference, Cape Town, 1998*, (eds Gurney, J., Gurney, J., Pascoe, M. & Richardson, S.), pp. 99–108. Red Roof Design.

Chesler, R. F., 2008. Geochemistry of the West Australian, West Kimberley Province Lamproites, *9th International Kimberlite Conference Extended Abstract*, pp. 9IKC–A–00086.

Chesley, J. T., Rudnick, R. L. & Lee, C.-T., 1999. Re-Os systematics of mantle xenoliths from the East African Rift: Age, structure and history of the Tanzanian Craton. *Geochimica et Cosmochimica Acta*, **63**, 1203–1217.

Chinn, I. L., 1995. *A Study of Unusual Diamonds from the George Creek K1 Kimberlite Dyke, Colorado.* PhD thesis, University of Cape Town.

Chrenko, R. M., McDonald, R. S. & Darrow, K. A., 1967. Infra-red spectra of diamond coat. *Nature*, **4**, 474–476.

Clifford, T. N., 1966. Tectono-metallogenic units and metallogenic provinces of Africa. *Earth and Planetary Science Letters*, **1**, 421–434.

Collins, A. T. & Woods, G. S., 1982. An anomaly in the infrared absorption spectrum of synthetic diamond. *Philosophical Magazine B*, **B46**, 77–83.

Craig, J. R. & Kullerud, G., 1969. Phase relations in the Cu-Fe-Ni-S system and their application to magmatic ore deposits. *Economic Geology Monograph*, **4**, 344–358.

Creaser, R. A., Papanastassiou, D. A. & Wasserburg, G. J., 1991. Negative thermal ion mass spectrometry of osmium, rhenium and iridium. *Geochimica et Cosmochimica Acta*, **55**, 397–401.

Crocket, R. N. & Mason, R., 1968. Foci of mantle disturbance in Southern Africa and their economic significance. *Economic Geology*, **63**, 532–540.

Dale, C. W., Gannoun, A., Burton, K. W., Argles, T. W. & Parkinson, I. J., 2007. Rhenium-Osmium isotope and elemental behaviour during subduction of oceanic crust and implications for mantle recycling. *Earth and Planetary Science Letters*, **253**, 211–225.

Daly, S. J., Fanning, C. M. & Fairclough, M. C., 1998. Tectonic evolution and exploration potential of the Gawler Craton. *AGSO Journal of Australian Geology and Geophysics*, **17**, 145–168.

Davies, G., 1976. The A nitrogen aggregate in diamond-its symmetry and possible structure. *Journal of Physics C: Solid State Physics*, **9**, L537–L542.

Davies, G., 1979. Cathodoluminescence. In: *Properties of Diamond*, (ed. Field, J.), pp. 165–181. Academic Press, London.

Davies, G., 1981. Decomposing the IR absorption spectra of diamonds. *Nature*, **290**, 40–41.

Davies, G., Collins, A. T. & Spear, P., 1984. Sharp infra-red absorption lines in diamond. *Solid State Communications*, **49**(5), 433–436.

de Vries, R. C., 1975. Plastic deformation and "work-hardening" of diamond. *Materials Research Bulletin*, **10**(11), 1193–1199.

Deines, P. & Harris, J. W., 1995. Sulfide inclusion chemistry and carbon isotopes of African diamonds. *Geochimica et Cosmochimica Acta*, **59**, 3173–3188.

Downes, P. J., Griffin, B. J. & Griffin, W. L., 2007. Mineral Chemistry and zircon geochronology of xenocrysts and altered mantle and crustal xenoliths from the Aries micaceous kimberlite: Constraints on the composition and age of the central Kimberley Craton, Western Australia. *Lithos*, **93**, 175–198.

Drummond, B. J., Finlayson, D. M., Harrington, H. J. & Wright, C., 1989. The impact of regional deep seismic profiling on the interpretation of geological maps. *BMR Sympsosium*, **5**.

Eggler, D. H., 1978. The effect of CO_2 upon partial melting of peridotite in the system Na_2O-CaO-Al_2O_3-MgO-SiO_2-CO_2 to 35kbar, with an analysis of melting in a peridotite-H_2O-CO_2 system. *American Journal of Science*, **278**, 305–343.

Eggler, D. H. & Wendlandt, R. F., 1979. Experimental studies on the relationship between kimberlite magma and partial melting of peridotite. In: *Kimberlites, Diatremes and Diamonds*, (eds Boyd, F. & Meyer, H.), pp. 330–338. American Geophysical Union, Washington, D.C.

Eggler, D. H., Meen, J. K., Welt, F., Dudas, F. O., Furlong, K. P., McCallum, M. E. & Carlson, R. W., 1988. Tectonomagmatism of the Wyoming Province. *Colorado School of Mines Quarterly*, **83**, 25–40.

Evans, T., 1992. Aggregation of Nitrogen in Diamond. In: *The Properties of Natural and Synthetic Diamond*, (ed. Field, J.), pp. 259–290. Academic Press, London.

Evans, T. & Harris, J. W., 1989. Nitrogen aggregation, inclusion equilibration temperatures and the age of diamonds. *Proceedings of the 4th International Kimberlite Conference, Perth, 1986, Geological Society of Australia Special Publication*, **16**, 386–388.

Evans, T. & Qi, Z., 1982. The kinetics of aggregation of nitrogen in diamond. *Proceedings of the Royal Society of London, Ser A*, **361**, 109–127.

Evans, T., Kiflawi, I., Luyten, W., van Tendeloo, G. & Woods, G. S., 1995. Conversion of platelets into dislocation loops and voidite formation in Type IaB diamonds. *Proceedings of the Royal Society of London, Ser A*, **449**, 295–313.

Fallon, P. J., Brown, L. M., Barry, J. C. & Bruley, J., 1995. Nitrogen determination and characterization in natural diamond platelets. *Philosophical Magazine A*, **72**, 21–37.

Finnerty, A. A. & Boyd, F. R., 1987. Thermobarometry for garnet peridotites: basis for the determination of thermal and compositional structure of the upper mantle. In: *Mantle Xenoliths*, (ed. Nixon, P.), pp. 381–402. John Wiley and Sons, Chichester.

Fishwick, S., Kennett, B. L. N. & Reading, A. M., 2005. Contrasts in lithospheric structure within the Australian craton - insights from surface wave tomography. *Earth and Planetary Science Letters*, **231**, 163–176.

Foley, S. F., 1989. The Genesis of lamproitic magmas in a reduced fluorine-rich mantle. *Geological Society of Australia, Special Publication*, **14**, 616–631.

Foley, S. F., 1991. The origin of kimberlite and lamproite in veined lithospheric mantle. *CPRM Special Publication*, **2/91**, 109–111.

Foley, S. F., 1992. Vein-plus-wall-rock melting mechanisms in the lithosphere and the origin of potassic alkaline magmas. *Lithos*, **28**, 435–453.

Foster, D. A. & Gray, D. R., 2000. Evolution and structure of the Lachlan Fold Belt (Orogen) of eastern Australia. *Annual Review of Earth and Planetary Science Letters*, **28**, 47–80.

Foster, J. G., Lambert, D. D., Frick, L. R. & Maas, R., 1996. Re-Os isotopic evidence for genesis of Archaen nickel ores from uncontaminated komatiites. *Nature*, **382**, 703–706.

Gao, S., Rudnick, R. L., Carlson, R. W., McDonough, W. F. & Liu, Y.-S., 2002. Re-Os evidence for replacement of ancient mantle lithosphere beneath the North China craton. *Earth and Planetary Science Letters*, **198**, 307–322.

Gellatly, D. C., 1971. Possible Archaean rocks at the Kimberley region, Western Australia. *Geological Society of Australia, Special Publication*, **3**, 93–101.

Giles, D., Betts, P. G. & Lister, G. S., 2004. 1.8 - 1.5-Ga links between the North and South Australian Cratons and the Early-Middle Proterozoic configuration of Australia. *Tectonophysics*, **380**, 27–41.

Graham, S., Lambert, D. D., Shee, S. R., Smith, C. B. & Reeves, S., 1999. Re-Os isotopic evidence for Archean lithospheric mantle beneath the Kimberley block, Western Australia. *Geology*, **27**(5), 431–434.

Gramlich, J. W., Murphy, T. J., Garner, E. L. & Shields, W. R., 1973. The atomic weight of rhenium. *Journal of Research, National Bureau of Standards, Section A*, **77**, 691–698.

Griffin, T. J., 1989. A major thrust between the Gibb River and Hooper Terranes in the King Leopold Orogen, West Kimberley region. *Professional Paper, Western Australia Geological Survey*, **26**, 69–81.

Griffin, T. J. & Grey, K., 1990. Kimberley Basin, *Geology and Mineral Resources of Western Australia, Geological Survey of Western Australia Memoir*, Vol. 3, pp. 293–304.

Griffin, T. J. & Myers, J. S., 1988. Geological Note: a Proterozoic terrane boundary in the King Leopold Orogen, Western Australia. *Australian Journal of Earth Sciences*, **35**, 131–132.

Griffin, T. J., Page, R. W., Sheppard, S. & Tyler, I. M., 2000. Tectonic implications of Palaeoproterozoic post-collisional, high-K felsic igneous rocks from the Kimberley region of northwestern Australia. *Precambrian Research*, **101**, 1–23.

Griffin, W. L. & Ryan, C. G., 1995. Trace elements in indicator minerals: area selection and target evaluation in diamond exploration. *Journal of Geochemical Exploration*, **53**, 311–337.

Griffin, W. L., Jaques, A. L., Sie, S. H., Ryan, C. G., Cousens, D. R. & Suter, G. F., 1988. Conditions of diamond growth: a proton microprobe study of inclusions in West Australian diamonds. *Contributions to Mineralogy and Petrology*, **99**, 143–158.

Gurney, J. J., 1989. Diamonds. In: *Kimberlites and Related Rocks II: Their Mantle/Crust Setting, Diamonds and Diamond Exploration. Proceedings of the 4th International Kimberlite Conference, Perth 1986.*, (ed. Ross, J.), pp. 935–965. Blackwell Scientific Publications.

Gurney, J. J. & Switzer, G. S., 1973. The discovery of garnets closely related to diamonds in the Finsch Pipe, South Africa. *Contributions to Mineralogy and Petrology*, **39**, 103–116.

Gurney, J. J., Helmstaedt, H. H., le Roex, A. P., Nowicki, T. E., Richardson, S. H. & Westerlund, K. J., 2005. Diamonds: Crustal Distribution and Formation Processes in Time and Space and an Integrated Deposit Model. *Economic Geology 100th Anniversary Volume*, pp. 143–177.

Haggerty, S. E., 1986. Diamond genesis in a multiply constrained model. *Nature*, **320**, 34–38.

Hall, A. E. & Smith, C. B., 1984. Lamproite Diamonds - Are they different?. In: *Kimberlite occurrence and origin: A basis for conceptual models in exploration, University Extension Publication*, (eds Glover, J. & Harris, P.), Vol. 8, pp. 167–212. The University of Western Australia.

Handler, M. R., Bennett, V. C. & Esat, T. M., 1997. The persistence of off-cratonic lithospheric mantle: Os isotopic systematics of variably metsomatised southeast Australian xenoliths. *Earth and Planetary Science Letters*, **151**, 61–75.

Hanley, P. L., Kiflawi, I. & Lang, A. R., 1977. On Topographically Identifiable Sources of Cathodoluminescence in Natural Diamonds. *Philosophical Transactions of the Royal Society*, **284**, 329–368.

Harris, J. W., 1968. The recognition of diamond inclusions. Part I: Syngenetic inclusions. *Industrial Diamond Review*, **28**, 402–410.

Harris, J. W., 1992. Diamond geology. In: *The Properties of Natural and Synthetic Diamond*, (ed. Field, J.), pp. 345–393. Academic Press, London.

Harris, J. W. & Collins, A. T., 1985. Studies of Argyle diamonds. *Industrial Diamond Review*, **3**, 128–130.

Harris, J. W. & Gurney, J. J., 1979. Inclusions in diamond. In: *The properties of diamond*, (ed. Field, J.), pp. 555–591. Academic Press, New York.

Harris, J. W., Hawthorne, J. B., Oosterveld, M. M. & Wehmeyer, E., 1975. A classification scheme for diamond and a comparative study of South African diamond characteristics. In: *Physics and Chemistry of the Earth*, (eds Ahrens, L., Dawson, J., Duncan, A. & Erlank, A.), pp. 765–783. Pergamon Press, London, Oxford.

Harris, J. W., Milledge, H. J., Barron, T. H. K. & Munn, R. W., 1970. Thermal expansion of garnets included in diamond. *Journal of Geophysical Research*, **75**, 5775–5792.

Harrison, E. R. & Tolansky, S., 1964. Growth history of a natural octahedral diamond. *Proceedings of the Royal Society, ser A*, pp. 490–496.

Hawthorne, J., 1975. Model of a kimberlite pipe. *Physics and Chemistry of the Earth*, **9**, 1–10.

Henriques, R. C., 1965. Thermal expansion of inclusions in diamond. *Diamond Research 1965. Supplement to Industrial Diamond Review*, pp. 31–32.

Hughes, F. E. & Smith, C. B., 1990. Ellendale diamond deposits. In: *Geology of the Mineral Deposits of Australia and Papua New Guinea*, (ed. Hughes, F.), pp. 1115–1122. The Australasian Institute of Mining and Metallurgy, Melbourne.

Humble, P., 1982. The structure and mechanism of formation of platelets in natural type Ia diamond. *Proceedings of the Royal Society of London, Ser A*, **381**, 65–81.

Idnurm, M., 2000. Towards a high resolution Late Palaeoproterozoic - earliest Mesoproterozoic apparent polar wander path for northern Australia. *Australian Journal of Earth Sciences*, **47**, 405–429.

Idnurm, M., Giddings, J. W. & Plumb, K. A., 1995. Apparent polar wander and reversal stratigraphy of the Palaeo-Mesoproterozoic southeastern McArthur Basin, Australia. *Precambrian Research*, **72**, 1–41.

James, D. E., Fouch, M. J., VanDecar, J. C., van der Lee, S. & Group, K. S., 2001. Tectospheric structure beneath southern Africa. *Geophysical Research Letters*, **28**, 2485–2488.

Janse, A. J. A., 1994. Is Clifford's Rule still valid? Affirmative examples from around the world. In: *Diamonds: Characterization, Genesis and Exploration. Proceedings of the 5th International Kimberlite Conference, Brazil, 1991*, (eds Meyer, H. & Leonardos, O.), pp. 215–235. Brazil Companhia de Pesquisa de Recursos Minerais.

Jaques, A. L., Hall, A. E., Sheraton, J., Smith, C. B. & Roksandic, Z., 1991. Peridotitic Planar Octahedral diamonds from the Ellendale lamproite pipes, Western Australia, *Diamonds: Characterization, Genesis and Exploration. Proceedings of the 5th International Kimberlite Conference, Brazil, 1991*, pp. 69–77.

Jaques, A. L., Hall, A. E., Sheraton, J. W., Smith, C. B., Sun, S.-S., Drew, R. M., Foudoulis, C. & Ellingsen, K., 1989. Composition of crystalline inclusions and C-isotopic composition of Argyle and Ellendale diamonds. *Proceedings of the 4th International Kimberlite Conference*, .

Jaques, A. L., Lewis, J. D. & Smith, C. B., 1986. The kimberlites and lamproites of Western Australia. *Geological Survey of Western Australia*, **Bulletin 132**(Plate 1).

Jaques, A. L., Lewis, J. D., Smith, C. B., Gregory, G. P., Ferguson, J., Chappell, B. W. & McCulloch, M. T., 1984. The diamond-bearing ultrapotassic (Lamproitic) rocks of the West Kimberley Region, Western Australia. In: *Kimberlites I: Kimberlites and Related Rocks, Proceedings of the 3rd International Kimberlite Conference*, (ed. Kornprobst, J.), pp. 225 – 254. Elsevier.

Jaques, A. L., O'Neill, H. S. C., Smith, C. B. & Moon, J., 1990. Diamond-bearing peridotite xenoliths from the Argyle (AK1) pipe. *Contributions to Mineralogy and Petrology*, **104**, 255–276.

Jordan, T. H., 1975. The continental tectosphere. *Reviews of Geophysics*, **13**, 1–12.

Jordan, T. H., 1978. Composition and development of the continental tectosphere. *Nature*, **274**, 544–548.

Jordan, T. H., 1988. Structure and formation of the continental tectosphere. *Journal of Petrology*, **29**, 11–37.

Kamiya, Y. & Lang, A. R., 1964. On the structure of coated diamonds. *Philosophical Magazine*, **11**, 347–356.

Karlstrom, K. E. & Houston, R. S., 1984. The Cheyenne Belt: Analysis of a Proterozoic suture in southern Wyoming. *Precambrian Research*, **25**, 415–446.

Kennett, B. L. N., 2003. Seismic structure in the mantle beneath Australia. In: *Evolution and Dynamics of the Australian Plate*, (eds Hills, R. & Mueller, R.), Vol. 22, pp. 7–23. Geological Society of Australia Special Publication.

Kesson, S. E. & Ringwood, A. E., 1989. Slab-mantle interactions 2.The formation of diamonds. *Chemical Geology*, **78**, 97–118.

Kiflawi, I. & Bruley, J., 2000. The nitrogen aggregation sequence and the formation of voidites in diamond. *Diamond and Related Materials*, **9**, 87–93.

King, J. M., Shigley, J. E., Gelb, T. H., Guhin, S. S., Hall, M. & Wang, W., 2005. Characterization and grading of natural-color yellow diamonds. *Gems and Gemology*, **41**(2), 88–115.

Kramers, J., 1979. Lead, uranium, strontium, potassium and rubidium in inclusion-bearing diamonds and mantle-derived xenoliths from southern Africa. *Earth and Planetary Science Letters*, **42**, 58–70.

Lang, A. R., 1963. Applications of 'limited projection topographs' and 'direct beam topographs' in diffraction topography. *British Journal of Applied Physics*, **14**(12), 904–907.

Lang, A. R., 1964. A proposed structure for nitrogen impurity platelets found in diamond. *Proceedings of the Physical Society, London*, **84**, 871–876.

Lang, A. R., 1965. X-ray topography of diamond. In: *Physical Properties of Diamond*, (ed. Berman, R.), pp. 67–115. Clarendon Press, Oxford.

Lang, A. R., 1974. On the growth-sectorial dependence of defects in natural diamonds. *Proceedings of the Royal Society of London*, **340**, 233–248.

Lang, A. R., 1979. Internal structure. In: *The properties of diamond*, (ed. Field, J.), pp. 425–469. Academic Press, London.

Lax, M. & Burstein, E., 1955. Infrared lattice absorption in ionic and homopolar crystals. *Physical Review*, **97**, 39–52.

Li, Z. X., 2000. Palaeomagnetic evidence for unification of the North and West Australian cratons by ca. 1.7 Ga: new results from the Kimberly Basin of northwestern Australia. *Geophysical Journal International*, **142**, 173–180.

Li, Z. X., Bogdanova, S. V., Collins, A. S., Davidson, A., de Waele, B., Ernst, R. E., Fitzsimons, I. C. W., Fuck, R. A., Gladkochub, D. P., Jacobs, J., Karlstrom, K. E., Lu, S., Natapov, L. M., Pease, V., Pisarevsky, S. A., Thrane, K. & Vernikovsky, V., 2008. Assembly, configuration, and break-up history of Rodinia: A synthesis. *Precambrian Research*, **160**, 179–210.

Lillie, R. J., 1985. Tectonically buried continent/ocean boundary, Ouachita Mountains, Arkansas. *Geology*, **13**, 18–21.

Lorenz, V., 2003. Maar-Diatreme Volcanoes, their Formation, and their Setting in Hard-rock or Soft-rock Environments. *Geolines*, **15**, 72–83.

Loubser, J. H. N. & van Wyk, J. A., 1981. *Diamond Conference Abstracts, Reading*, pp. 35–40.

Lucas, H., Ramsay, R. R., Hall, A. E., Smith, C. B. & Sobolev, N. V., 1989. Garnets from Western Australian kimberlites and related rocks. *Proceedings of the 4th International Kimberlite Conference, Perth, 1986, Geological Society of Australia Special Publication*, **16**, 809–819.

Ludwig, K. R., 1991. ISOPLOT: A Plotting and Regression Program for Radiogenic-isotope Data. *US Geological Survey Open File Report*, 39.

Lugmair, G. W. & Galer, S. J. G., 1992. Age and isotopic relationships among the angrites Lewis Cliff 86010 and Angra dos Reis. *Geochimica et Cosmochimica Acta*, **56**(4), 1673–1694.

Luguet, A., Pearson, D. G., Jaques, A. L., Bulanova, G. P., Smith, C. B., Roffey, S. & Rayner, M. J., 2006. Deep Structure of the lithospheric mantle under a mobile zone: the Re-Os approach. *Geophysical Research Abstracts*, **8**(04320).

Luguet, A., Pearson, D. G., Jaques, A. L., Smith, C. B., Bulanova, G. P., Carter, G., Roffey, S., Rayner, M. J. & Lorand, J.-P., 2008. Age constraints on the lithosphere beneath the Halls Creek mobile belt and implications for diamonds of the Argyle lamproite deposit. *9th International Kimberlite Conference Extended Abstracts*, **9IKC-A-00263**.

McCallum, M. E., 1991. The Sloan 1 and 2 kimberlite complex near the southern boundary of the State Line district of the Colorado-Wyoming Kimberlite Province. *Wyoming Geological Association Guidebook*, **42nd Field Conference**, 229–250.

McCulloch, M. T., Jaques, A. L., Nelson, D. R. & Lewis, J. D., 1983. Nd and Sr isotopes in kimberlites and lamproites from western Australia: an enriched mantle origin. *Nature*, **302**, 400–403.

McDonald, G. D., Collerson, K. D. & Kinny, P. D., 1997. Late Archaean and Early Proterozoic crustal evolution of the Mount Isa Block, northwest Queensland, Australia. *Geology*, **25**, 1095–1098.

Meisel, T., Walker, R. J. & Morgan, J. W., 1996. The osmium isotopic composition of the Earth's primitive upper mantle. *Nature*, **383**, 517–520.

Meisel, T., Walker, R. J., Irving, A. J. & Lorand, J.-P., 2001. Osmium isotopic compositions of mantle xenoliths: A global perspective. *Geochimica et Cosmochimica Acta*, **65**(8), 1311–1323.

Mendelssohn, M. J. & Milledge, H. J., 1995a. Geologically Significant Information from Routine Analysis of the Mid-Infrared Spectra of Diamonds. *International Geology Reviews*, **37**, 95–110.

Mendelssohn, M. J. & Milledge, H. J., 1995b. Morphological Characteristics of Diamond Populations in Relation to Temperature-Dependent Growth and Dissolution Rates. *International Geology Reviews*, **37**, 285–312.

Meyer, H. O. A. & Boyd, F. R., 1972. Composition and origin of crystalline inclusions in natural diamonds. *Geochimica et Cosmochimica Acta*, **36**, 1255–1273.

Mickus, K. L. & Keller, G. R., 1992. Lithospheric structure of the south-central United States. *Geology*, **20**, 335–338.

Mitchell, R. H., 1995. *Kimberlites, Orangeites, and Related Rocks*, Plenum Press, New York.

Mitchell, R. H., 2006. Potassic Magmas Derived from Metasomatized Lithospheric Mantle: Nomenclature and Relevance to Exploration for Diamond-bearing Rocks. *Journal of the Geological Society of India*, **67**(3), 317–327.

Mitchell, R. H. & Bergman, S. C., 1991. *Petrology of Lamproites*, Plenum Press, New York.

Mitchell, R. H. & Keays, R. R., 1981. Adundance and distribution of gold, palladium, and iridium in some spinel and garnet lherzolites: Implications for the nature and origin of precious metal-rich intergranular components in the upper mantle. *Geochimica et Cosmochimica Acta*, **45**, 2425–2442.

Mohammed, K., Davies, G. & Collins, A. T., 1982. Uniaxial stress measurements on optical transitions in yellow-luminescing brown diamonds. *Journal of Physics C: Solid State Physics*, **15**, 2789–2800.

Moore, M. & Lang, A. R., 1972. On the internal structure of natural diamonds of cubic habit. *Philosophical Magazine*, **26**, 1313–1325.

Moore, M. & Lang, A. R., 1975. Growth and dissolution features on diamond octahedron faces; Studies by X-ray topography, cathodoluminescence and optical micrography. *Acta Crystallographica A*, **31**, S213.

Morgan, J. W., Wandless, G. A., Petrie, R. K. & Irving, A. J., 1981. Composition of the Earth's upper mantle - I. Siderophile trace elements in upper mantle nodules. *Tectonophysics*, **75**, 47–67.

Myers, J. S., 1990. Precambrian tectonic evolution of part of Gondwana, southwestern Australia. *Geology*, **18**, 537–540.

Myers, J. S., 1993. Precambrian history of the West Australian Craton and adjacent orogens. *Annual Review of Earth and Planetary Science Letters*, **21**, 453–485.

Myers, J. S., Shaw, R. D. & Tyler, I. M., 1996. Tectonic evolution of Proterozoic Australia. *Tectonics*, **15**, 1431–1446.

Navon, O., 1999. Diamond Formation in the Earth's Mantle. In: *Volume 2, Proceedings of the 7th International Kimberlite Conference, Cape Town, 1998*, (eds Gurney, J., Gurney, J., Pascoe, M. & Richardson, S.), pp. 584–604. Red Roof Design, Cape Town.

Nelson, D. R., 1995. Compilation of SHRIMP U-Pb zircon geochronology data, 1994. *Western Australia Geological Survey*, **Record 1995/3**, 244pp.

Nelson, D. R., 1998. Compilation of SHRIMP U-Pb zircon geochronology data, 1997. *Western Australia Geological Survey*, **Record 1998/2**, 242pp.

Nier, A. O., 1950. A redetermination of the relative abundances of the isotopes of carbon, nitrogen, oxygen, argon and potassium. *Physical Review*, **77**, 789–793.

Nutman, A. P. & Kinny, P. D., 1994. SHRIMP zircon geochronology of the southern Gascoyne Complex and the northwest margin of the Yilgarn Craton, Western Australia. *Geological Society of Australia Abstracts 37*, 320.

Nutman, A. P., Chernyshev, I. V., Baadsgaard, H. & Smelov, A. P., 1992. The Aldan Shield of Siberia, USSR: the age of its Archaean components and evidence for widespread reworking in the mid-Proterozoic. *Precambrian Research*, **54**, 195–210.

Nyblade, A. A. & Pollack, H. N., 1993. A global analysis of heat flow from Precambrian terrains: Implications for the thermal structure of Archaean and Proterozoic lithosphere. *Journal of Geophysical Research*, **98**, 12 207 – 12 218.

Orlov, Y. L., 1973. *Mineralogy of the Diamond. Izdatel'stvo Nauka SSSR*, Translated in 1977 from Russian, John Wiley and Sons, New York.

Orlov, Y. L., 1977. *The mineralogy of diamond*, John Wiley and Sons.

Otter, M. L., 1990. *Diamonds and their mineral inclusions from the Sloan diatremes of the Colorado-Wyoming State Line Kimberlite District, North America.* PhD thesis, University of Cape Town.

Page, R. W., Griffin, T. J., Tyler, I. M. & Sheppard, S., 2001. Geochronological constraints on tectonic models for Australian Palaeoproterozoic high-K granites. *Journal of the Geological Society, London*, **158**, 535–545.

Pearson, D. G. & Shirey, S. B., 1999. Chapter 6, Isotopic Dating of Diamonds. In: *Application of Radiogenic Isotopes to Ore Research and Exploration*, (eds Lambert, D. & Ruiz, J.), Vol. 12 of *Review in Economic Geology*, pp. 143–171. Society of Economic Geologists, Littleton, Colorado.

Pearson, D. G., Shirey, S. B., Bulanova, G. P., Carlson, R. W. & Milledge, H. J., 1999. Re-Os isotope measurements of single sulfide inclusions in a Siberian diamond and its nitrogen aggregation systematics. *Geochimica et Cosmochimica Acta*, **63**(5), 703–711.

Pearson, D. G., Shirey, S. B., Carlson, R. W., Boyd, F. R., Pokhilenko, N. P. & Shimizu, N., 1995a. Re-Os, Sm-Nd, and Rb-Sr isotope evidence for thick Archaean lithospheric mantle beneath the Siberian craton modified by multistage metasomatism. *Geochimica et Cosmochimica Acta*, **59**(5), 959–977.

Pearson, D. G., Shirey, S. B., Harris, J. W. & Carlson, R. W., 1998. Sulphide inclusions in diamonds from the Koffiefontein kimberlite, S Africa: constraints on diamond ages and mantle Re-Os systematics. *Earth and Planetary Science Letters*, **160**, 311–326.

Pearson, D. G., Snyder, G. A., Shirey, S. B., Taylor, L. A., Carlson, R. W. & Sobolev, N. V., 1995b. Archaean Re-Os age for Siberian eclogites and constraints on Archaean tectonics. *Nature*, **374**, 711–713.

Phaal, C., 1965. Surface studies of diamond. *Industrial Diamond Review*, **25**, 486–489 and 591–595.

Phaal, C. & Zuidema, G., 1966. Transmission electron microscopy of synthetic diamond. *Philosophical Magazine*, **14**(127), 79–86.

Philips, D., Harris, J. W. & Kiviets, G. B., 2004. $^{40}Ar/^{39}Ar$ analyses of clinopyroxene inlcusions in African diamonds: implications for source ages of detrital diamonds. *Geochimica et Cosmochimica Acta*, **68**, 151–165.

Pidgeon, R. T., Smith, C. B. & Fanning, C. M., 1989. Kimberlite and lamproite emplacement ages in western australia. In: *Kimberlites and Related Rocks I: Their Composition, Occurrence, Origin and Emplacement. Proceedings of the 4th International Kimberlite Conference, Perth 1986. Geological Society of Australia Special Publication 14.*, (ed. Ross, J.), pp. 369–381. Blackwell Scientific Publications.

Plumb, K. A., 1979. The tectonic evolution of Australia. *Earth Science Reviews*, **14**, 205–249.

Plumb, K. A., Ahmad, M. & Wygralak, A. S., 1990. Mid-Proterozoic basins of the North Australian Craton: regional geology and mineralisation. *Australian Institute of Mining and Metallurgy Monograph*, **14**, 881–902.

Plumb, K. A., Derrick, G. M., Needham, R. S. & Shaw, R. D., 1981. The Proterozoic of northern Australia. In: *Precambrian of the Southern Hemisphere*, (ed. Hunter, D.), pp. 205–307. Elsevier, Amsterdam.

Pollack, H. N. & Chapman, D. S., 1977. On the regional variation of heat flow, geotherms and lithospheric thickness. *Tectonophysics*, **38**, 279–296.

Prider, R. T., 1960. The leucite lamproites of the Fitzroy Basin, Western Australia. *Journal of the Geological Society of Australia*, **6**, 71–118.

Ramsay, R. R., Edwards, D., Taylor, W. R., Rock, N. M. S. & Griffin, B. J., 1994. Compositions of garnet and spinel from the Aries diamoniferous kimberlite pipe, central Kimberley Block, Western Australia - implications for exploration. *Journal of Geochemical Exploration*, **51**, 59–78.

Richardson, S. H., 1986. Latter-day origin of diamonds of eclogitic paragenesis. *Nature*, **322**, 623–626.

Richardson, S. H., 1990. Age and early evolution of the continental mantle. In: *Continental Mantle*, (ed. Menzies, M.), pp. 55 – 65. Clarendon Press, Oxford.

Richardson, S. H. & Harris, J. W., 1997. Antiquity of peridotitic diamonds from the Siberian craton. *Earth and Planetary Science Letters*, **151**, 271–277.

Richardson, S. H. & Shirey, S. B., 2008. Continental mantle signature of Bushveld magmas and coeval diamonds. *Nature*, **453**, 910–913.

Richardson, S. H., Gurney, J. J., Erlank, A. J. & Harris, J. W., 1984. Origin of diamonds in old enriched mantle. *Nature*, **310**, 198–202.

Richardson, S. H., Harris, J. W. & Gurney, J. J., 1993. Three generations of diamond from old continental mantle. *Nature*, **366**, 256–258.

Richardson, S. H., Harris, J. W. & Pöml, P. F., 2006. Antiquity of harzburgitic diamonds from the Venetia kimberlite, Limpopo Belt, Kaapvaal Craton. *16th Annual V.M. Goldschmidt Conference, Melbourne, Abstracts*, .

Richardson, S. H., Pöml, P. F., Shirey, S. B. & Harris, J. W., 2008. Age and origin of peridotitic diamonds from Venetia, Limpopo Belt, Kaapvaal-Zimbabwe Craton. *9th International Kimberlite Conference Extended Abstracts*, **9IKC-A-00023**.

Richardson, S. H., Shirey, S. B. & Harris, J. W., 2004. Episodic diamond genesis at Jwaneng, Botswana, and implications for Kaapvaal craton evolution. *Lithos*, **77**, 143–154.

Richardson, S. H., Shirey, S. B., Harris, J. W. & Carlson, R. W., 2001. Archean subduction recorded by Re-Os isotopes in eclogitic sulfide inclusions in Kimberley diamonds. *Earth and Planetary Science Letters*, **191**, 257–266.

Robertson, R., Fox, J. J. & Martin, A. E., 1934. Two types of diamonds. *Philosophical Transactions of the Royal Society*, **A232**(719), 463–535.

Robinson, D. N., 1979. *Surface textures and other features of diamonds.* PhD thesis, University of Cape Town.

Robinson, D. N., Scott, J. A., van Niekerk, A. & Anderson, V. G., 1989. The sequence of events reflected in the diamonds of some southern African kimberlites, *Kimberlites and Related Rocks II: Their Mantle/Crust Setting, Diamonds and Diamond Exploration. Proceedings of the 4th International Kimberlite Conference, Perth 1986.*, Vol. 14, pp. 990–1000. Geological Society of Australia Special Publication.

Roy-Barman, M. & Allègre, C. J., 1994. $^{187}Os/^{186}Os$ ratio of mid-ocean ridge basalts and abyssal peridotites. *Geochimica et Cosmochimica Acta*, **58**(22), 5043–5054.

Rudnick, R. L. & Nyblade, A. A., 1999. The thickness and heat production of Archaean lithosphere: constraints from xenolith thermobarometry and surface heat flow. In: *Mantle Petrology: Field Observations and High Pressure Experimentation: a Tribute to Francis R. (Joe) Boyd*, (eds Fei, Y., Bertka, C. & Mysen, B.), Vol. 6, pp. 3–12. The Geochemical Society, Houston.

Rudnick, R. L., McDonough, W. F. & O'Connell, R. H., 1998. Thermal structure, thickness and composition of continental lithosphere. *Chemical Geology*, **145**, 395–411.

Sambridge, M. & Lambert, D. D., 1997. Propagating errors in decay equations: Examples from the Re-Os isotopic system. *Geochimica et Cosmochimica Acta*, **61**(4), 3019–3024.

Schmitz, M. D., 2002. *Geological and Thermochronological Evolution of the Lower Crust of Southern Africa.* PhD thesis, Massachusetts Institute of Technology.

Schmitz, M. D., Bowring, S. A., de Wit, M. J. & Gartz, V., 2004. Subduction and terrane collisions stabilize the western Kaapvaal craton tectosphere 2.9 billion years ago. *Earth and Planetary Science Letters*, **222**, 363–376.

Seal, M., 1963. The growth history of natural diamonds as revealed by etching experiments, *Proceedings of the 1st International Conference of Diamonds in Industry, Paris, 1962*, pp. 361–376. Industrial Diamond Information Bureau, London.

Seal, M., 1965. Structure in diamonds as revealed by etching. *American Mineralogist*, **50**, 105–123.

Seal, M. & Wasmund, H., 1969. Monochromatic ultraviolet microscopy of diamonds. *Diamond Research 1969. Supplement to Industrial Diamond Reviews*, pp. 29–33.

Sheppard, S., Griffin, T. J. & Tyler, I. M., 1997. The tectonic setting of granites in the Halls Creek and King Leopold Orogens, Northwest Australia. *Australian Geological Survey Organisation*, **Record 1997/44**, 107–109.

Shirey, S. B. & Walker, R. J., 1995. Carius tube digestions for low-blank rhenium-osmium analysis. *Analytical Chemistry*, **67**, 2136–2141.

Shirey, S. B. & Walker, R. J., 1998. The Re-Os Isotope System in Cosmochemistry and High-Temperature Geochemistry. *Annual Reviews of Earth and Planetary Science Letters*, **26**, 423–500.

Shirey, S. B., Harris, J. W., Richardson, S. H., Fouch, M. J., James, D. E., Cartigny, P., Deines, P. & Viljoen, F., 2002. Diamond Genesis, Seismic Structure, and Evolution of the Kaapvaal-Zimbabwe Craton. *Science*, **297**, 1683–1686.

Shirey, S. B., Harris, J. W., Richardson, S. H., Fouch, M. J., James, D. E., Cartigny, P., Deines, P. & Viljoen, F., 2003. Regional patterns in the paragenesis and age of inclusions in diamond, diamond composition, and the lithospheric seismic structure of Southern Africa. *Lithos*, **71**, 243–258.

Shirey, S. B., Pearson, D. G., Richardson, S. H., Harris, J. W. & Carlson, R. W., 2000. Application of the Re-Os microchemistry to sulfide inclusions in diamond and implications for Archean craton evolution. *Eos Transactions of the American Geophysical Union*, **81**, S428.

Shirey, S. B., Richardson, S. H. & Harris, J. W., 2004. Integrated models of diamond formation and craton evolution. *Lithos*, **77**, 923–944.

Skinner, E. M. W., Smith, C. B., Bristow, J. W., Scott-Smith, B. H. & Dawson, J. B., 1985. Proterozoic kimberlites and lamproites and a preliminary age for the Argyle Lamproite Pipe, Western Australia. *Transactions of the Geological Society of South Africa*, **88**, 335–340.

Smith, C. B. & Lorenz, V., 1989. Volcanology of the Ellendale lamproite pipes, Western Australia. In: *Kimberlites and Related Rocks I: Their Composition, Occurrence, Origin and Emplacement. Proceedings of the 4th International Kimberlite Conference, Perth 1986. Geological Society of Australia Special Publication 14.*, (ed. Ross, J.), pp. 505–519. Blackwell Scientific Publications.

Smith, C. B., Lucas, H., Hall, A. E. & Ramsay, R. R., 1994. Diamond prospectivity and indicator mineral chemistry: a Western Australian perspective. In: *Diamonds: Characterization, Genesis and Exploration. Proceedings of the 5th International Kimberlite Conference, Brazil, 1991*, (eds Meyer, H. & Leonardos, O.), pp. 313–318. Brazil Companhia de Pesquisa de Recursos Minerais.

Smith, C. B., Pearson, D., Bulanova, G. P., Beard, A. D., Carlson, R. W., Sims, K., Chimuka, L. & Muchemwa, E., 2008. Extremely depleted lithospheric mantle and diamonds beneath the southern Zimbabwe Craton. *9th International Kimberlite Conference Extended Abstracts*, **9IKC-A-00195**.

Smoliar, M. I., Walker, R. J. & Morgan, J. W., 1996. Re-Os ages of Group IIA, IIIA, IVA and IVB iron meteorites. *Science*, **271**, 1099–1102.

Sobolev, E. V., Lenskaya, S. V. & Lisoivan, V. I., 1968. The relation between the "spike" extra reflections in the Laue patterns of natural diamonds and their optical properties. *Soviet Physics-Doklady*, **12**, 665–668.

Sobolev, N. V., Galimov, E. M., Smith, C. B., Maltsev, K. A., Yefimova, E. S., Hall, A. E. & Usova, L. V., 1989. A Comparitive Study of the Morphology, Inclusions and Carbon Isotopic Composition of Diamonds from alluvials of the King George River and Argyle Lamproite Mine (Western Australia), and of Cube Microdiamonds from Northern (in Russian, translated by Linette Reynolds). *Geologiya i Geofizika*, **12**, 3–19.

Spetsius, Z. V., Belousova, E. A., Griffin, W. L., O'Reilly, S. Y. & Pearson, N. J., 2002. Archean sulfide inclusions in Paleozoic zircon megacrysts from the Mir kimberlite, Yakutia: implications for the dating of diamonds. *Earth and Planetary Science Letters*, **199**, 111–126.

Stachel, T. & Harris, J. W., 2008. The origin of cratonic diamonds - constraints from mineral inclusions. *Ore Geology Reviews*, **34**(1-2), 5–32.

Stachel, T., Lorenz, V., Smith, C. B. & Jaques, A. L., 1991. Evolution of Four Individual Lamproite Pipes, Ellendale Volcanic Field (Western Australia), *Kimberlites, Related Rocks and Mantle Xenoliths. Proceedings of the 5th International Kimberlite Conference, Brazil, 1991*, pp. 177–194. Brazil Companhia de Pesquisa de Recursos Minerais.

Sun, S. S., Jaques, A. L. & McCulloch, M. T., 1986. Isotopic evolution of the Kimberley block, Western Australia. *4th International Kimberlite Conference, Extended Abstracts*, pp. 346–348.

Sunagawa, I., 1984a. Morphology of natural and synthetic diamond crystals. In: *Materials Science of the Earth's Interior*, (ed. Sunagawa, I.), pp. 303–330. Terra Scientific, Tokyo.

Sunagawa, I., 1984b. Growth of crystals in nature. In: *Materials Science of the Earth's Interior*, (ed. Sunagawa, I.), pp. 63–105. Terra Scientific, Tokyo.

Sutherland, G. B. B. M., Blackwell, D. E. & Simeral, W. G., 1954. The problem of the two types of diamond. *Nature*, **174**, 901–904.

Suzuki, S. & Lang, A. R., 1976a. Internal structures of natural diamonds revealing mixed growth habit. *Diamond Research 1976. Supplement to Industrial Diamond Review, London*, pp. 39–47.

Suzuki, S. & Lang, A. R., 1976b. Occurrences of facetted re-entrants on rounded growth surfaces of natural diamonds. *Journal of Crystal Growth*, **34**, 29–37.

Sykes, L. R., 1978. Intraplate seismicity, reactivation of preexisting zones of weakness, alkaline magmatism, and other tectonism post-dating continental fragmentation. *Reviews of Geophysics and Space Physics*, **16**, 621–688.

Takagi, M. & Lang, A., 1964. X-ray Bragg reflexion, "spike" reflexion and ultra-violet absorption topography of diamonds. *Proceedings of the Royal Society of London, Ser A*, **281**, 310–322.

Taylor, W. R., Canil, D. & Milledge, H. J., 1996. Kinetics of Ib to IaA nitrogen aggregation in diamond. *Geochimica et Cosmochimica Acta*, **60**(23), 4725–4733.

Taylor, W. R., Jaques, A. L. & Ridd, M., 1990. Nitrogen-defect aggregation characteristics of some Australasian diamonds: Time-temperature constraints on the source regions of pipe and alluvial diamonds. *American Mineralogist*, **75**, 1290–1310.

Taylor, W., Richardson, M. & Bennett, V., 2000. Geochemistry of mantle xenoliths and xenocrysts from the Skerring kimberlite, Western Australia - evidence for a $\sim$ 800 Ma lithosphere refertilisation event. *Geological Society of Australia, Abstracts No. 59. 15th Australian Geological Convention, Sydney, July 2000*, .

Thom, J., 1975. Remaining Precambrian areas - Kimberley Region. *Geological Survey of Western Australia*, **Memoir 2**, 160–193.

Tolansky, S., 1965. Optical studies on diamond. In: *Physical Properties of Diamond*, (ed. Berman, R.), pp. 135–173. Clarendon Press, Oxford.

Turchenko, S., 1993. The Anabar Shield. In: *Precambrian Geology of the USSR*, (eds Rundqvist, D. & Mitrofanov, F.). Elsevier.

Tyler, I. & Griffin, T., 1990. Structural development of the King Leopold Orogen, Kimberley region, Western Australia. *Journal of Structural Geology*, **12**(5/6), 703–714.

Tyler, I. & Page, R., 1996. Palaeoproterozoic deformation, metamorphism and igneous intrusion in the central zone of the Lamboo Complex, Halls Creek Orogen. *Geological Society of Australia Abstracts*, **41**, 450.

Tyler, I., Page, R. & Griffin, T., 1999. Depositional age and provenance of the Marboo Formation from SHRIMP U-Pb zircon geochronology: implications for the early Palaeoproterozoic tectonic evolution of the Kimberley region, Western Australia. *Precambrian Research*, **95**, 225–243.

Urusovskaya, A. & Orlov, Y., 1964. Nature of plastic deformation of diamond crystals. *Doklady Akademii Nauk SSSR*, **154**, 1099.

van der Hilst, R., Kennett, B. & Shibatani, T., 1998. Upper mantle structure beneath Australia from portable array deplotment. In: *Structure and Evolution of the Australian Continent*, (eds Doolet, J., Goleby, J., van der Hilst, B. & Klootwijk, R.), pp. 39–57. American Geophysical Union, Washington, D.C.

van Heerden, L. A. & Gurney, J. J., 1995. The carbon isotopic composition of harzburgitic, lherzolitic, websteritic and eclogitic paragenesis diamonds from southern Africa: a comparison of genetic models. *South African Journal of Geology*, **98**(2), 119–125.

van Heerden, L. A., Boyd, S. R., Milledge, H. J. & Pillinger, C. T., 1995. The Carbon-and Nitrogen-Isotope Characteristics of the Argyle and Ellendale Diamonds, Western Australia. *International Geology Reviews*, **37**, 39–50.

Viljoen, K., 2002. An infrared investigation of inclusion-bearing diamonds from the Venetia kimberlite, Northern Province, South Africa: implications for diamonds from craton-margin settings. *Contributions to Mineralogy and Petrology*, **144**, 98–108.

Viljoen, K., Dobbe, R., Smit, B., Thomassot, E. & Cartigny, P., 2004. Petrology and geochemistry of a diamondiferous lherzolite from the Premier diamond mine, South Africa. *Lithos*, **77**, 539–552.

Völkening, J., Walczyk, T. & Heumann, K., 1991. Osmium isotope ratio determinations by negative thermal ionization mass spectrometry. *International Journal of Mass Spectrometry and Ion Processes*, **105**, 147–159.

Wade, A. & Prider, R., 1940. The leucite-bearing rocks of the West Kimberley area, Western Australia. *Mineralogical Magazine*, **25**, 373–383.

Walker, J., 1979. Optical absorption and luminescence in diamond. *Progress in Physics*, **42**, 1605–1659.

Walker, R., Carlson, R., Shirey, S. & Boyd, F., 1989. Os, Sr, Nd, and Pb isotope systematics of southern African peridotite xenoliths and implications for the chemical evolution of the subcontinental mantle. *Geochimica et Cosmochimica Acta*, **53**, 1583–1595.

Walker, R., Morgan, J., Smoliar, M., Beary, E. & Czamanske, G., 1997. Applications of the ^{190}Pt-^{186}Os isotope system to geochemistry and cosmochemistry. *Geochimica et Cosmochimica Acta*, **61**, 4799–4808.

Wellman, P., 1973. Early Miocene potassium-argon age for the Fitzroy lamproites of Western Australia. *Journal of the Geological Society of Australia*, **19**, 471–474.

Wellman, P., 1978. Gravity evidence for abrupt changes in mean crustal density at the junction of Australian crustal blocks. *BMR Journal of Australian Geology and Geophysics*, **3**, 153–162.

Westerlund, K., Shirey, S., Richardson, S., Carlson, R., Gurney, J. & Harris, J., 2006. A subduction wedge origin for Paleoarchean peridotitic diamonds and harzburgites from the Panda kimberlite, Slave craton: evidence from Re-Os isotope systematics. *Contributions to Mineralogy and Petrology*, **152**, 275–294.

White, S., de Boorder, H. & Smith, C., 1995. Structural controls of kimberlite and lamproite emplacement. *Journal of Geochemical Exploration*, **53**, 245–264.

White, S. H. & Muir, M. D., 1989. Multiple reactivation of coupled orthogonal fault systems: An example from the Kimberley region in north Western Australia. *Geology*, **17**, 618–621.

Wild, R., Evans, T. & Lang, A., 1967. Birefringence, X-ray topography and electron microscopic examination of the plastic deformation of diamond. *Philosophical Magazine*, **15**, 267–279.

Wilks, E. & Wilks, J., 1991. *Properties and Application of Diamond*, Butterworth-Heinemann Ltd.

Woods, G., 1986. Platelets and the infrared absorption of type Ia diamonds. *Proceedings of the Royal Society*, **A407**, 219–238.

Woods, G. & Collins, A., 1983. Infrared absorption spectra of hydrogen complexes in type I diamonds. *Journal of Physics and Chemistry of Solids*, **44**(5), 353–478.

Wyatt, B., Sumpton, J., Stiefenhofer, J., Shee, S. & Smith, T., 1999. Kimberlites in the Forrest River Area, Kimberley region, Western Australia. In: *Volume 2, Proceedings of the 7th International Kimberlite Conference, Cape Town, 1998*, (eds Gurney, J., Gurney, J., Pascoe, M. & Richardson, S.), pp. 912 – 922. Red Roof Design, Cape Town.

Wyllie, P., 1979. Magmas and volatile components. *American Mineralogist*, **64**, 469–500.

Yefimova, E., Sobolev, N. & Pospelova, L., 1983. Sulfide inclusions in diamond and specific features of their paragenesis. *Zap. Vses. Mineral. Ova.*, **112**, 300–310.

Appendix 1: Fourier Transform Infrared Analyses

Sample	Analysis	A (1282)	B (1282)	D (1282)	fit (1344)	IaA (ppm)	IaB (ppm)	N total (ppm)	%N as IaB	Platelet Peak Position	Platelet Peak Area	H Peak Position	H Peak Area	Temp in °C
EL01	1	20.31	5.47	1.68	1.47	335	435	770	56.46	1365.38	191.12	3105.80	2.30	1150
EL01	2	20.14	5.25	1.68	1.43	332	417	749	55.65	1365.38	191.41	3106.80	3.10	1150
EL01	3	19.86	4.99	1.52	1.36	328	396	724	54.72	1365.38	179.40	3106.80	2.70	1150
EL01	4	19.49	4.71	1.38	1.28	322	374	695	53.75	1365.38	172.50	3106.80	2.30	1150
EL01	5	19.70	4.28	1.38	1.22	325	340	665	51.13	1365.38	161.72	3106.80	2.60	1149
EL01	6	18.22	3.23	1.10	0.98	301	256	557	46.03	1364.41	127.15	3106.80	1.40	1148
EL05	1	13.18	7.37	2.41	1.79	217	585	803	72.91	1365.38	247.49	3106.80	1.60	1168
EL05	2	14.34	8.60	2.72	2.05	237	683	920	74.27	1365.38	293.82	3106.80	1.20	1166
EL05	3	14.70	9.57	3.05	2.27	243	760	1003	75.80	1365.38	314.53	3106.80	1.30	1166
EL05	4	14.84	9.68	3.07	2.29	245	768	1013	75.83	1365.38	316.79	3106.80	1.10	1166
EL05	5	14.82	9.65	3.09	2.29	245	766	1011	75.80	1365.38	326.69	3106.80	1.20	1166
EL05	6	14.70	9.25	2.94	2.20	242	735	977	75.19	1365.38	311.11	3106.80	1.70	1166
EL10	1	3.35	0.11	0.05	0.08	55	9	64	14.07	1360.56	2.45	0.00	0.00	1161
EL10	2	7.26	0.81	0.29	0.29	120	64	184	34.97	1361.52	35.68	3108.70	0.10	1164
EL10	3	8.03	0.91	0.36	0.33	132	72	205	35.26	1361.52	41.49	0.00	0.00	1162
EL10	4	7.01	0.62	0.20	0.24	116	49	165	29.80	1361.52	22.84	0.00	0.00	1161
EL12	1b	21.21	8.12	5.00	2.52	350	644	994	64.80	1368.27	263.31	3105.80	1.60	1153
EL12	2b	26.46	9.45	5.12	2.83	437	751	1187	63.22	1369.23	309.65	3106.80	1.90	1147
EL12	3b	25.00	9.28	5.22	2.80	412	736	1149	64.10	1369.23	311.08	3105.80	1.50	1148
EL12	4b	25.02	6.27	2.72	1.86	413	498	911	54.68	1368.27	215.20	3106.80	2.30	1145
EL12	5b	19.46	10.68	7.84	3.43	321	848	1169	72.55	1369.23	368.54	3107.80	2.00	1158
EL12	2	34.36	8.56	2.86	2.38	567	680	1247	54.52	1369.23	295.67	3106.80	1.90	1137
EL12	4	22.10	7.73	4.51	2.38	365	613	978	62.72	1368.27	259.01	3105.80	1.60	1151

Sample	Analysis	A (1282)	B (1282)	D (1282)	fit (1344)	IaA (ppm)	IaB (ppm)	N total (ppm)	%N as IaB	Platelet Peak Position	Platelet Peak Area	H Peak Position	H Peak Area	Temp in °C
EL12	5	22.86	7.04	3.97	2.18	377	559	936	59.72	1368.27	230.34	3106.80	1.80	1149
EL12	6	20.16	7.91	5.37	2.54	333	628	960	65.36	1368.27	263.99	3106.80	1.70	1154
EL12	7	23.36	8.04	4.59	2.46	386	638	1024	62.34	1368.27	265.05	3106.80	1.90	1149
EL12	8	21.36	9.58	6.32	3.00	353	761	1113	68.33	1369.23	324.65	3106.80	2.00	1154
EL12	9	21.91	8.43	5.31	2.64	361	669	1031	64.93	1368.27	284.72	3106.80	1.60	1152
EL12	10	23.13	7.47	4.33	2.32	382	593	975	60.85	1367.31	245.54	3106.80	1.30	1149
EL12	11	22.41	7.61	4.60	2.38	370	604	974	62.05	1368.27	253.56	3106.80	1.20	1150
EL16	1	13.95	4.50	1.63	1.21	230	357	587	60.81	1365.38	159.95	3106.80	2.00	1162
EL16	2	0.00	0.00	0.00	0.00	0	0	0	0.00	0.00	0.00	0.00	0.00	-
EL16	3	0.00	0.00	0.00	0.00	0	0	0	0.00	0.00	0.00	0.00	0.00	-
EL16	4	4.34	0.42	0.05	0.14	72	33	105	31.80	1360.56	11.05	3105.80	0.60	1175
EL16	5	6.33	1.11	0.01	0.27	104	88	193	45.81	1361.52	32.62	3105.80	1.00	1175
EL16	6	11.56	3.50	1.05	0.91	191	278	469	59.32	1365.38	122.67	3106.80	3.50	1166
EL16	7	5.89	1.19	0.39	0.35	97	94	192	49.29	1363.45	46.71	3105.80	1.00	1178
EL20	1b	26.29	5.41	3.75	1.95	434	429	863	49.74	1367.31	159.21	3106.80	3.60	1141
EL20	2	33.22	4.17	1.09	1.35	548	331	879	37.64	1366.34	148.52	3106.80	4.60	1128
EL20	3	36.31	5.34	0.90	1.54	599	424	1023	41.45	1366.34	199.77	3106.80	3.80	1129
EL20	5	33.45	4.96	1.34	1.52	552	394	945	41.63	1366.34	175.14	3106.80	4.40	1131
EL20	6	34.16	4.42	1.19	1.43	564	351	915	38.37	1366.34	158.83	3106.80	4.60	1128
EL20	6b	26.43	5.74	3.85	2.02	436	456	892	51.12	1368.27	158.81	3105.80	5.00	1141
EL23	1	25.23	2.82	0.92	0.99	416	224	640	34.96	1365.38	105.00	3106.80	4.90	1133
EL23	2	32.23	5.62	1.77	1.69	532	446	978	45.62	1368.27	201.42	3106.80	5.50	1134
EL23	3	30.30	5.58	1.65	1.63	500	443	943	46.98	1366.34	201.99	3106.80	6.60	1136
EL23	4	29.06	6.02	2.04	1.75	480	478	957	49.92	1366.34	210.18	3106.80	7.20	1139
EL23	5	32.00	5.57	1.54	1.64	528	442	971	45.59	1367.31	201.35	3106.80	4.80	1134

Sample	Analysis	A (1282)	B (1282)	D (1282)	fit (1344)	IaA (ppm)	IaB (ppm)	N total (ppm)	%N as IaB	Platelet Peak Position	Platelet Peak Area	H Peak Position	H Peak Area	Temp in °C
EL23	6	31.60	5.30	1.72	1.62	521	420	942	44.64	1367.31	190.84	3106.80	3.30	1134
EL23	7	27.82	5.00	1.84	1.54	459	397	856	46.40	1366.34	180.27	3106.80	5.30	1138
EL23	8	27.84	4.79	1.53	1.45	459	380	840	45.30	1366.34	177.62	3106.80	4.80	1137
EL23	9	32.83	5.46	1.69	1.66	542	434	976	44.47	1368.27	200.22	3106.80	5.60	1133
EL23	10	26.01	3.72	1.21	1.20	429	296	725	40.79	1365.38	130.04	3106.80	3.90	1136
EL24	1b	42.70	3.18	2.69	1.66	704	252	957	26.38	1370.20	82.63	3105.80	2.00	1114
EL24	5b	40.22	3.09	1.97	1.47	664	245	909	26.96	1368.27	103.42	3105.80	1.00	1116
EL25	1	52.21	6.55	0.92	1.98	862	520	1382	37.65	1374.05	143.18	3105.80	121.20	1118
EL25	2	49.40	7.33	1.64	2.19	815	582	1397	41.65	1374.05	146.10	3105.80	131.40	1121
EL25	3	50.58	7.12	1.73	2.19	835	565	1400	40.38	1374.05	155.70	3105.80	125.00	1120
EL25	4	48.66	7.67	2.02	2.30	803	609	1412	43.12	1374.05	140.23	3105.80	131.70	1123
EL25	6	45.35	8.25	2.35	2.40	748	655	1403	46.67	1374.05	141.94	3105.80	132.70	1126
EL26	1	23.24	3.40	1.29	1.12	383	270	653	41.28	1365.38	127.75	3106.80	2.90	1139
EL26	2	20.70	3.48	1.24	1.09	342	276	618	44.72	1365.38	128.37	3106.80	2.60	1144
EL26	3	13.58	1.88	0.67	0.62	224	150	374	40.04	1363.45	70.42	3106.80	1.60	1152
EL26	4	14.52	4.92	1.71	1.30	240	391	630	61.97	1365.38	177.53	3106.80	1.90	1161
EL26	5	17.99	7.67	2.74	1.97	297	609	906	67.25	1365.38	264.28	3106.80	2.50	1158
EL26	6	13.93	3.06	0.99	0.87	230	243	473	51.42	1363.45	106.99	3106.80	4.00	1158
EL26	7	20.98	2.58	0.82	0.87	346	205	551	37.18	1365.38	87.75	3106.80	6.90	1139
EL26	8	30.49	4.00	1.68	1.40	503	317	820	38.68	1366.34	132.48	3105.80	5.00	1131
EL31	1	32.63	4.55	1.81	1.54	538	361	899	40.13	1366.34	167.19	3106.80	2.90	1130
EL31	2	14.29	1.54	0.58	0.57	236	122	358	34.09	1365.38	62.30	3105.80	0.10	1147
EL31	3	26.98	3.91	1.67	1.33	445	311	756	41.11	1365.38	143.74	3105.80	0.40	1136
EL31	4	31.88	4.42	1.35	1.42	526	351	877	40.01	1365.38	161.26	3106.80	2.00	1131
EL31	5b	12.54	10.28	8.19	3.33	207	816	1023	79.77	1369.23	295.78	3106.80	6.20	1171

Sample	Analysis	A (1282)	B (1282)	D (1282)	fit (1344)	IaA (ppm)	IaB (ppm)	N total (ppm)	%N as IaB	Platelet Peak Position	Platelet Peak Area	H Peak Position	H Peak Area	Temp in °C
EL31	6b	10.55	11.62	9.11	3.68	174	923	1097	84.13	1370.20	360.26	3106.80	2.80	1177
EL31	7	28.30	4.70	1.84	1.50	467	373	840	44.42	1365.38	169.86	3105.80	0.70	1136
EL31	8	35.46	5.46	1.94	1.75	585	434	1019	42.58	1365.38	201.80	3106.80	0.50	1130
EL31	9	31.03	5.96	2.84	1.93	512	473	985	48.01	1365.38	206.60	3105.80	1.40	1136
EL31	10	31.97	4.97	1.85	1.60	527	395	922	42.82	1365.38	185.69	3106.80	0.70	1133
EL31	11	33.06	5.62	2.08	1.76	546	447	992	45.01	1365.38	208.86	3106.80	0.60	1133
EL32	2	26.57	9.59	3.13	2.47	438	761	1200	63.46	1366.34	328.78	3106.80	2.80	1147
EL32	3	20.12	5.80	2.02	1.58	332	461	793	58.13	1365.38	213.51	3105.80	4.70	1151
EL32	4	16.33	4.36	1.51	1.20	269	346	615	56.22	1363.45	156.63	3106.80	5.40	1156
EL32	5	16.15	4.10	1.38	1.14	266	326	592	55.00	1362.48	148.63	3106.80	9.70	1156
EL32	8	28.48	8.81	2.92	2.34	470	699	1169	59.81	1366.34	318.82	3106.80	5.60	1144
EL32	9	23.13	7.27	2.50	1.94	382	577	959	60.18	1365.38	266.29	3106.80	3.80	1149
EL32	10	20.11	5.77	1.95	1.56	332	458	790	58.01	1365.38	212.50	3106.80	6.60	1151
EL32	11	17.57	4.27	1.45	1.20	290	339	629	53.91	1363.45	154.71	3106.80	9.20	1153
EL32	12	13.96	3.76	1.52	1.08	230	299	529	56.46	1364.41	129.60	3106.80	9.10	1160
EL33	1	21.71	5.60	2.34	1.63	358	444	803	55.36	1371.16	165.00	3105.80	40.60	1148
EL33	2	24.70	5.70	1.73	1.58	408	453	860	52.61	1375.98	80.30	3105.80	78.90	1144
EL33	3	23.21	8.05	3.16	2.19	383	640	1022	62.55	1372.13	112.69	3106.80	133.00	1150
EL33	4	16.14	5.97	4.30	1.98	266	474	740	64.03	1367.31	165.55	3105.80	10.70	1159
EL33	5	24.44	6.75	2.50	1.88	403	536	939	57.06	1373.09	108.42	3105.80	91.80	1146
EL33	6	23.28	5.64	2.25	1.65	384	448	832	53.82	1373.09	143.54	3105.80	51.30	1146
EL33	7	21.89	6.58	3.02	1.92	361	522	883	59.12	1368.27	233.74	3106.80	13.80	1150
EL33	8	21.03	5.51	2.40	1.62	347	438	785	55.78	1368.27	203.86	3105.80	16.00	1149
EL33	9	23.21	5.71	2.22	1.65	383	453	836	54.20	1370.20	168.20	3105.80	48.60	1146
EL33	10	24.89	6.56	2.45	1.85	411	521	932	55.92	1374.05	93.78	3105.80	93.40	1145

Sample	Analysis	A (1282)	B (1282)	D (1282)	fit (1344)	IaA (ppm)	IaB (ppm)	N total (ppm)	%N as IaB	Platelet Peak Position	Platelet Peak Area	H Peak Position	H Peak Area	Temp in °C
EL33	11	24.30	6.67	2.33	1.83	401	529	930	56.91	1374.05	81.96	3105.80	109.40	1146
EL33	12	24.99	6.33	2.11	1.75	412	503	915	54.93	1374.05	88.90	3105.80	97.40	1145
EL33	13	23.59	6.26	2.58	1.81	389	497	886	56.07	1370.20	183.40	3105.80	51.30	1147
EL34	1b	12.46	9.07	7.19	2.95	206	720	926	77.79	1371.16	285.83	3105.80	1.30	1171
EL34	6b	13.13	11.06	10.13	3.83	217	878	1095	80.22	1373.09	365.79	3106.80	7.10	1170
EL34	6c	13.32	11.01	9.35	3.67	220	874	1094	79.91	1373.09	357.13	3105.80	6.80	1170
EL34	11b	16.36	9.41	7.49	3.12	270	747	1017	73.46	1371.16	310.67	3105.80	1.40	1162
EL34	12	14.41	9.36	7.63	3.11	238	743	981	75.76	1372.13	304.99	3106.80	1.80	1166
EL34	13	12.72	10.01	7.85	3.22	210	795	1005	79.11	1373.09	339.49	3106.80	4.30	1171
EL35	1	2.09	0.45	0.13	0.13	35	36	70	50.69	1359.59	9.40	3104.90	0.20	1206
EL35	2	2.09	0.30	0.12	0.10	34	24	59	41.20	1359.59	9.37	3106.80	0.10	1201
EL35	3	2.58	0.62	0.20	0.17	43	49	92	53.53	1360.56	17.67	3106.80	0.50	1202
EL35	4	2.78	1.02	0.33	0.26	46	81	127	63.89	1360.56	34.32	3105.80	0.70	1205
EL35	5	2.79	1.03	0.29	0.25	46	81	127	63.88	1361.52	36.24	3105.80	1.00	1205
EL35	6	2.60	0.90	0.26	0.23	43	72	115	62.56	1361.52	30.66	3106.80	1.00	1206
EL35	7	2.25	0.43	0.15	0.13	37	34	71	48.03	1359.59	14.24	3107.80	0.40	1203
EL36	1	0.00	0.00	0.00	0.00	0	0	0	0.00	0.00	0.00	0.00	0.00	-
EL36	2	1.57	2.54	0.76	0.55	26	202	228	88.61	1362.48	85.28	3106.80	7.70	1229
EL36	3	2.10	3.30	0.88	0.70	35	262	296	88.33	1361.52	106.37	3105.80	9.00	1221
EL36	4	2.20	3.50	0.81	0.72	36	278	314	88.45	1361.52	99.21	3105.80	8.30	1220
EL36	5	2.27	3.62	0.86	0.75	38	287	325	88.45	1361.52	104.88	3106.80	10.00	1219
EL36	6	2.13	2.76	0.63	0.57	35	219	254	86.16	1361.52	79.10	3105.80	15.30	1220
EL36	7	1.83	4.14	1.35	0.92	30	329	359	91.58	1364.41	127.72	3106.80	20.60	1226
EL36	8	0.00	0.00	0.00	0.00	0	0	0	0.00	0.00	0.00	0.00	0.00	-
EL38	1	18.07	3.91	2.93	1.43	298	310	608	51.00	1365.38	105.80	3106.80	2.60	1151

Sample	Analysis	A (1282)	B (1282)	D (1282)	fit (1344)	IaA (ppm)	IaB (ppm)	N total (ppm)	%N as IaB	Platelet Peak Position	Platelet Peak Area	H Peak Position	H Peak Area	Temp in °C
EL38	2	20.10	2.64	1.23	0.95	332	209	541	38.70	1365.38	83.59	3106.80	2.70	1141
EL38	3	18.95	5.14	3.40	1.73	313	408	721	56.63	1366.34	152.16	3106.80	2.80	1152
EL38	5	17.33	3.51	1.99	1.18	286	279	565	49.36	1365.38	100.39	3105.80	2.80	1151
EL38	6	15.60	5.97	4.63	2.04	257	474	731	64.79	1368.27	177.44	3106.80	5.40	1161
EL38	7	16.31	6.34	4.76	2.13	269	503	772	65.16	1369.23	187.94	3105.80	3.60	1160
EL38	8	19.84	2.84	1.43	1.01	327	225	553	40.76	1365.38	85.91	3105.80	3.00	1143
EL38	9	18.43	3.31	2.37	1.24	304	263	567	46.35	1365.38	91.57	3106.80	2.40	1148
EL43	1	18.10	6.22	1.87	1.58	299	494	792	62.31	1365.38	183.91	3106.80	7.30	1156
EL43	2	17.09	5.30	1.91	1.44	282	421	703	59.89	1365.38	164.33	3106.80	6.10	1156
EL43	3	21.44	7.16	1.94	1.79	354	568	922	61.63	1365.38	223.78	3106.80	5.70	1151
EL43	4	18.05	5.46	1.71	1.44	298	434	732	59.29	1365.38	172.43	3106.80	4.20	1155
EL43	5	24.92	6.78	1.31	1.66	411	538	949	56.69	1365.38	219.19	3106.80	5.30	1145
EL43	6	22.50	6.70	1.70	1.69	371	532	903	58.90	1365.38	203.57	3106.80	4.50	1149
EL50	1	13.79	2.04	0.64	0.65	227	162	390	41.65	1362.48	72.58	3106.80	2.00	1153
EL50	2	18.36	4.45	1.45	1.24	303	353	656	53.85	1365.38	148.34	3106.80	2.10	1152
EL50	3	19.19	4.93	1.63	1.36	317	391	708	55.28	1365.38	170.62	3106.80	1.60	1151
EL50	4	12.58	1.55	0.51	0.53	208	123	331	37.25	1361.52	57.52	3106.80	1.90	1152
EL50	5	18.24	3.05	0.93	0.92	301	243	544	44.62	1364.41	106.64	3105.80	1.60	1147
EL50	6	17.61	2.97	0.98	0.91	291	236	527	44.83	1364.41	104.22	3106.80	1.70	1148
EL50	7	14.60	2.19	0.80	0.71	241	174	415	41.93	1362.48	78.56	3106.80	1.30	1151
EL50	8	17.43	3.58	1.30	1.06	288	284	572	49.71	1364.41	126.46	3106.80	1.30	1151
EL50	9	15.37	2.84	0.97	0.85	254	225	479	47.04	1362.48	98.90	3106.80	1.70	1153
EL51	1	8.61	5.62	5.26	2	142	446	588	75.86	1371.39	141.07	3107.3	7.4	1180
EL51	2	9.98	5.38	5.16	1.96	165	427	592	72.18	1372.35	118.52	3107.3	17.9	1175
EL51	3	8.4	5.82	5.38	2.05	139	462	601	76.94	1372.35	144.55	3107.3	11.4	1181

Sample	Analysis	A (1282)	B (1282)	D (1282)	fit (1344)	IaA (ppm)	IaB (ppm)	N total (ppm)	%N as IaB	Platelet Peak Position	Platelet Peak Area	H Peak Position	H Peak Area	Temp in °C
EL51	4	8.66	5.56	5.27	1.99	143	441	584	75.54	1372.35	129.07	3107.3	14.2	1179
EL51	5	10.58	5.58	5.44	2.05	175	443	617	71.73	1372.35	107.42	3107.3	16.1	1173
EL52	2	8.32	6.53	5.55	2.18	137	518	655	79.06	1368.49	225.35	3106.4	1.7	1182
EL52	3	7.94	7.49	6.18	2.45	131	595	726	81.95	1369.46	253.34	3109.2	5.8	1184
EL52	4	5.7	6.85	5.4	2.16	94	544	638	85.25	1369.46	251.15	3107.3	5.5	1194
EL52	5	5.88	6.79	5.47	2.17	97	539	636	84.75	1369.46	246.55	3107.3	15.4	1193
EL53	1	11.46	6.13	6.1	2.28	189	487	676	72.02	1372.35	104.08	3107.3	10.2	1171
EL53	2	7.15	5.52	5.13	1.93	118	438	556	78.79	1373.31	115.95	3107.3	18.4	1186
EL53	3	6.62	5.44	4.91	1.87	109	432	541	79.81	1371.39	139.95	3107.3	6.3	1188
EL53	4	6.74	5.49	4.97	1.89	111	436	547	79.67	1371.39	145.46	3107.3	4.8	1187
EL53	5	8.8	5.62	5.34	2.01	145	446	591	75.44	1372.35	121.16	3107.3	8.1	1179
EL53	6	6.86	5.86	5.34	2.02	113	465	578	80.43	1373.31	136.19	3107.3	11.7	1187
EL54	1	12.58	1.89	1.25	0.72	208	150	358	41.99	1362.71	56.47	3107.3	4	1155
EL54	2	3.32	0.73	0.2	0.2	55	58	113	51.41	1363.67	23.41	3108.3	3.8	1194
EL54	3	11.46	2.37	1.82	0.89	189	188	377	49.91	1364.63	67.15	3108.3	3.5	1162
EL54	4	6.22	2.28	1.25	0.68	103	181	284	63.79	1364.63	86.33	3108.3	5.3	1184
EL54	5	6.26	1.03	0.48	0.35	103	82	185	44.23	1363.67	40.18	3108.3	3.2	1174
EL54	6	10.16	1.44	0.78	0.53	168	115	282	40.61	1363.67	45.35	3107.3	3.6	1160
EL55	1	9.81	3.46	3.36	1.32	162	275	436	62.91	1368.49	75.75	3107.3	1.6	1172
EL55	2	9.47	3.59	3.29	1.32	156	285	441	64.60	1367.53	84.12	3107.3	5.2	1173
EL55	3	8.59	4.28	3.9	1.53	142	340	481	70.54	1365.6	115.07	3108.3	1.2	1178
EL55	4	7.74	4.29	3.46	1.44	128	341	469	72.74	1364.63	136.95	3107.3	1.7	1181
EL55	5	7.87	4.23	3.36	1.41	130	336	466	72.14	1364.63	136.94	3108.3	1.2	1181
EL55	6	8.71	4.47	4.12	1.6	144	355	499	71.17	1368.49	104.31	3107.3	2.2	1178
EL56	1	5.99	6.19	5.2	2.03	99	492	590	83.25	1373.31	149.43	3107.3	16.6	1192

Sample	Analysis	A (1282)	B (1282)	D (1282)	fit (1344)	IaA (ppm)	IaB (ppm)	N total (ppm)	%N as IaB	Platelet Peak Position	Platelet Peak Area	H Peak Position	H Peak Area	Temp in °C
EL56	2	4.56	5.66	4.42	1.78	75	449	524	85.66	1372.35	165.52	3107.3	13.2	1200
EL56	3	6.21	5.89	4.96	1.94	102	467	570	82.02	1370.42	175.89	3108.3	8.8	1190
EL56	4	4.87	5.46	4.56	1.78	80	434	514	84.38	1372.35	158.38	3107.3	14.7	1197
EL56	5	4.19	5.68	4.58	1.81	69	451	520	86.71	1373.31	162.16	3107.3	23.6	1202
EL56	6	4.57	5.93	4.86	1.9	75	471	546	86.21	1373.31	167.71	3107.3	14.3	1200
EL56	7	4.54	6.1	5.04	1.96	75	484	559	86.59	1374.28	180.24	3107.3	11.8	1200
EL57	1	9.63	4.85	4.57	1.76	159	385	544	70.77	1369.46	104.99	3107.3	0.2	1175
EL57	2	10.99	4.41	4.25	1.66	181	350	532	65.90	1369.46	86.14	3107.3	1.2	1170
EL57	3	9.9	4.49	4.28	1.66	163	356	520	68.56	1369.46	88.92	3107.3	4.1	1173
EL57	4	10.97	4.63	4.47	1.73	181	368	549	67.03	1369.46	89.66	3107.3	3.3	1170
EL57	5	9.3	4.78	4.47	1.73	153	379	533	71.21	1369.46	104.74	3107.3	0.8	1176
EL59	1	11.01	1.25	0.15	0.39	182	99	281	35.37	1362.71	40.58	3107.3	5.2	1154
EL59	2	18.09	4.51	1.63	1.28	298	358	656	54.53	1364.63	179.15	3108.3	3.7	1152
EL59	3	17.91	6.29	2.78	1.77	295	500	795	62.83	1365.6	252.07	3107.3	3.1	1156
EL59	4	20.79	9.11	4.49	2.57	343	723	1066	67.83	1366.56	369.24	3108.3	2.3	1154
EL59	5	22.03	7.03	2.91	1.96	363	558	922	60.56	1365.6	292.63	3107.3	3.1	1150
EL59	6	9.26	1.34	-0.26	0.3	153	106	259	41.01	1361.74	37.33	3107.3	4.4	1162
EL59	7	17.05	5.18	2.06	1.45	281	412	693	59.40	1365.6	197.56	3107.3	3.4	1156
EL60	1	5.4	4.77	4.17	1.61	89	378	468	80.96	1370.42	106.54	3107.3	3.9	1194
EL60	2	4.81	4.52	3.97	1.52	79	359	438	81.90	1371.39	110.54	3107.3	12.8	1197
EL60	3	4.37	4.6	3.98	1.53	72	365	437	83.51	1372.35	115.9	3107.3	15.5	1200
EL60	4	5.16	4.87	4.19	1.62	85	387	472	81.98	1372.35	104.56	3107.3	17.5	1195
EL60	5	8.14	4.92	4.08	1.66	134	391	525	74.43	1369.46	86	3107.3	3.5	1181
EL60	6	5.37	4.33	3.93	1.5	89	344	433	79.51	1370.42	108.78	3107.3	4.5	1193
EL60	7	5.96	4.62	4.17	1.59	98	367	465	78.87	1369.46	100.44	3107.3	2.7	1190

Sample	Analysis	A (1282)	B (1282)	D (1282)	fit (1344)	IaA (ppm)	IaB (ppm)	N total (ppm)	%N as IaB	Platelet Peak Position	Platelet Peak Area	H Peak Position	H Peak Area	Temp in °C
EL61	1	8.21	3.57	2.17	1.09	136	283	419	67.64	1363.67	138.73	3107.3	5.4	1178
EL61	2	6.05	4.99	3.5	1.52	100	396	496	79.88	1364.63	182.15	3107.3	2.2	1190
EL61	3	6.25	4.77	3.4	1.47	103	378	482	78.60	1364.63	178.49	3107.3	2.2	1189
EL61	4	7.18	4.26	2.87	1.31	118	338	457	74.08	1363.67	172.1	3107.3	3.1	1184
EL61	5	8.51	3.48	2.06	1.06	140	276	417	66.31	1363.67	136.11	3107.3	3.6	1177
EL62	1	11.57	6.31	6.26	2.34	191	501	692	72.41	1370.42	148.98	3107.3	1.3	1171
EL62	2	12.78	6.26	6.16	2.33	211	497	708	70.23	1371.39	144.49	3107.3	2.3	1168
EL62	3	15.75	6.99	7.03	2.65	260	555	815	68.11	1372.35	151.47	3108.3	1.3	1162
EL62	4	10.25	6.98	6.55	2.48	169	554	724	76.62	1373.31	174.06	3107.3	0.9	1175
EL62	5	15.5	6.29	6.25	2.39	256	500	755	66.16	1371.39	138.5	3108.3	1.2	1161
EL62	6	13.72	6.62	6.35	2.44	226	526	752	69.90	1371.39	142.78	3107.3	1.9	1166
EL64	1	4.25	6.59	4.34	1.9	70	523	593	88.18	1366.56	215.03	3107.3	14.1	1202
EL64	2	2.92	7.26	4.98	2.1	48	576	624	92.29	1367.53	0.42	3108.3	37.4	1214
EL64	3	2.83	6.16	4.32	1.81	47	489	536	91.30	1366.56	212.42	3107.3	54.5	1214
EL64	4	2.42	5.76	4.17	1.71	40	458	497	91.98	1366.56	204.91	3107.3	44.6	1219
EL64	5	2.44	5.79	4.17	1.72	40	460	500	91.94	1366.56	201.11	3107.3	35.1	1218
EL64	6	2.08	5.86	4.2	1.73	34	466	500	93.12	1365.6	197.61	3107.3	37.3	1223
EL65	1	4.69	0.96	0.2	0.26	77	76	154	49.62	1361.74	23.58	3107.3	4.5	1184
EL65	2	4.82	0.95	0.14	0.25	79	75	155	48.66	1361.74	19.56	3107.3	1.5	1183
EL65	3	4.27	0.67	0.15	0.2	70	53	123	42.92	1360.78	20.26	3107.3	0.8	1183
EL65	4	4.12	0.58	0.15	0.18	68	46	114	40.31	1360.78	14.88	3107.3	2.2	1182
EL65	5	2.1	0.38	0.06	0.1	35	30	65	46.56	1359.81	5.94	3107.3	1.9	1204
EL65	6	4.62	0.82	0.2	0.23	76	65	141	45.96	1361.74	22.62	3107.3	0.3	1183
EL66	1	9.41	3.96	3.24	1.37	155	314	469	66.91	1364.63	124.47	3108.3	0.5	1174
EL66	2	7.65	3.9	3.23	1.33	126	310	436	71.06	1364.63	126.63	3107.3	0.7	1181

Sample	Analysis	A (1282)	B (1282)	D (1282)	fit (1344)	IaA (ppm)	IaB (ppm)	N total (ppm)	%N as IaB	Platelet Peak Position	Platelet Peak Area	H Peak Position	H Peak Area	Temp in °C
EL67	1	2.06	4.38	1.85	1.05	34	348	382	91.11	1362.71	138.78	3108.3	15.4	1223
EL67	2	2.74	5.09	3.1	1.41	45	404	449	89.94	1362.71	158.67	3107.3	2.2	1215
EL67	3	2.7	5.05	3.04	1.39	44	401	445	90.01	1362.71	155.41	3107.3	4.2	1215
EL67	4	2.86	5.42	3.27	1.49	47	430	477	90.12	1363.67	172.42	3107.3	2.3	1213
EL67	5	2.76	5.71	3.27	1.54	46	453	499	90.87	1364.63	194.02	3107.3	5.5	1215
EL67	6	2.49	5.51	2.92	1.44	41	438	479	91.41	1365.6	193.51	3108.3	10.2	1218
EL67	7	2.74	5.83	3.42	1.58	45	463	508	91.10	1365.6	220.39	3108.3	13.7	1215
EL67	8	2.48	5.25	2.18	1.25	41	417	458	91.06	1364.63	173.84	3108.3	2.9	1218
EL69	1	8.02	4.71	3.46	1.5	132	374	506	73.87	1365.6	171.35	3107.3	9.2	1181
EL69	2	7.78	4.9	3.54	1.54	128	389	517	75.18	1365.6	185.75	3107.3	7.7	1182
EL69	3	4.69	5.89	4.37	1.81	77	468	545	85.79	1365.6	206.4	3107.3	12.8	1199
EL69	4	4.37	6.07	4.49	1.85	72	482	554	86.98	1366.56	213.7	3108.3	13.5	1201
EL69	5	4.3	5.93	4.37	1.81	71	471	542	86.92	1366.56	210.15	3107.3	14.4	1202
EL69	6	4.08	6.07	4.44	1.84	67	482	549	87.73	1366.56	202.39	3107.3	13.8	1203
EL69	7	3.92	6.24	4.53	1.88	65	495	560	88.44	1366.56	202.72	3107.3	11.8	1204
EL69	8	6.09	5.41	4	1.68	100	430	530	81.05	1365.6	187.62	3107.3	12.9	1190
EL69	9	5.15	5.71	4.23	1.76	85	453	538	84.21	1365.6	197.92	3107.3	14.9	1196

Appendix 2: Traverse Diagrams for FTIR Data

The growth zoning, as well as the across-plate variations of the nitrogen content, nitrogen aggregation, platelet peak strength and hydrogen peak strength for each diamond plate are described below. The traverse diagrams with the positions of the FTIR analyses on the CL images, and the FTIR traverses are also presented. CL images of both sides of the each diamond plate is given in Appendix 3.

EL01

The diamond shows continuous, regular octahedral growth zoning from core to rim. The growth zones are all moderately luminescent, with slight variability between adjacent growth zones. This is reflected in the nitrogen content, which stays relatively constant from core to rim, with an average around 700 ppm. % B aggregation across the plate varies between 46 and 56 %. Analyses could not be made in the core of the diamond due to the presence of inclusions and the rosette fracture system. Platelet peak area, hydrogen peak area and the aggregation state decrease with the total nitrogen content in analysis 6. This was one of the first samples to be laser cut. The cut did not go all the way through the diamond. It is very difficult to align the laser along the same line, so the diamond was cleaved and broken with some tools, resulting in the rough texture on bottom left of the front of the diamond.

EL05

The diamond is moderately luminescent and no growth zoning is visible. Whereas this could be indicative of diamond growth in very uniform conditions, it is more likely that the plate was cut with an orientation parallel to the {111} octahedral plane, and so, no growth layers are visible. This diamond has high nitrogen content, which stays relatively constant in the range 800 to 1010 ppm, with slightly higher values in the core than in the rim. %B aggregation stays constant throughout the diamond at 72 - 75 %. Hydrogen peak area increases slightly towards the rim of the diamond, showing a negative correlation to the total nitrogen content.

EL10

The diamond plate developed significant fractures during laser cutting and polishing, which made FTIR analyses tricky. The growth zones show alternating layers of luminescent and non-luminescent zones with a fairly uniform octahedral growth habit. No core is visible as it seems that the plate surface did not intersect the centre of the diamond. Due to the fractures and inclusions, a representative FTIR traverse could not be obtained across the diamond. Platelet peak area shows a positive correlation with the nitrogen content, which remains low varying between 64 and 200 ppm. The platelet peak area also shows some positive correlation with the %B aggregation, apart from in analysis 3, where it shows an inversed correlation. There is almost no hydrogen in the diamond, although hydrogen peak area increases slightly to 0.1 (not visible in the graph) in analysis 3, corresponding to the highest nitrogen content.

EL12

The diamond is dominated by regular octahedral growth layers, which are more visible from the back view of the plate. The diamond has a relatively non-luminescent, nitrogen-poor core. Some variation can be seen in the subsequent growth layers, though they are all similarly moderately luminescent. Very

luminescent growth layers, with interspersed non-luminescent portions are seen towards the bottom part of the plate. The light reflections make it difficult to fully interpret the growth, though as these layers cross-cut the octahedral growth layers of the rest of the diamond, it seems they are due to a different stage of diamond growth, after a period of resorption. Due to the high nitrogen content in this diamond (900 to 1200 ppm), the traverse is plotted on a log scale. Variations in platelet peak area show some positive correlation with across-plate variations in nitrogen content. % B aggregation (54 - 69 %) remains relatively constant throughout. Hydrogen peak area does not appear to show any correlation with either the nitrogen content or platelet peak area.

EL16

This diamond is a macle, with the twin plane visible through the centre of the plate. A large core of nitrogen-free non-luminescent diamond is visible. It looks like there was a period of resorption on the one side of this core, before subsequent growth of non-luminescent diamond. Diamond growth has an octahedral habit with alternating layers of moderately luminescent and non-luminescent diamond and a rim of moderately luminescent diamond. Nitrogen content in these layers vary between 200 and 600 ppm. Platelet peak areas and %B aggregation both increase in portions with high nitrogen content. Hydrogen peak area remains zero or low, with slight increases where nitrogen content increases. While external morphology suggests that the diamond could be an aggregate; the pointed shape of some growth layers suggests that the external morphology is rather due to an unusual growth feature.

EL20

The octahedral growth zones are only slightly visible. The diamond is predominantly moderately luminescent with some alternating zones that are less luminescent or nitrogen-poor. The growth zones become darker and less luminescent towards the rim. The light reflections in the centre of the diamond are due to the presence of the rosette fracture system. This makes the interpretation of the fine growth features of the less luminescent core quite difficult, though the complexity is probably due to the presence of the inclusions at the growth centre of the diamond. FTIR analyses of the core region could not be taken due to the fracture system. The octahedral growth layers cross-cut those of the core, suggesting a period of resorption. A faint twin plane can be viewed through the centre of the diamond where growth layers do not meet up. Across-plate nitrogen content shows slight variation between 860 and 1020 ppm. Platelet peak area shows a positive correlation with nitrogen content while hydrogen peak area shows a weakly negative correlation. %B aggregation varies from 38 to 51 %.

EL23

This diamond has a broken edge as it fragmented slightly during laser cutting of the plate. The plate shows regular octahedral growth habit with strong contrasting layers of luminescent and non-luminescent growth. The layers toward the rim are moderately luminescent. The light reflections on the back of the plate are due to the presence of cracks. A Sulphide inclusion is present in the moderately luminescent core. From the back view of the plate, a set of cracks are visible, which cause some offset along the growth layers. Nitrogen content is relatively high, in the range 840 to 980 ppm, apart from two rim analyses towards the top right of the plate (1 and 10) that have slightly lower nitrogen (640 and 724

ppm, respectively). Platelet peak area and nitrogen aggregation (34 - 50 %) show a positive correlation with total nitrogen content. Though the hydrogen peak area also decreases in analyses 1 and 10, along with the nitrogen content, they dont correlate along the entire traverse. The decrease in hydrogen peak area from analyses 4 to 6 is not reflected in the nitrogen content.

EL24

A Large portion of the diamond is characterised by dark, low-luminescent octahedral growth. Growth layers that are slightly more luminescent are visible in this portion. This growth is truncated with a sharp transition to more moderately luminescent growth, indicating more nitrogen-rich conditions. Along the rim of the diamond there are two dark low-luminescent areas, a continuation of the octahedral growth though these were truncated by resorption of the diamond. The plate was not cut through the growth centre of the diamond, but is roughly parallel to the {110} crystal plane. Some fractures and cracks on the front of the plate developed during cutting and polishing.

EL25

As with EL01, the laser cut did not go all the way through the diamond and as it is difficult to position the laser in the same position, the diamond was cleaved open resulting in a broken surface. The diamond is moderately luminescent and there are no growth layers visible. This is most likely due to the orientation of the cut – if it is cut parallel to the {111} octahedral crystal planes, no growth layering can be viewed. This sample has very high nitrogen content between 1380 and 1411 ppm and similarly high hydrogen peak areas (121 - 132), the highest average for the suite. All measured parameters stay relatively constant through the traverse, correlating with the CL image, which shows no visible growth layering.

EL26

This plate fractured during cutting, the uneven broken surface can be seen on the one side of the plate. The diamond shows complex growth structures indicating several micro growth centres in an overall octahedral habit. Very fine alternating layers of luminescent and non-luminescent diamond indicate a highly variable growth environment in the centre of the diamond. Towards the rim the growth is not as fine scale and it becomes more moderately luminescent. Light reflections on the colour CL images are due to inclusions and fractures. This diamond shows a strong variation in nitrogen content between 370 and 910 ppm. Platelet peak strength correlates strongly with the variable total nitrogen content. %B aggregation also correlates with the total nitrogen content, but not as strongly as the platelet peak. Hydrogen peaks are present, though they dont display any correlation with either the nitrogen content or the platelet peak area. Analysis 7 has the greatest hydrogen peak area but does not correspond with any of the other parameters.

EL31

At least three growth centres can be seen, with in a fairly uniform octahedral growth environment. On the front view of the plate, two areas of fine, more complex, non-luminescent growth is seen. Overall the diamond is predominantly moderately luminescent diamond, with intermittent periods of growth in higher nitrogen conditions (highly luminescent) and nitrogen-poor conditions (non-luminescent/dark layers). The diamond has variable nitrogen content between 750 to 1100ppm, with one anomalously low

analysis giving 358 ppm. Nitrogen content can be positively correlated with platelet peak area, hydrogen peak area and %B aggregation. Analyses 5 and 6, both along the rim, show the highest nitrogen content, greatest platelet peak area and highest %B aggregation. The hydrogen peak is zero to very low, with the highest hydrogen peak areas corresponding to portions with the greatest nitrogen content. The olivine inclusion in the diamond causes some light reflections in the colour CL images.

EL32

The diamond has a luminescent core with alternating layers of more luminescent and non-luminescent growth layers. There is a sharp transition to non-luminescent growth zones towards the rim, which does not correspond with the nitrogen data. The nitrogen content in these layers is so high, that the analyses 1,6 and 7 were considered off-scale and could not be quantified accurately to be included on the traverse. The centre of the diamond shows complex growth features, likely due to several growth centres around inclusions. The diamond has grown in an overall octahedral habit. Total nitrogen content and platelet peak area show a very close positive correlation, with no correlation with either the %B aggregation or the hydrogen peak area. From analyses 2 to 5 and 9 to 12, the hydrogen peak area seems to show a negative correlation with the total nitrogen. Nitrogen content is relatively high and variable with a range from 520 to 1200 ppm. Light reflections on the colour CL images are from the presence of inclusions and fractures due to breakage during cutting and polishing.

EL33

The core of the diamond is non-luminescent nitrogen-poor, which then alternates with more moderately luminescent, nitrogen-rich growth layers. These layers have a rounded shape, due to either the presence of inclusions or intermittent periods of resorption. The octahedral layering visible towards the right side of the plate cross-cuts the oscillatory zoning suggesting that there was a period of resorption before a new stage of octahedral growth. The fractures and inclusions in the diamond give rise to light reflections in the colour CL image. Nitrogen content is high, ranging between 740 and 1020 ppm, which shows a positive correlation with the hydrogen peak area, apart from analysis 7. The platelet peak area and %B aggregation dont correlate with the total nitrogen content at all. %B aggregation remains relatively constant between 54 and 64 %. The portions with the lowest nitrogen content are the non-luminescent core and two analyses which correspond with the octahedral layers towards the right which cross-cut the oscillatory zoning of the rest of the plate. The high hydrogen peak areas are the second highest in the suite.

EL34

Light reflections on the CL image due to fractures, make the growth layers very difficult to view and describe accurately. Growth layers in an octahedral habit can be seen. From the back of the plate it looks like the core has more luminescent, nitrogen-rich growth which is followed by a zone of low luminescence and then moderate luminescence towards the rim of the diamond. There are portions where the growth layers dont match up, suggestive of a twin plane. The herringbone pattern characteristic of the twin pane was largely resorbed and only seen in small portion on the surface. Nitrogen content is extremely high (> 900 ppm). Analyses 2-5 and 7-10 were could not be quantified accurately, as they were extremely high

and off-scale, as in EL32. Platelet peak area shows a positive correlation to nitrogen content. Hydrogen peak areas also correlate with nitrogen content, with analyses 6b and 6c showing the greatest hydrogen peaks and the highest nitrogen content. The diamond has a high %B aggregation (75 to 80 %), which stays relatively constant throughout. Analyses 6b and 6c are reruns in similar positions.

EL35

The diamond has several different growth centres with an overall octahedral growth habit. There are very fine alternating layers of non-luminescent and moderately to low luminescent diamond, which are interrupted by periods of resorption indicating multi-stage growth. Deformation lines in the diamond give rise to the green CL lines. Some light reflections are visible due to the presence of inclusions. This diamond has very low nitrogen contents (60 - 130 ppm). Platelet peak area, hydrogen peak area and %B aggregation all correlate positively with the nitrogen content. %B aggregation has a range between 40 and 64 %.

EL36

A Core of cubic diamond growth is visible with alternating layers of very luminescent, bright diamond and non-luminescent diamond. Resorption of this layer is visible on the front view of the plate. This is followed by octahedral growth of very luminescent diamond. Light reflections due to inclusions are present mainly in this layer. A Period of resorption was followed by regular octahedral growth zones of very low luminescence towards the rim of the diamond. Lamination lines give rise to the green CL lines. Nitrogen varies dramatically across the diamond due to the strong contrast between the luminescent and non-luminescent growth layers. The two analyses along the rim (1 and 8) both have no detectable nitrogen (Type II) while the central portions show variation between 230 and 360 ppm, probably average values of contrasting layers of no nitrogen and high nitrogen content. There is some correlation between nitrogen content and both the platelet peak area and the hydrogen peak area, though neither show a full positive correlation. Nitrogen is highly aggregated with %B aggregation between 86 to 91 %.

EL38

There are many light reflections from inclusions and cracks in the diamond which make it difficult to view the growth layers. The front view of the diamond shows a core of moderately luminescent octahedral growth which is followed by two fine alternating layers of more luminescent and non-luminescent diamond. The growth layers towards the rim of the diamond are very uniform, moderately luminescent diamond. Due to many fractures in the diamond, FTIR analyses could not be made through the centre of the plate. The nitrogen content varies between 540 and 772 ppm and shows a strong positive correlation with both the %B aggregation and the platelet peak area. The %B aggregation varies between 38 and 65 %. The core region (analyses 6 and 7) has the highest nitrogen content, as well as the greatest platelet peak areas, %B aggregation. Although the hydrogen peak areas are the highest in the core region, hydrogen peak area does not correlate well with the total nitrogen content in the rest of the diamond.

EL43

The diamond has fine octahedral growth layers, which alternate between low luminescent and moderately luminescent diamond. There is one fine layer of non-luminescent growth visible from the back view of the

plate. The centre of the plate has many fractures, so analyses could not be made through the centre of the diamond. Nitrogen content varies between 700 to 950 ppm and shows a strong correlation with the platelet peak area. %B aggregation is relatively constant between 57 to 64 %. The hydrogen peak areas in analyses 4 to 6 show some correlation with the nitrogen content.

EL50

The macle line isnt clearly visible in the growth layering, however there are portions where the octahedral growth layers dont meet up (zoomed in image to illustrate – on the B/W image). The diamond has fine alternating layers of moderately luminescent diamond with less-luminescent and non-luminescent layers. The light reflections are due to inclusions and fractures in the diamond. Towards the bottom of the plate octahedral layers are cross-cut, which seems to indicate a period of resorption followed by a new diamond growth episode, also of octahedral habit. Nitrogen content across the plate varies between 330 and 710 ppm and shows a strong positive correlation with the nitrogen content. %B aggregation varies between 41 and 55 % and also shows a positive correlation with nitrogen content though not as pronounced as the platelet peak area. Hydrogen peak areas do not show any correlation with total nitrogen content.

EL51

The diamond broke during cutting and polishing and light reflections due to both inclusions and cracks make the growth layers difficult to view. The growth layers are more visible from the front of the plate. The complex fine growth layers are difficult to interpret, though a rim of octahedral growth has overgrown the central portion of the diamond, which has several micro growth centres of low luminescence. The nitrogen content is relatively constant between 580 and 620 ppm with %B aggregation between 72 and 77 %. Platelet peak area shows a negative correlation with the hydrogen peak area, with analysis 2 showing the lowest platelet peak area and the greatest hydrogen peak area.

EL52

This diamond has uniform octahedral growth with a core of oscillatory growth. This core has an inner zone of non-luminescent growth followed by layers of moderate luminescence. Slight curvature in the growth layers around the core indicate a period of resorption, before growth of the octahedral layers which continue to the rim of the diamond. The rounded oscillatory zoning in the core could be due to inclusions in the diamond, intermittent periods of resorption during the early growth of the diamond or cubo-octahedral growth. Nitrogen content ranges from 630 to 730 ppm and shows a positive correlation with the platelet peak area. %B aggregation stays constant between 80 and 85 %. The hydrogen peak area shows no correlation with any of the other parameters and increases dramatically from the one end to the other.

EL53

Apart from limited non-luminescent growth towards the bottom of the front view of plate, the diamond is moderately luminescent. Fine growth layers of octahedral habit have been interrupted by several periods of resorption. The oscillatory zoning visible on the back of the plate dont correlate directly with the layers on the front of the plate (see CL images in Appendix 3). Light reflections on the image are due to the two deep etch pits. The nitrogen content does not vary greatly across the plate, ranging from 540 to

680 ppm. It shows a negative correlation with the platelet peak area. %B aggregation remains relatively constant between 72 and 80 % and shows no correlation with the nitrogen content or the platelet peak area. The hydrogen peak area shows strong variation across the plate, with does not appear to correlate strongly with the nitrogen content.

EL54

The diamond has many cracks that give rise to light reflections which make it difficult to view the growth zoning in the diamond and made FTIR analyses through the centre of the diamond difficult. From the back view of the plate (see CL images in Appendix 3), the octahedral layers are more visible. The growth core of the diamond towards the bottom right of the image is predominantly non-luminescent diamond. There were intermittent periods of resorption, which in addition to the presence of inclusions, gave rise to the irregular, complex growth patterns in this core region. There appears to be an annealed crack through this core region. Outside of the core, the growth layers are moderately luminescent, with a few alternating layers of low luminescence towards the top right of the diamond. Nitrogen content varies between 112 and 380 ppm across the plate and can be strongly correlated with the platelet peak area. Apart from analysis 2, the hydrogen peak area can be roughly correlated with the platelet peak area and nitrogen content. The %B aggregation does not correlate with the nitrogen content and varies between 40 and 64 %.

EL55

The back plate surface is much larger than the front surface, owing to the fact the diamond is not symmetrical. This, in addition to inclusions and cracks, yield light reflections in the CL image. The back surface gives a better view of the growth zoning. The diamond has two distinct growth environments resulting in a very luminescent core of octahedral diamond, which underwent a period of resorption prior to the growth of the very low luminescent, also of octahedral habit. The low luminescent growth was not uniform, there are indications that this occurred in several phases, with intermittent periods of resorption (eg. See top left of the back plate). As with EL32, the analyses with the highest nitrogen contents are in zones with extremely low luminescence. The nitrogen content does not vary greatly and ranges between 430 to 500 ppm and does not correlate with the strong contrast in luminescence seen between zones in the CL image. The nitrogen content shows no correlation with either the platelet peak area or the hydrogen peak area. The %B aggregation varies slightly between 63 and 73 %.

EL56

The macle line in this diamond is not as clear as in EL16, also partly due to numerous light reflections from the cracks and inclusions in the diamond. The diamond has an octahedral growth habit, a luminescent core region followed by moderately luminescent growth. Within this zone there are several micro growth centres of non-luminescent diamond. Fractures fill about half of the plate, so a traverse through the centre of the diamond was tricky, though analysis 3 comes close enough. The nitrogen content varies between 510 and 590 ppm and apart from analysis 2, seems to show good positive correlation with the platelet peak area. %B aggregation remains relatively constant between 82 and 87 %. The hydrogen peak area shows no correlation with the nitrogen content.

EL57

This diamond has a complex growth history marked by several different micro growth centres (more visible on the back view of the plate, Appendix 3) and several periods of resorption that interrupted growth. The diamond has alternating layers of moderately luminescent octahedral growth, though the outer layers become less luminescent. Light reflections in the top right of the plate are from cracks in the diamond as well as the rosette fracture system. There is minimal across-plate nitrogen variation, it varies slighty between 510 and 550 ppm. Nitrogen content shows no correlation with either the platelet peak area or the hydrogen peak area. Nitrogen is highly aggregated, with %B between 65 and 71 %

EL59

The diamond fractured during polishing, and only one side of the plate still has a planar surface. Due to the fracturing, growth zoning was not always clear. Nitrogen content ranges from 280 to 1100 ppm and correlates strongly with both the platelet peak area and the %B aggregation (35 - 68 %). The hydrogen peak area shows a negative correlation with the nitrogen content.

EL61

The twin plane is visible down the centre of the diamond. Small etch pits all along this twin plane cause light reflections on the CL image. The octahedral growth layering has multiple centres and strongly contrasting layers of non-luminescent and moderately luminescent growth layers are visible. A large non-luminescent centre is visible on the back view of the plate. Nitrogen content shows a positive correlation with both the platelet peak area and the %B aggregation. It varies between 416 and 500 ppm, with %B aggregation between 66 and 80 %. The hydrogen peak area shows a negative correlation with the nitrogen content. Analysis 2 shows the greatest nitrogen content, yet corresponds to a low luminescent growth zone on the CL image. This indicates that the FTIR analyses are an average value of various growth layers through the depth of the plate.

EL62

The diamond fractured during laser cutting, and only one side of the plate could be polished. The light reflections from the fractures make that no growth zoning can be viewed. Platelet peak area and %B aggregation show a positive correlation, though neither correlate with the total nitrogen content. This shows minimal variation in the range 690 to 815 ppm. Hydrogen peak area shows no correlation with nitrogen content or either of the other parameters.

EL64

A large proportion of the diamond is filled with inclusions and fractures, which makes it difficult to view the growth zoning. From the back view of the plate, faint octahedral zoning of moderate luminescence is visible. A core of non-luminescent diamond is visible from the back view of the plate, followed by a region of resorption before growth of moderately luminescent octahedral layers. Obtaining a representative FTIR traverse through the centre of the diamond was not possible due the presence of a large fracture system. This diamond shows a dramatic decrease in platelet peak area in analysis 2, which shows no correlation with the nitrogen content or the %B aggregation. Nitrogen content ranges from 497 to 625 ppm and the %B aggregation is reasonably high, between 88 and 93 %. Hydrogen peak areas are quite high, with only

two samples showing higher hydrogen peaks, namely EL25 and EL33.

EL65

This diamond has regular octahedral growth layering with a very luminescent core. On the front view of the plate, the layers in the top right cross cut the octahedral layering of the rest of the diamond. This suggests a period of resorption that was followed by less-luminescent growth layers, evident also in the substantially lower nitrogen content of analysis 5. Oscillatory zoning towards the left of the plate are due to the small inclusions. The green CL lines on the image are due to deformation lamellae in the diamond. The platelet peak area and the nitrogen content show a strong positive correlation, with nitrogen content remaining low throughout the sample, in the range 65 to 155 ppm. %B aggregation is between 40 and 50 %. Hydrogen peak areas vary across the traverse and show no correlation with the nitrogen content or either the platelet peak area or the %B aggregation.

EL66

The plate has many fractures, which developed predominantly during cutting and polishing. As a result of the abundant light reflections, no growth zoning can be viewed and only two FTIR analyses could be taken. No traverse diagram is presented, however the FTIR data is shown in Appendix 1. Nitrogen content for the two analyses were 430 and 470 ppm, with high %B aggregation - 71 % and 67 %, respectively.

EL67

The diamond has a core of very luminescent diamond, from the front view the growth layers arent clearly visible, but from the back view, alternating layers of non-luminescent diamond is seen. This core has an uneven outline due to resorption. The core is overgrown by octahedral growth layers that are fairly non-luminescent. Nitrogen content varies between 380 and 510 ppm and shows a positive correlation to the platelet peak area. %B aggregation is quite high between 89 and 92 %. The hydrogen peak areas vary across the traverse, with no correlation to the nitrogen content, though analysis 7 shows the highest hydrogen peak area as well both the highest platelet peak area and nitrogen content. This does not correspond with the low luminescent diamond seen in the CL image, but seems to indicate that the analysis is an average of several growth layers through the plate.

EL69

The diamond has octahedral growth layers on either side of the twin plane that is seen through the middle of the diamond. Below the twin plane are regular, moderately luminescent growth layers, while the growth above the twin plane was more variable with intermittent layers of non-luminescent growth. Nitrogen content ranges from 505 to 560 ppm and shows some correlation with the platelet peak area. %B aggregation varies slightly between 73 and 88 %. The hydrogen peak area shows no correlation with the nitrogen content, platelet peak area or the %B aggregation.

EL01 FTIR Traverse

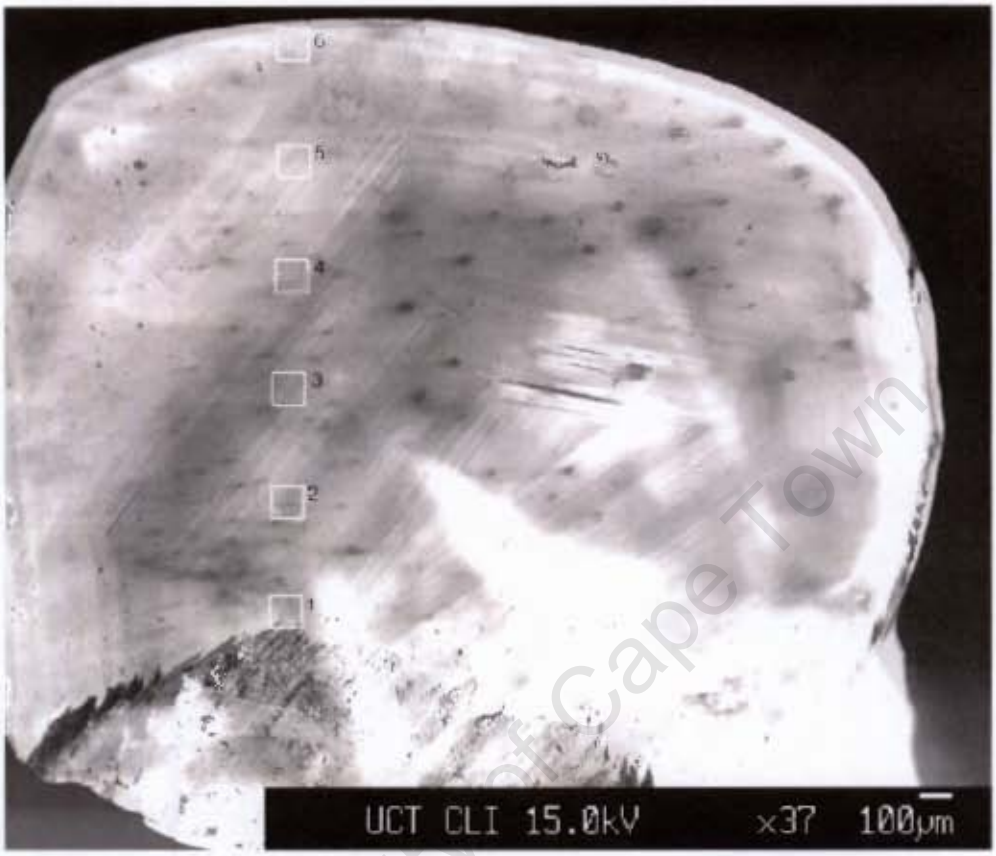

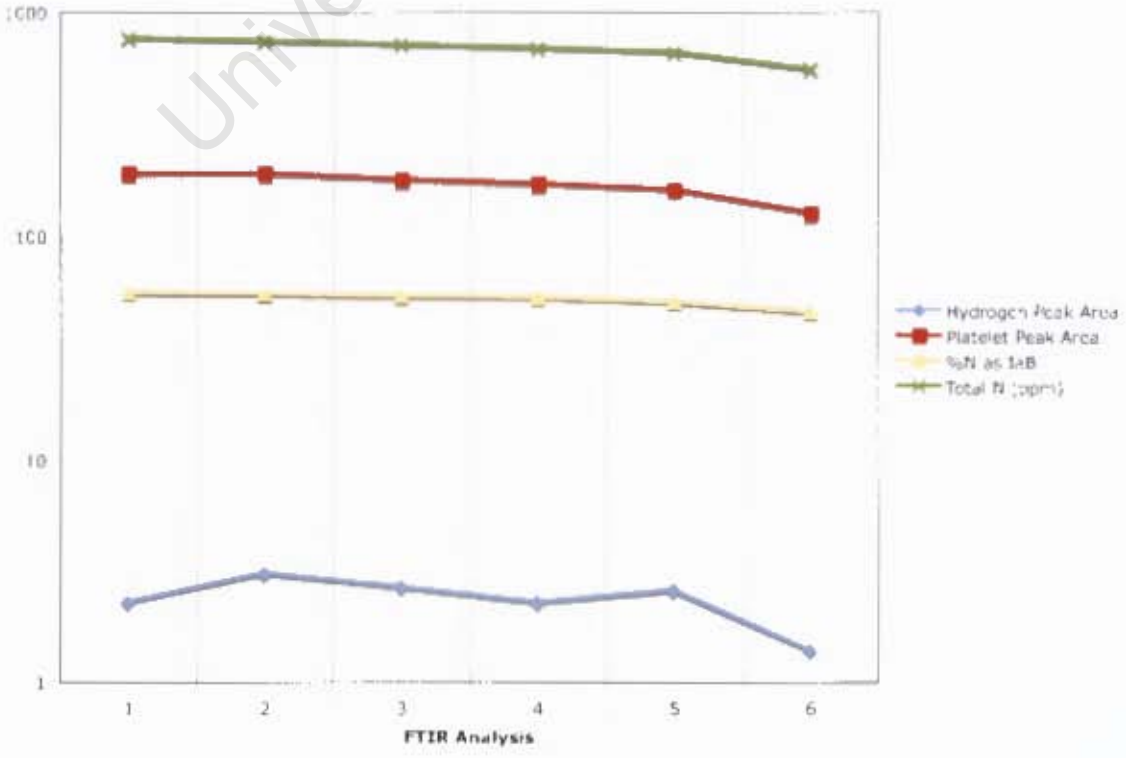

EL05 FTIR Traverse

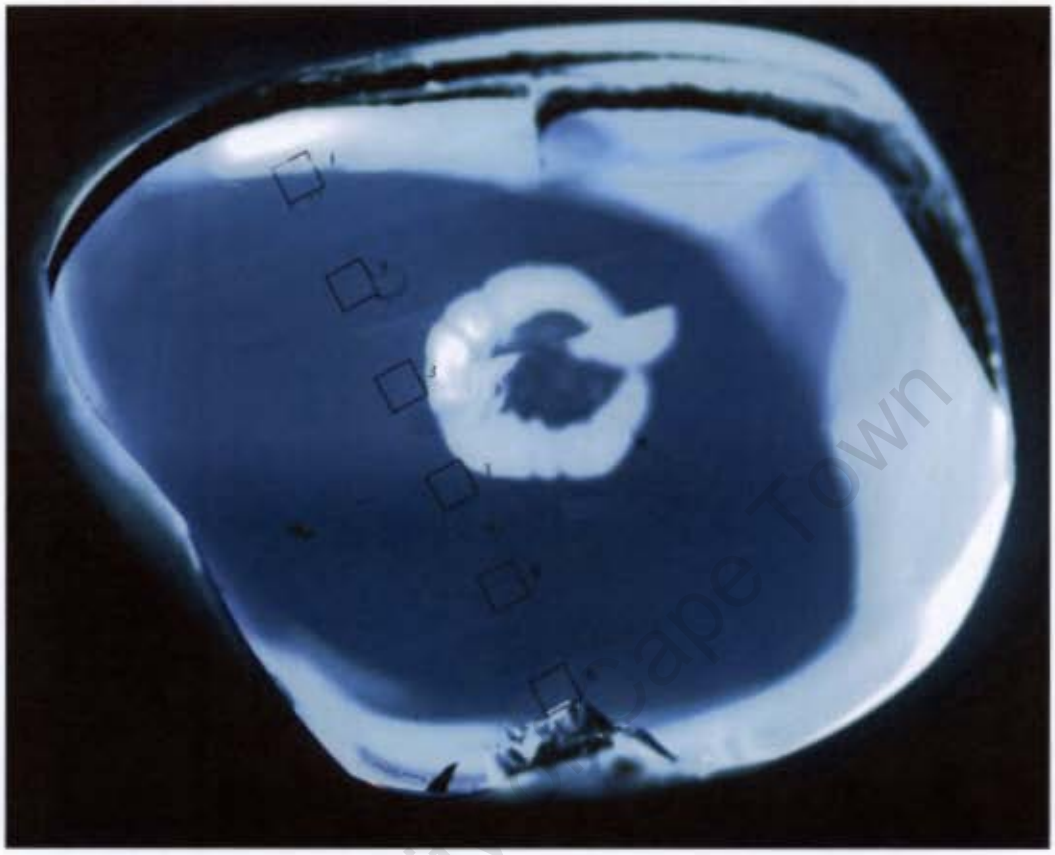

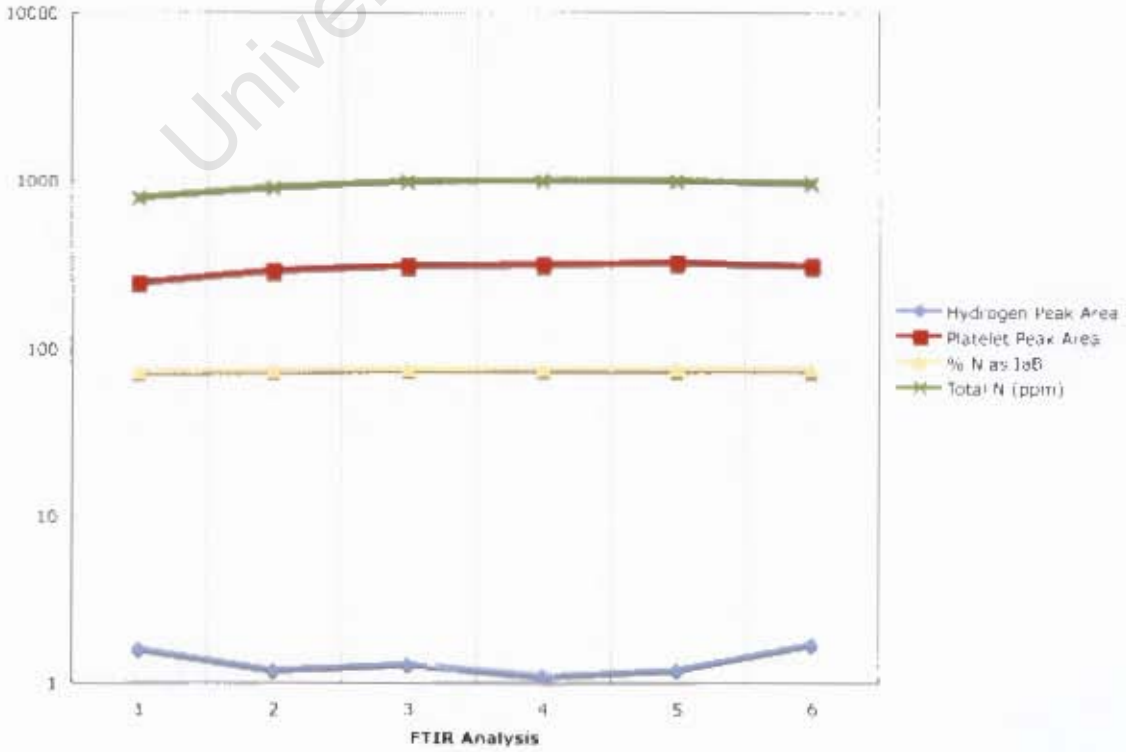

EL10 FTIR Traverse

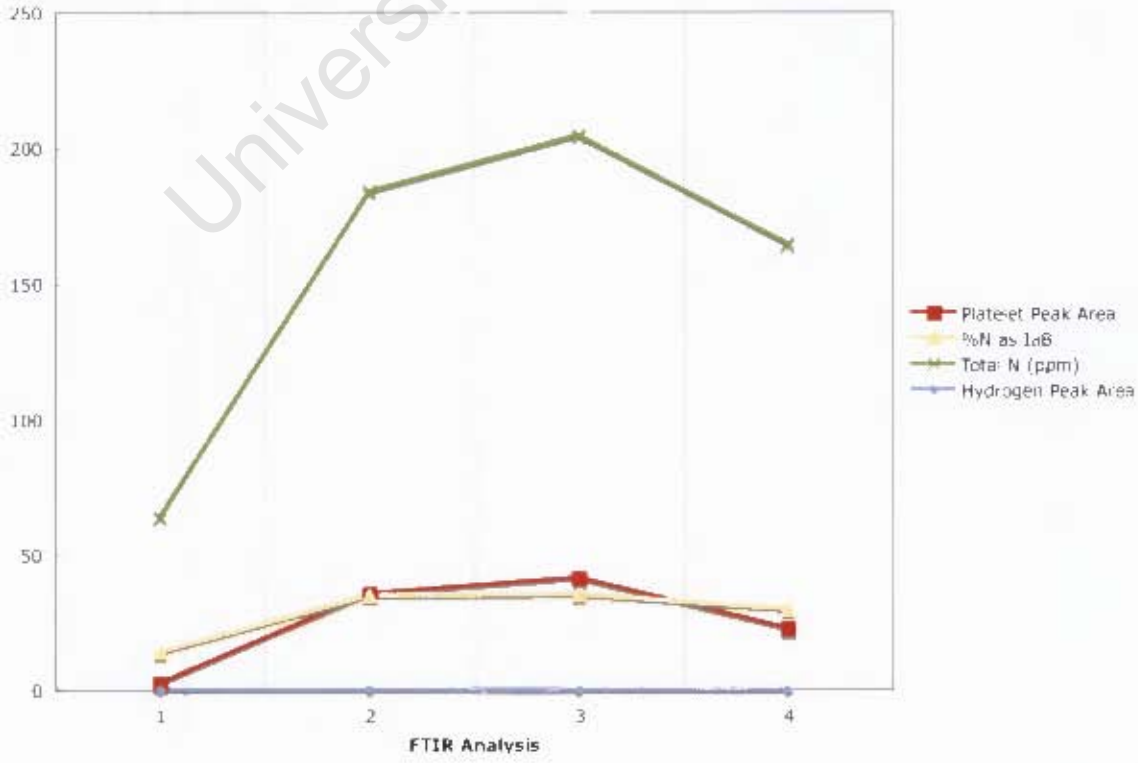

EL12 FTIR Traverse

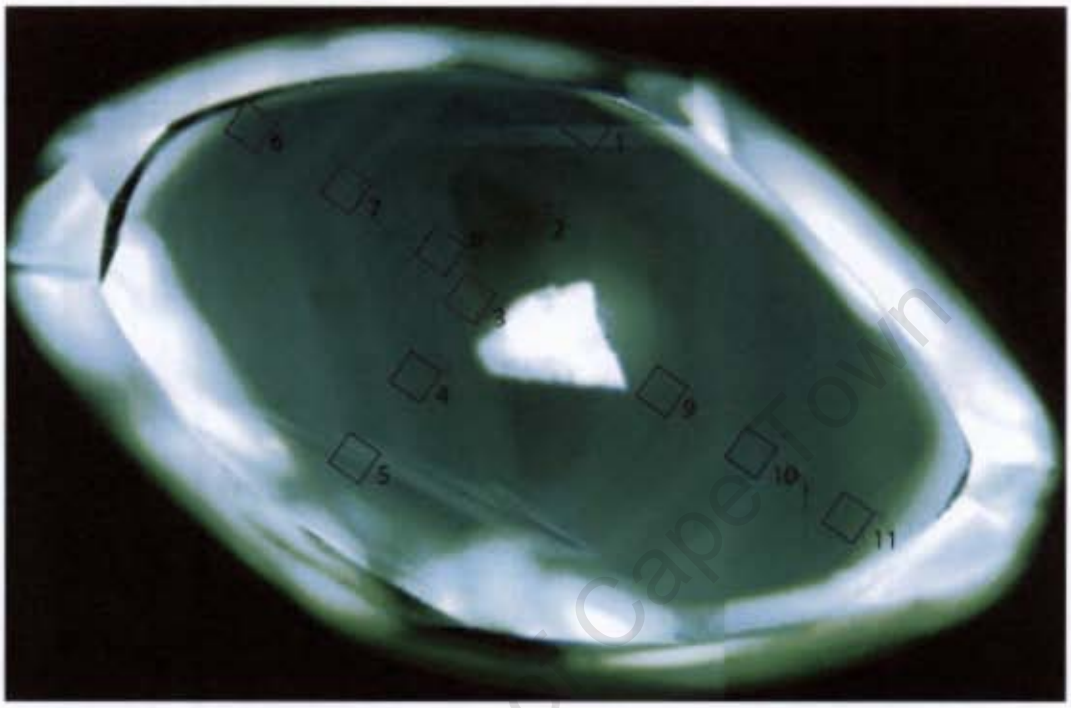

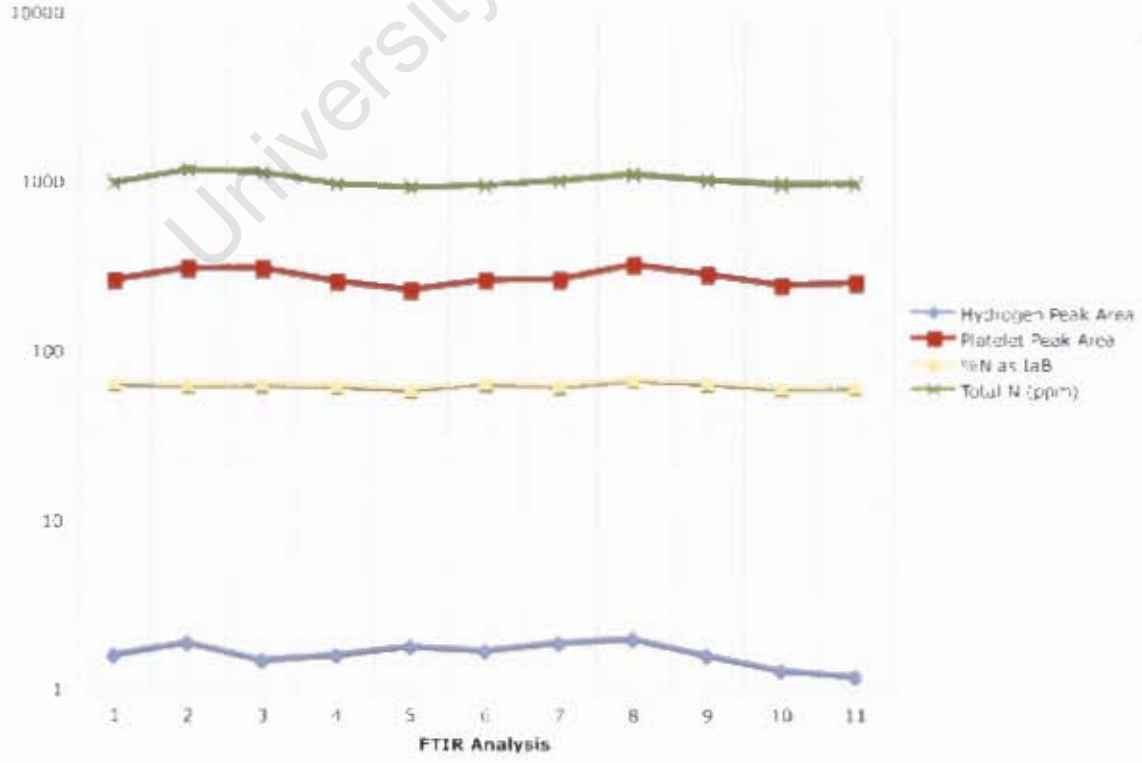

EL16 Traverse Diagram

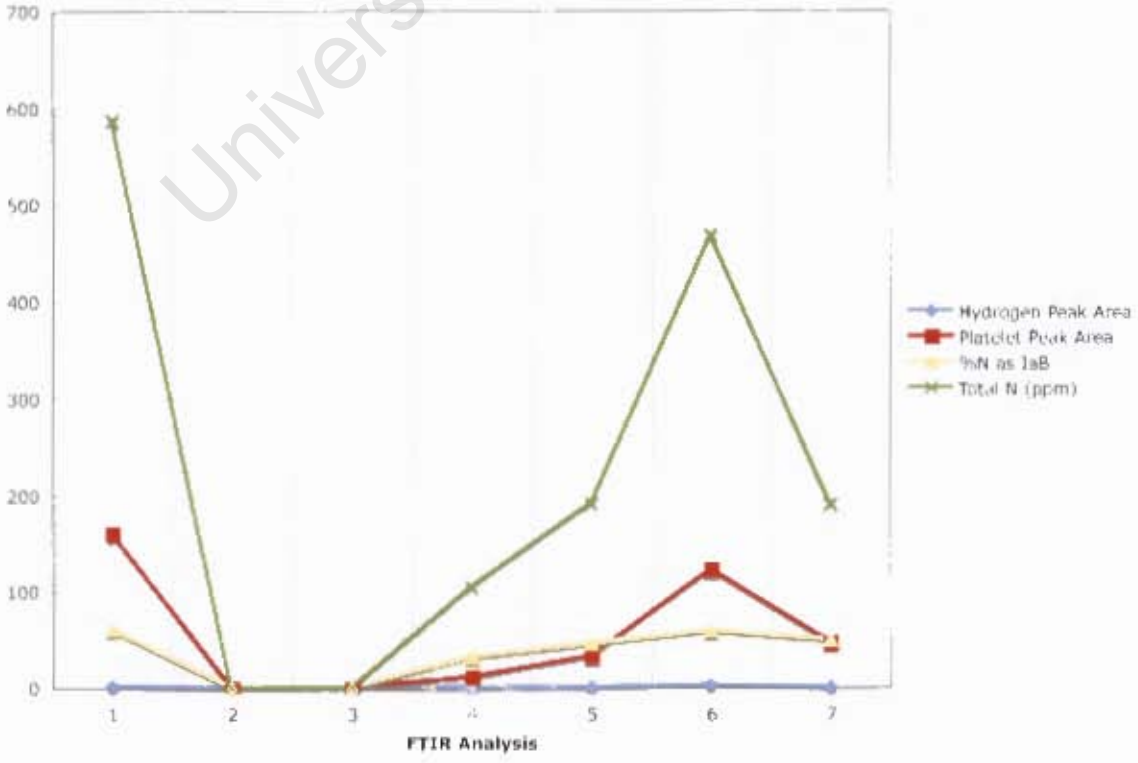

EL20 FTIR Traverse

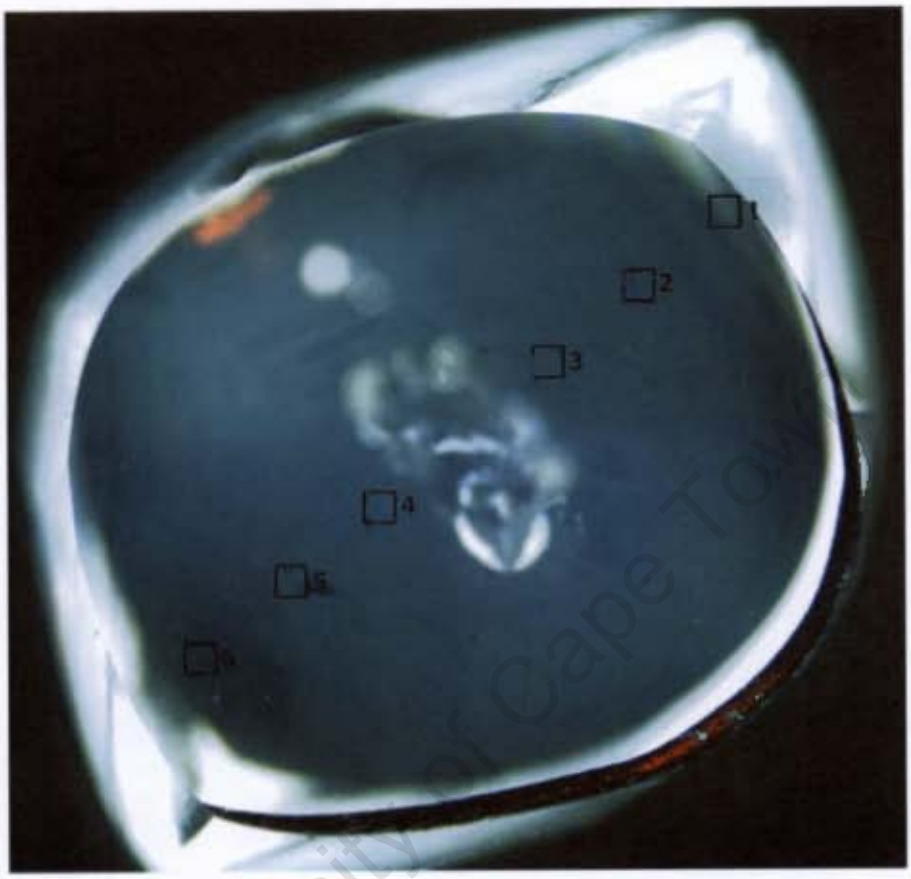

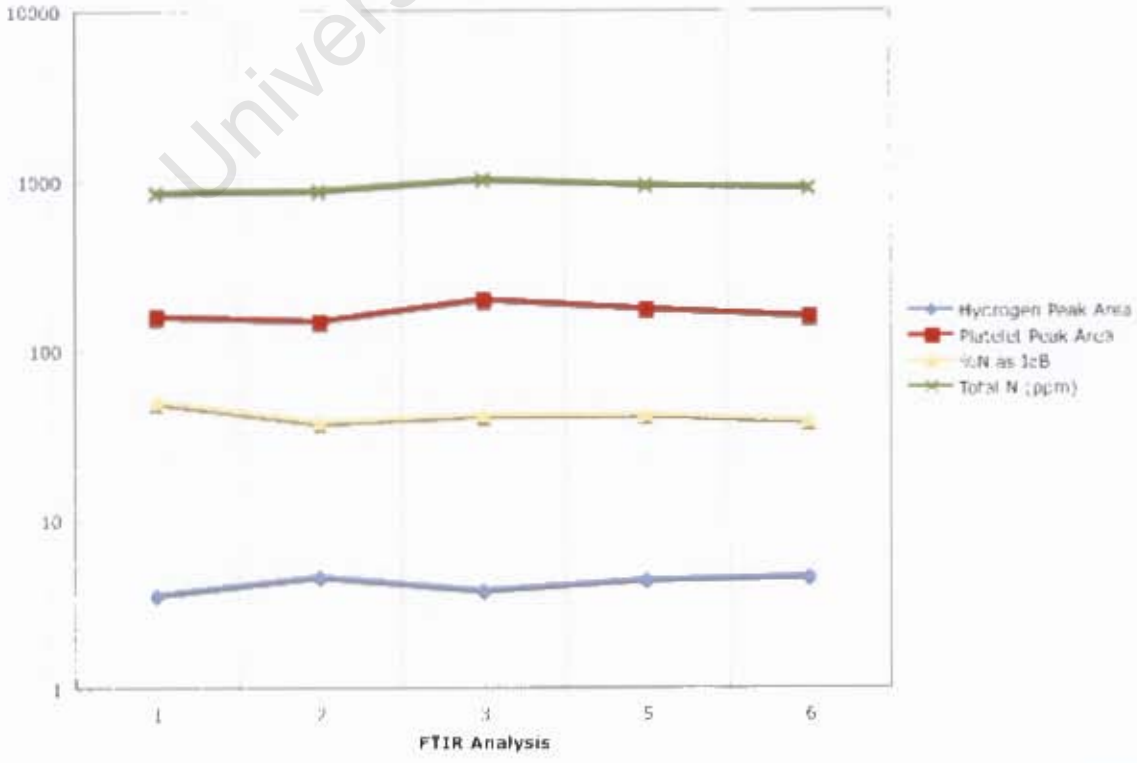

EL23 FTIR Traverse

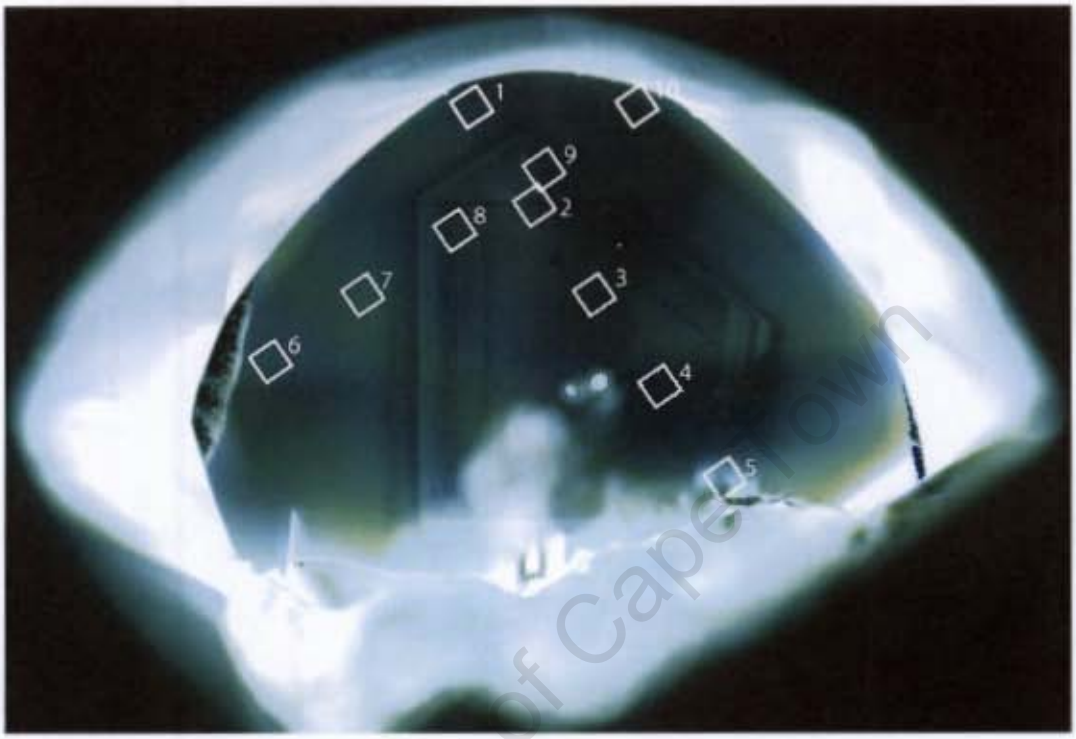

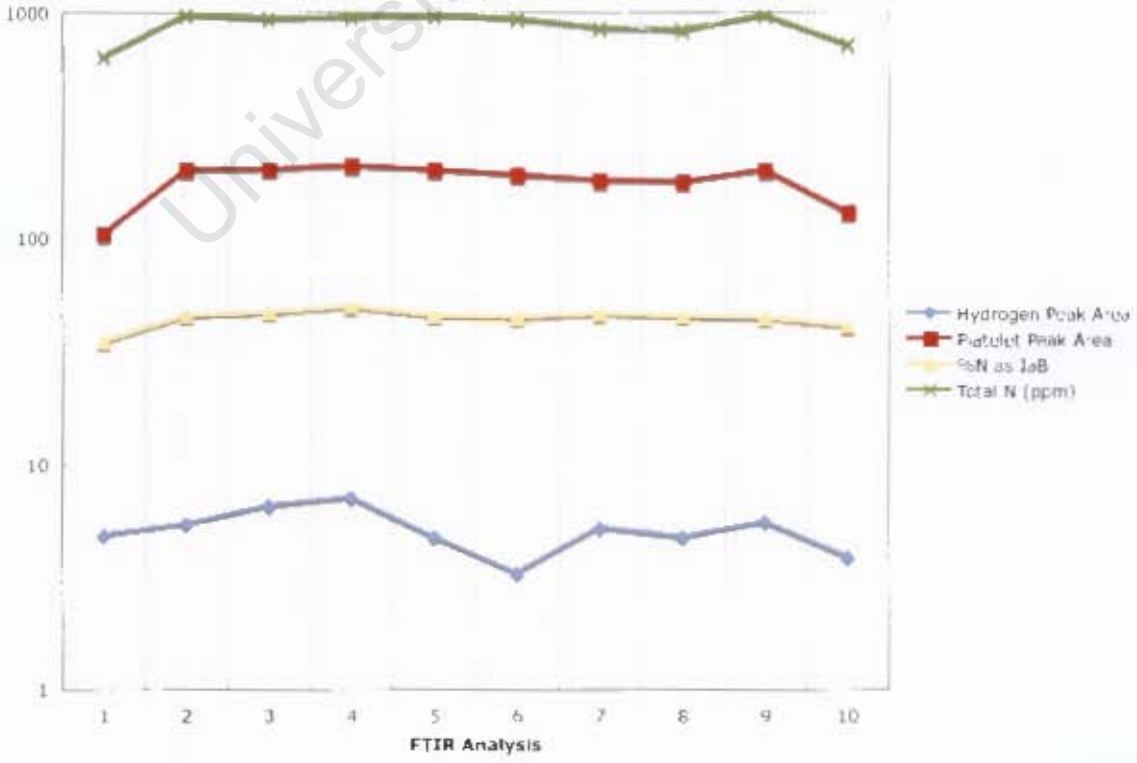

EL26 FTIR Traverse

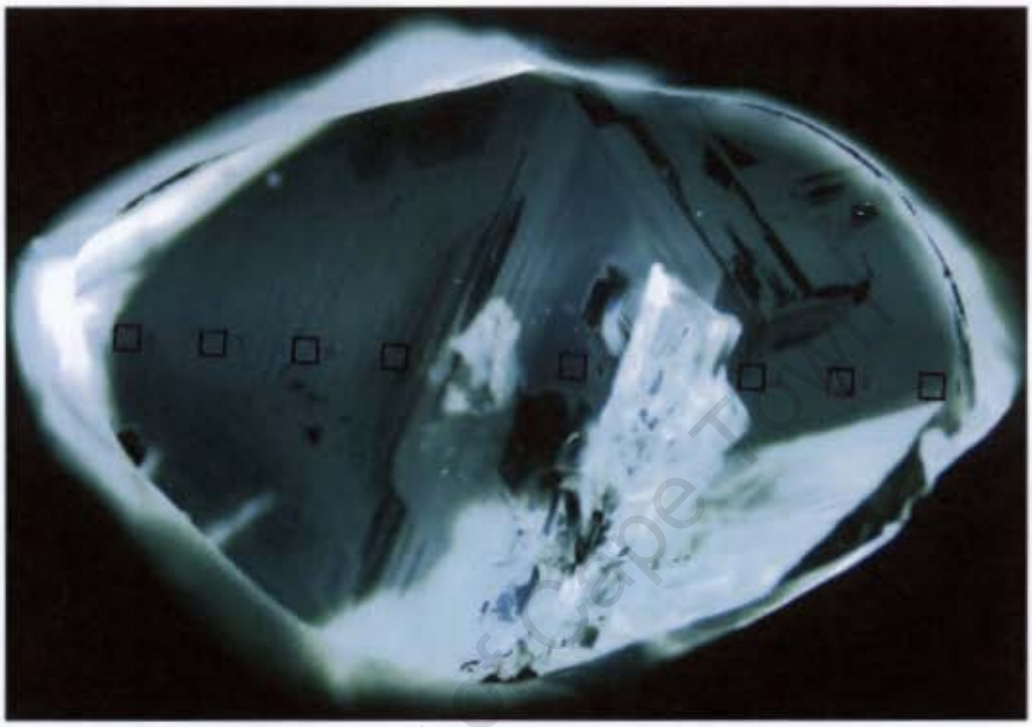

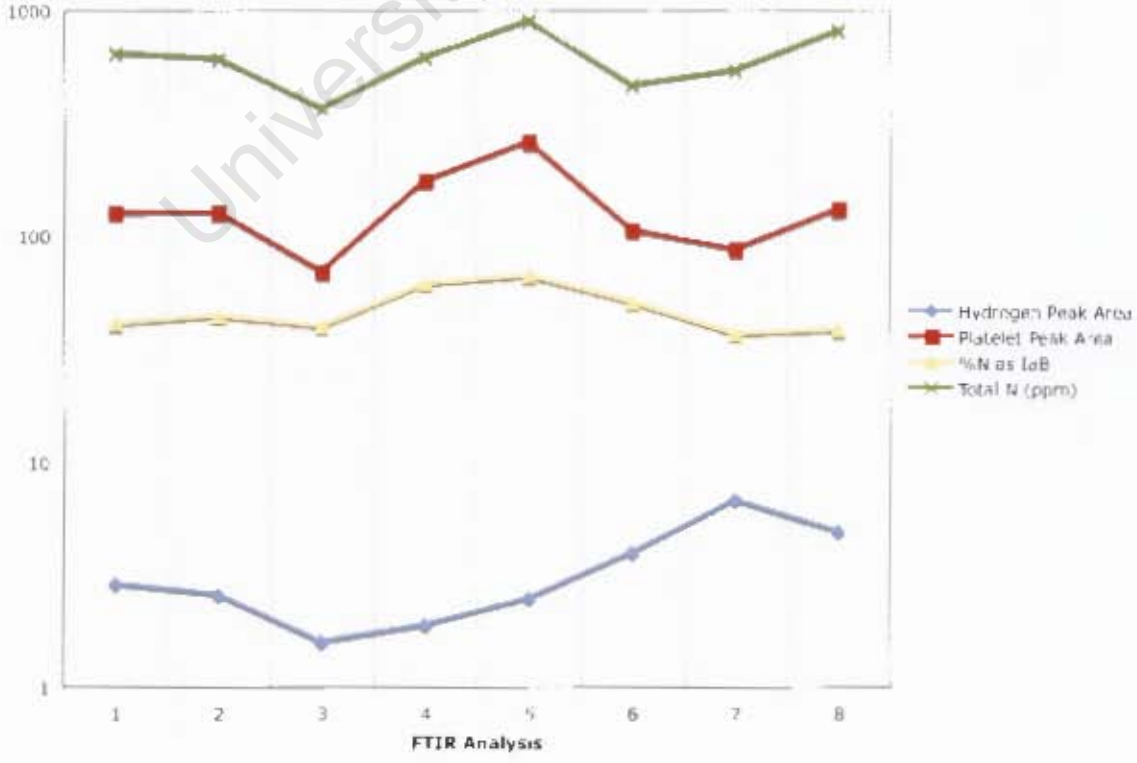

EL31 FTIR Traverse

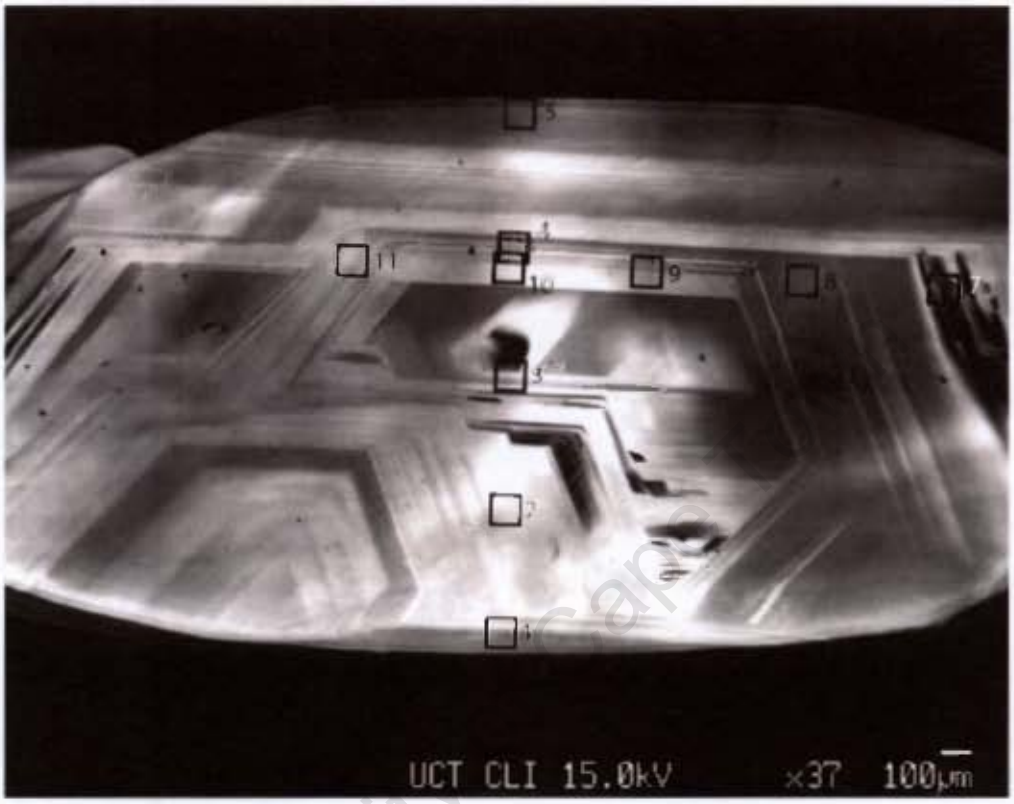

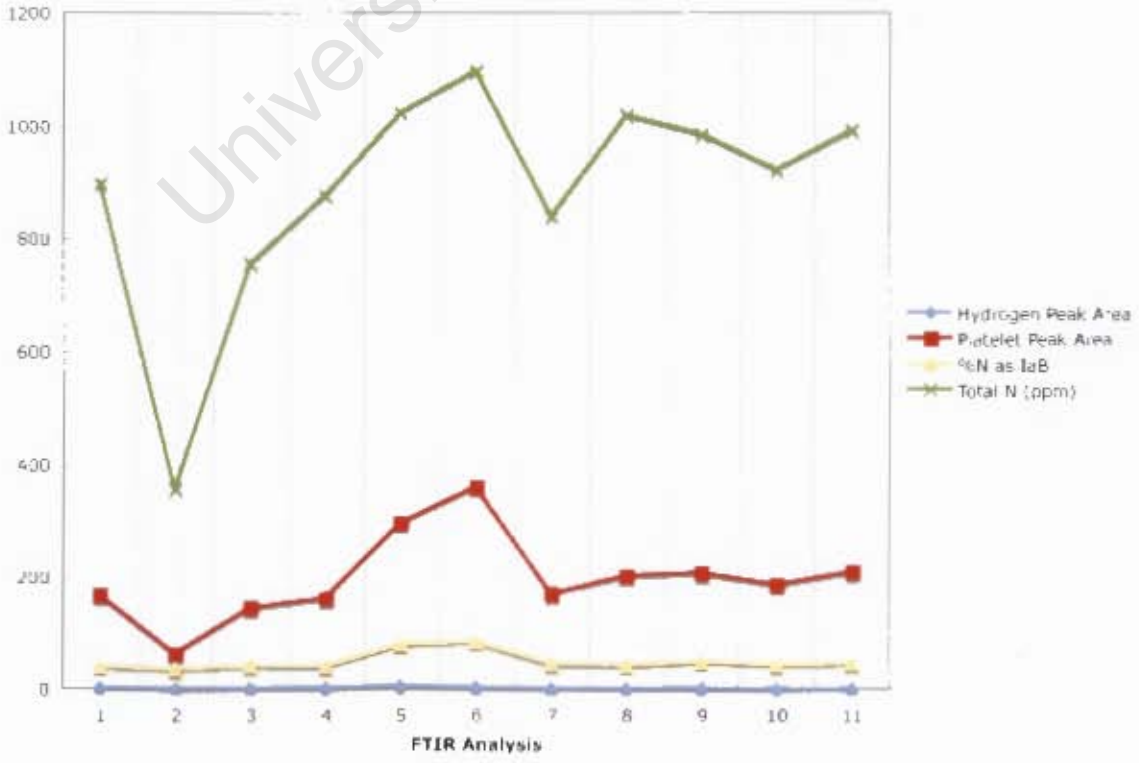

EL32 FTIR Traverse

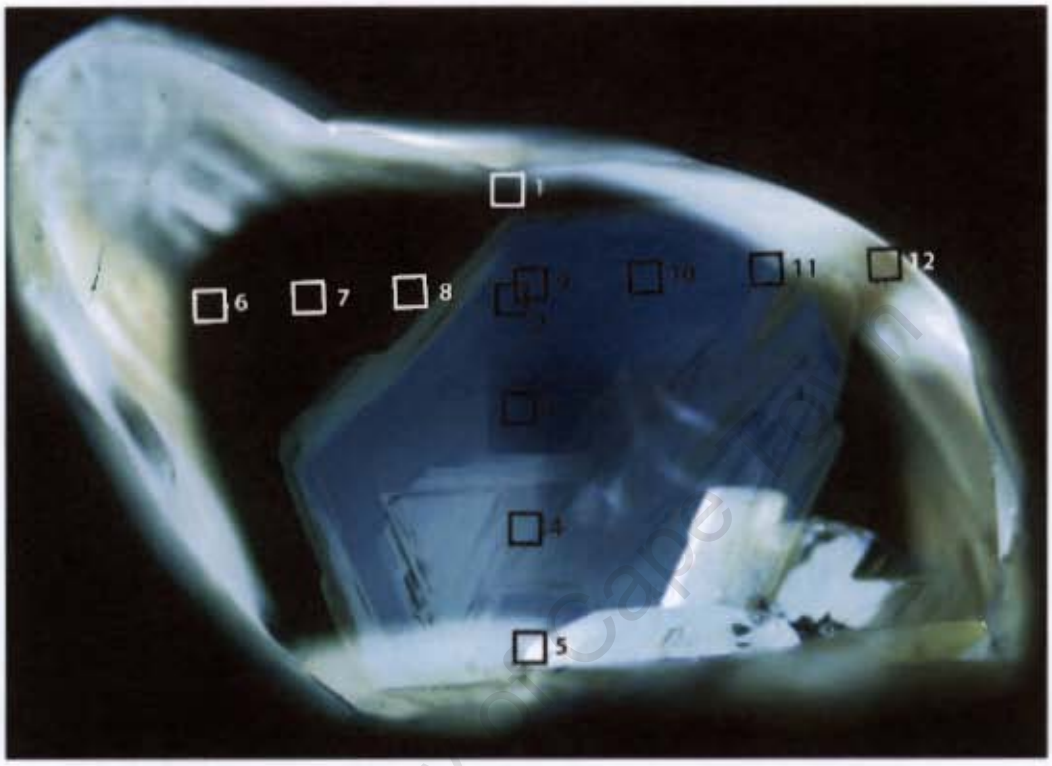

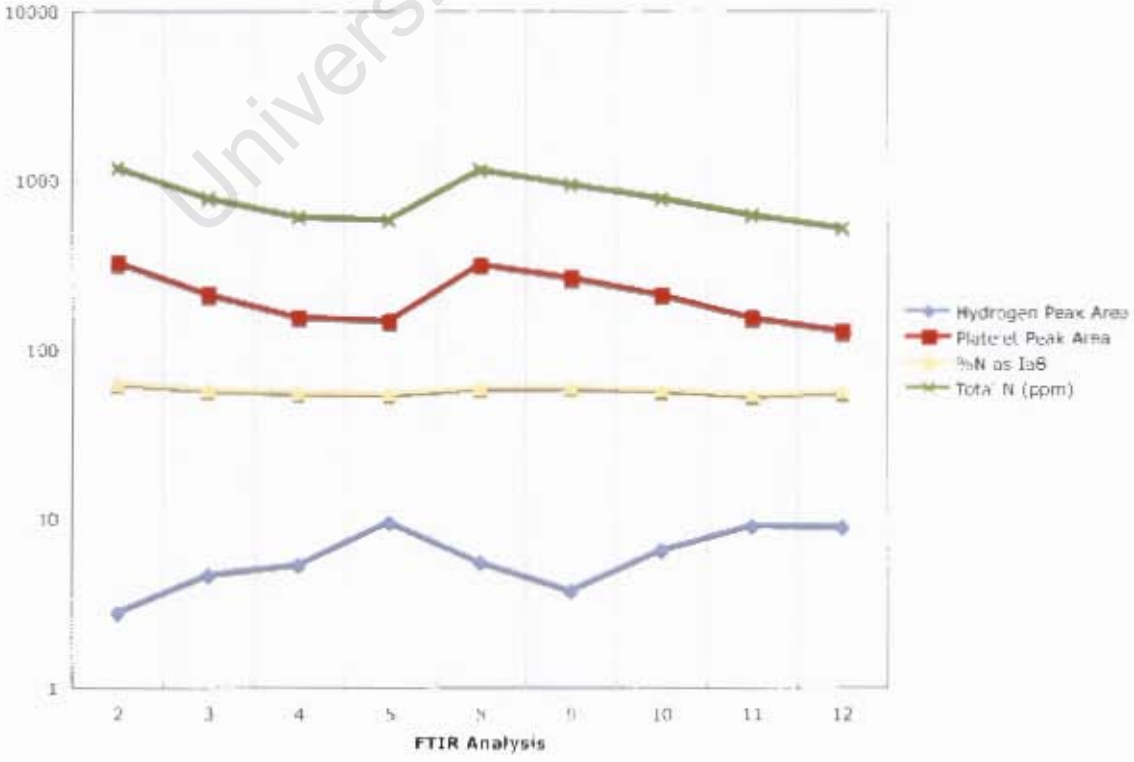

EL33 FTIR Traverse

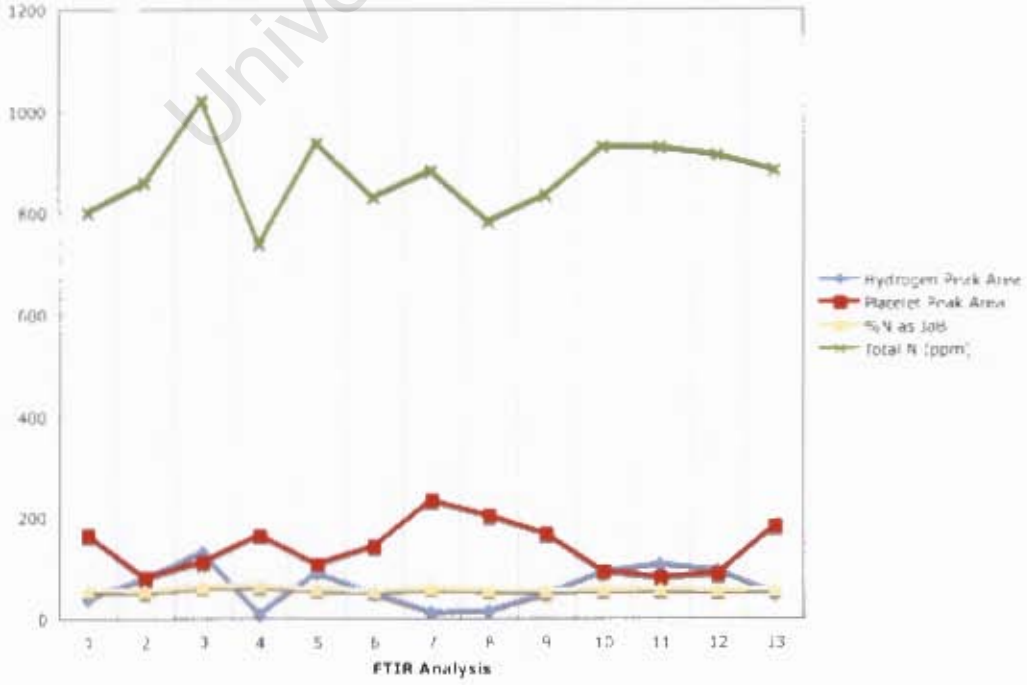

EL34 FTIR Traverse

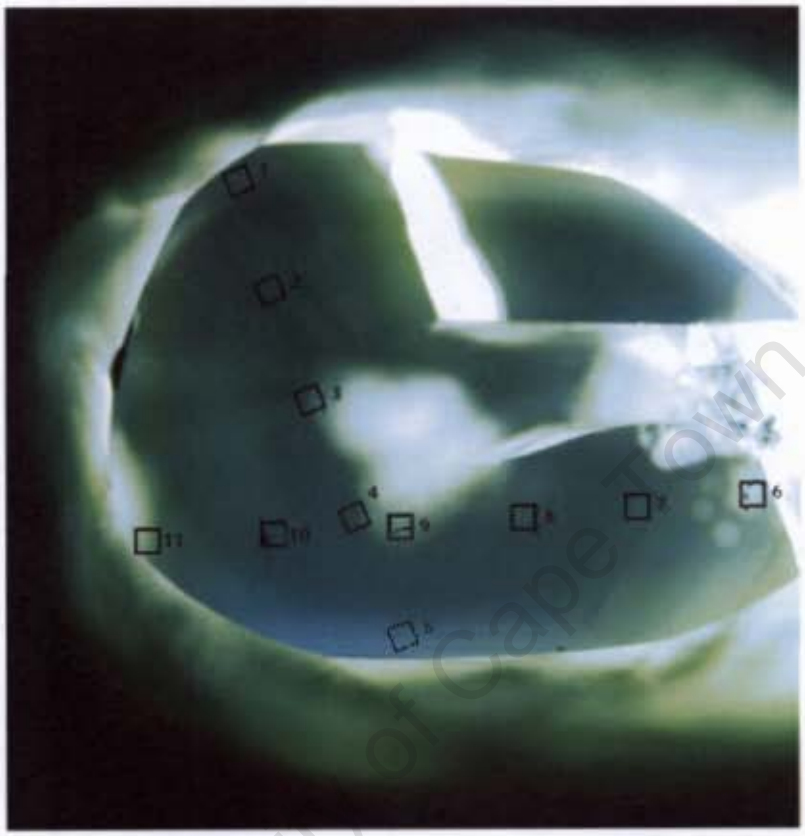

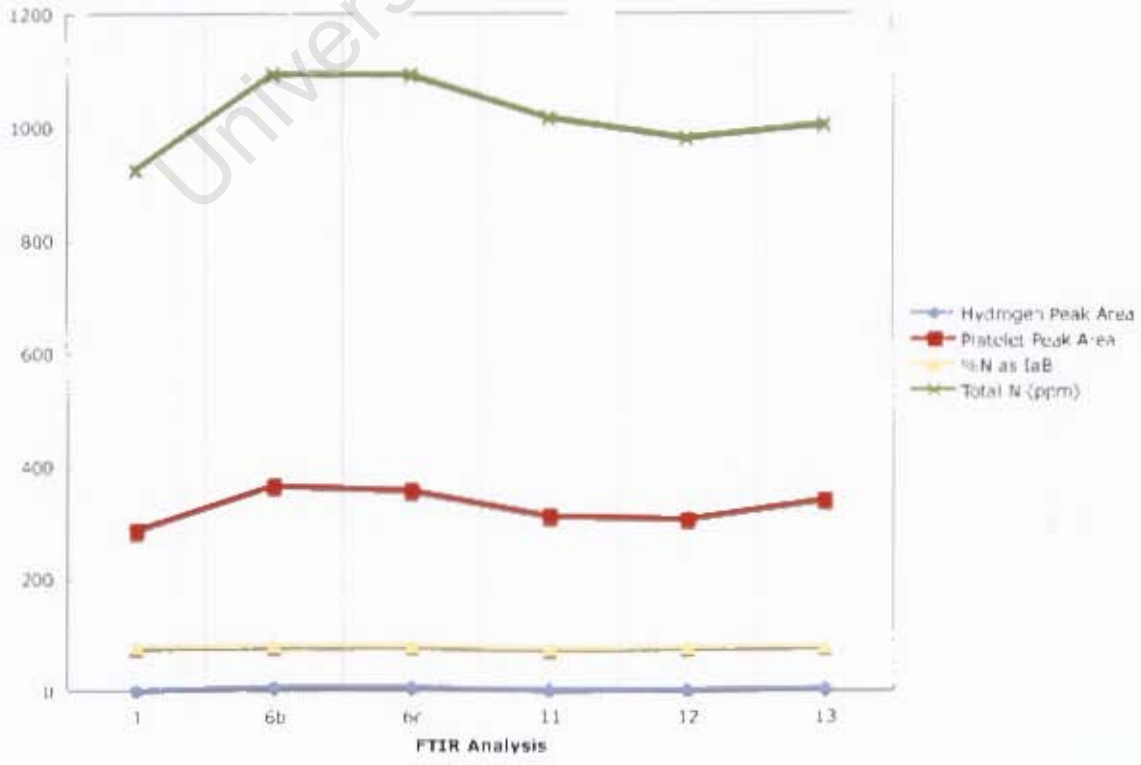

EL35 FTIR Traverse

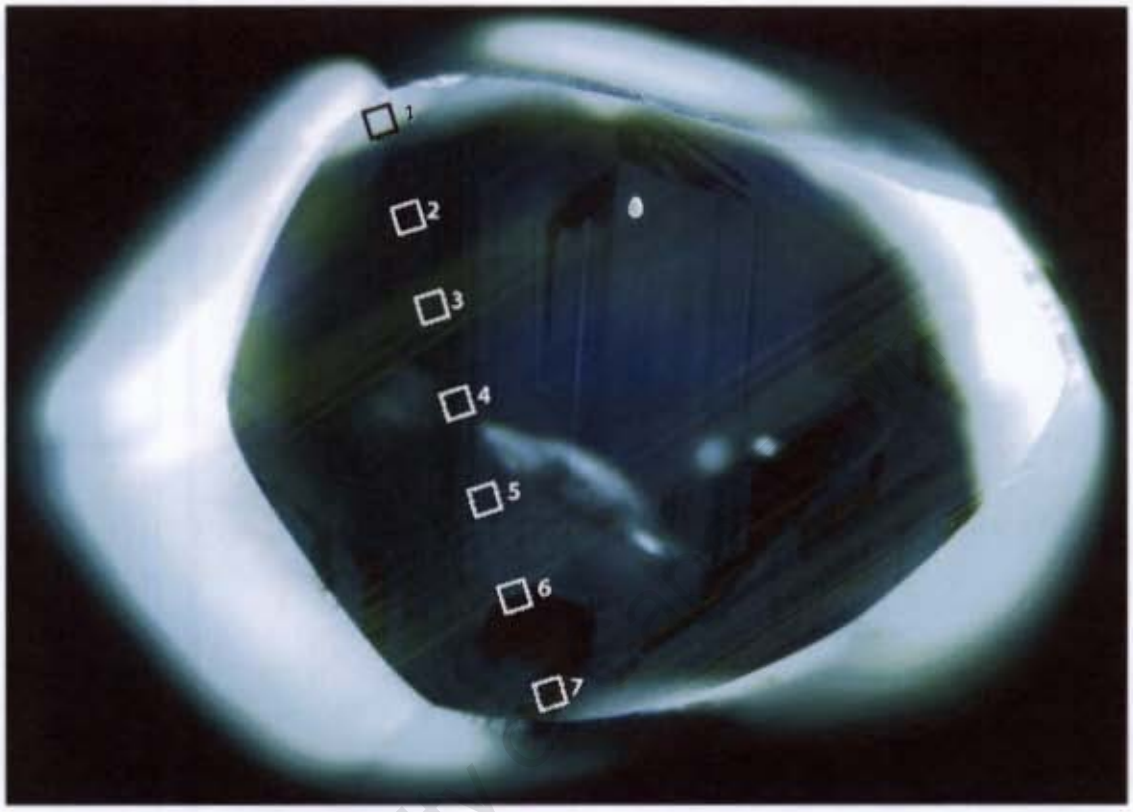

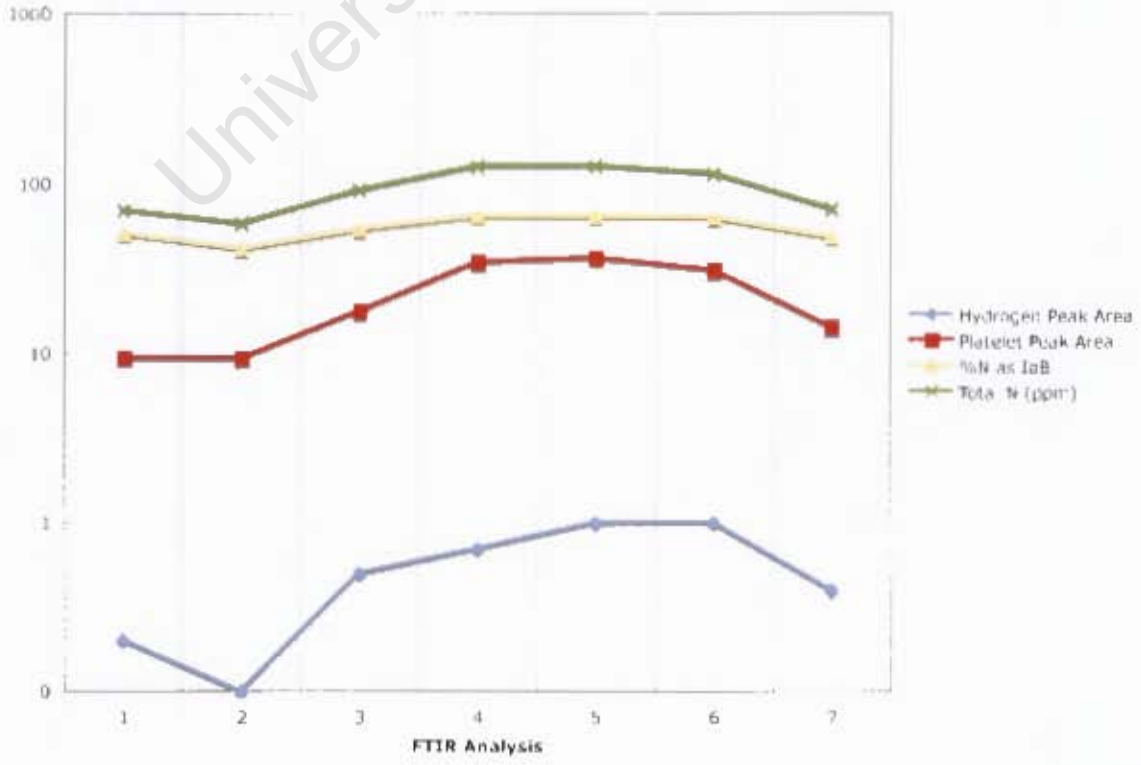

EL36 FTIR Traverse

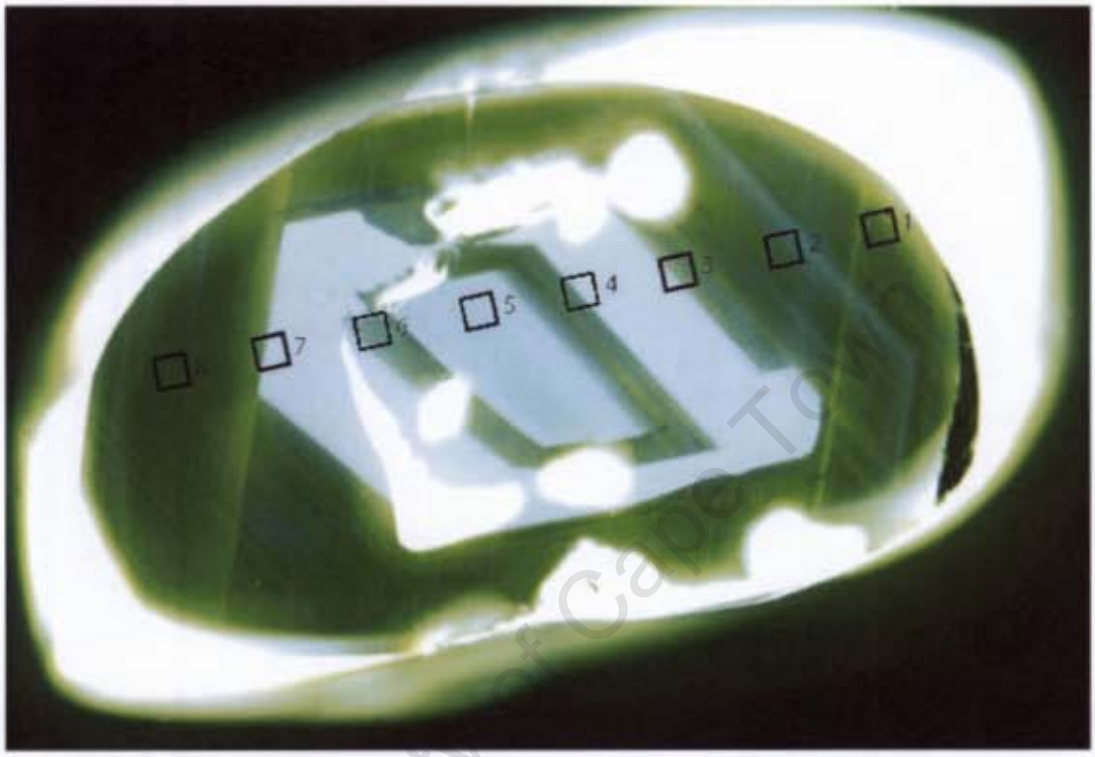

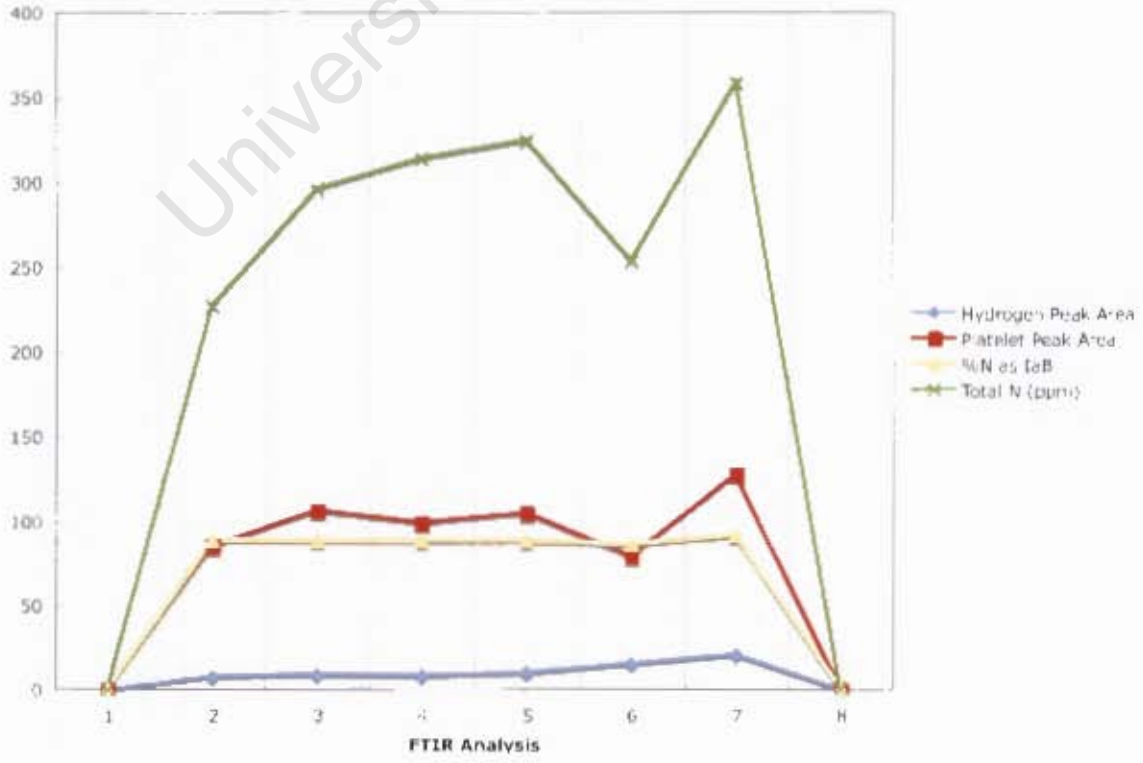

EL38 FTIR Traverse

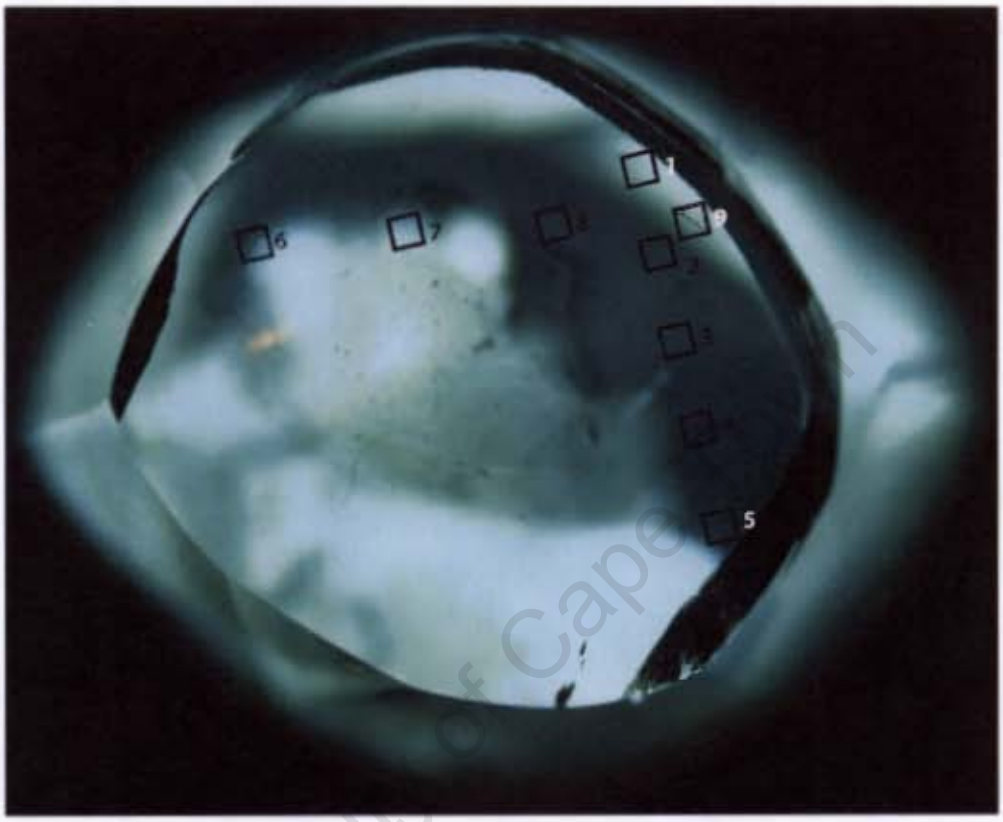

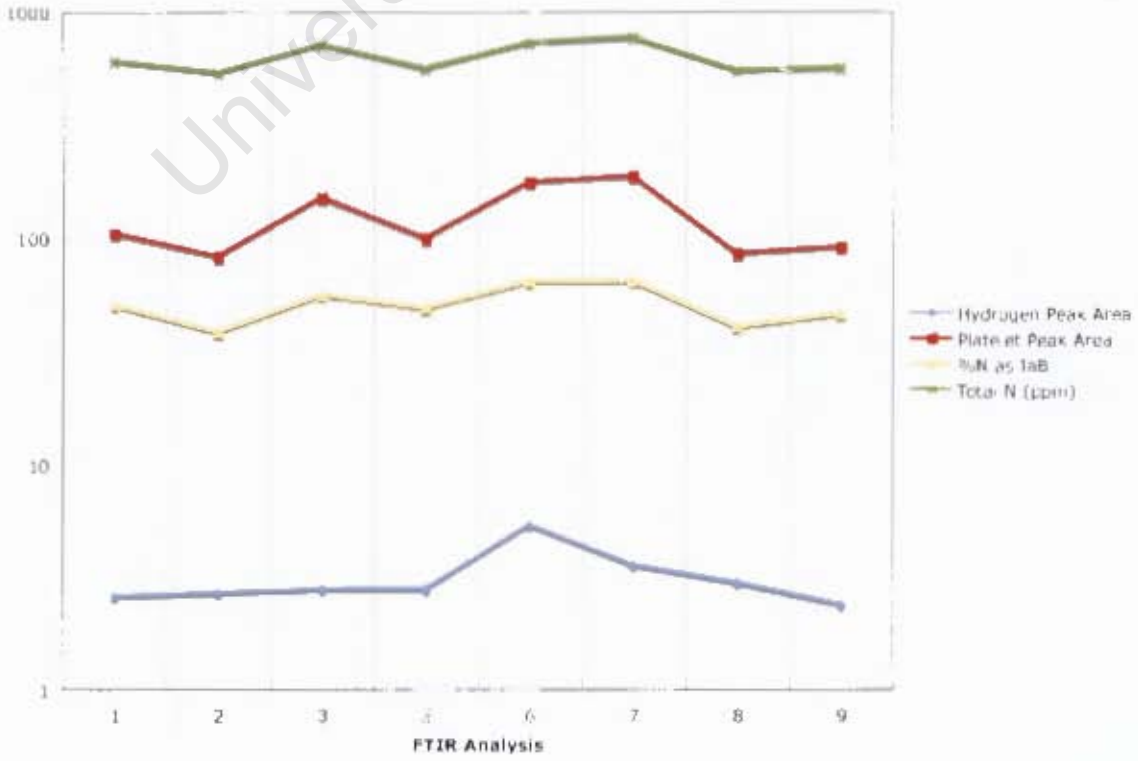

EL43 FTIR Traverse

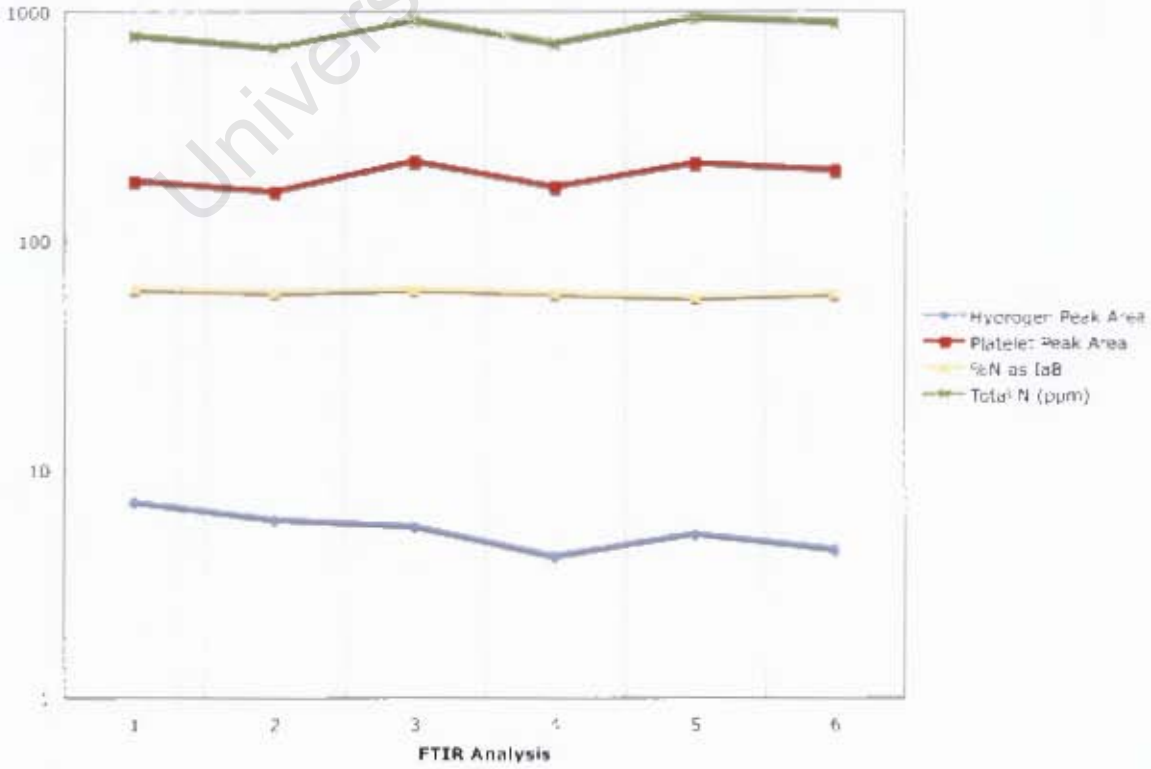

EL50 FTIR Traverse

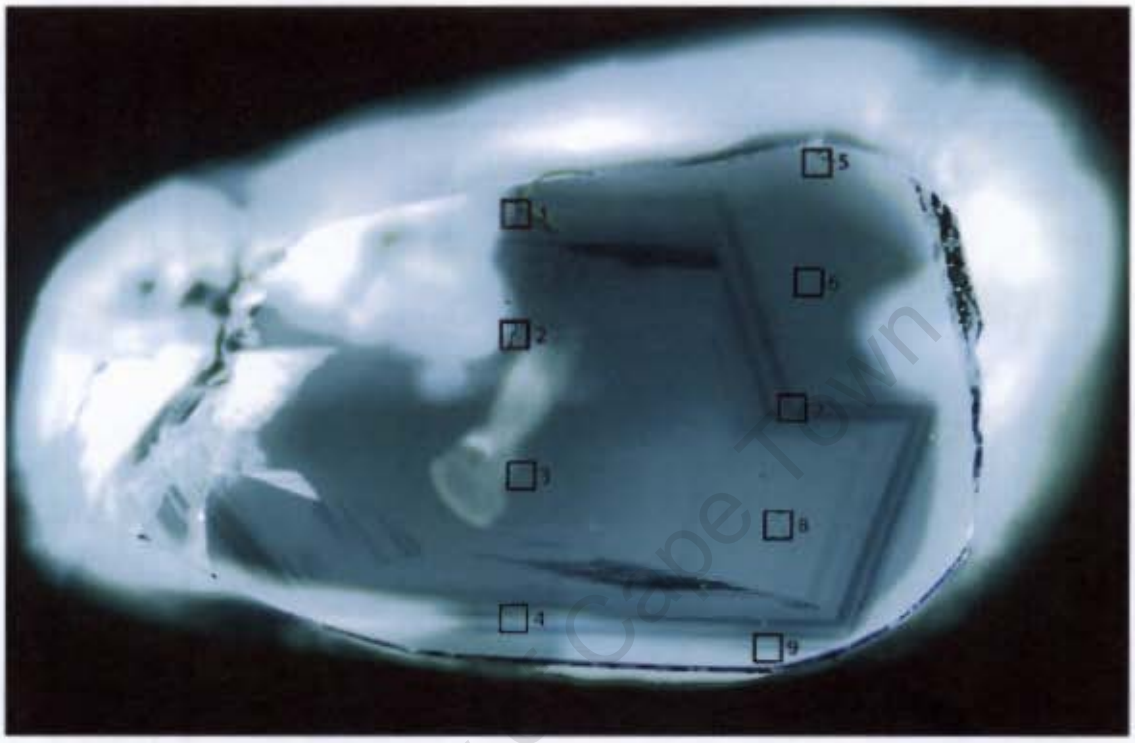

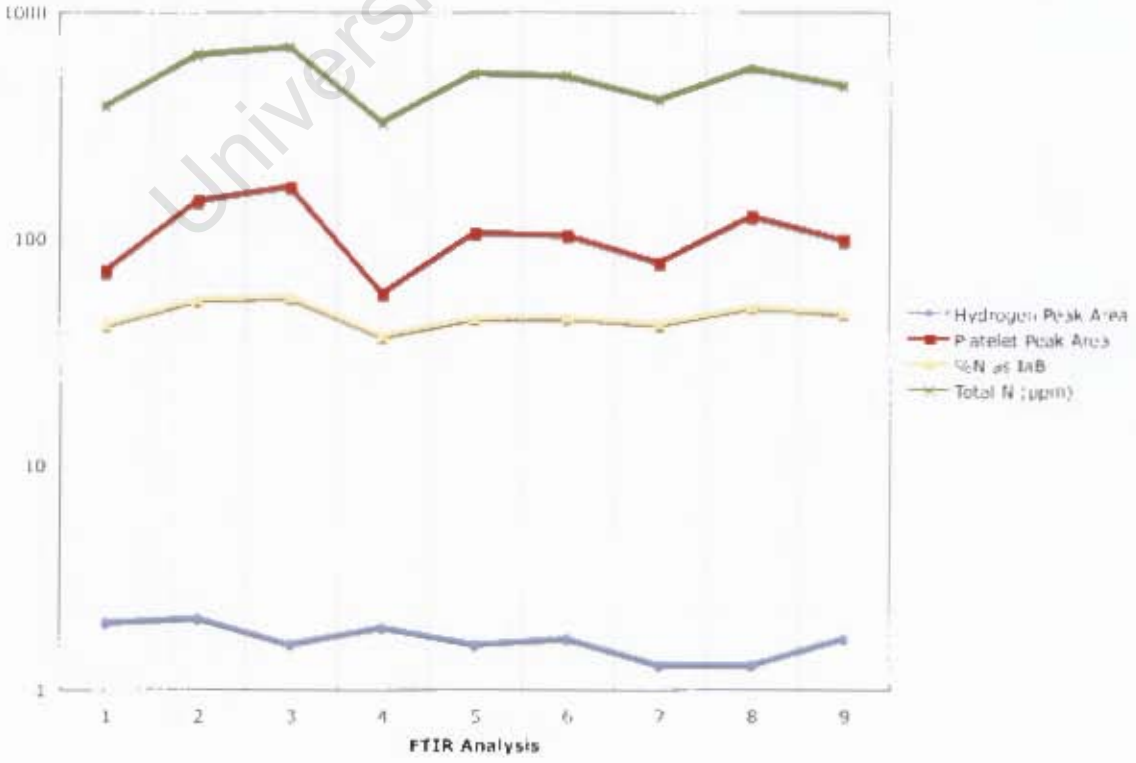

EL51 FTIR Traverse

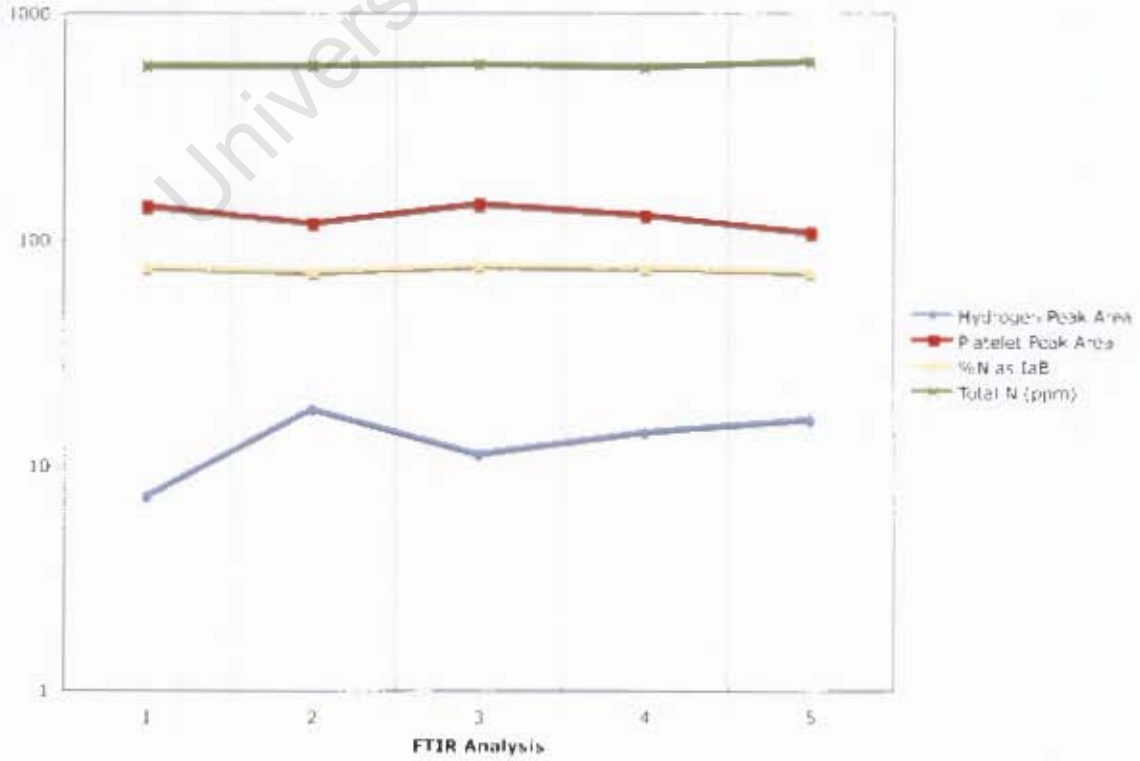

EL52 FTIR Traverse

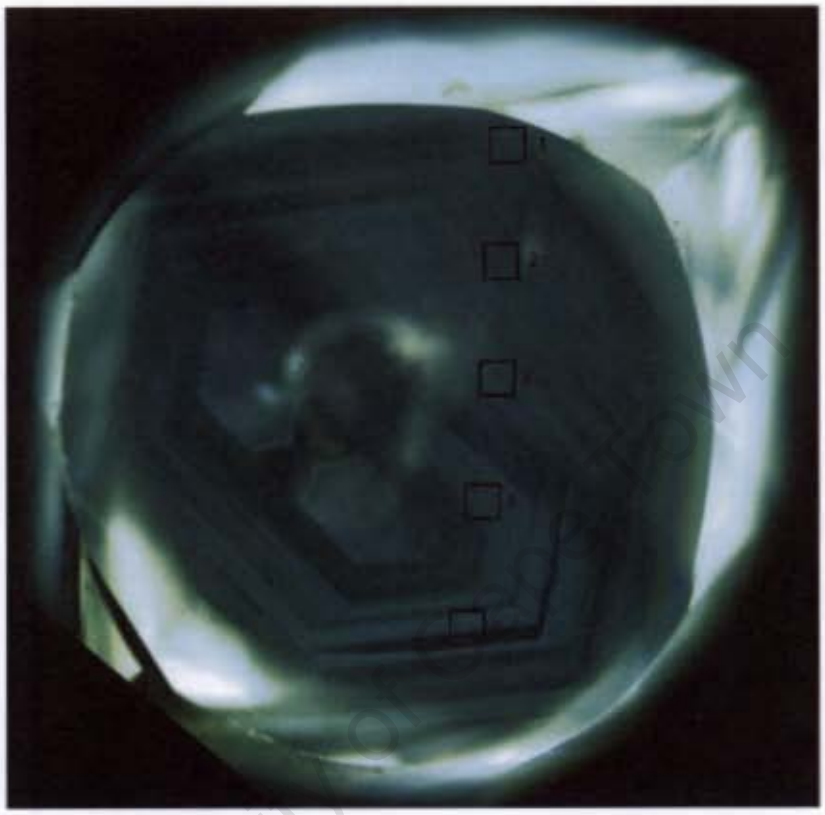

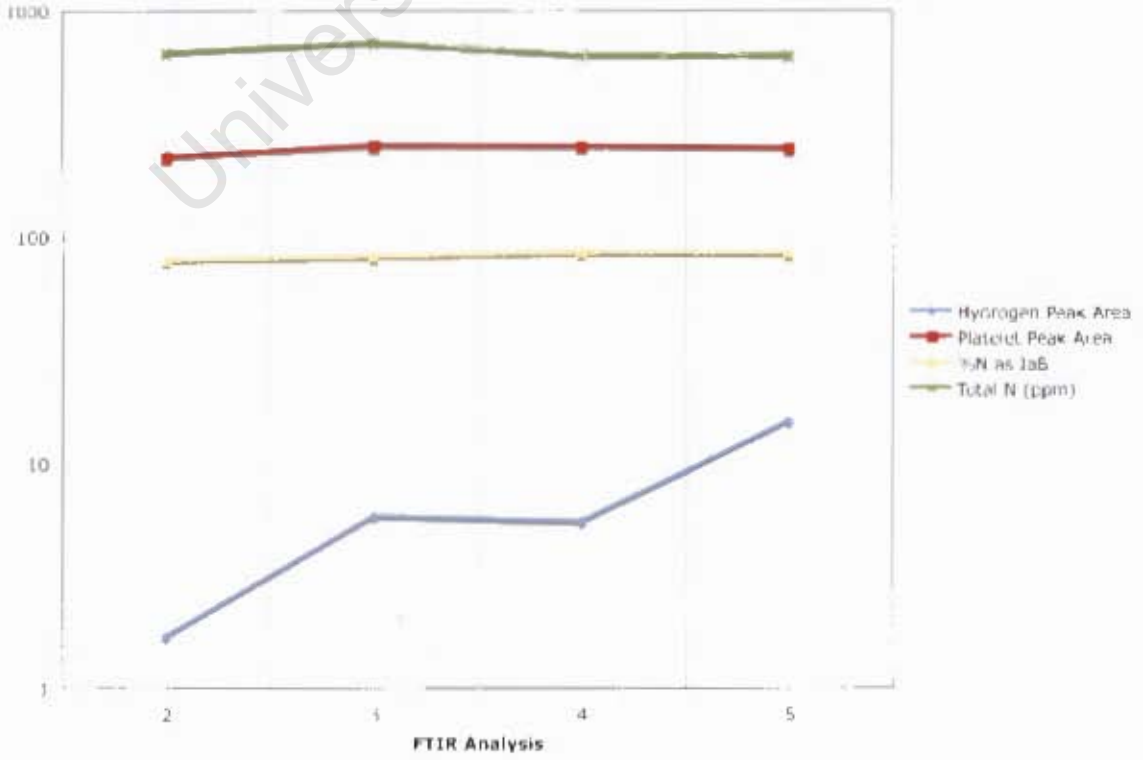

EL53 FTIR Traverse

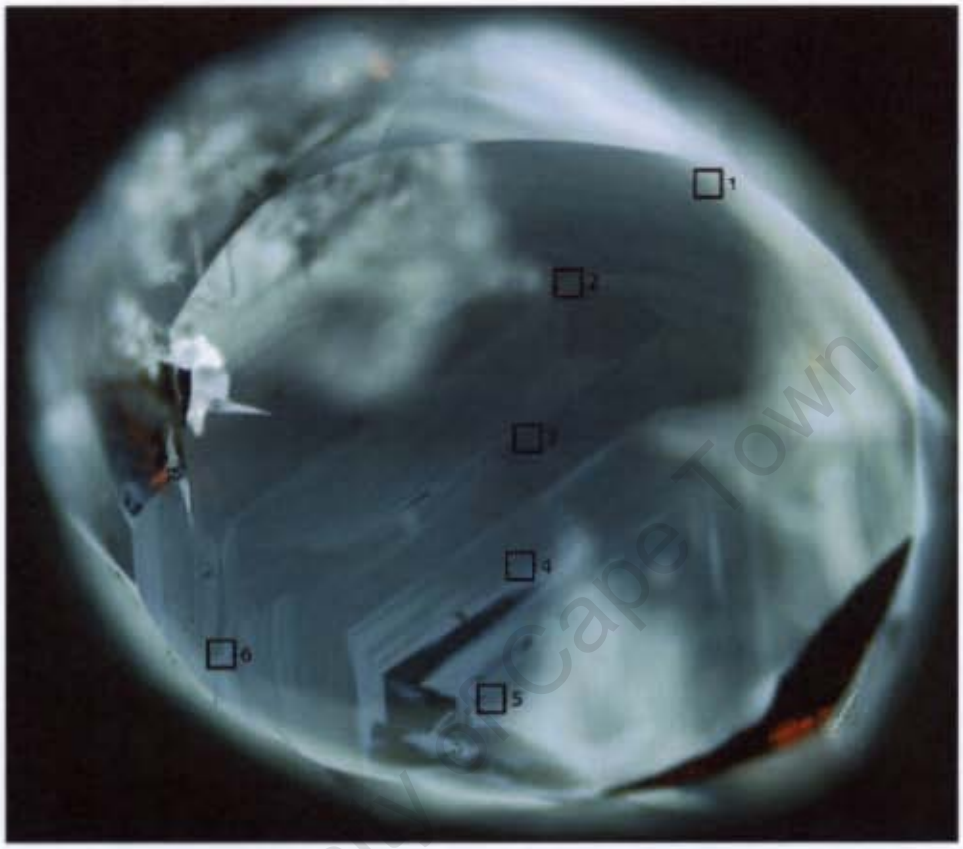

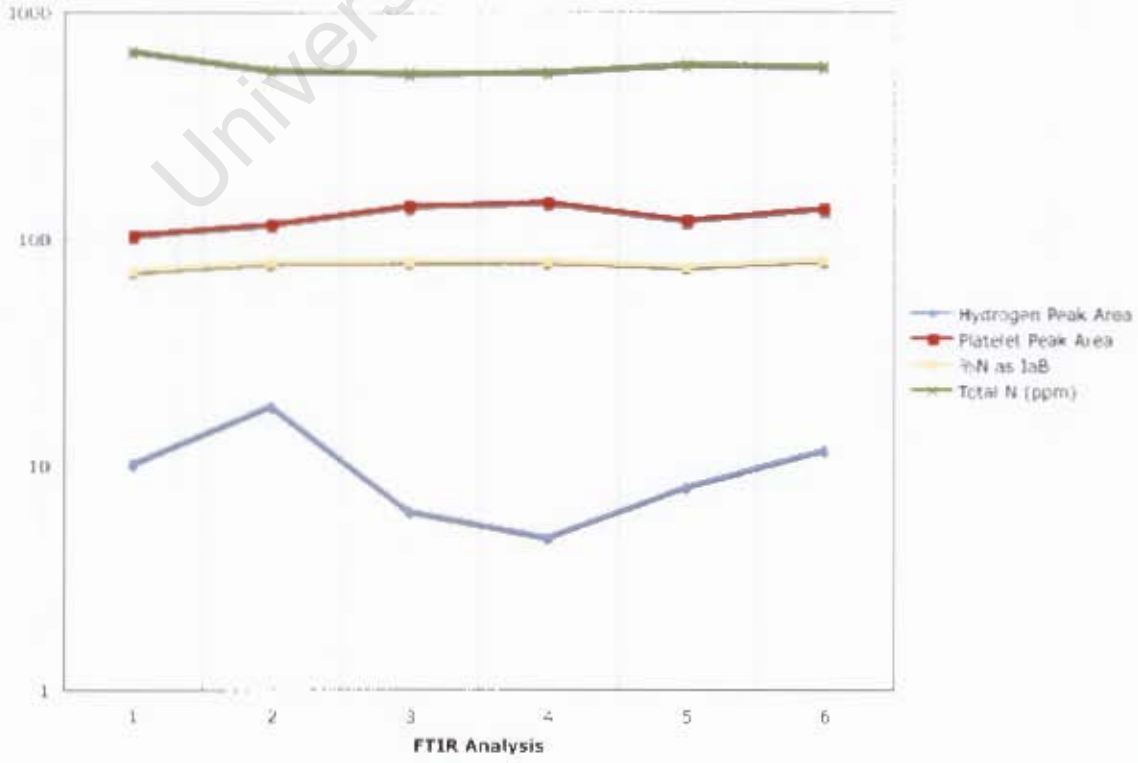

EL54 FTIR Traverse

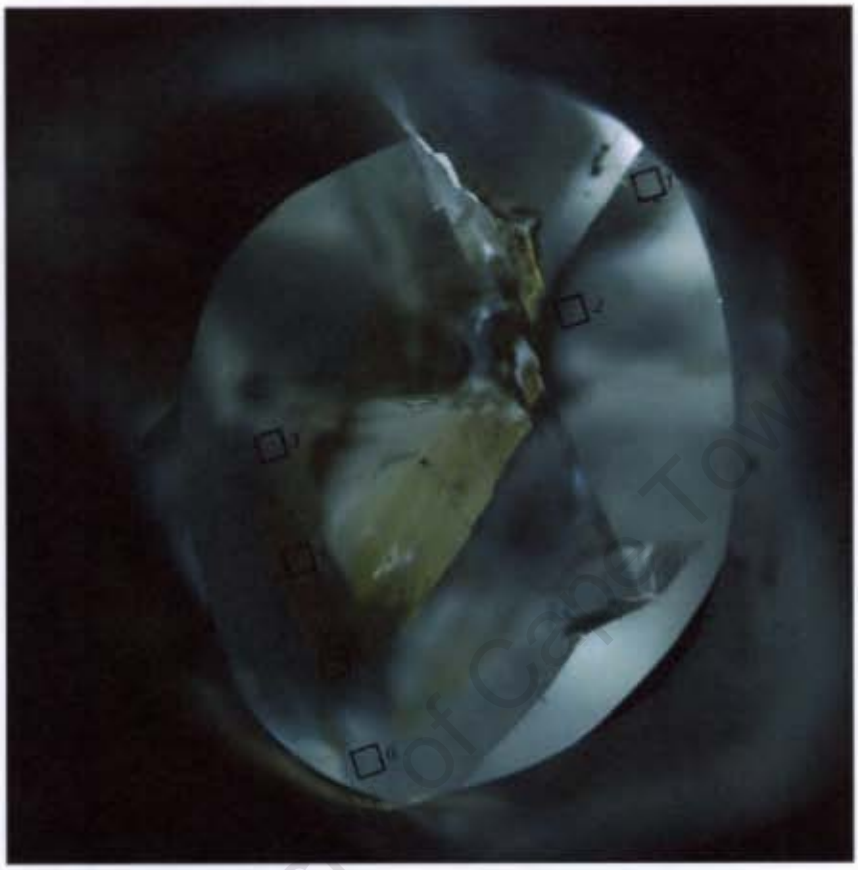

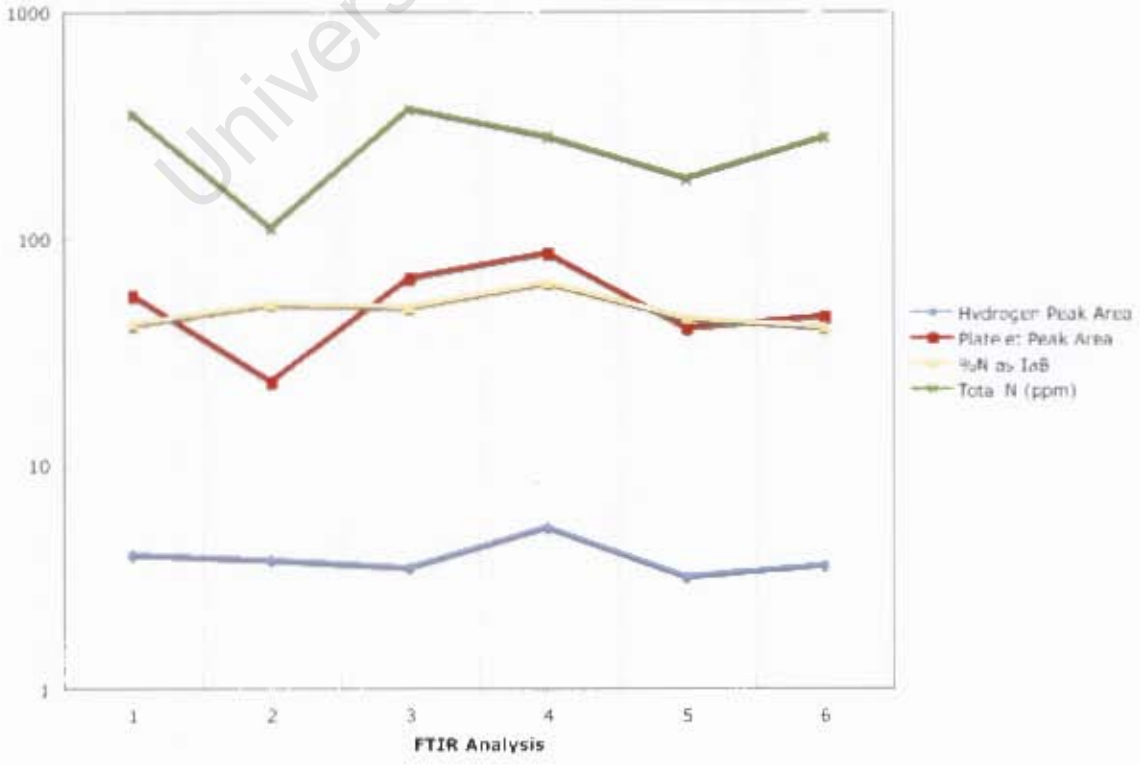

EL55 FTIR Traverse

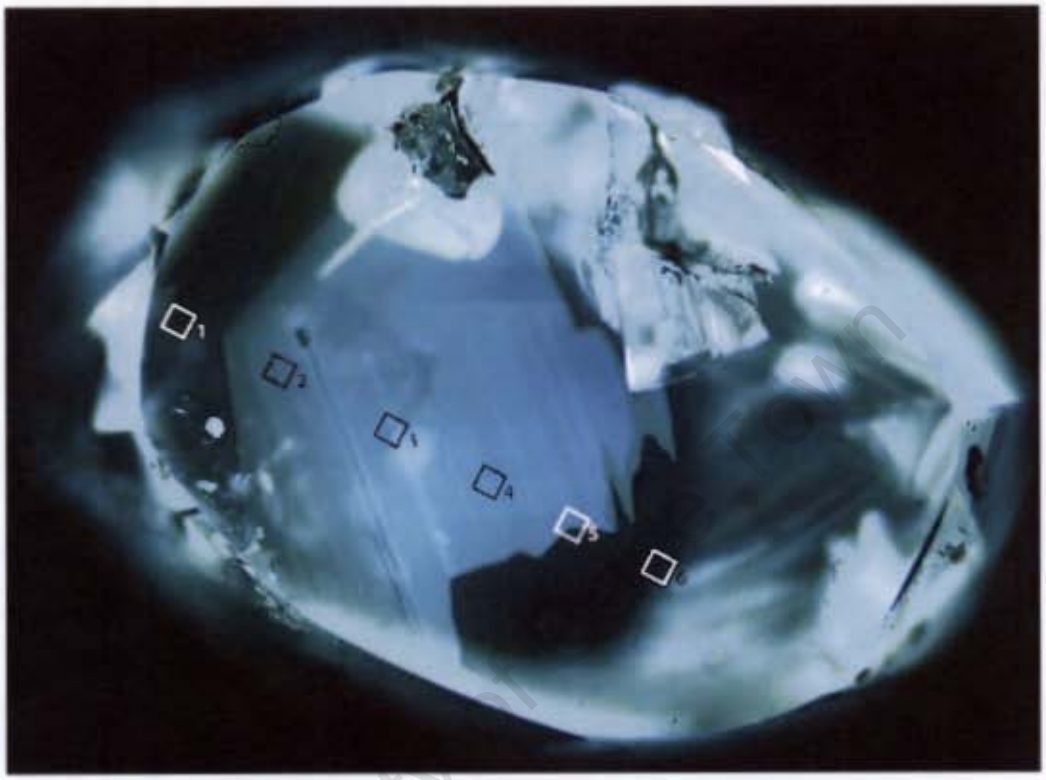

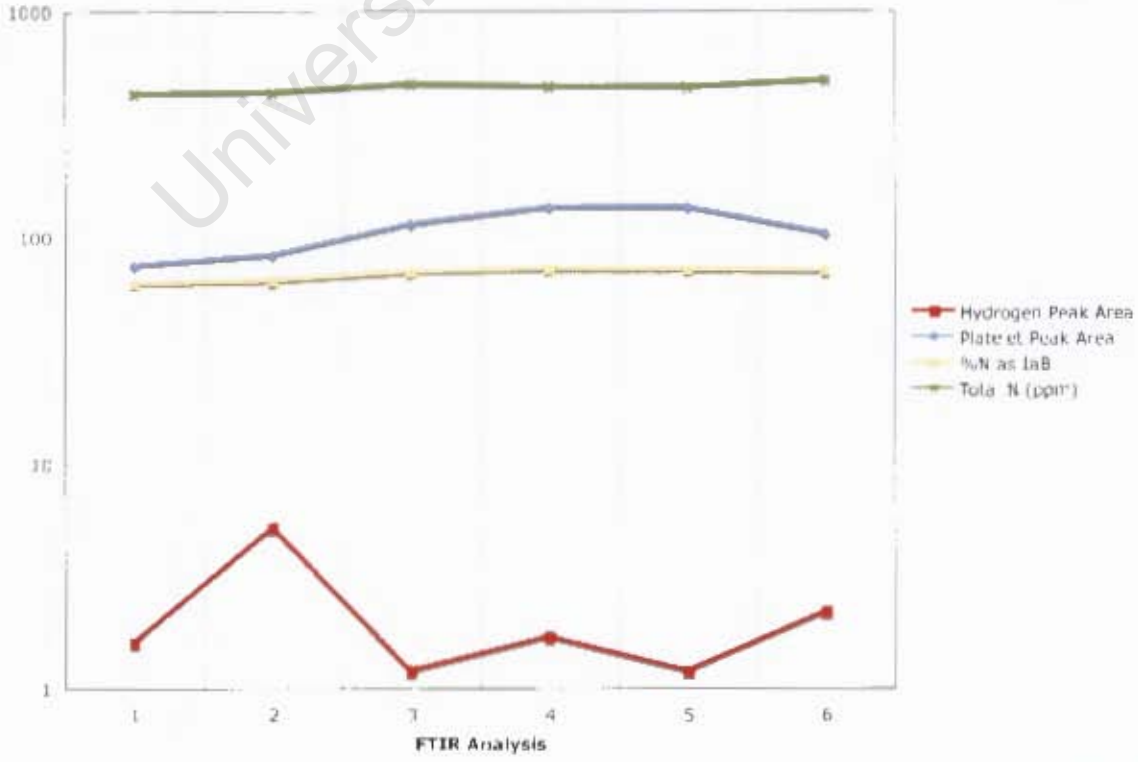

EL56 FTIR Traverse

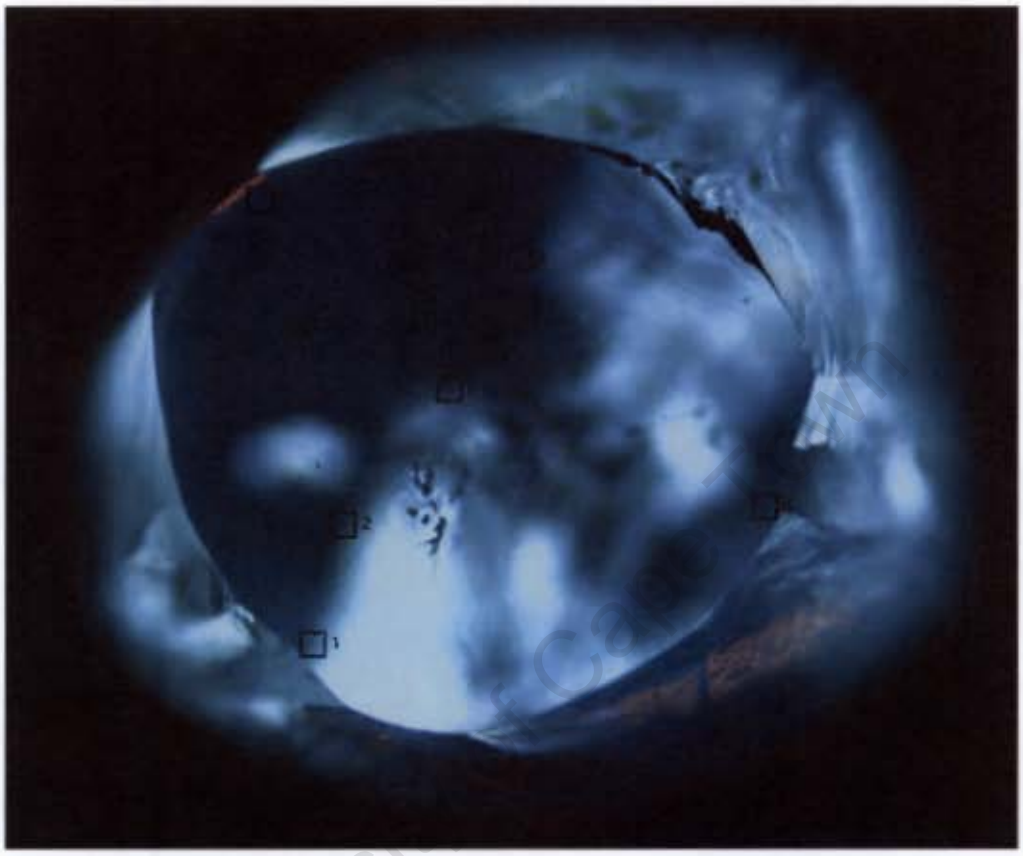

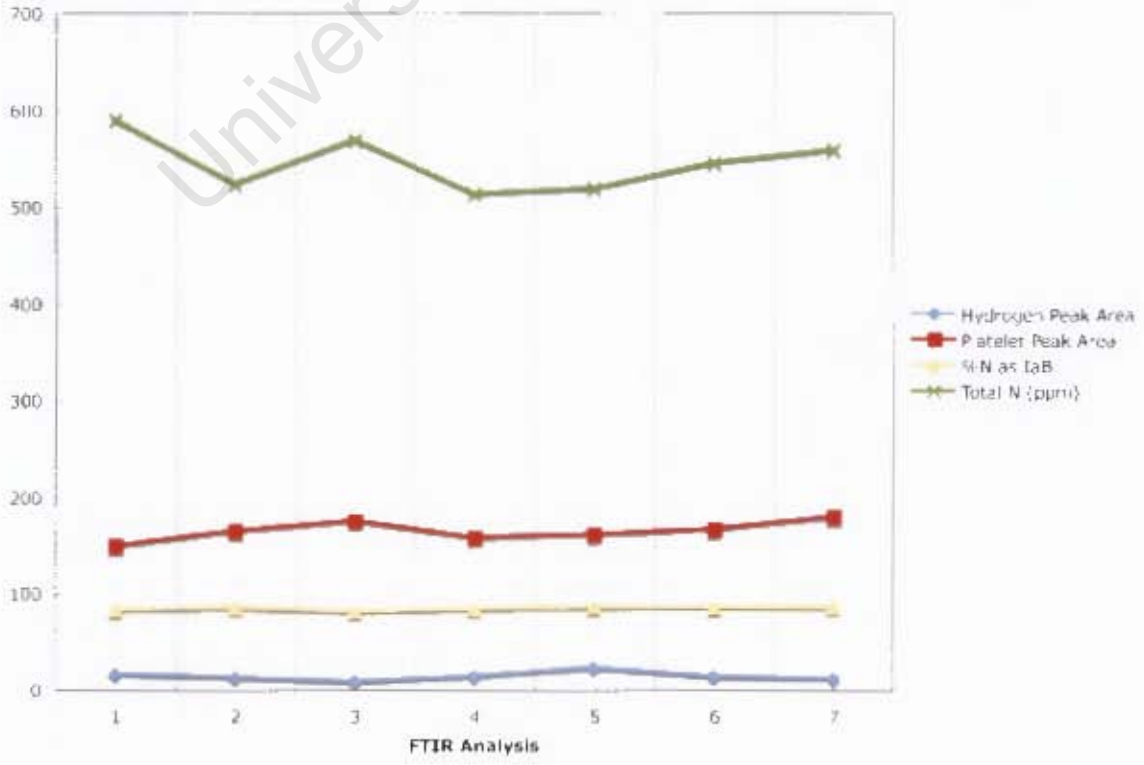

EL59 FTIR Traverse

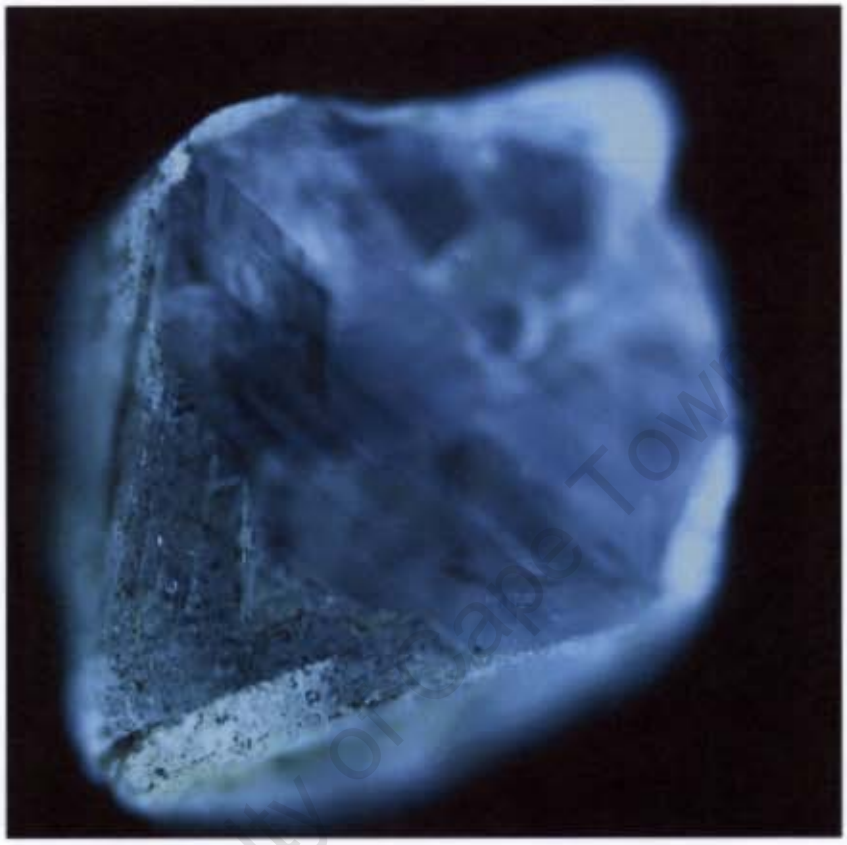

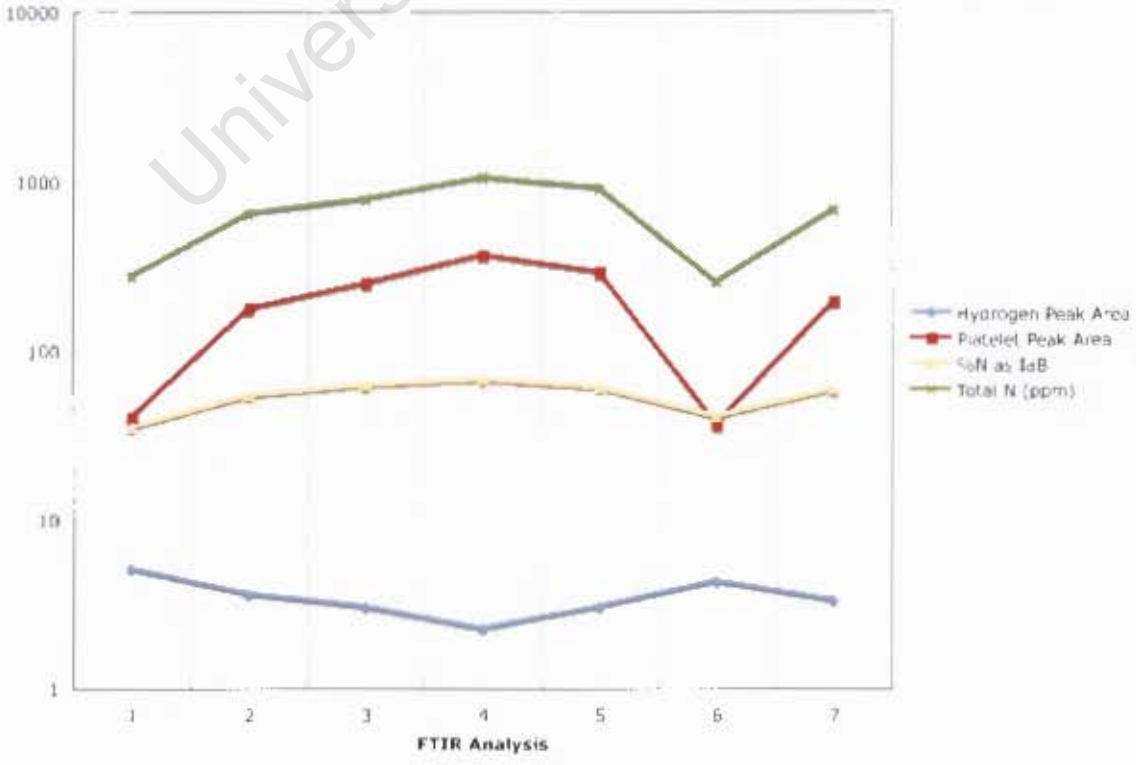

EL61 FTIR Traverse

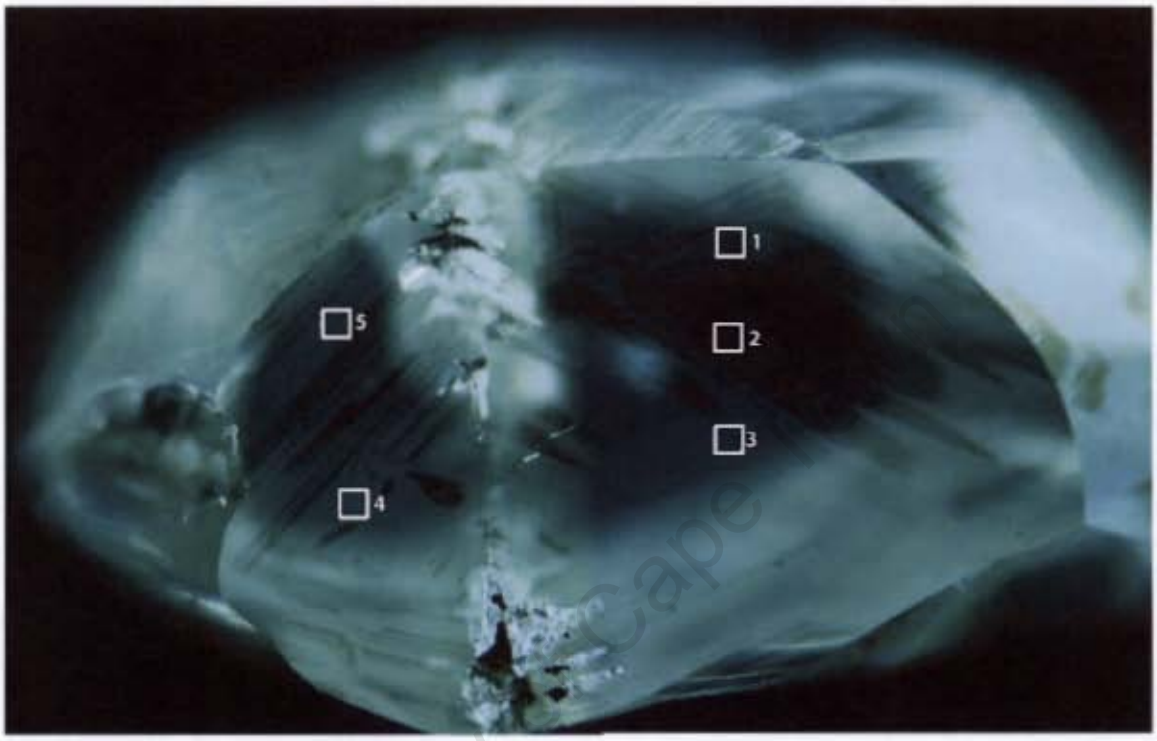

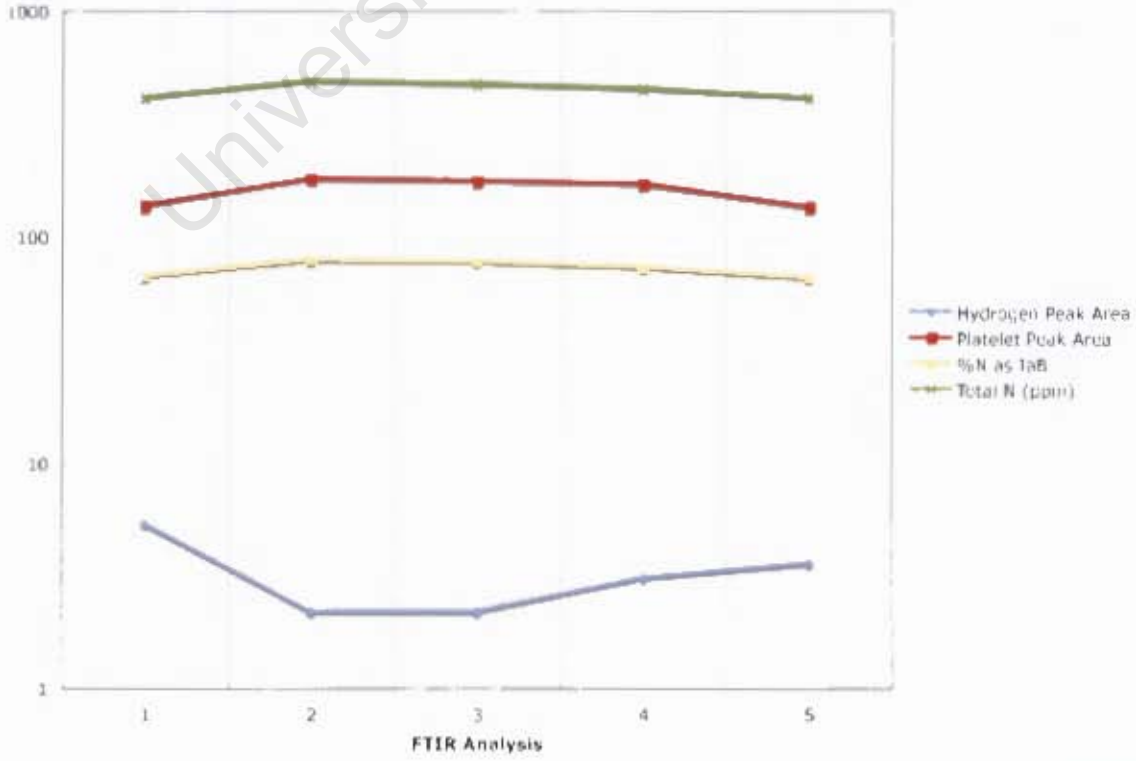

EL62 FTIR Traverse

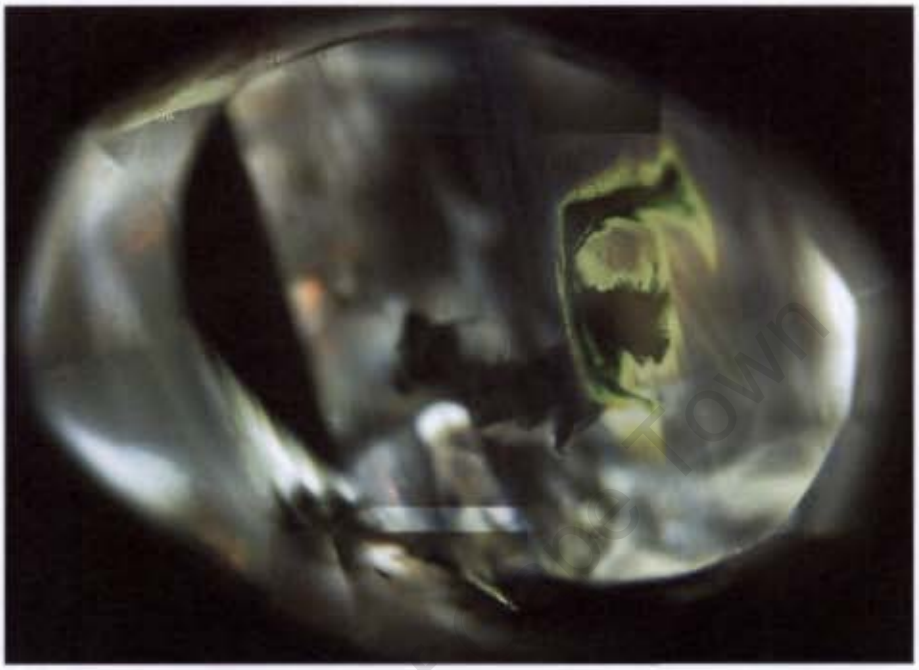

The diamond fractured during cutting and only one side could be polished. As a result of the light reflections, growth zoning could not be viewed

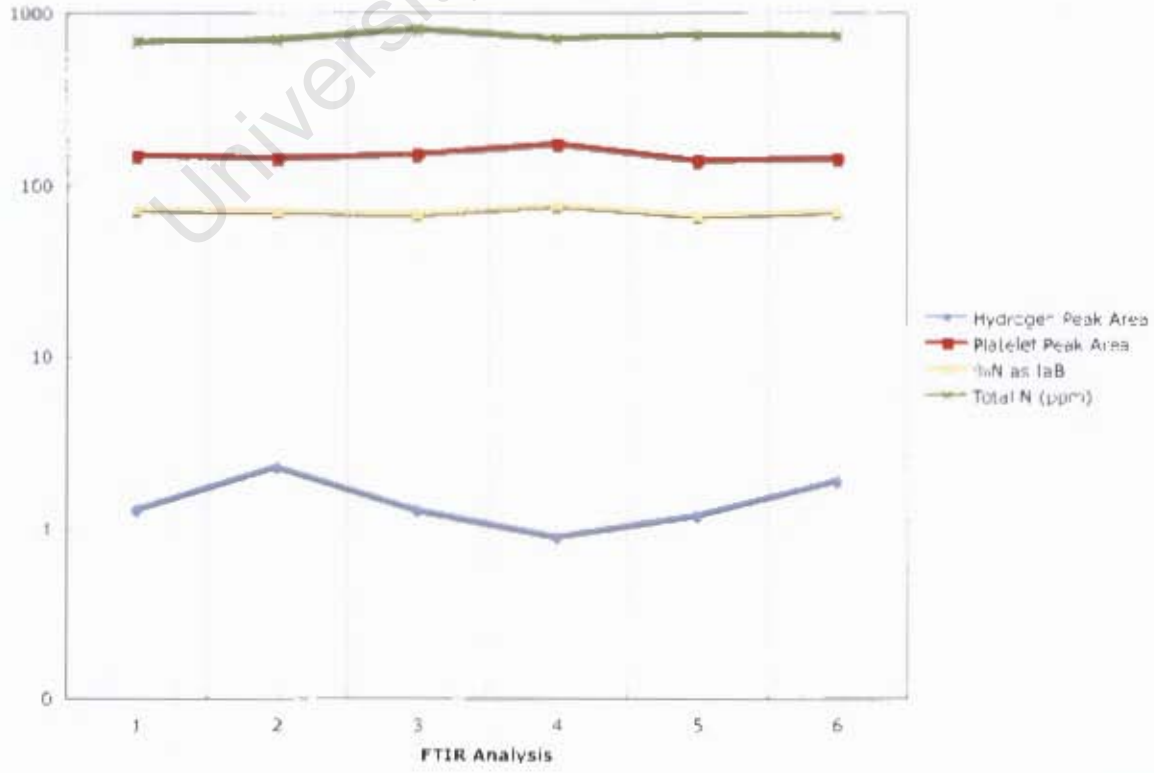

EL64 FTIR Traverse

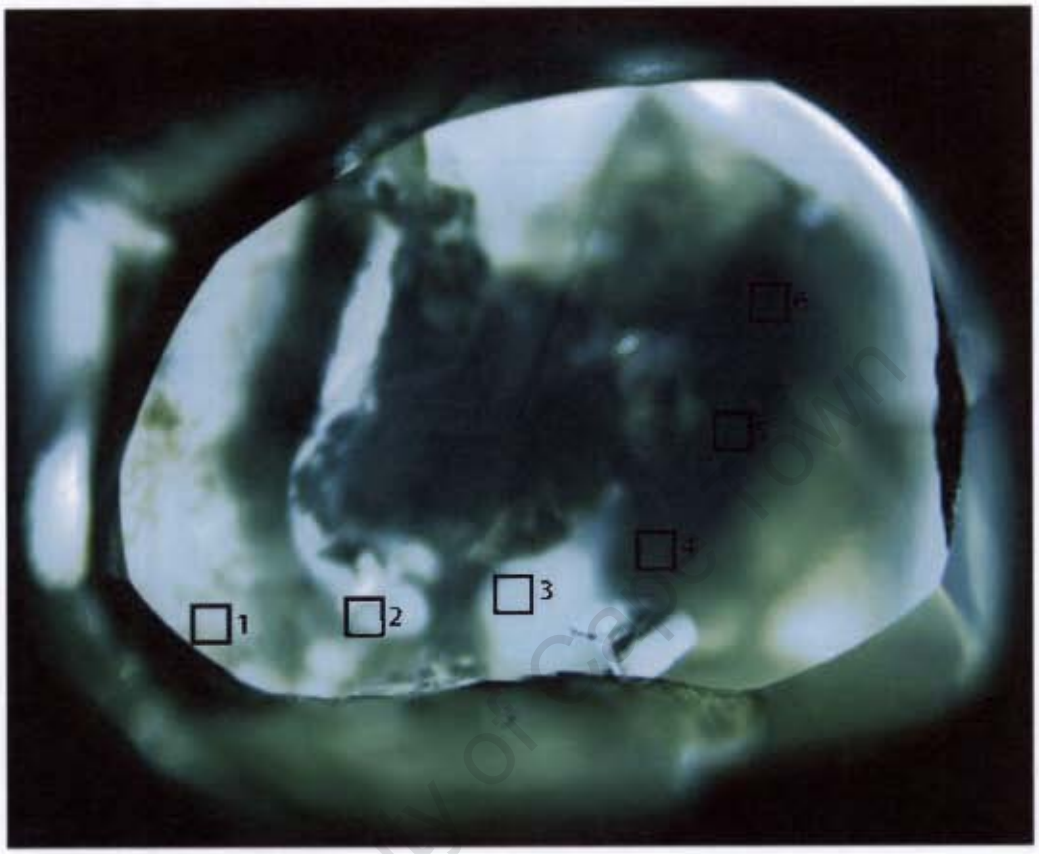

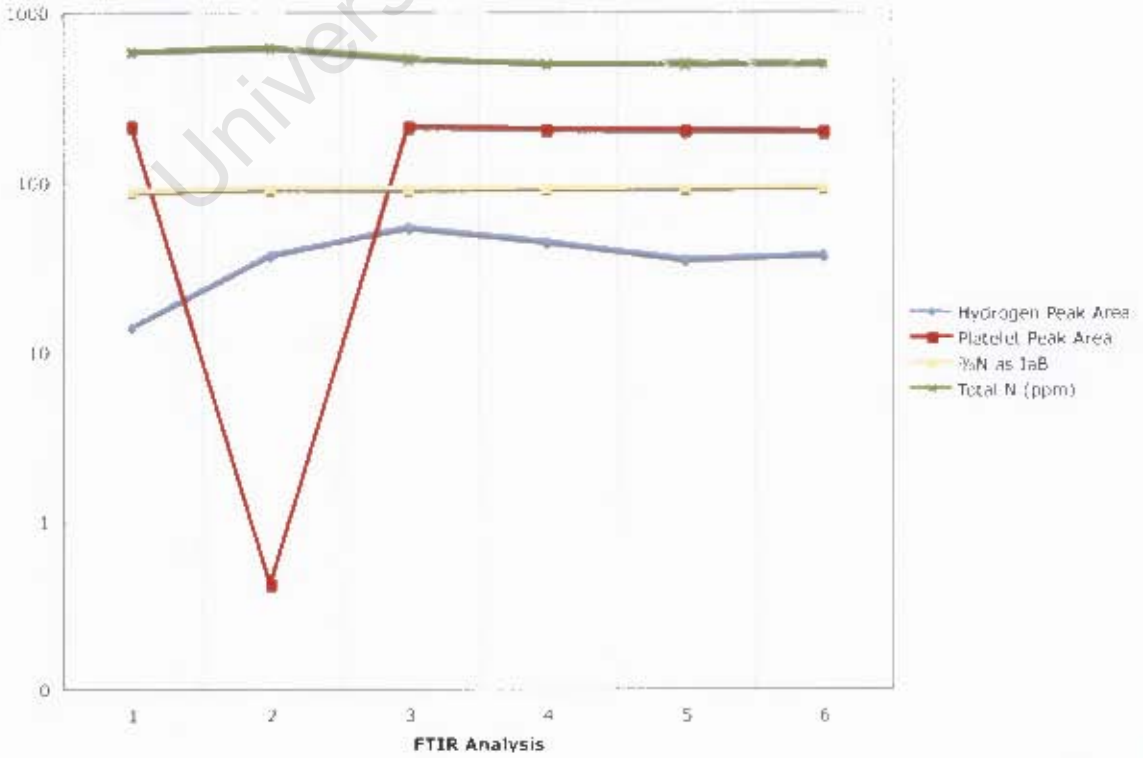

EL65 FTIR Traverse

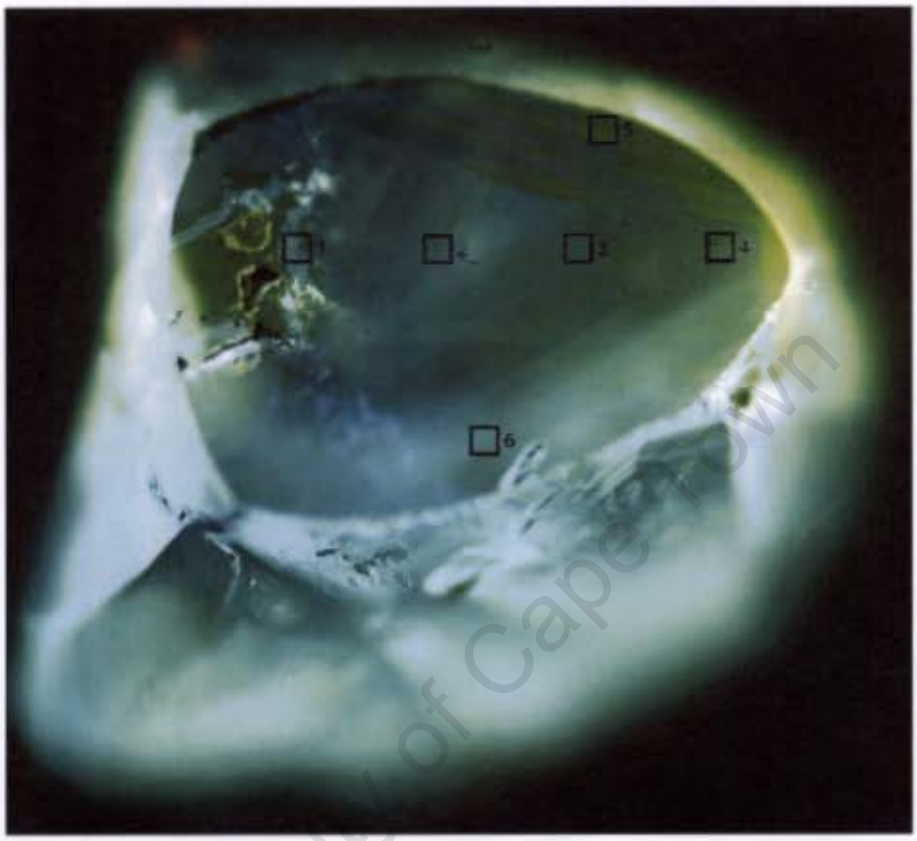

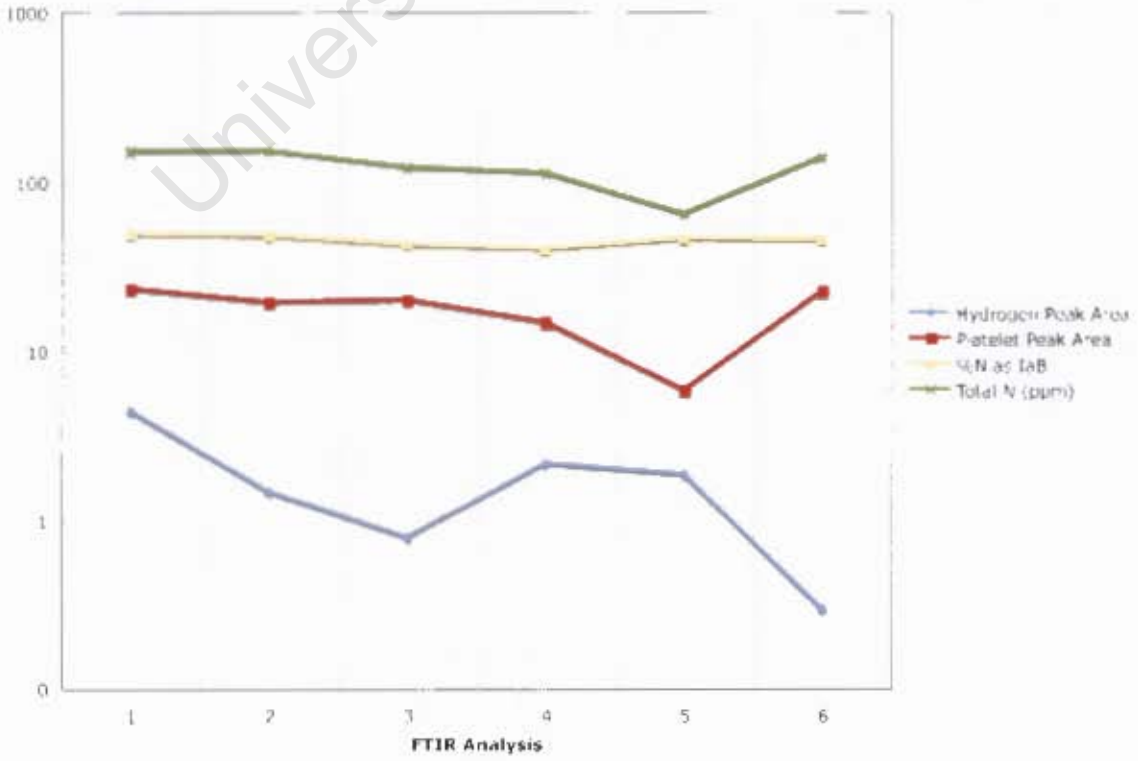

EL67 FTIR Traverse

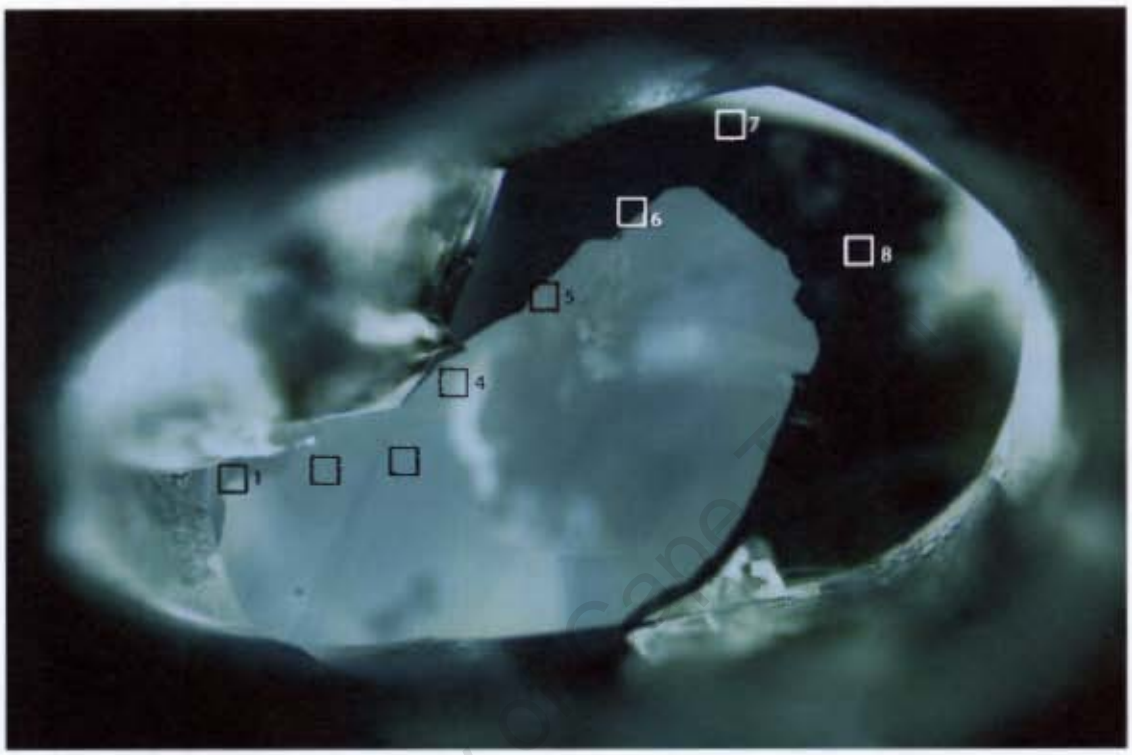

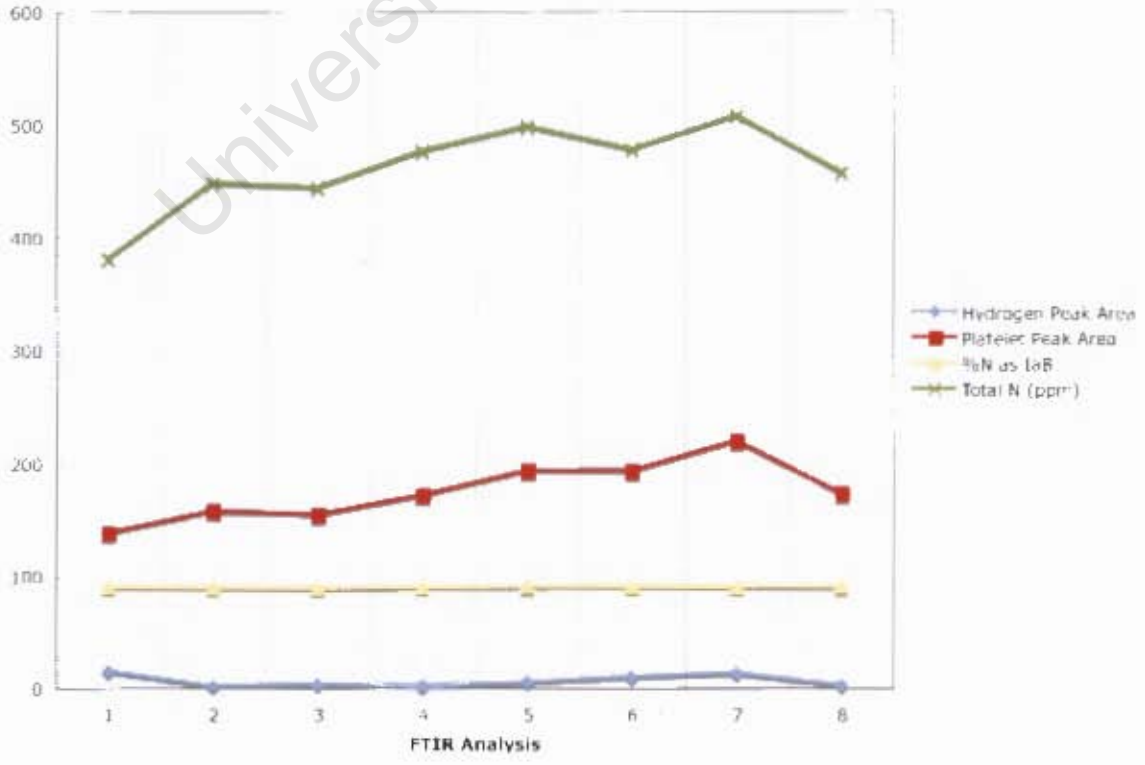

EL69 FTIR Traverse

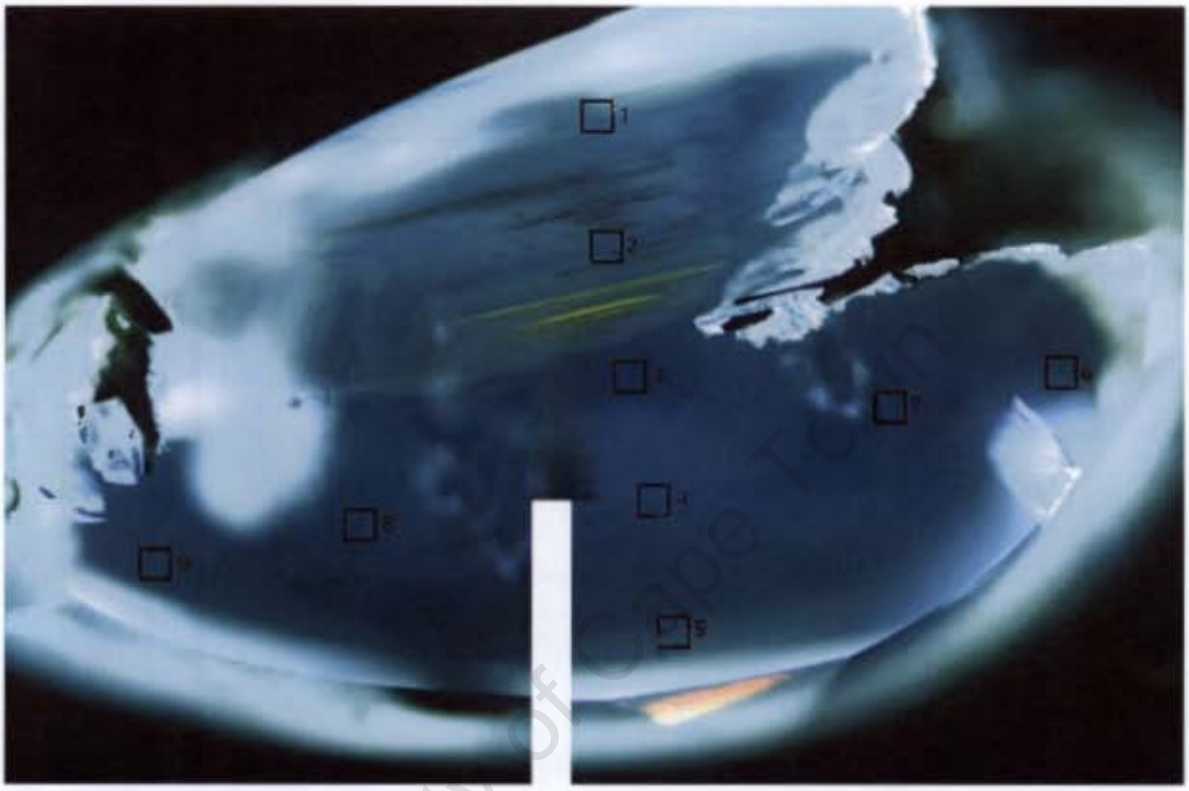

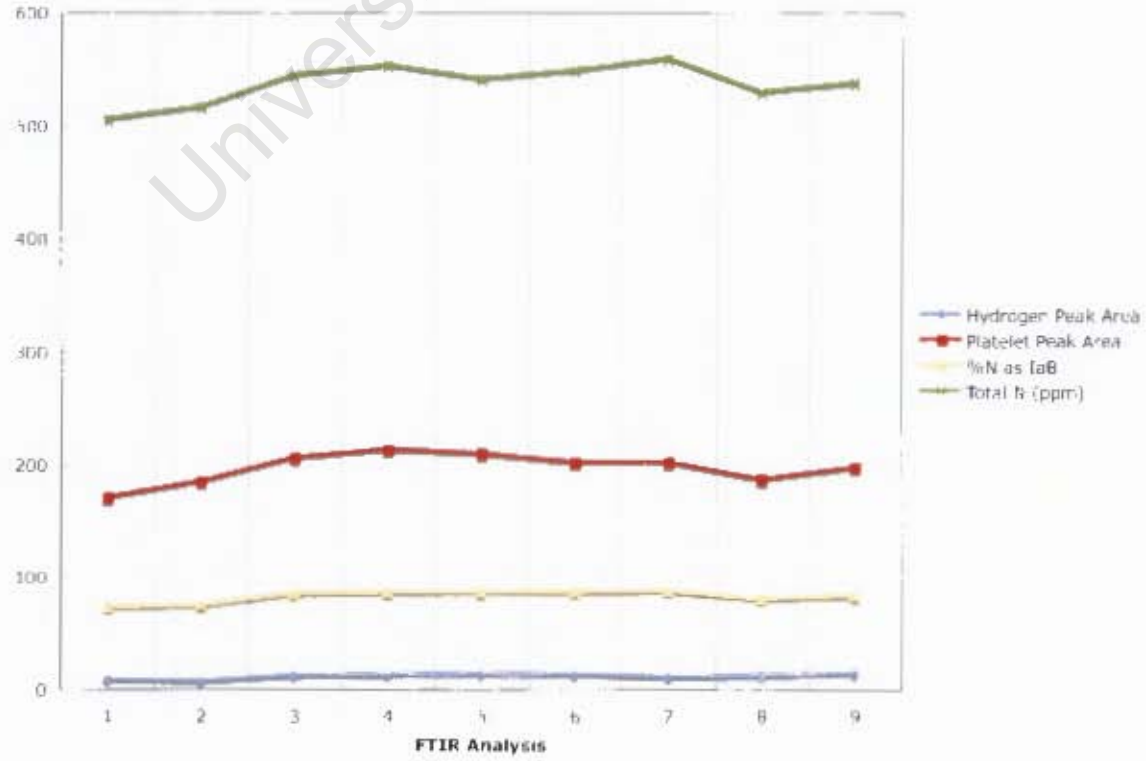

Appendix 3: Diamond Plate Photos and Cathodoluminescence (CL) Images

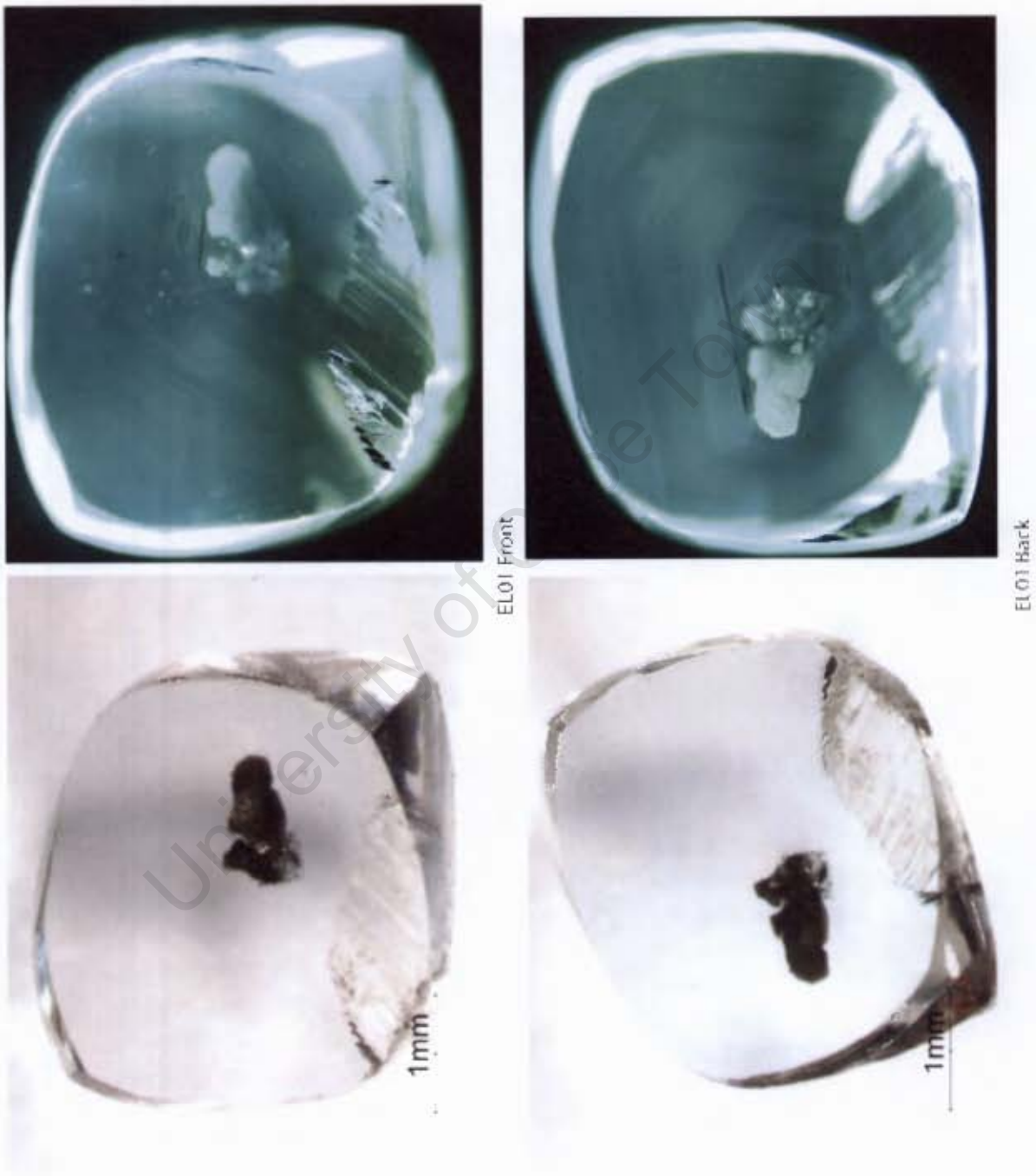

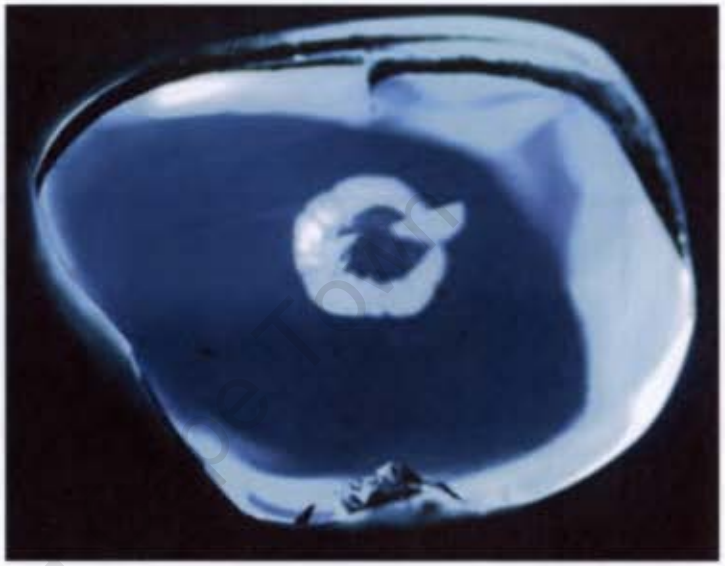

EL05 front

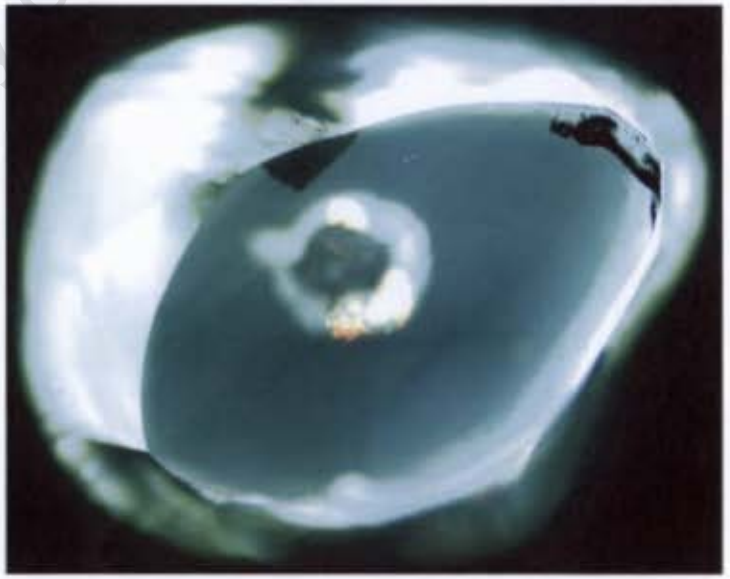

EL05 back

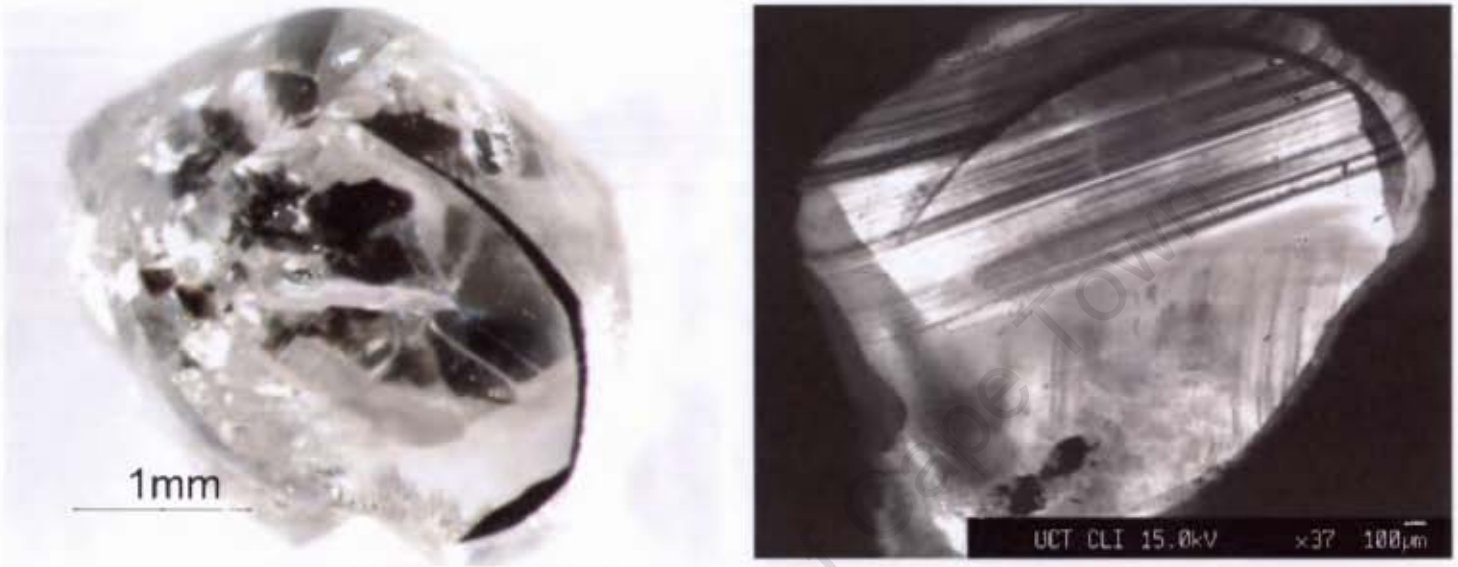

EL10 front

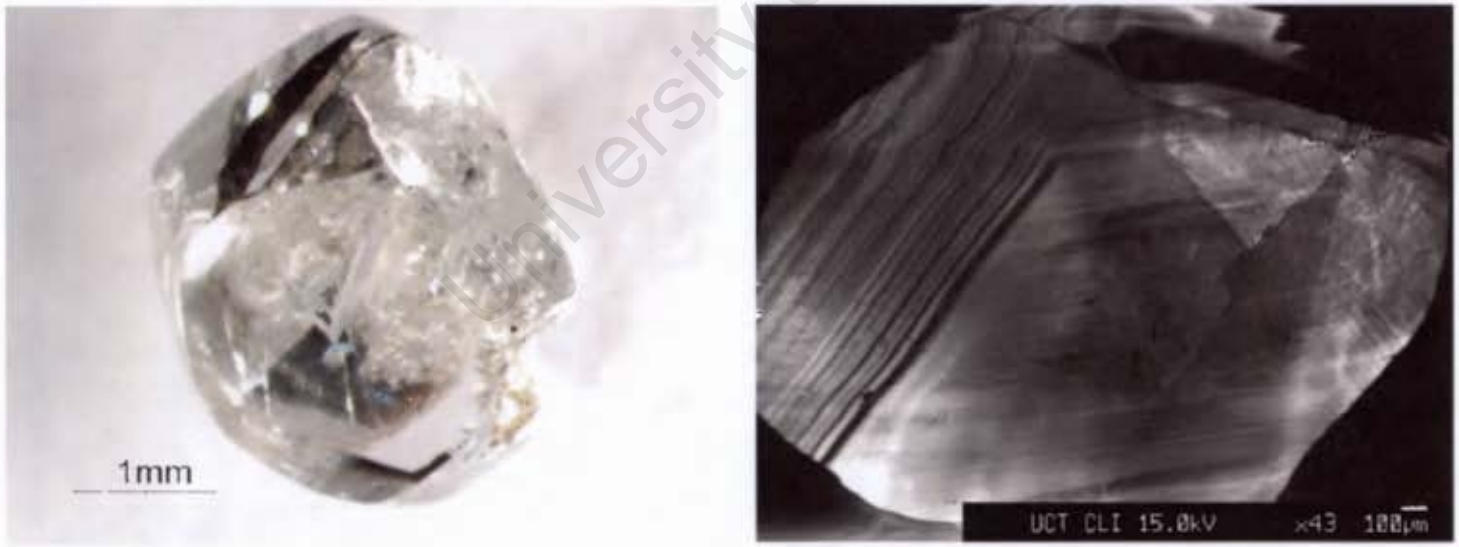

EL10 back

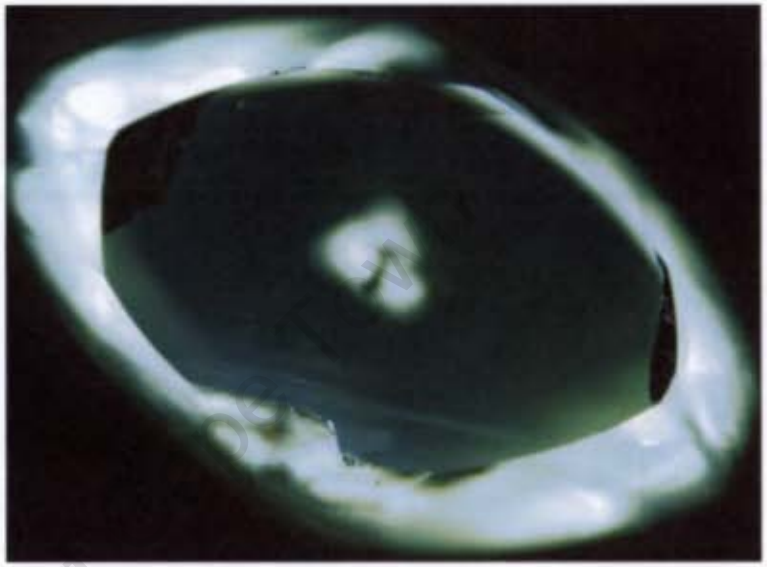

EL12 front

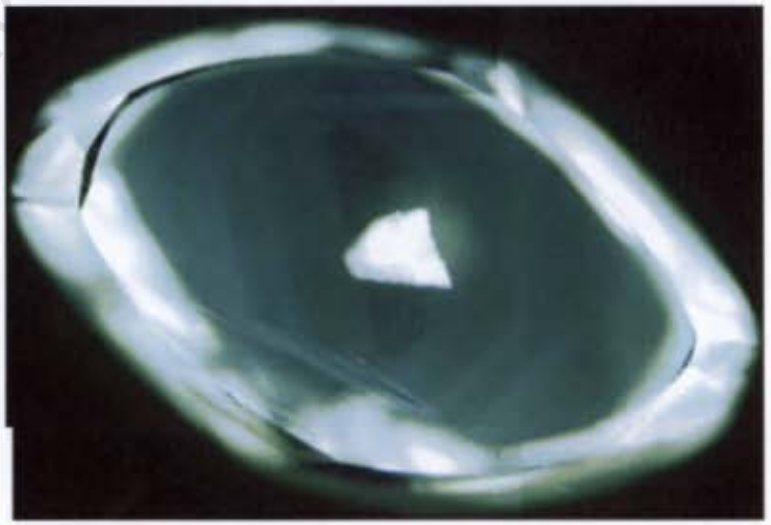

EL12 back

EL16 front

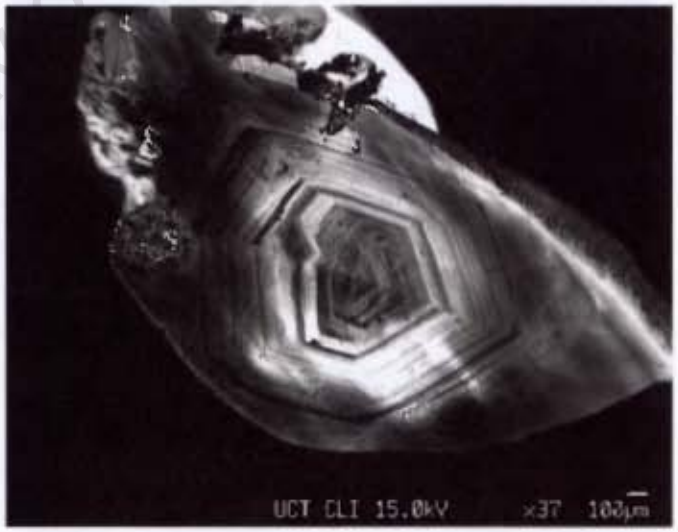

EL16 back

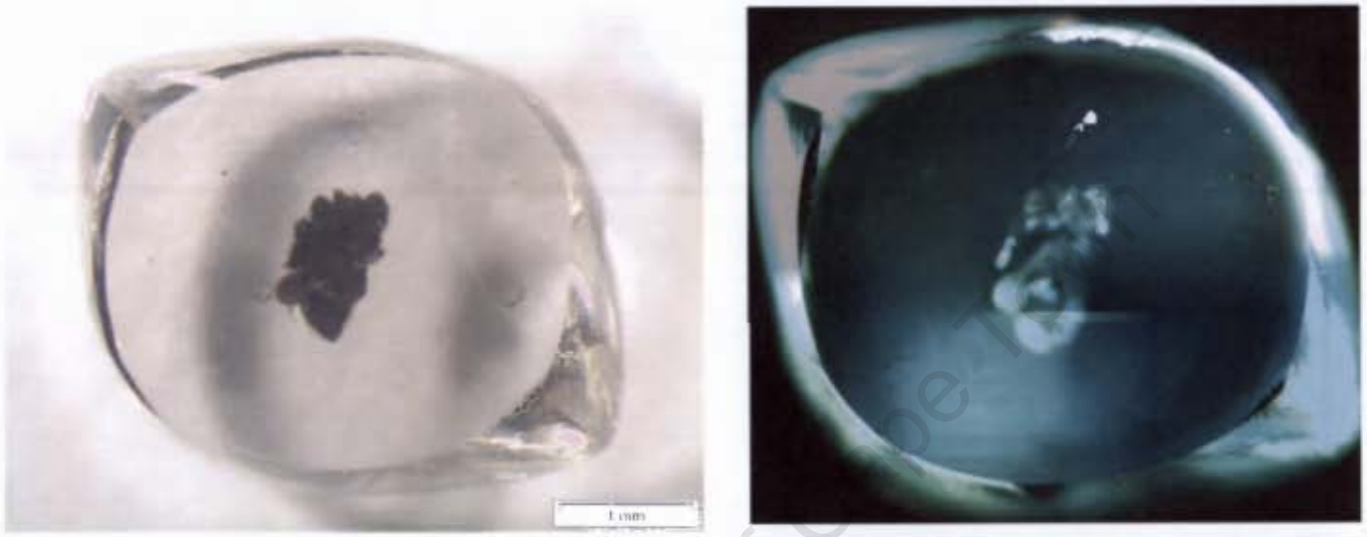

EL20 front

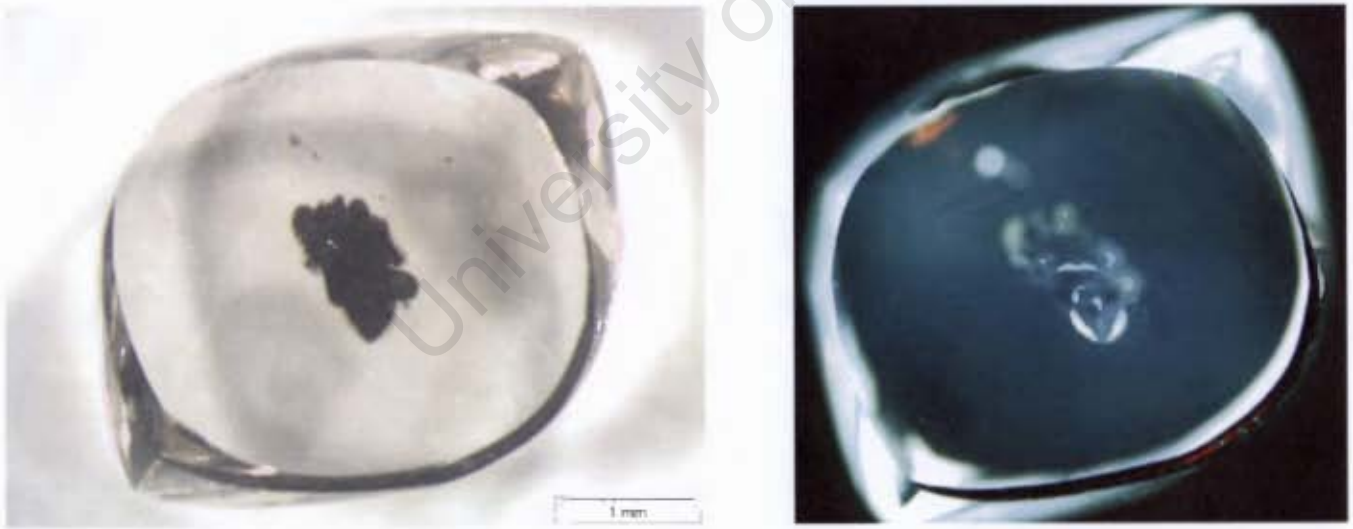

EL20 back

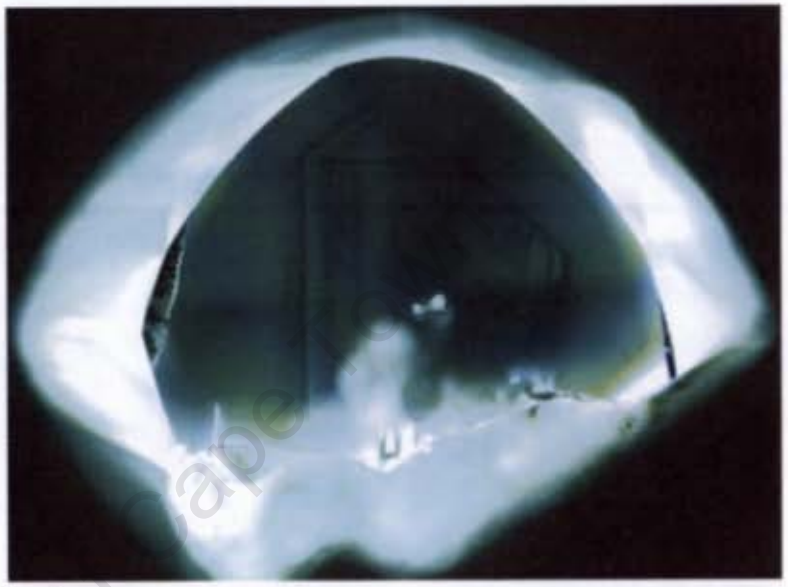

FL23 front

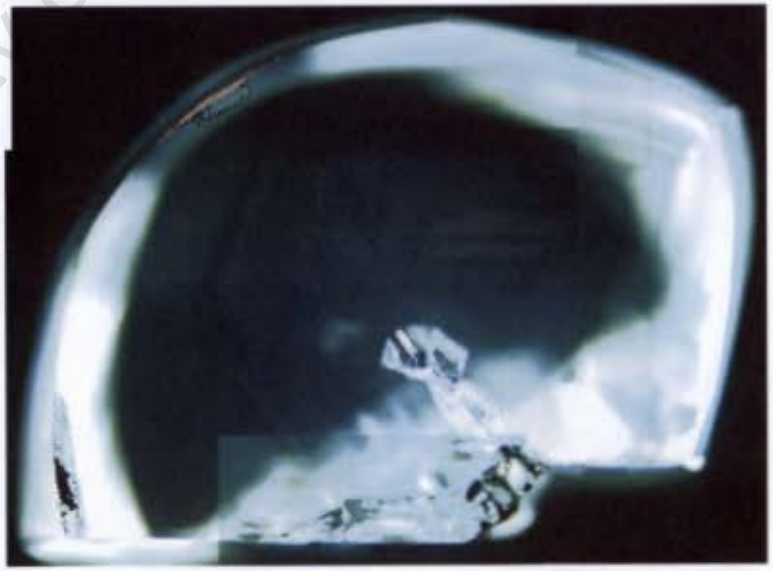

FL23 back

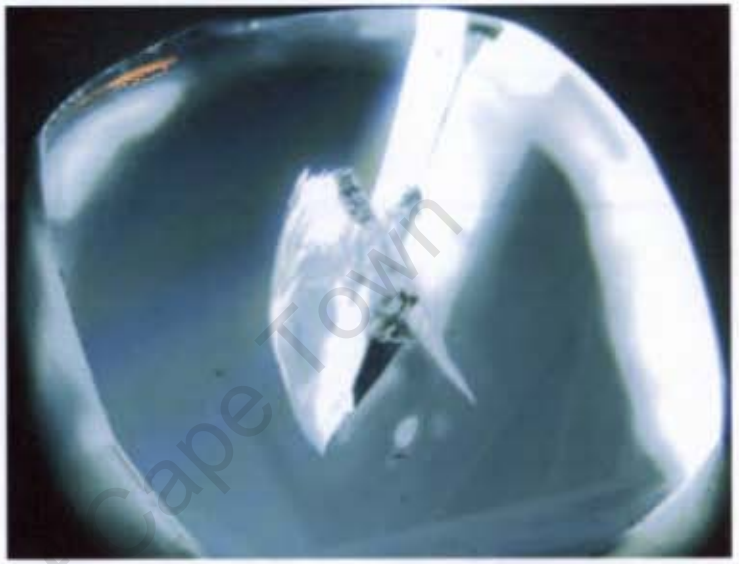

EL24 front

EL24 back

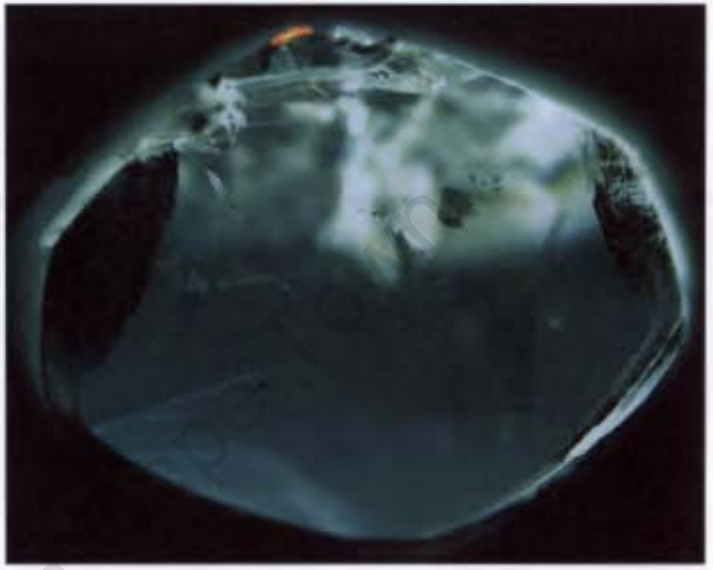

EL25 front

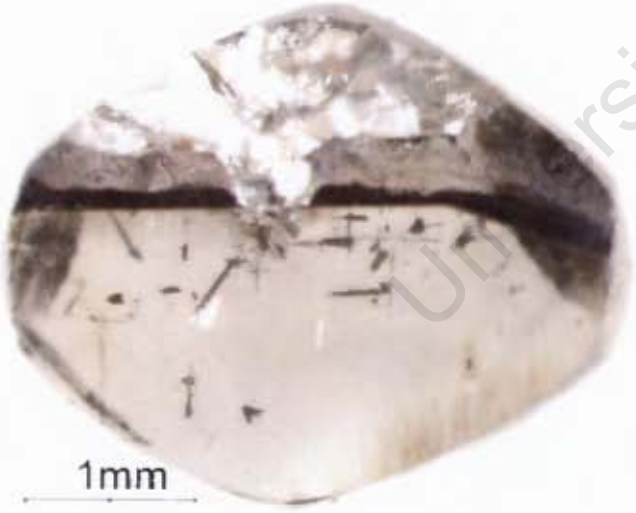

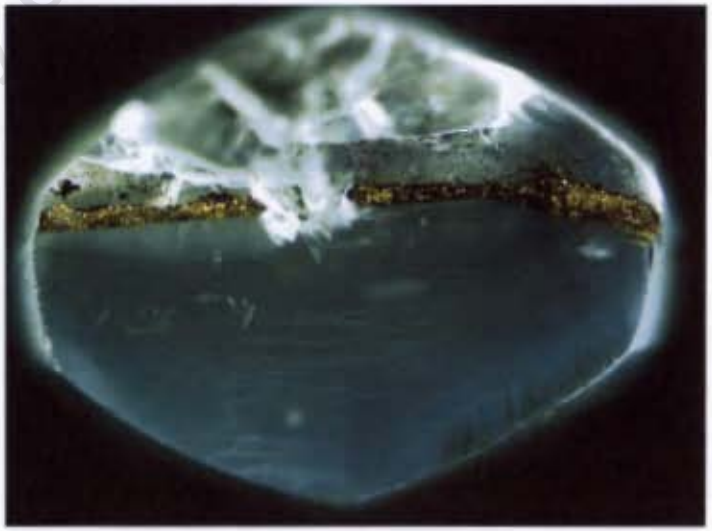

EL25 back

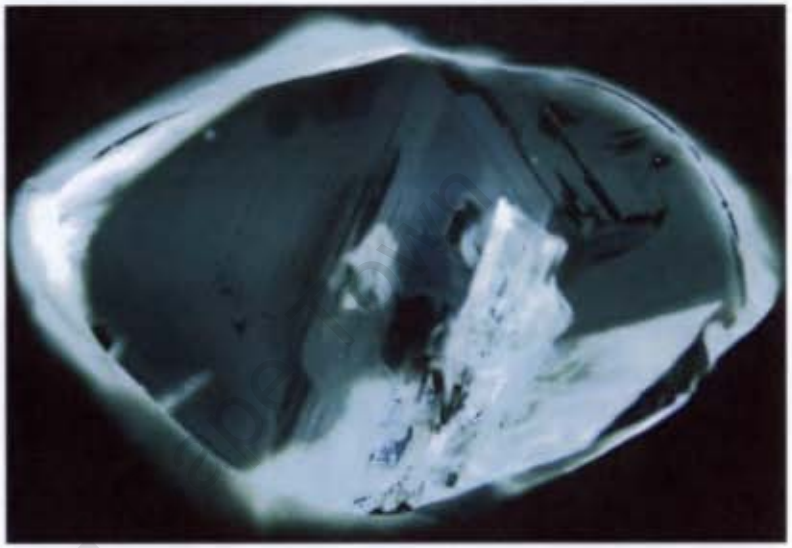

EL26 front

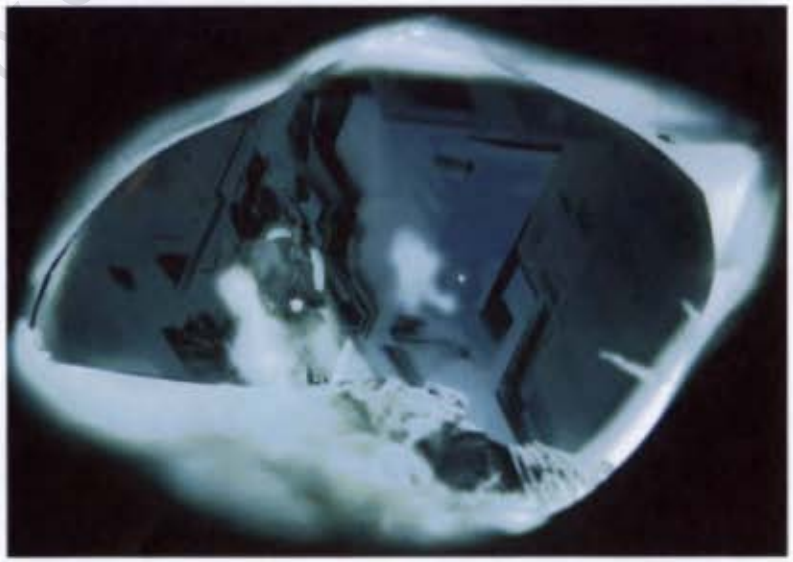

EL26 back

EL31 front

EL31 back

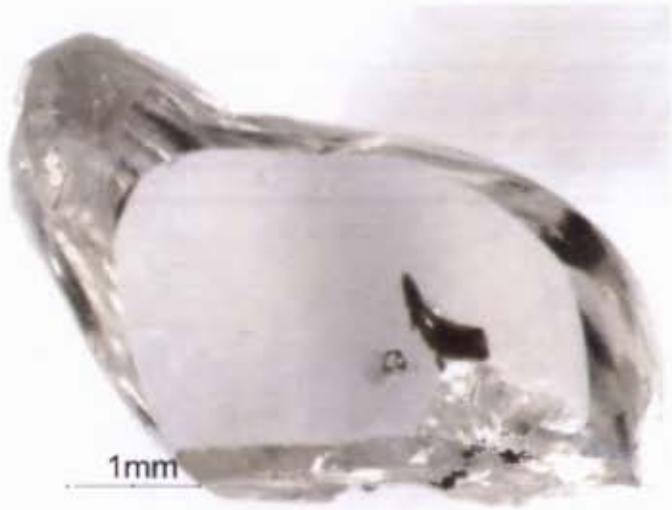

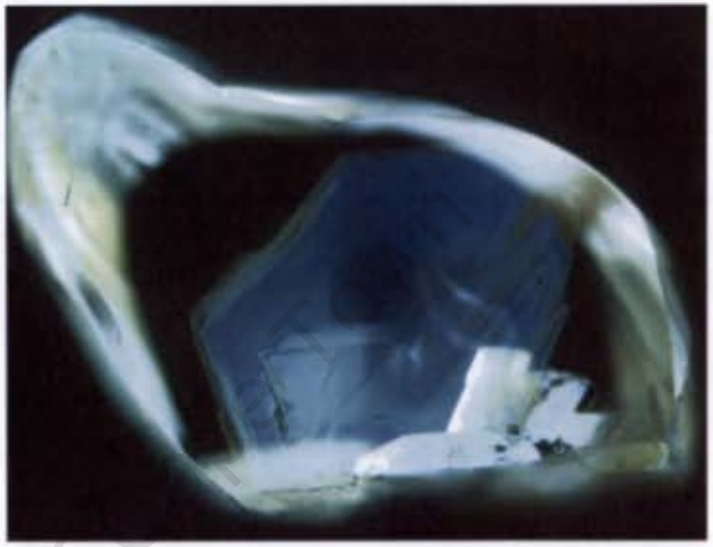

EL32 front

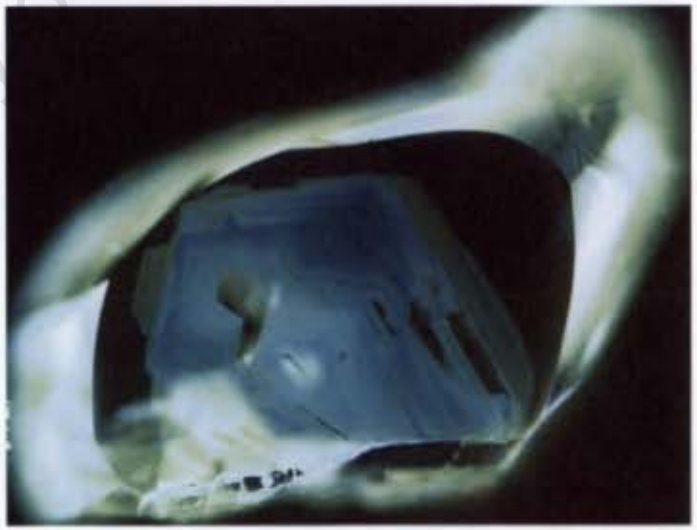

EL32 back

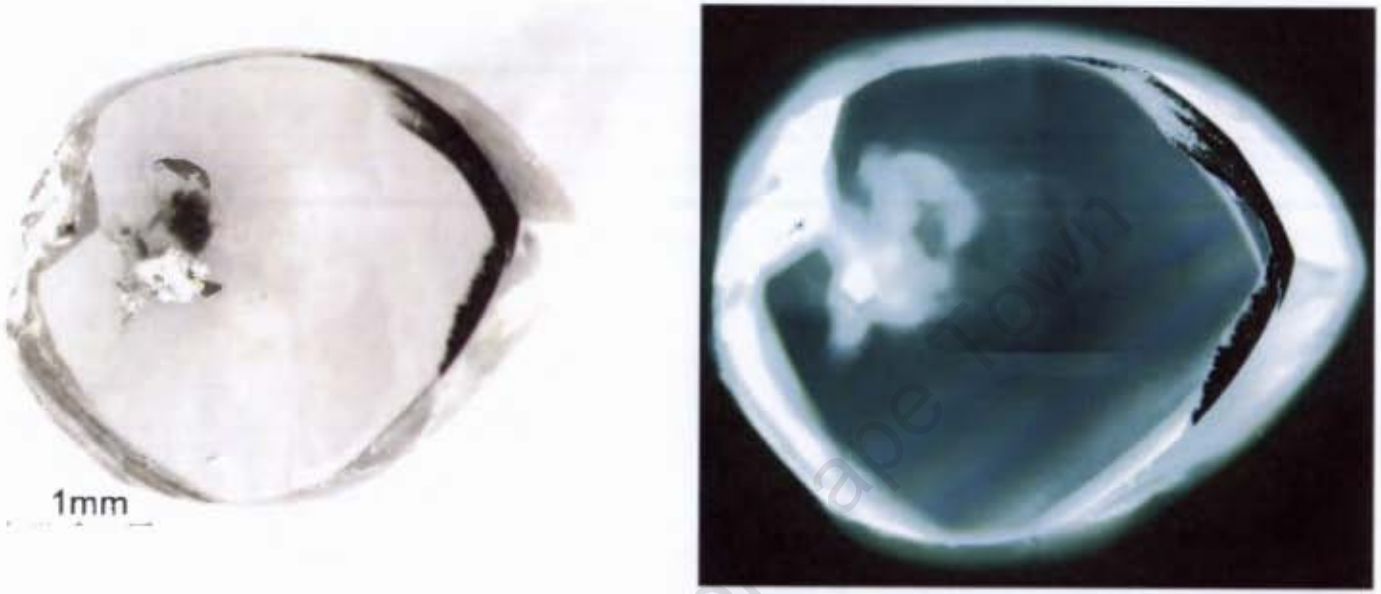

EL33 front

EL33 back

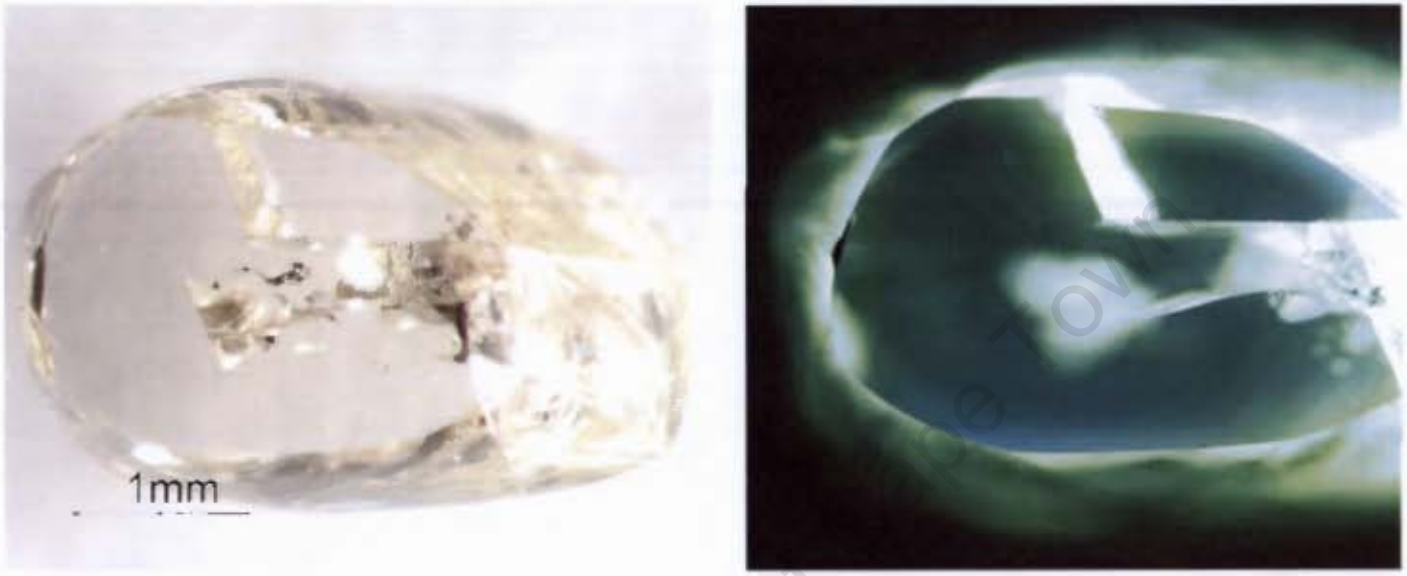

EL34 front

EL34 back

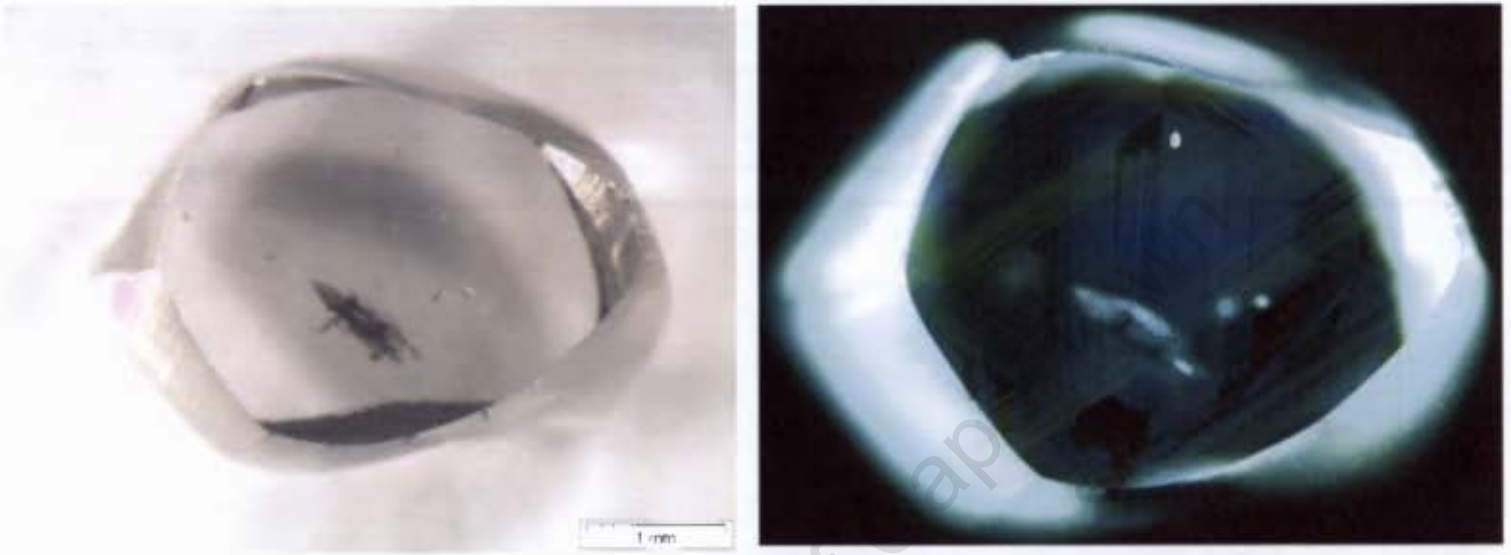

EL35 front

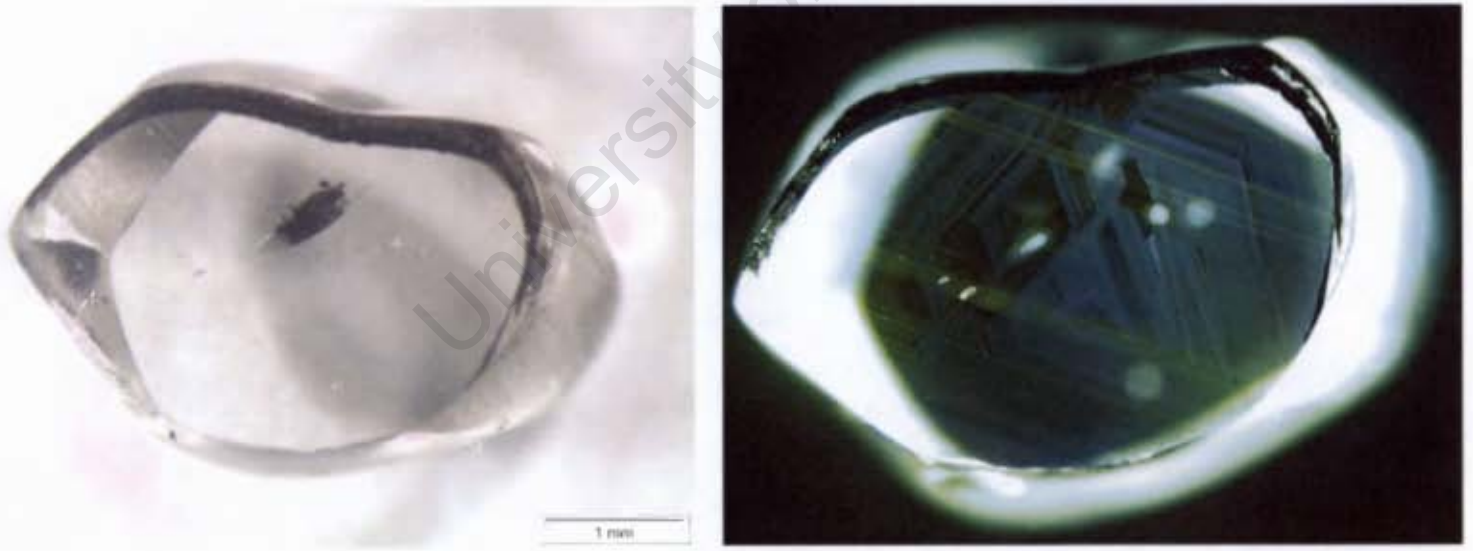

EL35 back

EL36 front

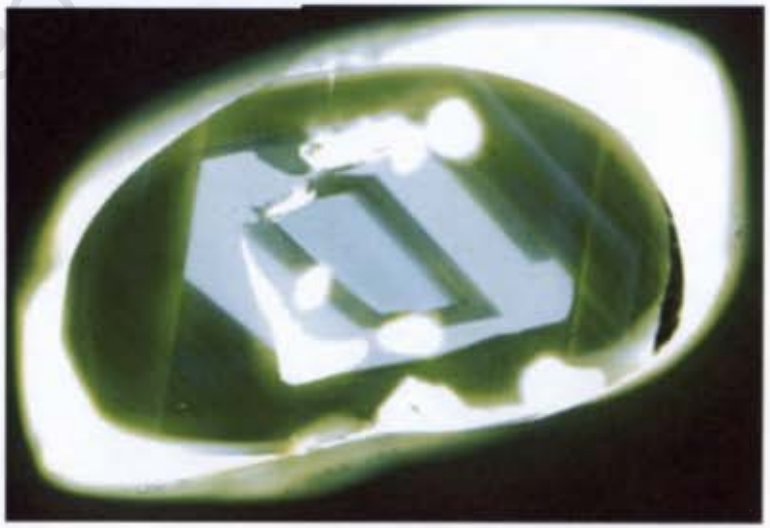

EL36 back

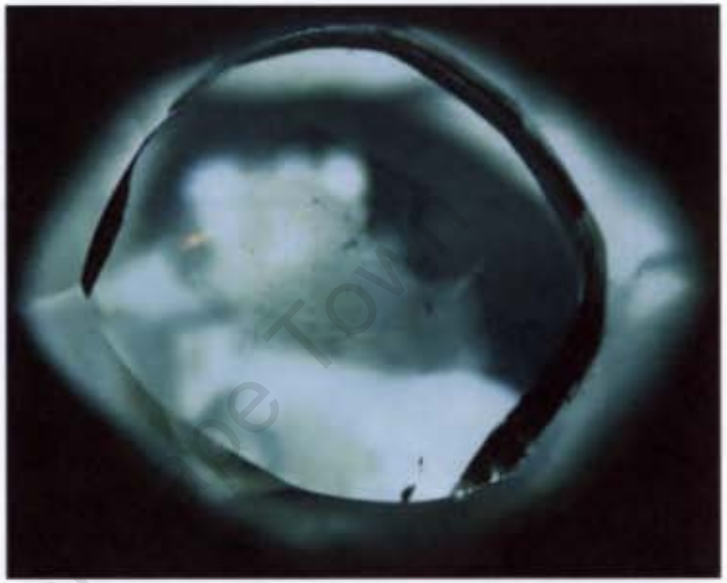

EL38 front

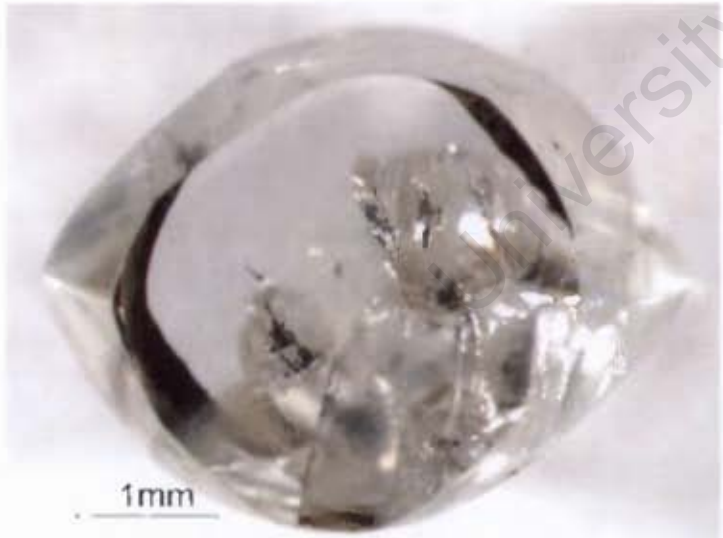

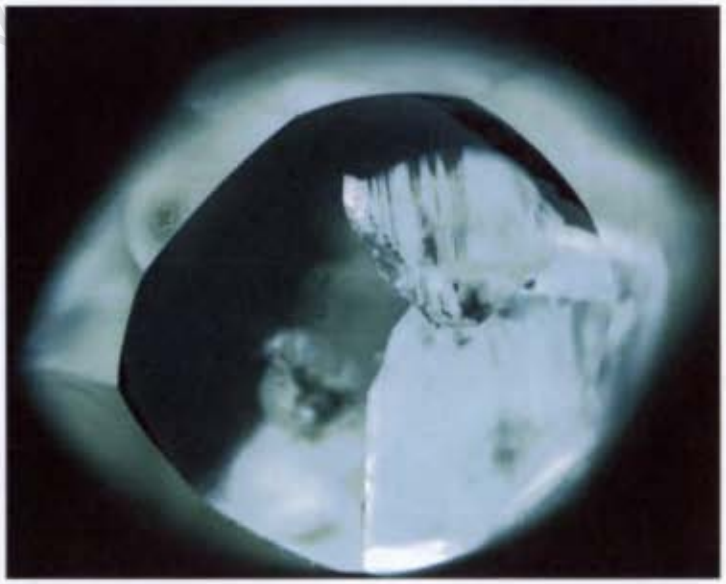

EL38 back

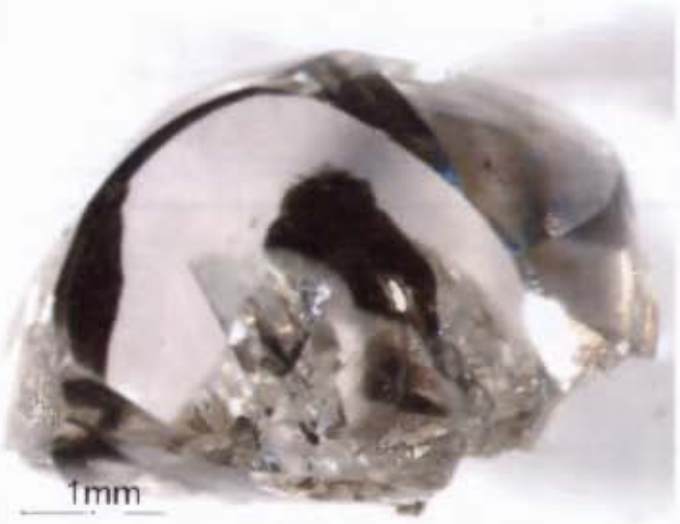

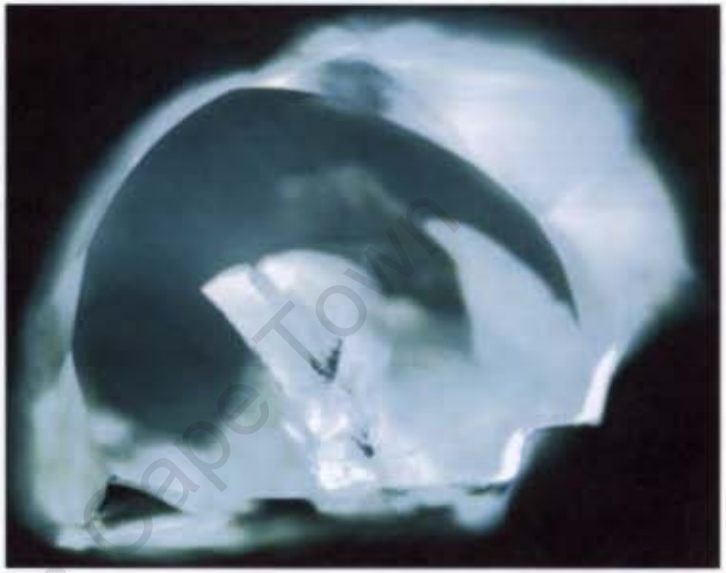

FL43 front

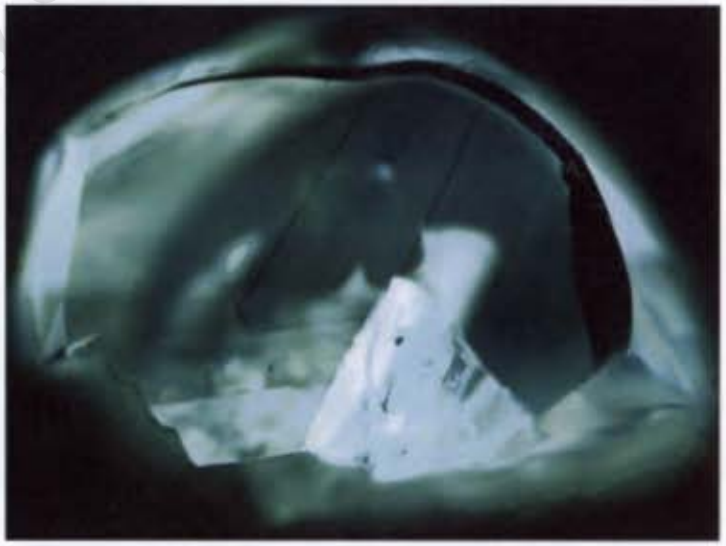

FL43 back

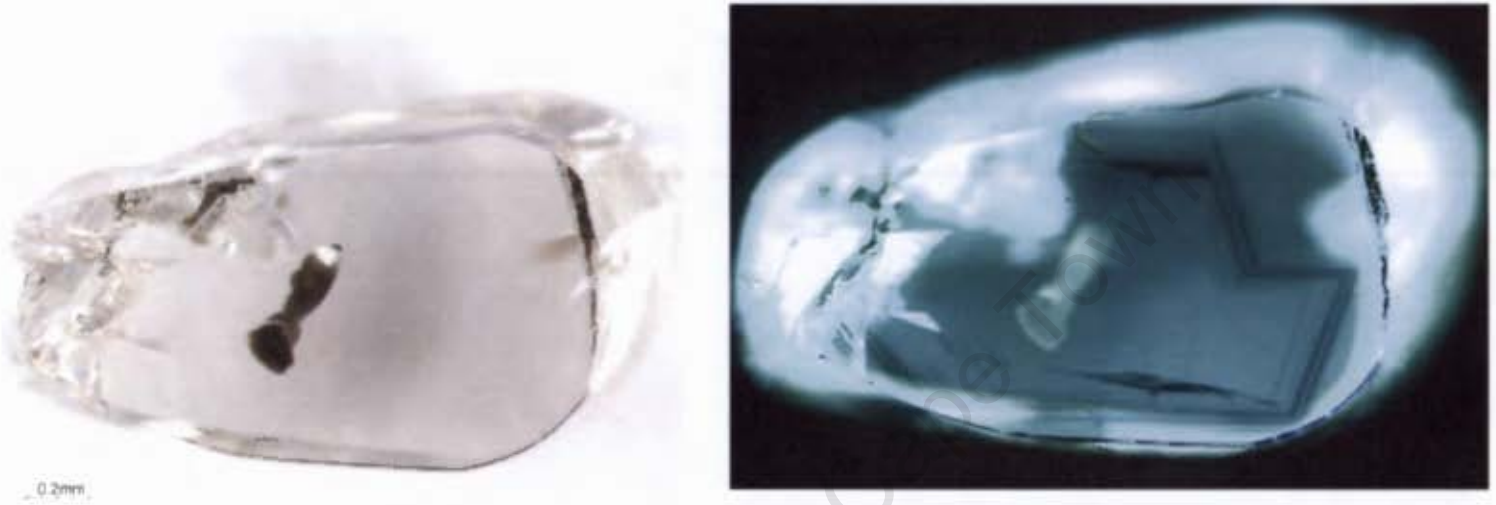

EL50 front

EL50 back

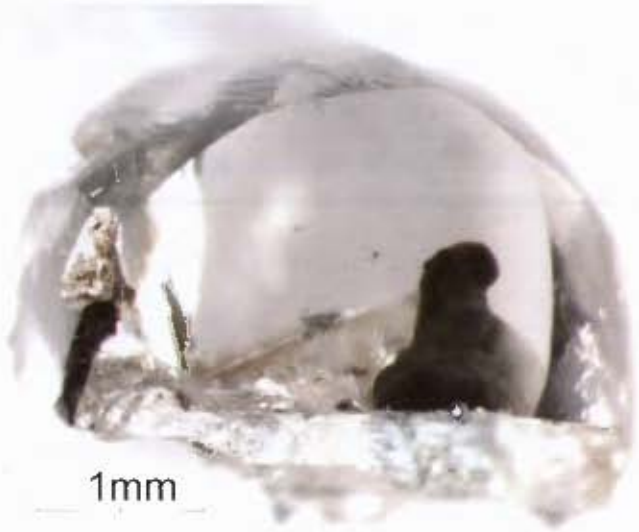

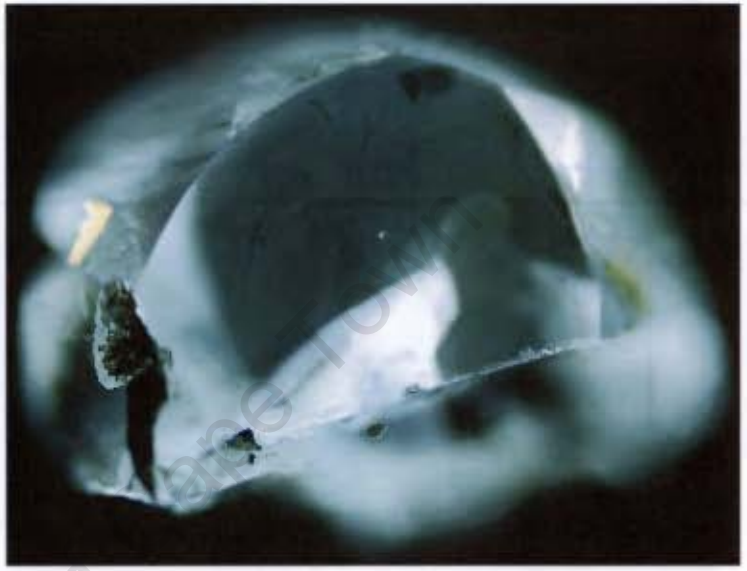

EL51 front

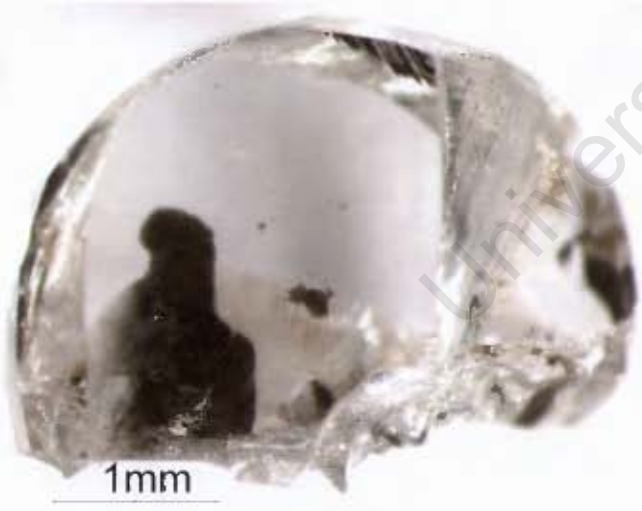

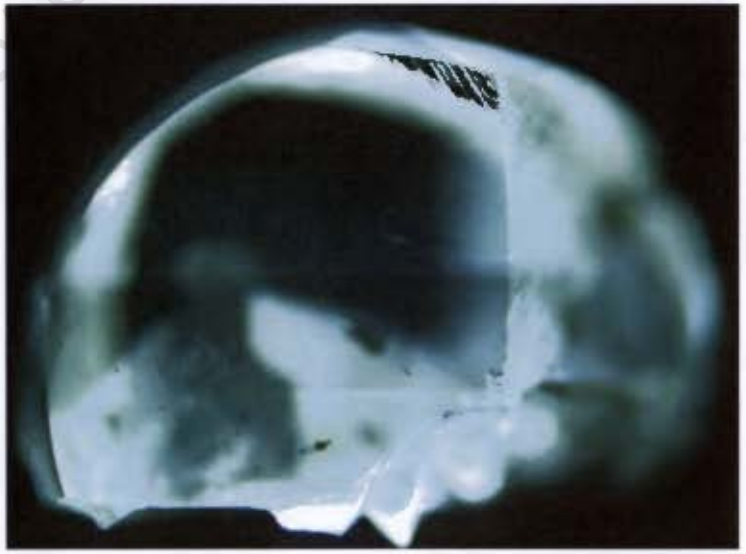

EL51 back

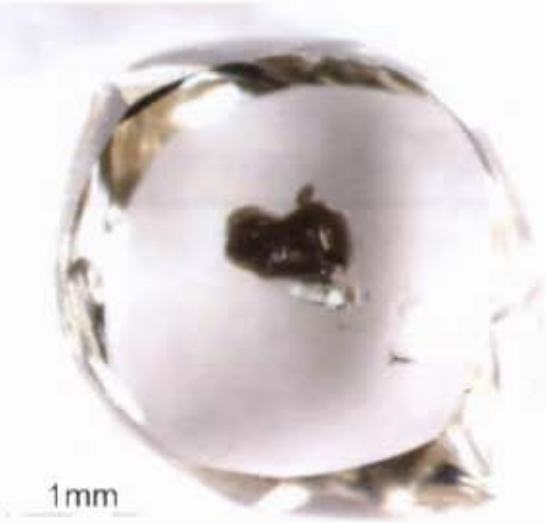

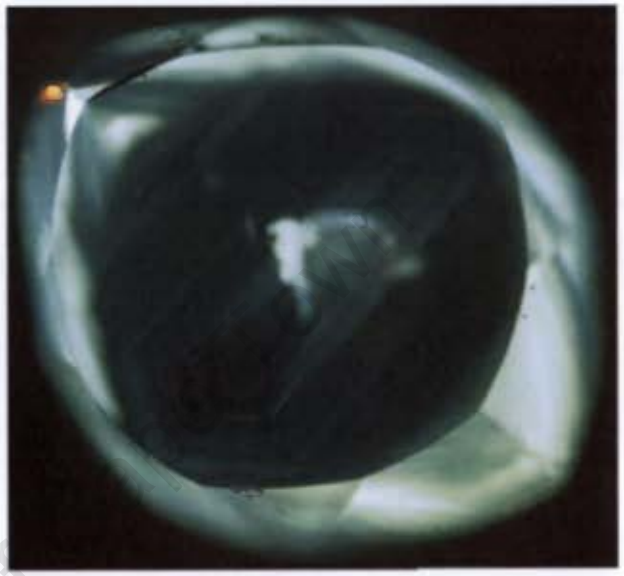

EL52 front

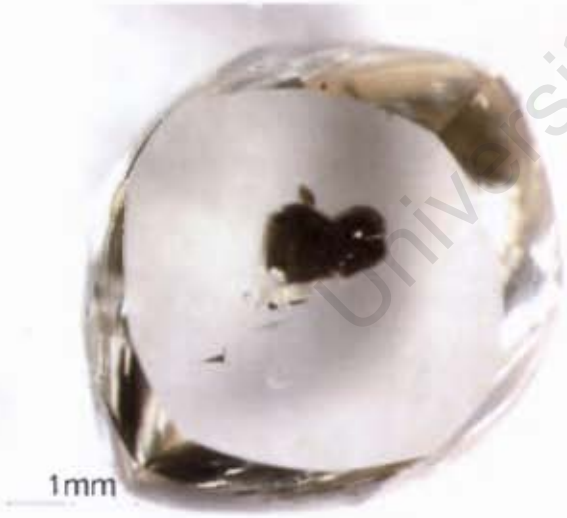

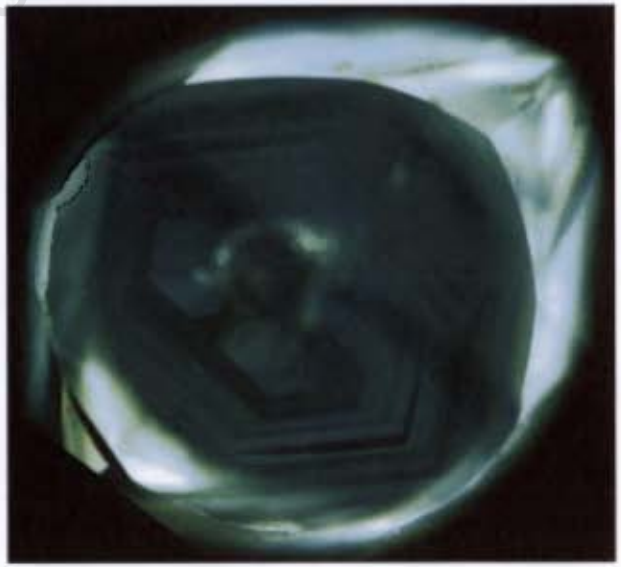

EL52 back

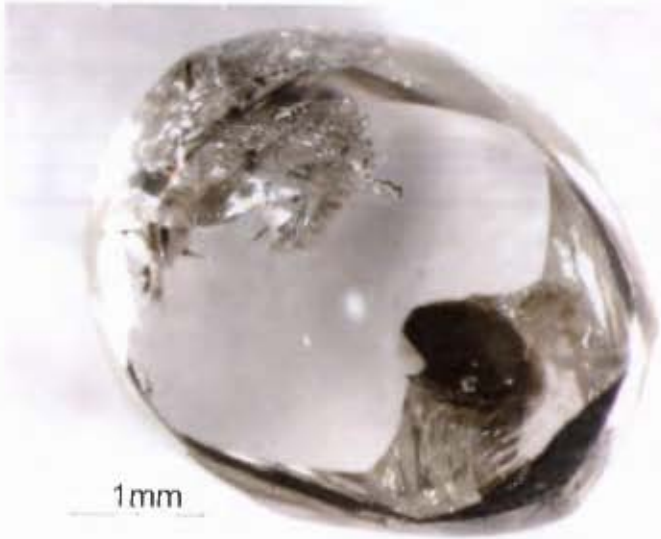

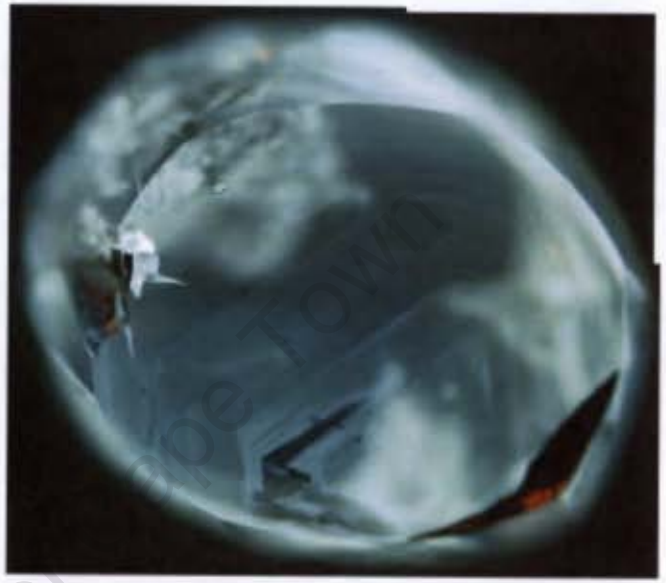

EL53 front

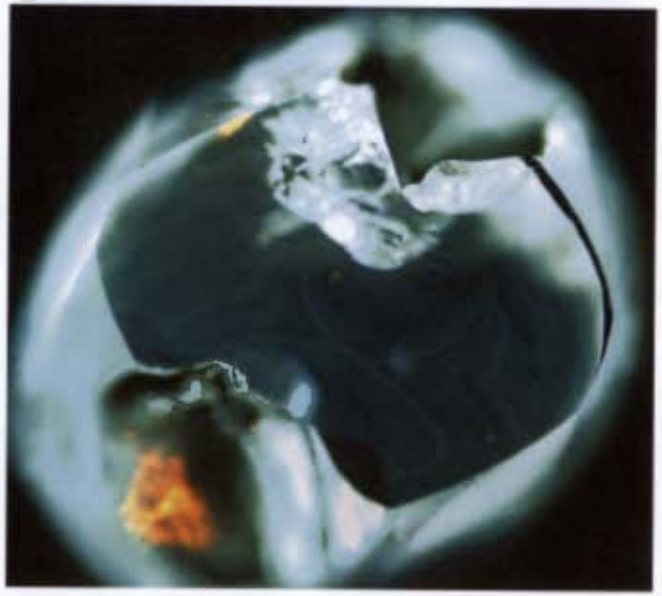

EL53 back

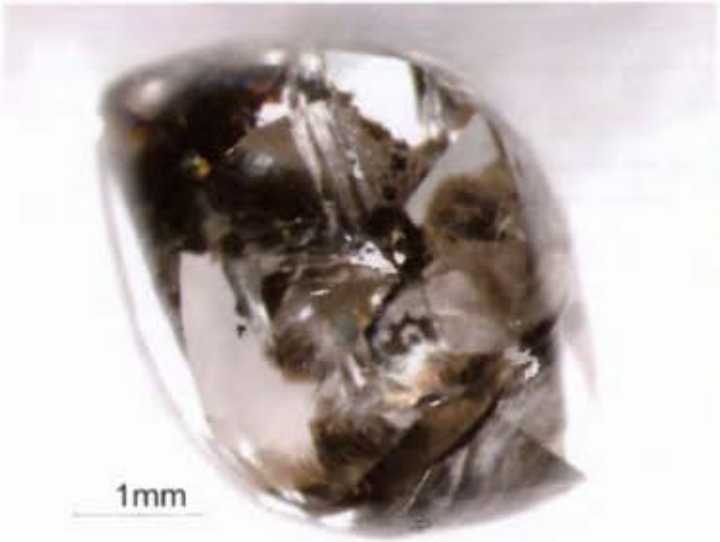

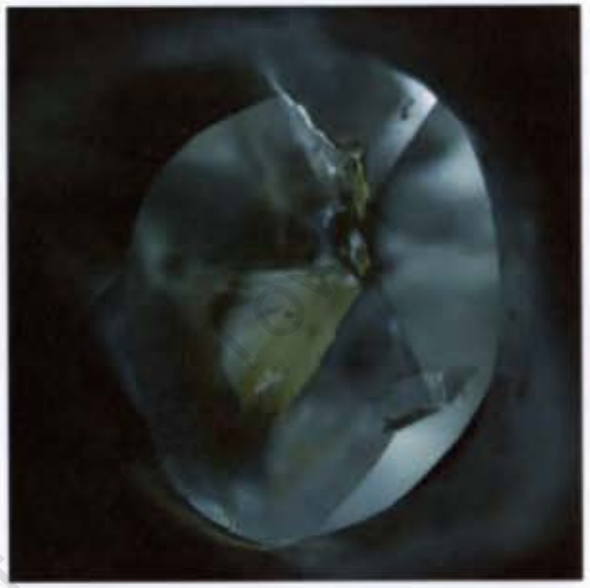

EL54 front

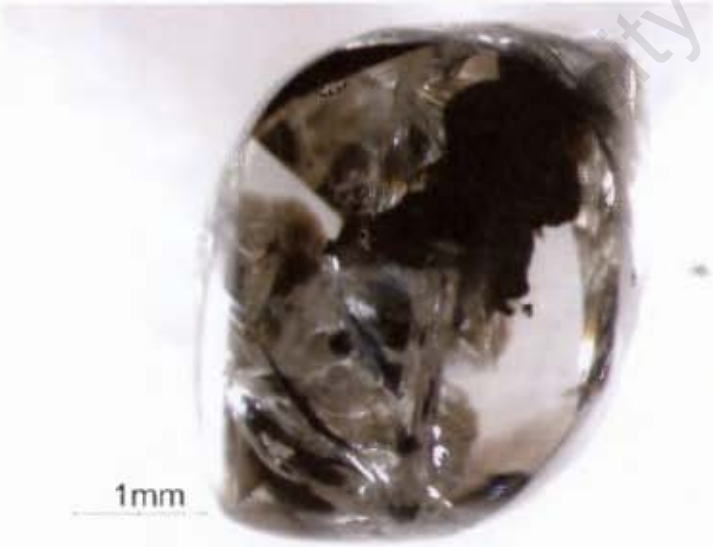

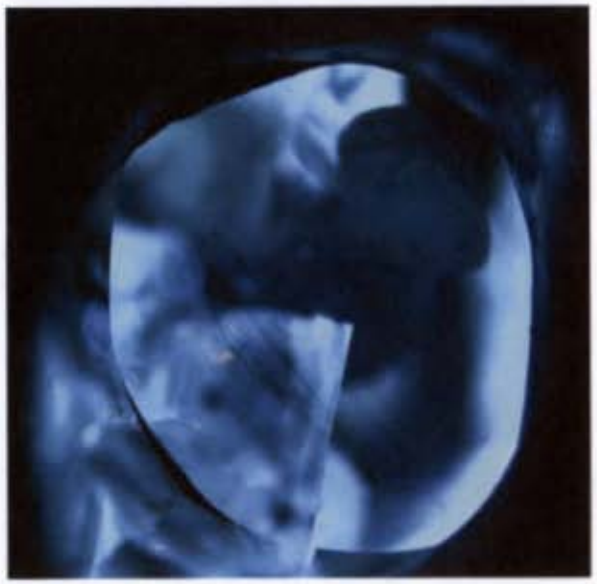

EL54 back

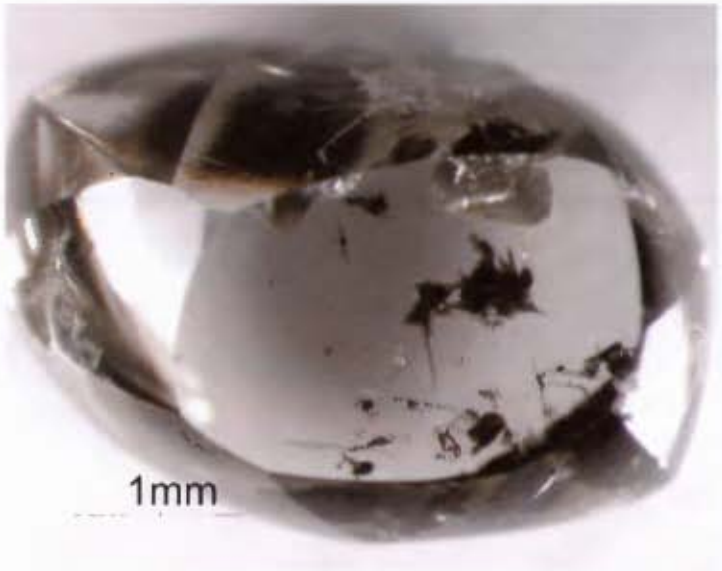

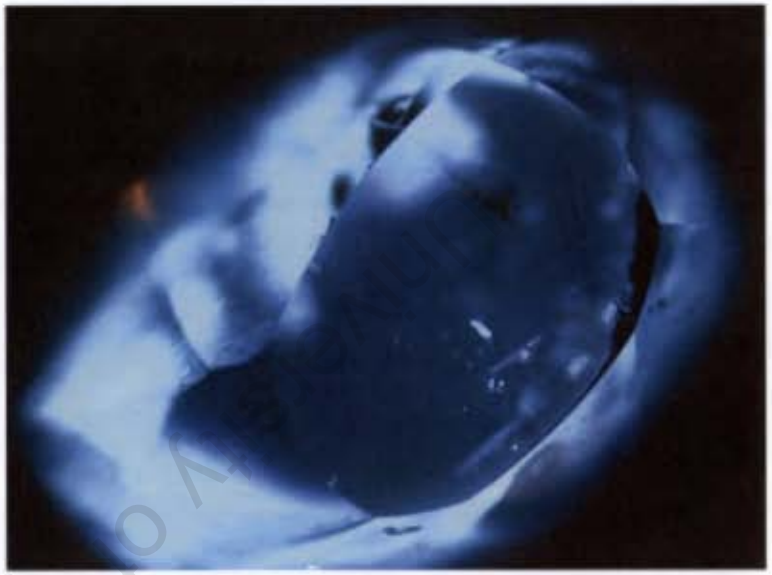

EL55 front

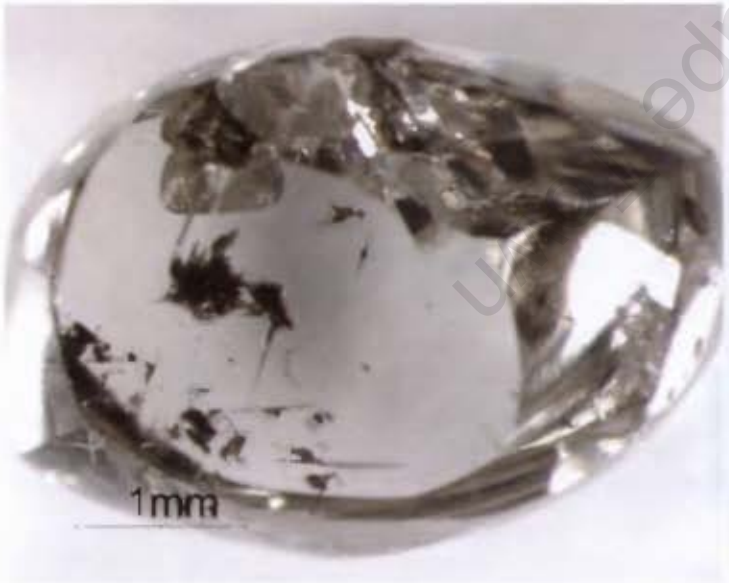

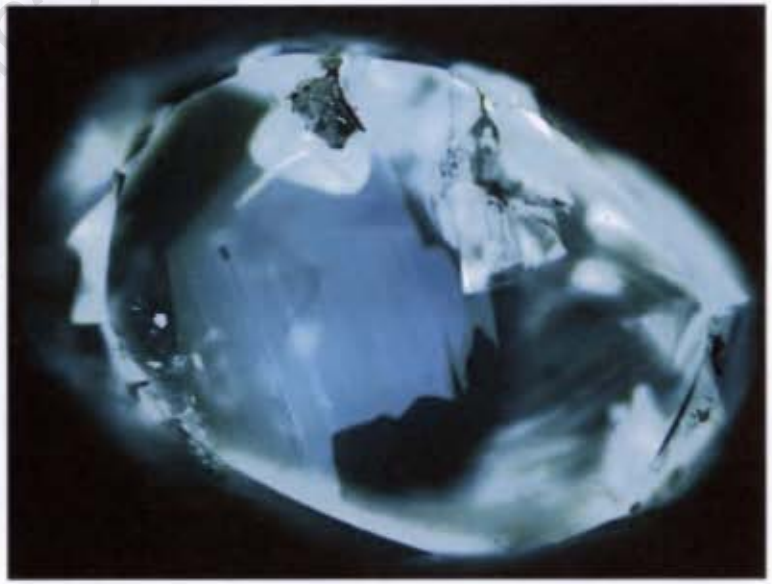

EL55 back

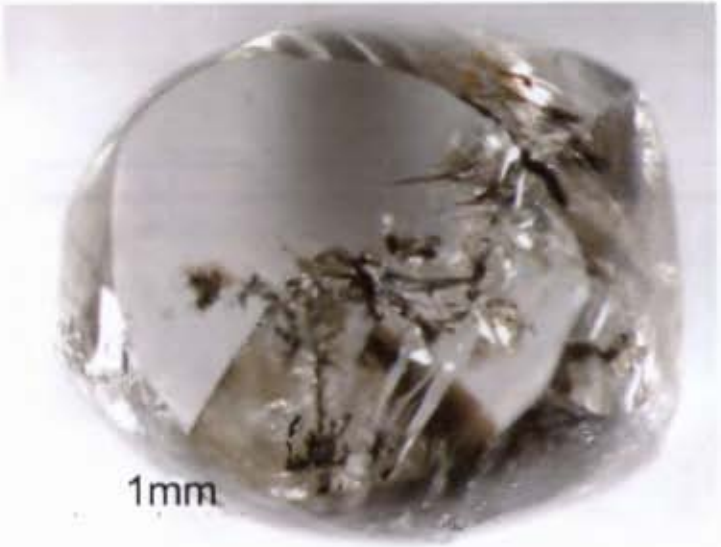

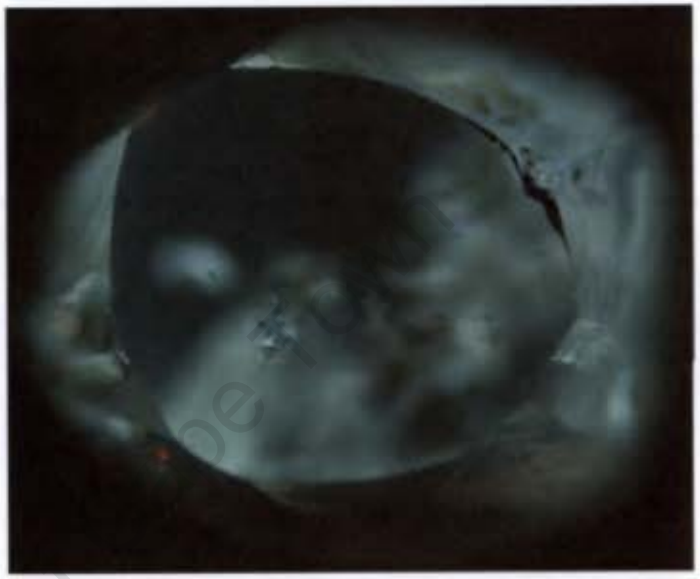

EL56 front

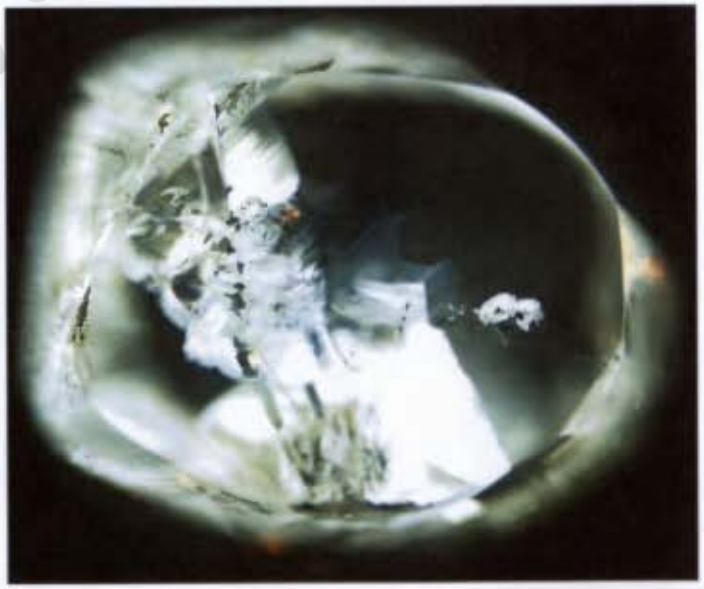

EL56 back

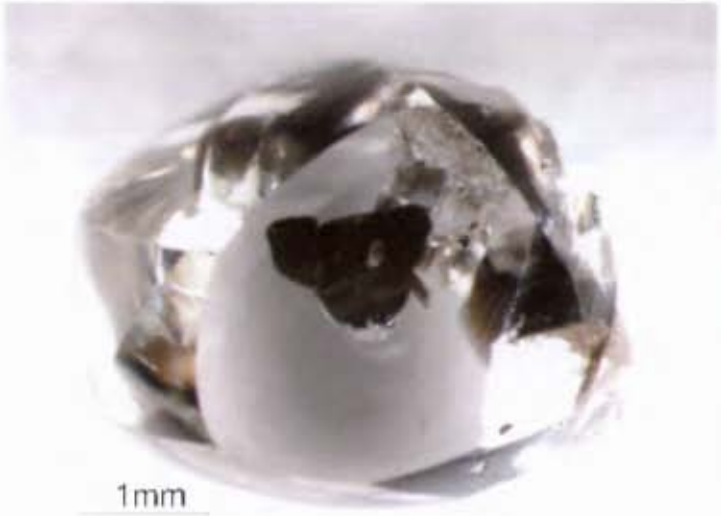

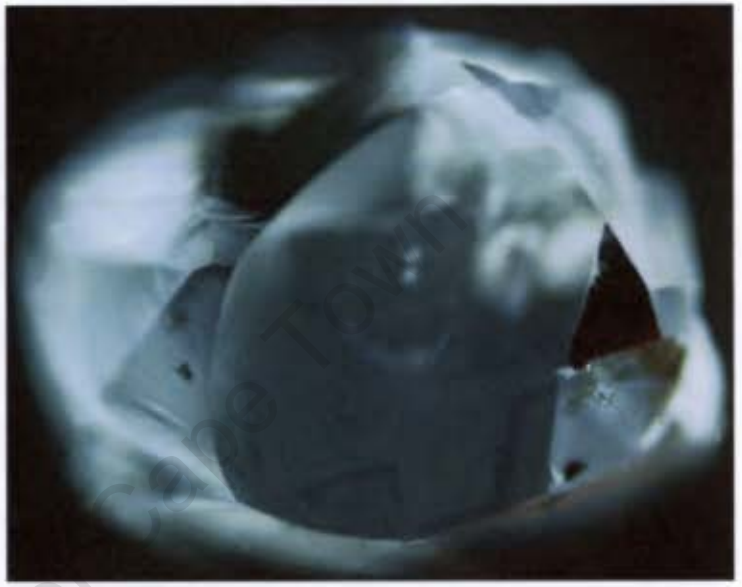

EL57 front

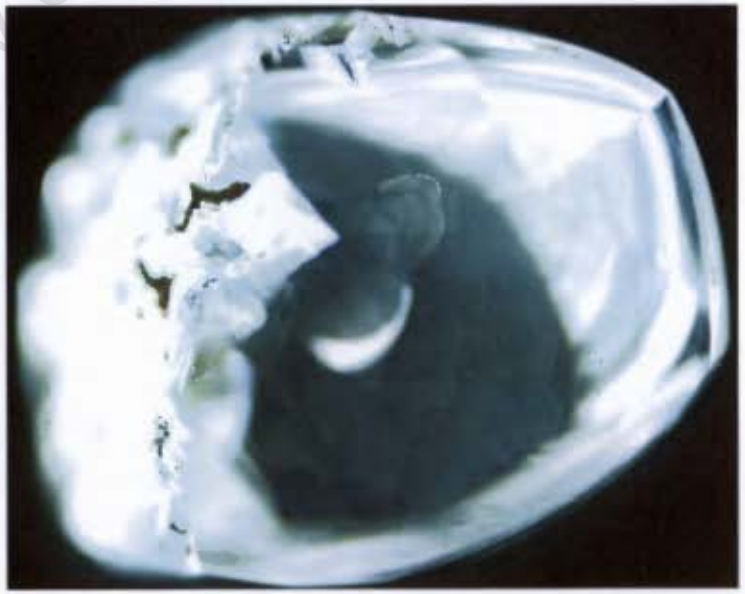

EL57 back

EL59

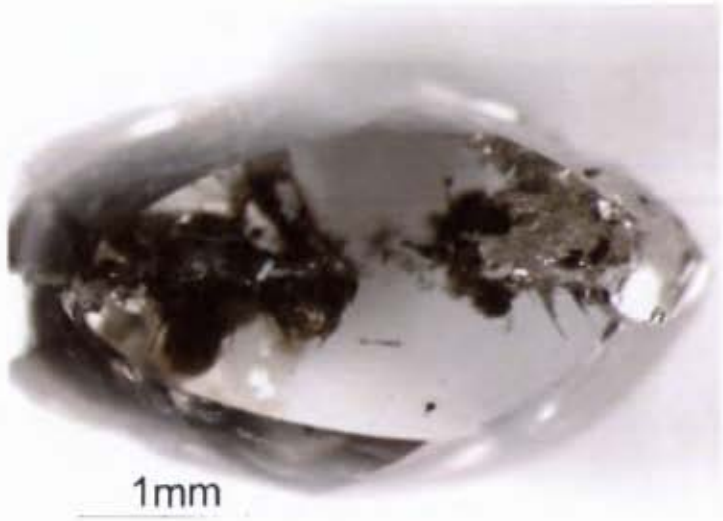

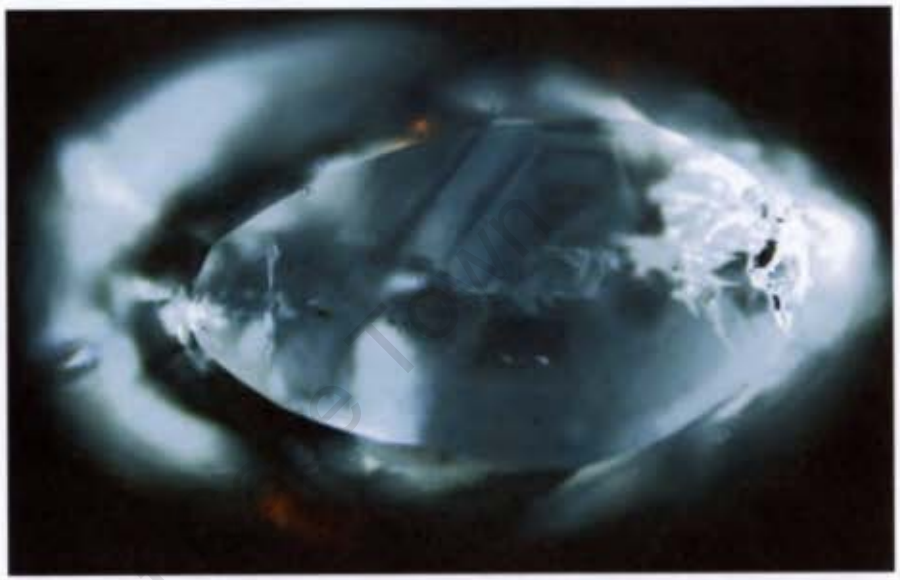

EL60 front

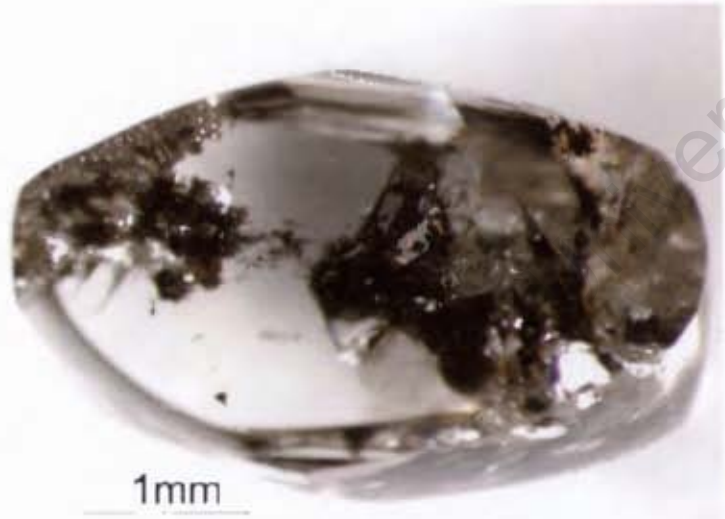

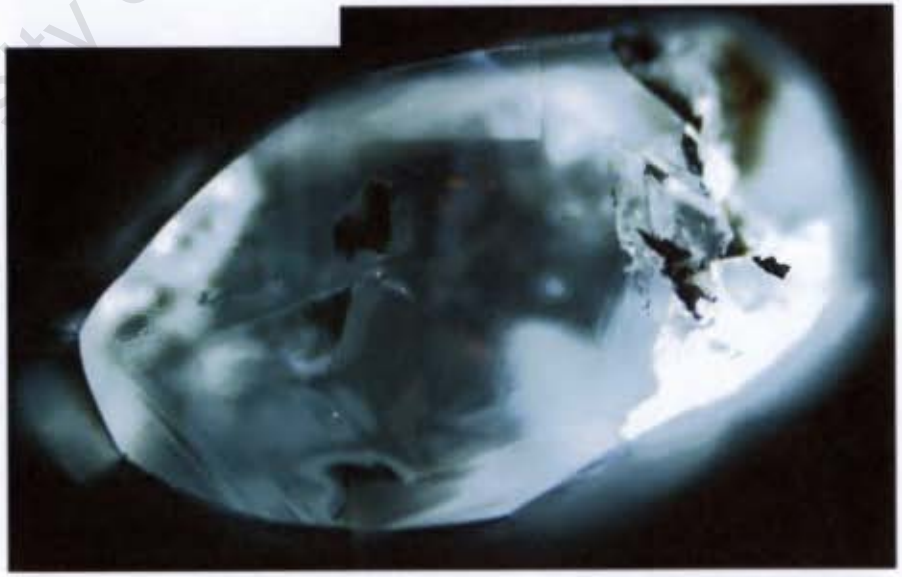

EL60 back

1mm

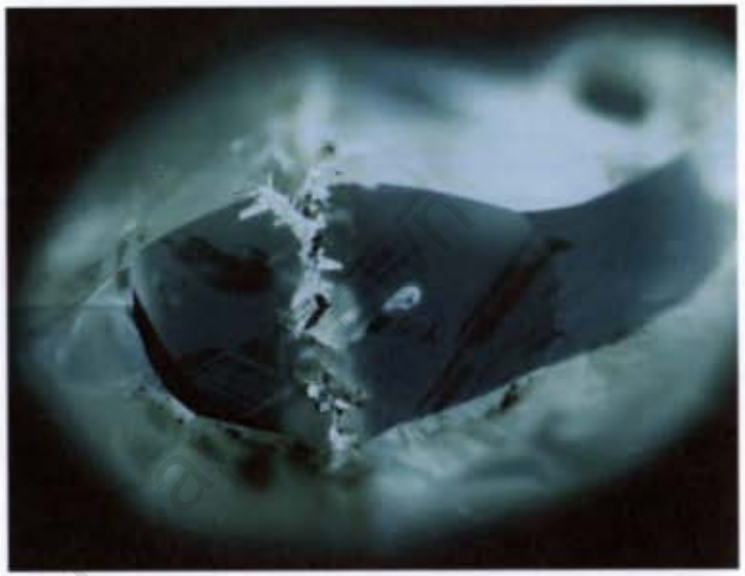

EL61 front

1mm

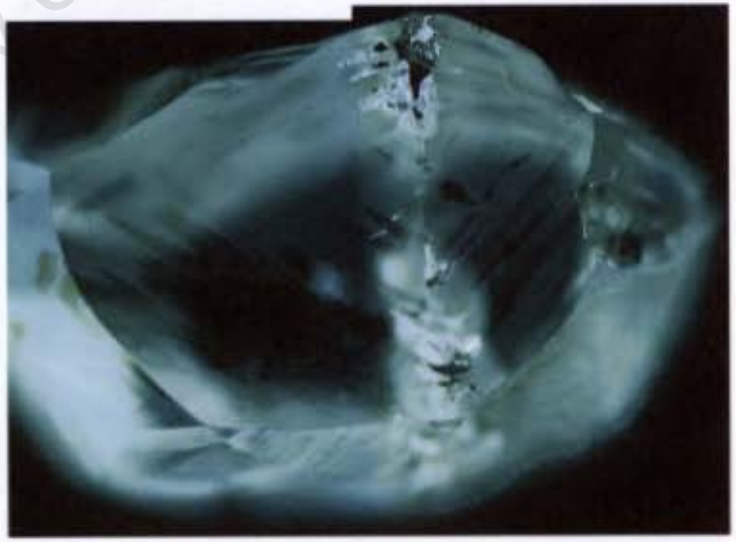

EL61 back

EL62 front

EL62 back

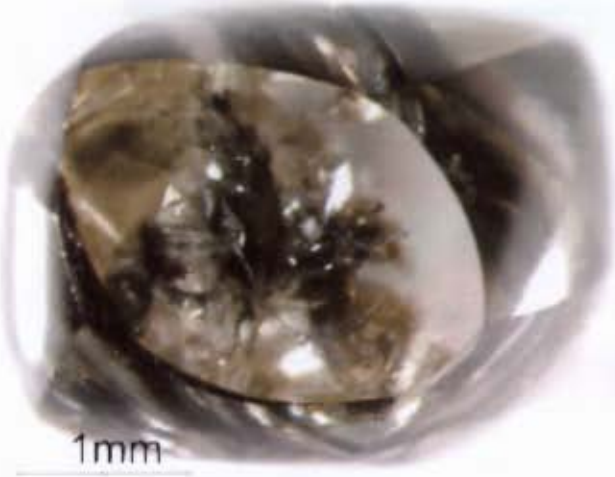

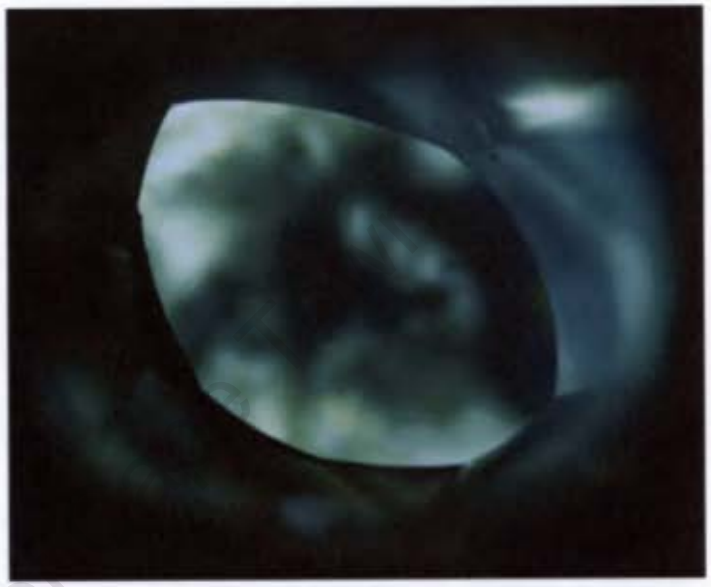

EL64 front

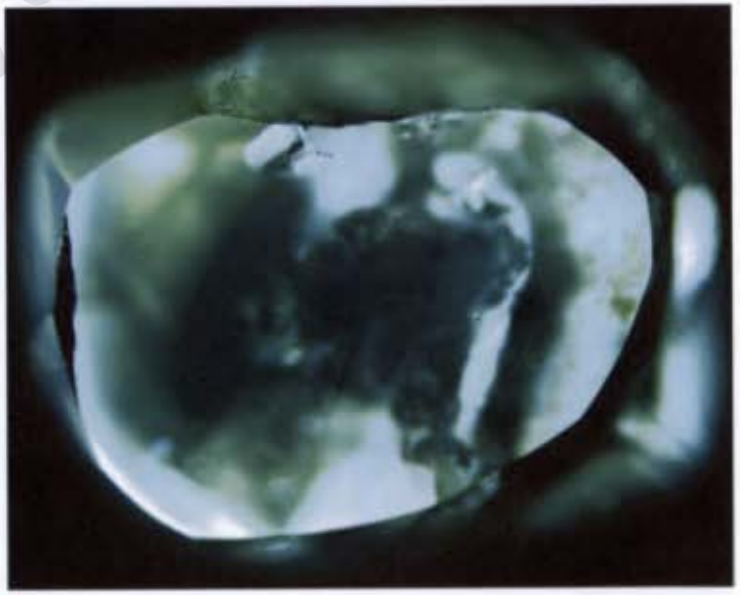

EL64 back

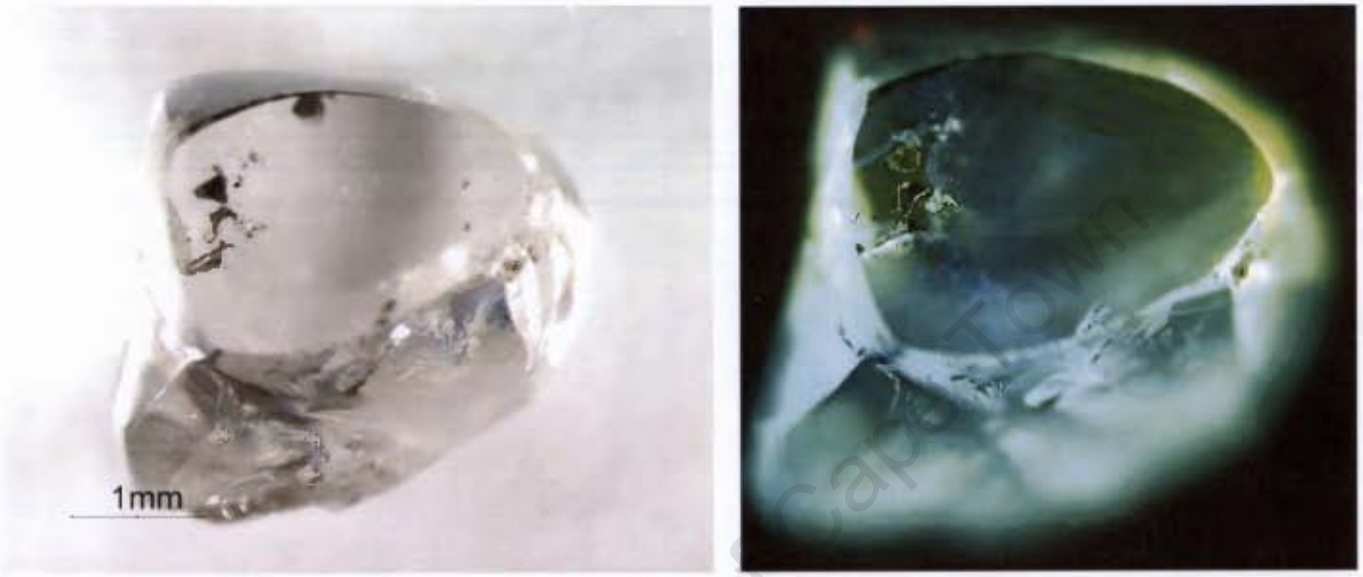

EL65 front

EL65 back

Fl 66 front

Fl 66 back

EL67 front

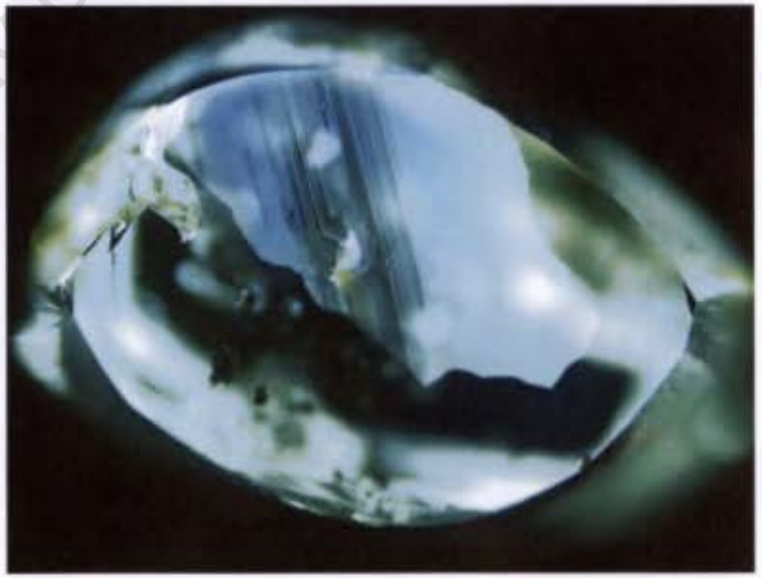

EL67 back

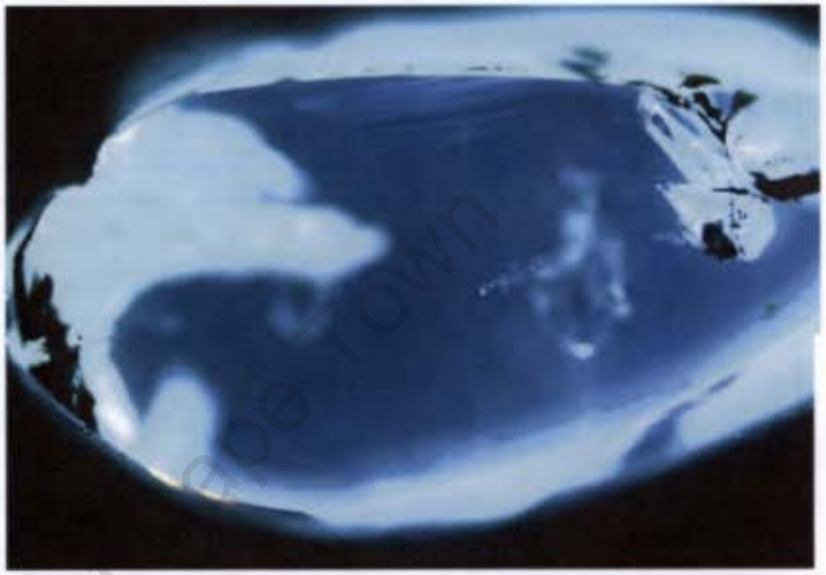

EL69 front

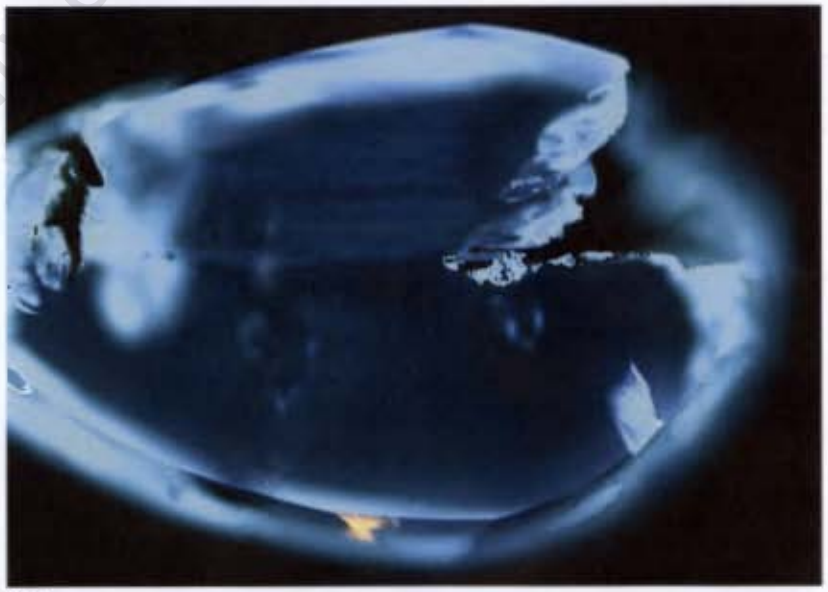

EL69 back